"FDT" Violation in Proteins

by

Salman Seyedi

A Dissertation Presented in Partial Fulfillment
of the Requirements for the Degree
Doctor of Philosophy

Approved June 2018 by the
Graduate Supervisory Committee:

Dmitry V. Matyushov, Chair
Oliver Beckstein
Sara M. Vaiana
Robert Ros

ARIZONA STATE UNIVERSITY

December 2018

ABSTRACT

Bio-molecules and proteins are building blocks of life as is known, and understanding their dynamics and functions are necessary to better understand life and improve its quality. While ergodicity and fluctuation dissipation theorem (FDT) are fundamental and crucial concepts regarding study of dynamics of systems in equilibrium, biological function is not possible in equilibrium.

In this work, dynamical and orientational structural crossovers in low-temperature glycerol are investigated. A sudden and notable increase in the orientational Kirkwood factor and the dielectric constant is observed, which appears in the same range of temperatures that dynamic crossover of translational and rotational dynamics occur.

Theory and electrochemistry of cytochrome c is also investigated. The seeming discrepancy in reorganization energies of protein electron transfer produced by atomistic simulations and those reported by protein electrochemistry (which are smaller) is resolved. It is proposed in this thesis that ergodicity breaking results in an effective reorganization energy (0.57 eV) consistent with experiment.

Ergodicity breaking also affects the iron displacement in heme proteins. A model for dynamical transition of atomic displacements in proteins is provided. Different temperatures for rotational and translational crossovers of water molecules are reported, which all are ergodicity breaking transitions depending on the corresponding observation windows. The comparison with Mössbauer spectroscopy is presented.

Biological function at low temperatures and its termination is also investigated in this research. Here, it is proposed that ergodicity breaking gives rise to the violation of the FDT, and this violation is maintained in the entire range of physiological temperatures for cytochrome c. Below the crossover temperature, the protein returns to the FDT, which leads to a sudden jump in the activation barrier for electron

transfer.

Finally the interaction of charges in dielectric materials is discussed. It is shown that the potential of mean force between ions in polar liquids becomes oscillatory at short distances.

Dedicated to:

Mojgan, Mostafa, Khadij & Reza

ACKNOWLEDGMENTS

I would like to express my sincere appreciation to Prof. Dmitry V. Matyushov for the guidance and help he has patiently provided to me at every level. He has been a role model for me in scientific integrity and curiosity. Next, I must thank all my group-mates whom I have learned a lot from in our mutual projects and through our exciting discussions, namely Dr. Daniel Martin, Dr. Mohammadhasan Dinpajooh, and Morteza Moghimi. I would also like to express my gratitude to my committee members: Professors Robert Ros, Oliver Beckstein, and Sara Vaiana for their very valuable time and their insights as I progressed through the program. Furthermore, I would like to acknowledge the ASU personnel, in general, and those in physics department and biophysics center, in particular, whose work facilitated my PhD journey. Finally, I would like to thank my family and friends for all the support they provided to me and everything they did to assist me in ways that are too many to name.

GLOSSARY

Cyt-c Cytochrome Complex

ENS Elastic Neutron Scattering

Eq Equation

ET Electron Transfer

eV electron Volt

FDT Fluctuation Dissipation Theorem

Fig Figure

MD Molecular Dynamics

MSA Mean Spherical Approximation

MSD Mean Square Displacement

MSF Mean Square Fluctuations

NPT Number Pressure Temperature, an ensemble with constant values of Number of particles, Pressure and Temperature

NS Neutron Scattering

ns nano second

NVE Number Volume Energy, an ensemble with constant values of Number of particles, Volume and Energy

NVT Number Volume Temperature, an ensemble with constant values of Number of particles, Volume and Temperature

Ox Oxidized

PDT Protein Dynamical Transition

ps pico second

Red Reduced

SAM Self Assembled Mono-layer

ST Stocks

vdW van der Waals

TABLE OF CONTENTS

CHAPTER Page

CHAPTER Page

LIST OF TABLES

LIST OF FIGURES

Figure Page

Figure Page

Figure Page

Figure Page

Figure Page

Chapter 1

INTRODUCTION

1.1 FDT and its Violation

Fluctuation Dissipation Theory (FDT) is a very powerful tool in theoretical and experimental physics. The first example of FDT is probably provided by the Einstein famous paper on Brownian motion [31]. The Einstein relation reads $D = \mu k_B T$, where D is the diffusion constant, μ is mobility (characterizing the response of the system to a weak external force), k_B is the Boltzmann constant and T is the absolute temperature. More generally, the FDT relates the response of a system influenced by a small external perturbation to the instantaneous fluctuations of the unperturbed system by a proportionality factor, namely temperature. This property is main theme of the FDT which we come back to in many points in this work. For a system in equilibrium with the bath and assuming detailed balance, one can write ((1.1))[32]:

$$R_{AP}(t, t_0) = \frac{1}{k_B T} \frac{\delta}{\delta t_0} C_{AB}(t, t_0) \theta(t - t_0) \tag{1.1}$$

Here

$$R_{AP}(t, t_0) = \delta A(t)/\delta P \tag{1.2}$$

represents the (impulse) response of the system to the impulse perturbation

$$\delta P(t, t_0) = \delta P \delta(t - t_0) \tag{1.3}$$

($\delta(t - t_0)$ is the Dirac delta function) and

$$C(t, t_0) = \langle A(t) B(t_0) \rangle \tag{1.4}$$

is the correlation of the observables A and B (with B coupled with P in Hamiltonian $H(t) = H_0 - P(t)B$). (One can always choose observables in a way to have a mean of zero $\langle A\rangle = \langle B\rangle = 0$ without losing the generality and this is what assumed here). Heaviside function $\theta(t - t_0)$ insures that causality is satisfied. For simplicity we consider A and B to be the same variable $A = B$. Assuming a step function for perturbation $\delta P(t) = \delta P\theta(t)$, one can integrate over t_0 from 0 to t to get

$$\chi(t) = \frac{1}{k_B T}(C(0) - C(t)) \tag{1.5}$$

where $\chi(t) = \int_0^t R(t, t_0)dt_0$ is the (integrated) response $\chi(t) = \langle A\rangle_t/\delta P$. This equation ((1.5)) is a fluctuation dissipation relation connecting dynamic variables for the classical equilibrium systems that satisfy detailed balance. The response term in this way is more accessible by experiment. The importance of this equation can be appreciated by recognizing the involved terms. Its applicability is broad because it gives you access to response of the system through the system dynamics and vise versa. In the static limit $t \to \infty$, $C(t)$ goes to zero and one gets [33]

$$\chi = \frac{1}{k_B T}\langle A^2\rangle \tag{1.6}$$

One can get the temperature from (eq. (1.5)) by plotting the response vs correlation. The results give a line with the slope of $s_0 = -\frac{1}{k_B T}$, so one can calculate the temperature T using the slope s_0. When in equilibrium, for a given energy, all configurations of the system will be visited by equal probability, and the temperature is the well defined value corresponding to the state of the system and the energy gained with particles by fluctuations is lost through dissipation. Any deviation from a line with slope s_0 is indicative of being out of equilibrium and violation of the fluctuation dissipation theorem. This deviation from equilibrium state disturbs both the thermodynamic description of the system and the system's temperature as a well defined thermodynamic parameter.

While there is no unified description for out of equilibrium systems, the intuition from the equations and definitions in the equilibrium state have been fruitful. As a result, many fluctuation dissipation relations have been used for non-equilibrium systems. There are good reviews on the subject (for instance, [34][35][36]) and the interested reader would find them very informative. Here, only a glimpse of the concept of effective temperature is presented.

One of the ways people used is the definition of an effective (fictive) temperature out of the deviation from FDT [37][38]. Literature on glassy systems[39] was among those proposing the use of an effective temperature and the mean field spin-glass models, are among those exactly solvable models [40][41]. The advantage of using (eq. (1.1)) is in providing a way to connect to the experimental investigation of the concept, which was done very recently for a system in non-equilibrium steady state[42].

While one sees the use of effective temperature in systems with broken ergodicity, the appearance of it is suggestive of the presence of ergodicity at some scale in the system. One needs to recognize that while the use of the effective temperature has been quiet helpful in describing different dynamics in many non-equilibrium and glassy [43] systems, the price one has to pay is that these temperatures are not definite for a given state of the system, and the effective temperature depends on the chosen variable in fluctuation dissipation relation. The different dynamics inside the system lead to different effective temperatures [44]. This violation of the FDT and the division into different dynamics (and so different time scales) can give rise to different behaviors of systems which are investigated in the following chapters (specifically look at Kirkwood factor jump in glycerol in lower temperatures Fig. 2.7 [45], figures 3.10 and 3.12 [46], Fig. 4.3 [15], and maybe most ilustrative of all, figure 5.1 [47]). We will see how mean square displacement(MSD) and dynamics of the system

follows FDT at low temperatures, and how at some temperature we see a deviation from the linear dependence and how it can be described by the provided theoretical framework. Also we see how FDT leads to termination of biological activity of the protein and why FDT violation seen in reorganization energies makes the biological activities possible and how the same theoretical framework (ergodicity breaking) can be utilized to describe these behaviors. This is the general theme of the whole of this work. Now lets move on starting with the basics of neutron scattering.

1.2 Neutron Scattering

To study any microscopic system, the interest is to know the relative position and motion of particles which are building the system, in other words one wants to know the structure and dynamics of the system. Depending on the properties of the system of interest (such as spacial and time scale of subsystems) and the amount of the required details, one can select techniques or tools that are suitable for the study. These techniques have many limitations and often a combination of them, accompanied with a lot of hard work of scientists and brilliant ideas, is the only way to improve the knowledge on a system.

One of the very important and useful tools which is suitable for studying many systems including liquids and biological systems, is neutron scattering, which is the focus of this chapter.

1.2.1 Why Neutrons

In this section the basic characteristics of the neutron scattering are provided.

Advantages and Disadvantages

Neutron has $m \sim 1.67 \times 10^{-27}kg$ (N), zero electric charge and zero (or negligible) electric dipole. Neutron, unlike the electrons and photons, does not interact with charged particles via electromagnetic interaction, but rather through very short range strong forces with nuclei, which makes it uniquely useful. Since the size of nuclei is typically 10^5 times smaller than their relative distances, neutrons can penetrate much deeper into the material and so reveal the properties deeper in the bulk rather that just a shallow surface. Moreover, because of the small cross section and short range forces, compared to the wavelength of neutrons (or size of system under investigation), the scattering centers can be considered as point particles. In other words, for neutron scattering, a nucleus can be considered as a point scatterer. Also, because neutrons have small absorption and small cross section with some materials, it is easier to control temperatures or other properties related, for example, to the sample holder and its environment.

Neutron also interacts hugely differently with different nuclei which provides the key advantage of being able to select the particles of interest for measurement using different isotopes. For instance, the cross section of a proton (82.03 barn) [1] is hugely bigger than that of a deuteron (7.64 barn), so by replacing some hydrogen atoms with deuterons the properties of the system are (mostly) conserved, but the subsection with deuterons can be considered invisible in comparison with the part with protons (for comparison, carbon scattering cross section is 5.551 barn). This trick is quite popular in neutron scattering studies of many molecules and of mixed systems.

Neutrons can cover a wide range of system sizes. For liquids or biological studies, cold and thermal neutrons are of most interest with ranges of wavelength from about

[1] Each barn is equal to 10^{-28} m^2. Different cross section values (coherent, incoherent and averages) of different elements can be found in Evaluated Nuclear Data File (ENDF) online database or "Barn Book"s.

1 Å up to 2 nm. The relative energy and energy transfer in this range is relatively small and measurement does not destroy the system.

While neutrons have many useful properties, they have their limitations as well. The small cross section, which was discussed as a huge advantage, means small interaction and small interaction means a need for more flux and time for measurements and also bigger samples, which can bring more limitations. The neutron sources are limited to the nuclear reactors and particle accelerators, which makes them quite expensive tools. The need for high flux/time and expensive sources are among the most important limitations of the neutron scattering. Also, neutron interaction is weak, which makes them harder to detect.

1.2.2 Basics of Neutron Scattering

The interpretation of neutron scattering data, and designing various experiments and techniques in the field, is based on the works led by Van Hove's paper [48], followed by the works of others. In this section, an attempt is made to provide steps, which guide the reader through the fundamental equations with self-consistency. The details of the calculations can be found in textbooks. Then, different sources of neutrons will be described and some techniques will be briefly discussed.

Theory

Here, the mathematical basics of the neutron scattering is provided. We start by representing the incident beam in the form of a plane wave (Eq. (1.7))

$$\boldsymbol{\psi} = \frac{1}{\sqrt{L^3}} \exp(i\mathbf{k}.\mathbf{r}) \tag{1.7}$$

where $\mathbf{k}$ is the wave-vector, $\mathbf{r}$ is the position and L is the size of the box which contains the neutron and the scatterer (This is a normalization factor which will disappear from

equations at the end). The differential cross section $\frac{d^2\sigma}{d\Omega dE'}$ is defined as the ratio of number of particles (here neutrons) with energies in a differential small range dE' from E' scattered per second into differential solid angle $d\Omega$ in the direction (θ, ϕ) divided by incident flux, differential solid angle $d\Omega$ and differential Energy interval dE'. Flux of incident neutrons comes as (Eq. (1.8))

$$\mathbf{\Phi} = \frac{1}{Volume} \times velocity = \frac{1}{L^3}\frac{\hbar \mathbf{k}}{m} \tag{1.8}$$

in which, m is the mass of the neutron. Writing the energy of a scattered neutron in terms of its wave-vector k' and some basic geometry, gives the density of the final state (Eq. (1.9))

$$\rho_{k'} = \frac{L^3 m k'}{(2\pi)^3 \hbar^2} d\Omega \tag{1.9}$$

Now, for the differential cross section, using the Fermi's golden rule one gets (Eq. (1.10))[49]

$$\left(\frac{d^2\sigma}{d\Omega dE'}\right)_{\lambda \to \lambda'} = \frac{k'}{k}\left(\frac{m}{2\pi\hbar^2}\right)^2 |\, \langle \mathbf{k}'\lambda' | \mathbf{V} | \mathbf{k}\lambda \rangle \,|^2 \delta(\Delta E_s + \Delta E_n) L^6 \tag{1.10}$$

(Eq. 2.15 of [49]), where, V gives the interaction/perturbation potential, ΔE_s is the energy change in the scattering system, $\Delta E_n = E - E'$, δ is delta-function, and λ and λ' are the labels of the energy states of the scattering system, before and after interaction, respectively. Now, assuming that the interactions are very short ranged (which is a reasonable assumption for strong interactions) and they only depend on the relative positions of the incident and scattering particle, and so substitution of scattering centres (nuclei) by delta functions and then Fourier transform V to the k space, following steps of reference [49] (in Born approximation regime, so Fermi pseudo-potential can be used), one gets (Eq. (1.11))[49]

$$\left(\frac{d^2\sigma}{d\Omega dE'}\right)_{\lambda\to\lambda'} = \frac{k'}{k}|\sum_j b_j \langle\lambda'|\exp(i\mathbf{q}.\mathbf{R_j})|\lambda\rangle|^2\delta(\Delta E_s + \Delta E_n) \tag{1.11}$$

Where the $\mathbf{q} = \mathbf{k} - \mathbf{k}'$ is proportional to the momentum transferred and the summation is over scattering centres while R_j represents the position of nucleus j, and b_j is the scattering length of the relevant nucleus. Now, by using the integral form of the delta-function and summing over λ' and averaging over λ (Boltzmann distribution), one gets (Eq. (1.12))[49]

$$\frac{d^2\sigma}{d\Omega dE'} = \frac{1}{h}\frac{k'}{k}\sum_{j,l} b_l b_j \int \langle\exp(-i\mathbf{q}.\mathbf{R}_l(0))\exp(i\mathbf{q}.\mathbf{R}_j(t))\rangle \exp(-i\omega t)dt \tag{1.12}$$

where, we have used $\omega\hbar = \Delta E_n$. Now, let's introduce two functions that are used very often in the literature, the intermediate scattering function $(I(\mathbf{q},t))$(Eq. (1.13)), and its Fourier-transform dynamic structure factor $(S(\mathbf{q},\omega))$ (Eq. (1.14))

$$I(\mathbf{q},t) = \frac{1}{N}\sum_{j,l}\langle\exp(-i\mathbf{q}.\mathbf{R}_l(0))\exp(i\mathbf{q}.\mathbf{R}_j(t))\rangle \tag{1.13}$$

$$S(\mathbf{q},\omega) = \frac{1}{h}\int I(\mathbf{q},t)\exp(-i\omega t)dt \tag{1.14}$$

where N is the number of scattering centres.

Assuming the scattering lengths of nuclei are uncorrelated and in the case that enough of them are present, they can be averaged (this average can be taken independently of the $< .. >$ average since the spin state of the nucleus is generally independent of its location). Then one can break the scattering cross section into two parts (Eq. (1.15))

$$\sum_{j,l}\langle b_j b_l\rangle NS_{jl} = \sum_{j,l}\langle b\rangle^2 NS_{jl} + \sum_j(\langle b^2\rangle - \langle b\rangle^2)NS_{jj} \tag{1.15}$$

By writing the two parts, namely coherent and incoherent, separately, we have(Eqs. (1.16) and (1.17)).

$$
\begin{aligned}
(\frac{d^2\sigma}{d\Omega dE'})_{coh} & \\
&= \langle b \rangle^2 \frac{1}{h}\frac{k'}{k}\sum_{jl}\int \langle \exp(-i\mathbf{q}.\mathbf{R}_l(0))\exp(i\mathbf{q}.\mathbf{R}_j(t))\rangle \exp(-i\omega t)dt \\
&= \frac{\sigma_{coh}}{4\pi}\frac{k'}{k}NS(\mathbf{q},\omega)
\end{aligned}
\tag{1.16}
$$

and

$$
\begin{aligned}
(\frac{d^2\sigma}{d\Omega dE'})_{incoh} & \\
&= (\langle b^2 \rangle - \langle b \rangle^2)\frac{1}{h}\frac{k'}{k}\sum_{j}\int \langle \exp(-i\mathbf{q}.\mathbf{R}_j(0))\exp(i\mathbf{q}.\mathbf{R}_j(t))\rangle \exp(-i\omega t)dt \\
&= \frac{\sigma_{incoh}}{4\pi}\frac{k'}{k}NS_s(\mathbf{q},\omega)
\end{aligned}
\tag{1.17}
$$

Here, $S_s(\mathbf{q},\omega)$ comes from $I_s(\mathbf{q},t)$ in which sub(s) denotes that the summation is taken only over cases where $j = l$. Moreover, $\sigma_{coh} = 4\pi \langle b \rangle^2$ and $\sigma_{incoh} = 4\pi(\langle b^2 \rangle - \langle b \rangle^2)$ are coherent and incoherent scattering cross sections, respectively (see footnote 1).

It is useful to introduce another important function, the time dependent pair correlation function $(G(\mathbf{r},t))$(also known as Van Hove function)(Eq. (1.18)),

$$
G(\mathbf{r},t) = \frac{1}{(2\pi)^3}\int I(\mathbf{q},t)\exp(-i\mathbf{q}.\mathbf{r})d\mathbf{q} \tag{1.18}
$$

So far, we have kept everything in the quantum form for the sake of completeness, but from now-on, the equations are usually represented in the classical limit, which gives better physical picture of the processes. One can think about $G(\mathbf{r},t)$ as it would

give the probability of finding a nucleus at $(\mathbf{r}, t)$, given that there is one at $\mathbf{r} = 0$ at t=0. And, for the incoherent part, $G_s(\mathbf{r}, t)$ would give the probability of finding a nucleus at $(\mathbf{r}, t)$, given that the same nucleus was at $\mathbf{r} = 0$ at t=0. However, this simple interpretation assumes no correlation between scattering length of the nucleus and it's location, which can be wrong, for instance, for a crystal with multiple elements. One, though, should be careful about the limits. So, for instance, the classical interpretation would result in $S(-\mathbf{q}, -\omega) = S(\mathbf{q}, \omega)$, which means the probability that a neutron loses energy $\hbar\omega$ is equal to the probability that the neutron gains the same amount of energy! The right equation, however, would be $S(-\mathbf{q}, -\omega) = \exp(-\hbar\omega\beta)S(\mathbf{q}, \omega)$, which is well known as detailed balance equation. It means that, although for the neutrons nucleus interaction, it does not matter in which direction the process goes, but it is much more likely (factor of $\exp(\hbar\omega\beta)$ to find the nucleus at a state of lower energy level than a higher one.

Different Sources and Techniques of Neutron Scattering

There are two practical sources for neutrons. First one is nuclear reactors which provide the cheaper neutrons. The other source is particle accelerators (spallation sources). The flux provided by the particle accelerator is pulse-shape and has a higher intensity, but is more expensive. Since the energy of neutrons in each of these two sources is much higher than needed, mediators are used to provide thermal or cold neutrons. The usual choice in a reactor is water, while in particle accelerator, the liquid hydrogen is a popular choice. Then the neutrons are provided, using neutron guides, for a few tens of instruments, each consisting of different tools and techniques, but generally including some or all of the following components: monochromator to select the wavelength of the neutron beam using Bragg's law; collimator to keep the neutrons with the same direction using parallel absorber plates; Chopper to make

short pulses or picking out a small band of energies; detector to count the neutrons by using nucleus interactions with ^3He or ^{10}B to produce charged particles which then can be detected. Other tools are used in different instruments, like spin turn coil for spin dependent measurements but the ones that named are the most important/basic ones.

Since neutrons are neutral and don't interact easily, it is hard to produce or detect them, and so, it is crucial to make the best out of the limited fluxes we can make. That's why there are many different instruments, which are separately designed to focus on a particular range of measurements in order to make the most effective and practical use of the neutrons. Depending on whether the energy exchange of the neutrons is measured or not, comes one of the main divisions in the field, namely elastic (without energy exchange), and inelastic (with energy exchange).

Elastic neutron scattering is focused on measuring intensity by changing the scattering angle. In this method, the intensity is measured in different angles either by step-scanning or by using detectors, which are position sensitive. Elastic scattering is insensitive to energy of neutrons (assuming the sensitivity of the detectors for neutrons with different energies can be averaged) and only counts them in specific angles. So, the function which is used to describe the result depends only on $\mathbf{q}$ as a variable. So, by integrating the differential cross section of the previous section with respect to energy, one can get the relevant cross section. For elastic scattering, the coherent part measures the structure factor ($S(\mathbf{q})$), which gives the correlations of atomic positions, while the incoherent part is an isotropic background. The diffraction experiments and Small-angle neutron scattering (SANS) experiments cover for big and small range of $\mathbf{q}$, respectively. For elastic (diffraction) one can write (Eq. (1.19))

$$S(\mathbf{q}) = \int \mathbf{S}(\mathbf{q},\omega)\mathbf{d}(\hbar\omega) = \mathbf{I}(\mathbf{q},\mathbf{0}) = \mathbf{1} + \int \mathbf{g}(\mathbf{r}) \exp(\mathbf{iq}.\mathbf{r})\mathbf{dr} \qquad (1.19)$$

which is called the structure factor and for incoherent part it gives the trivial answer $S_i = 1$ and $g(\mathbf{r})$ is known as static pair correlation function (or density-density correlation function). The small angle scattering is when the angle of diffraction is very small and so q is small ($q = 4\pi\frac{sin(\theta)}{\lambda} < 0.5\text{Å}^{-1}$), which means that large "r"s can be studied in this range.

In the inelastic scattering, the energy of neutrons are also of interest, so energy analysis are being established before detection. The methods for doing this, usually consist of using crystal analyser or time of flight method. Crystal analysers are arrays of single crystals, which are used in a 3-D form (aka triple axis spectrometers) to analyse the wave-vector of incident and scattered wave. Usually a set of measurements is performed at constant $\mathbf{q}$. Time of flight (TOF) method uses the fact that the neutrons with different energies have different speeds and so, they will take different times to go through the same path. This method is very important in spallation sources since they provide beams in pulses and it would make it inconvenient to use them by blocking all the flux with different energies to select only a fraction of it. In inelastic scattering, the information about energy changes can be resolved to get informations about time dependent (dynamics) properties of the system. But, since it is impossible to get time dependent pair correlation function ($G(\mathbf{r}, t)$) only based on the scattering data, the presence of a model is a necessity to interpret the data obtained from inelastic or quasi-elastic experiments. The quasi-elastic neutron scatterings are inelastic neutron scatterings which focus on the energy transitions close to 0 (small ω).

The other set of techniques in the inelastic neutron scattering are with the use of analysing spins of the neutrons. These are polarization analysis and spin-echo analysis. Neutron spin-echo (NSE) technique is basically based on the the Larmor precession and uses the fact that the spin flip probability within a perpendicular mag-

netic field should be proportional to the amount of time it spends in the field, and so for two regions of the space with the same length but opposite direction, the population of spins should not change if the speed of neutrons remain unchanged, and so any change in the population would indicate the change in the speed of neutrons. Notice that it is insensitive to neutrons' speed if it remains unchanged. This technique is very accurate and can measure the energy changes of neutrons to less than a nano electron volt (neV). Here the coherent and incoherent scattering is a key to get data about the structure and dynamics, and so for instance since the incoherent part provide information about self correlation it is important to improve the differentiation between which part comes from coherent scattering and what fraction is because of incoherent scattering.

Analyzing spins is another step forward to improve the techniques. NSE can looks at the difference between incident and scattered momentum components. It is very powerful tool to let us use bigger parts of the beam energy spectrum and so increasing the flux and have a very high resolution at the same time. Another point about NSE is that it gives a measure of $I(\mathbf{q}, t)$ at echo point, so it is directly a measure in time space and not ω.

1.3 MSD and Protein Dynamical Transition

Understanding the dynamics of the systems in condensed matter phases and biological systems is a very wide and important section in the field and Mean Square Displacement (MSD) of the atoms of a system is one of the important measures to help doing so. In this chapter, the MSD definition and tools to measure it will be mentioned very briefly and then what is called Protein Dynamical Transition (PDT) will be reviewed by providing different descriptions and models and discussions of the field mainstream (homogeneity is assumed in these cases, since $\frac{1}{3}$ implies that the

projection of the MSD on any of Cartesian axis gives similar value).

1.3.1 Definitions

MSD

Mean Square Displacement is defined as ((1.20))

$$MSD(t) = \frac{1}{3}\left\langle (\mathbf{r}(t) - \mathbf{r}(0))^2 \right\rangle \tag{1.20}$$

where the $\mathbf{r}(t)$ and $\mathbf{r}(0)$ gives the position of a particle at time t and time 0, and $< .. >$ denotes the averaging. One third is for convention and comes from the fact that in experiment we are usually dealing with the $(\mathbf{r}.\mathbf{q})$. MSD is a measure of the flexibility of the system and there are different experimental tools to measure it depending on the size and state of the system of interest, where among them neutron scattering, dynamic light scattering and Mössbauer spectroscopy are the most important ones. For small t, $\lim_{t\to 0}$, where the particles are in ballistic motion between collisions, each behaves like a free particle, and so MSD is quadratic in time. In the other limit, when $\lim_{t\to\infty}$ for liquids, particles displacement are diffusive and it is linear in time.

PDT

The system dynamic is a function of the energy of the system and of its temperature. At very low temperatures when the only mode available for the system's particles is their fluctuations around their equilibrium positions, and so can be considered in the harmonic vibrations, the MSD of particles is proportional to the square of their average amplitude. By increase of temperature the square of amplitude increases linearly and so MSD increases linearly with temperature (notice that this is only true at the temperatures that are low enough to limit all dynamics of the system in relevant time-scales except harmonic oscillation). At much higher temperatures

where all dynamics are accessible in the relevant time-windows, and diffusion makes the biggest contribution to the MSD, fluctuations are proportional to the energy of the system and so it's velocities and as a result the MSD. In the region in between, is where very interesting and complicated things happen.

In 1980 Keller et al. [50] used Mössbauer spectroscopy to deduce MSD of the iron atom at center of oxymyoglobin and to model the dynamics of the molecule. They broke the MSD into the vibrational, conformational and diffusional parts, and they comment that above T=240 K the results for the crystal and solution differ because of diffusion. Parak et al.[51] provide more experimental results for water solved iron and crystallized oxymyoglobin iron and discuss that based on their model should be 3 modes producing an unexpectedly large MSD where two modes have strong coupling to the iron, and so unlike nonspecific modes that do not couple strongly, these modes should be within protein's modes and describe protein dynamics.

In 1989 Doster et al. [52] used elastic and inelastic neutron scattering to measure the MSD and address the corresponding dynamic's time-scales. They used the term "Dynamical Transition" to describe their results, namely the striking change (decrease) in the intensity of elastic scattering with small values of q and the corresponding increase in the MSD and the deviation from the Gaussian behaviour above the temperature of 180 K (which is mainly the result of rotations of methyl groups, they also found the change of Gaussian from vibrating above 240K) and then the second change at 240K, which was considered as a resolution-dependent transition named the Dynamic Transition in analogy with glass transition. To conclude, there are new non-vibrational dynamics provide these behaviour above T 180K for time-steps 1-100 ps which mimics the MSD dependencies came from Mössbauer spectroscopy with much longer time-scales (10^{-7} s). So they suggest these dynamics could be coupled.

1.3.2 Views and Models

Since the early reports on the onset of increasing of MSD vs time, various views provided different models to describe the PDT. Some apparently non-converging results like the reports of different temperatures using different instruments and time-scales and analysis and interpretations of incoherent neutron scattering and Mössbauer spectrum (and sometimes wrong result from experiments without proper procedure!) have puzzled the scientific society and kept them away from arriving at a global agreement. In the following, three competing models in the mainstream are discussed.

Hans Frauenfelder's View(s)

Hans Frauenfelder is a well-known scientist and following his papers is useful not only because of their impacts on the field but also because they have been changing direction of focus during the years and cover a wide range of views. In 1991 Frauenfelder et al. [53] published a very well-cited paper which offered a complex landscape model to describe the dynamics of the proteins. In this view, proteins assume "conformational sub-states" in which the energy of them have so many valleys with nearly same energies, and for characterizing them statistics should be used. The Energy potential is a function of all coordinates of the conformation space where by different cross sections one can get different energy and length scales. They use these ideas to stress the similarity to glassy systems and suggest that the use of simple exponentials to describe protein behavior is inadequate and should be substituted by other functionalities, stretched exponentials for example, as is used to describe glass forming materials. By providing data for their example molecule ("Myoglobin"), they argue that binding of CO to the heme iron at low temperatures is a local phenomenon

independent of the whole protein relaxation and so only non-exponential time dependence would be sufficient to describe it (like β relaxation in glass formers), while the relaxation phenomena are usually collective processes including many atoms of a molecule and so an Arrhenius temperature dependence for relaxation time constant is not proper and we should use functions used for α relaxations in glass formers. They use this analogy and say that in the theoretical form, both can be discussed in rugged energy landscape (the α and β relaxation had been pointed before, for instance [52]).

This paper tries to provide a very wide view of the complexity of the proteins and makes use of the glass and glass-spin models to provide the basics for improving theory of this multi-dimensional landscape at a better "resolution". But beside that, they only distinguish the glasses and proteins with the possible changes in the energy landscape of proteins because of mutagenesis and evolution. Moreover they almost never mentioned how the environment, or more specifically the presence of solvent affect this "landscape" and alter the relations and dynamics and functions of the molecule, and whether it is still useful to use a landscape with the presence of a liquid as the solvent, which can not be described as a static landscape. Moreover, as long as heme is of interest, it is hard to get a real measure of the whole protein motions since the role of solvent in the heme interactions is significant. Due to these issues, solvent comes to the picture in a rather radical way. In a paper in 2002 Frauenfelder and Parak (and others[54]) described the motion of the proteins in terms of two different classes, namely slaved and non-slaved.

In this new picture, the protein is not by its own, but the hydration shell is included to make the landscape and plays a significant role. They compare the rates $k(T)$ of the motions of proteins and fluctuations of the solvent to make two groups of slaved and non-slaved motions. The slaved are those witch maintain the ratio of the rate to the solvent fluctuations rate $n(T) = k_{diel}(T)/k(T)$ where the rate of the solvent

fluctuations comes from the dielectric measurements of the bulk solvent ($k_{diel}(T)$). In this sense, n(T) is the measure of how the fluctuations of solvent get slowed by the protein and its hydration shell. These are the motions that are slaved by the solvent, and those motions with rates that don't keep this relation are independent fluctuations of the protein and hydration shell that are making the landscape and are independent of the bulk. To describe the connection of the protein and solvent they give a model where at very low temperatures the particle escapes one sub-conformation to another in a region with very small barriers between minima and rarely goes to the other parts of the conformational space (another statistical sub-state). However, this rate increases with increasing temperatures significantly, and they formulate a model of the Brownian motion in the conformation space where it can move around in the conformational space. To give an example they provide data for Myoglobin in a glycerol/water solvent with the ratio 3/1, but they claim that the picture is general and can be applied to very different proteins and conditions.

In a 2004 paper, the Fenimore et al. [1], get to the MSD and its temperature and time dependence. In this view the dynamic of proteins are divided to three classes of fluctuations. Here the non-slaved are not the protein and hydration shell, but the dry (aka dehydrated) vibrations of proteins. Second the "shell-coupled" processes where protein and β fluctuations in the hydration shell are coupled, the "solvent-slaved" motions are those that follow the α fluctuations of the bulk solvent. As a result, the picture of the landscape also changes: the conformational sub-states contain a number of sub-states with different structures with probably different functions, where the sub-states are containing different tiers, α and β, where the transitions of former are slaved with the bulk and the later which reside in the former, is coupled by hydration-shell and inside, it probably contains more unrefined structures. The MSD is divided into two parts (Eq. (1.21)); one part comes from the linear fit to

the low temperatures (from 10K to 170K) MSD($\langle x^2(T)\rangle_v$), and the other from the subtraction of the total MSD from the vibration part.

$$\langle x^2(T)\rangle = \langle x^2(T)\rangle_v + \langle x^2(T)\rangle_c \tag{1.21}$$

They follow similar procedure for other techniques to define $\langle x^2(T)\rangle_c$. They label the rate characteristic of different experiments by k_m where the rate and time are related as $k_m = 1/\tau$, where τ for Mössbauer experiments is 140 ns. For the elastic neutron scattering they use Heisenberg uncertainty = $\hbar/\Gamma$, where Γ is the energy resolution of the instrument. Then they apply the random walk model to describe the Fe MSD at T less than 250K (random walk of the heme iron in conformational sub-states). "s" is the length of the steps and $k_c(T)$ is the rate of them. For an infinite system it comes (Eq. (1.22))

$$\langle x^2(T)\rangle_c \simeq ns^2 = (\frac{k_c(T)}{k_m})s^2 \tag{1.22}$$

and for bounded systems it is accurate only for low temperatures. For higher temperatures they talk about two limiting situations. The first is the random walk in the square well, where the MSD converges to a constant independent of temperature. The other scenario is a harmonic potential where MSD comes as $\langle x^2(T)\rangle_c = k_bT/b$. The major claim here is that there are three processes determined by α and β rates. By convention they chose the 10^{-2}s as the limit for glasses and claiming that there is two glass temperatures for the protein (${T_g}^{\alpha} = 173$ and ${T_g}^{\beta}$ by extrapolation is 100K), and so t_d (dynamical transition temperature) for proteins is not special in a fundamental way and only indication of temperature where "$\langle x^2(T)\rangle_c$ appears to vanish". But to do so, a list of similarities between proteins and "glasses" is provided namely, inhomogeneity described by "energy landscape", with two types of fluctuations, α and

β, with rates $k_\alpha(T)$ and $k_\beta(T)$ respectively, and that they both also "show relaxation phenomena at liquid helium temperatures". Then by using Vogel-Tammann-Fulcher (Eq. (1.23)), and Arrhenius equation (Eq. (1.24)) for rates,

$$k_\alpha(T) \approx A_v \exp(\frac{-E_v}{k_b(T-T_0)}) \tag{1.23}$$

$$k_\beta(T) = A \exp(\frac{-H}{k_b T}) \tag{1.24}$$

they argue that the coupling of the hydration shell and MSD of Fe measured by Mössbauer experiment holds for temperatures around or less than 250 K. This comes from the second graph of the paper (Fig. 1.1 [2]) where they argue that the rate can be fitted with an Arhhenius form with parameters in the range of the typical β relaxation (the values for an Arrhenius fit for glycerol/water with 3/1 ratio is given earlier in the paper for comparison, namely H≈10-30 kJ/mol and log(A)≈ $14 - 15 s^{-1}$), and so they label it as the β relaxation. Then by dividing the MSD_c to two different regimes of temperature dependent, where above the 250K it is proportional to T and so justifies the harmonic potential scenario $\langle x^2(T)\rangle_c = k_b T/b$, and for bellow 250K where the temperature dependence of the MSD_c and k_β is the same and so they are coupled and the equation ((1.22)) should be used where they assume $k_c(T) = \epsilon k_\beta(T)$ and ϵ is the fraction of the shell water transition that causes the Fe to move.

In 2009 "A unified model of protein dynamics" paper [55] Frauenfelder et al. use different hydration levels to measure the α and β_h where now h is indication of the hydration level of the protein and β_h are the statistically independent β which are not dependent on α fluctuations. They embedded the solution in solid poly (vinyl) alcohol (PVA) to eliminate the collective relaxation and since α is viscosity related, so

[2] Fig.1 is second Figure from [1]

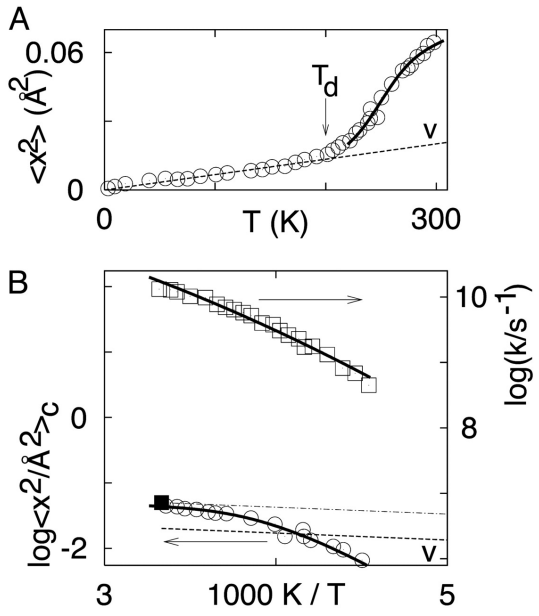

Figure 1.1: (A)The MSD From Mössbauer Scattering where the Dashed Line Is Vibrational Contribution, Denoted by V, (B) Give the Rate k_β of Dielectric Relaxation of Hydration Water of Metmyoglobin, (Right Vertical Axis) Compared with the Log (MDD_c) (Left Vertical Axis) [1]

they expect they be absent by using this technique. Then they propose that the MSD changes at higher temperatures arise from the fraction of the area of β_h spectrum that arises from the modes faster than the Mössbauer time-window (140ns). The spectrum can be fitted by equation 5 of the paper (Eq. (1.25)) where $k_\beta = 2\pi\nu$ and b and c are fitting parameters. The fraction area of spectrum with slower rates (a_β) than Mössbauer can be estimated by equation 6 of the paper (Eq. (1.26)) where k_M is mössbauer rate $(1/250\ ns^{-1})$.

$$\epsilon_\beta{}''(k_\beta, T) = \Delta\epsilon Im[1 + (ik_\beta/k_h(T))^b]^{-c} \tag{1.25}$$

$$a_\beta(T) = 1 - \int_{logk_M}^{\infty} \epsilon''(k_\beta, T)d(logk_\beta)/a''(T) \tag{1.26}$$

In another paper by Frauenfelder and co-workers ([56]), the time correlation func-

tion for gamma absorbtion is provided by $\langle \exp[-i\mathbf{q}.\mathbf{R}_C(0)] \exp[i\mathbf{q}.\mathbf{R}_C(t)] \rangle$ where the $\mathbf{R}_C(0)$ and $\mathbf{R}_C(t)$ are the quantum operators and quantum transition amplitude between them gives the conformational part of time correlation function. The brackets denotes quantum and ensemble averaging. Then by saying that the iron atom is coupled to the hydration shell fluctuations and they are to the macroscopic system, and by result of that for quantum systems that coupled to the macroscopic systems, the quantum dephasing occurs exponentially in time domain, they write the transition amplitude for ensemble of proteins as (Eq. (1.27))

$$\langle \exp[-i\mathbf{q}.\mathbf{R}_C(0)] \exp[i\mathbf{q}.\mathbf{R}_C(t)] \rangle = \int d(\log k_\beta) \rho(k_\beta, T) \exp(-\chi k_\beta |t|) \tag{1.27}$$

where the χk_β is the rate of dephasing, where the value of χ is obtained from fitting =1.8 and then kept constant. After integration of the intermediate correlation function (Equation 3 of the paper) with respect of time, the resulting scattering function S(ΔE_{exp}) (Eq. (1.28)) agrees with experimental data.

$$S(\Delta E_{exp}) = f_V(T) \int d(log k_\beta) \rho(k_\beta, T) \times \frac{1}{\pi} \frac{\frac{\Gamma}{2} + \chi \hbar k_\beta}{\Delta E_{exp}^2 + (\frac{\Gamma}{2} + \chi \hbar k_\beta)^2} \tag{1.28}$$

Here the f_V represent the vibrational fraction, $\rho(k_\beta, T)$ is the normalized distributions (divided by area), $E_{exp} = E_0 v/c$(E_0 is energy of gamma ray and v the velocity of the source) and Γ is the width of the energy due to life time of the nucleus.

For more data on neutron scattering with similar viewpoint, one check Magazu's papers on the issue, for instance ([57][58][59]). For a recent summary of Frauenfelder's view and his critics of other points of view, the 2013 paper [60] would be a good reference.

Wolfgang Doster's View

The term "protein dynamical transition" for proteins' motions coupled to the kinetic glass transition of the solvent, first introduced by Doster in two important papers ([61] [52]) employing calorimetry and infra-red spectroscopy (1986). Those were followed by intensive inelastic neutron scattering measurements on some biomolecules, mainly myoglobin, which showed similar temperature dependencies with the glass formers. The hydrogen bond network clusters where suggested on the former paper, while the later paper suggests a coupling between fast local and slow collective motions, a feature of dense glass formers.

In 1990 PRE ([62]) Doster et al. using the shape of the inelastic scattering function approximated the scaling behaviour based on mode-coupling theory (MCT) for simple liquids near liquid-glass transition. There the MCT (a theory which can approximate cage effect) is used to provide a connection between density fluctuations of the protein and scaling properties of liquid-glass transition in simple liquids, instead of mode-softening or stochastic description in their Nature paper ([52]).

In 1998 there was another work ([63]), which reported on the role of the solvent composition and its viscosity on kinetics of a protein. They studied binding of CO to Myoglobin. In this work they used different co-solvent concentration (which modifies the dielectric constant, chemical potential and the surface tension) and different viscosities to distinguish between intramolecular and surface-coupled dynamics. The results suggested that the viscosity of solvent does not affect the inner barriers, but it does affect the outer kinetic barrier, which controls entry of CO. They also suggested that the increase in the surface tension from co-solvents like glycerol causes increase in the water concentration around the protein and result in a reduction of viscosity at microscopic level comparing with the bulk viscosity. Here they just briefly mention

the protein-water hydrogen bonds.

In 1999 ([64]) the Mössbauer effect was used to study the solvent effect, here the 80% sucrose/water. They studied the temperature dependence of heme displacements and its coupling to the visco-elastic relaxation of the solvent. They used the Gaussian approximation and classical limit of $\langle x^2 \rangle = 0$ at $T = 0$ to analyse their data. Comparing their results for the mean square displacement of the heme and results from Franke, M (1992 [3]), they tried to illustrate the effect of viscosity on MSD, namely the increase in the dynamical transition temperature with increasing viscosity (Fig 7 of [64]).

In a more recent review article, Doster et al. in 2005 [65] provide a broad analysis of the experimental data, mainly dynamic neutron scattering for proteins and proteins-water time-resolved dynamics, by moment analysis of the intermediate scattering function and derive the time-dependent displacement distribution function. Based on this distribution function, they identify two types of displacements, torsional transitions and continuous motions. They claim that the continuous motion is based on small displacements and hydrogen bond fluctuations (which induce fast β processes) and the transition is a coupling effect of the protein to water. Its temperature dependence varies with the hydrogen bond strength and viscosity (discontinuity of OH bond stretching vibration near T_g of solvent). Moreover, by splitting the intermediate scattering function in two exponentials, and plotting the constructed displacement distribution (Eq. (1.29)), it has been shown that the side-chain (mostly methyl groups) rotation exists in dehydrated and hydrated transitions for proteins, and is weakly coupled to the solvent

[3] Franke, M. 1992. Konformationssubzustande in Myoglobin, Mössbauerspektroskopische Untersuchung und modellmassige Deutung der Reaktionskinetik mit CO. Ph.D. thesis. Friedrich-Alexander-Universitat, Erlangen-Nurnberg, Germany.

$$I(q,T,t_{res}) = A_1.exp(-q^2\langle\Delta x_1^2\rangle/2)) + A_2.exp(-q^2\langle\Delta x_2^2\rangle/2)) \tag{1.29}$$

where $\langle r^2\rangle = 3\langle\Delta x^2\rangle$.

The claim is that the change in the population of open hydrogen bonds above this temperature T_g results in a large decrease of the characteristic time of translational diffusion (long-range), and this is where the time resolution of the instrument starts to affect the reported transition temperature. The compact proteins can't undergo the glass transition, which "always involves the arrest of long-range transitional diffusion". So, they insist, the term "protein-dynamical transition" implies freezing of specific fraction of local motions because of coupling to the glass-forming solvent. It shows the relaxation time of water which is a dynamic property, drastically changes in a short temperature range. They differentiate their view from assigning α and β-processes to proteins (Hans' view), by insisting that the generalized Langevin equation with frequency dependent frictional forces gives the right description of observations. At higher temperatures, the frictional role of solvent molecules with much faster motions than the collective motions of protein is their main role. And around the glass transition, protein and solvent motions freeze at the same rate. They suggest that viscose coupling is the right term for the interaction of water with the protein, since the time-scale of the adjustment of water molecules is much faster than protein's collective displacements. Also the dependence of the dynamics of the protein on the solvent, is their reasoning, suggests a seascape instead of landscape (dynamic fast changing instead of self trapping at fixed energies).

In 2008[66], Doster makes it clear that by transition he means huge change in the corresponding relaxations times, which is kinetic and not a thermodynamic phenomenon. That the α relaxation changes, near a critical temperature, are super-Arrhenius. That the smoothness of the structural relaxation times in a log-scale for a

long range doesn't change the fact that in the linear temperature form quantities like displacements, specific heat and thermal expansion show a sudden onset at the glass transition temperature. He gets to the temperature 240K as the glass temperature with respect to 50 ps time scale. That the liquid behaviour as an associated behaviour of liquids can will be arrested bellow the glass transition temperature and can happen not only for bulk water but for hydration shell water molecules as well, and the difference between them is in the magnitude of diffusion coefficient and crystallization rate. Here, he take hydrogen-bond fluctuations as β processes and not only as their triggers (In 2010 review paper [67], he talks about "the hydration bond fluctuations, which give rise to fast β-processes."). Doster points out here that for the purpose of modeling, describing intensity of elastic scattering is not enough and successful models for proteins' dynamics, should be able to describe the spectral (inelastic) data.

In 2010 PRL Doster et al. [68], they use neutron backscattering to study the water in a deuterated protein "C-phycocyanin". They investigate the existence of the so-called hidden transition of the shell water. The integrate of the inelastic part of the scattering does not support the specific resolution independent change in temperature around 220K. The integrand amount of increase depends on the wave-vector as well as ω, nothing specific about 220K, while the elastic friction showed a drop in the 220K, which suggests the same transition temperature for both samples. Then they use the same model which was used by the Chen et al. [2] (more detain in 1.3.2) to analyse the spectra, an elastic line and a Kohlrausch-Williams-Watts function (Eq. (1.30) (equation 1 of the [68]))

$$S_{th}(q,\omega) = f_q \left(a_1 \delta(\omega) + a_2 \int_{-\infty}^{\infty} \frac{dt}{2\pi} e^{i\omega t - (\frac{|t|}{\tau})^{\beta}} \right) \tag{1.30}$$

which is Fourier transform of a stretched exponential and f_q is the Debye-Waller factor for phonon scattering outside resolution of instrument. Then they show that

different fitting procedures to obtain the rates provide different results.

In 2011, Doster [69] talks about the confusion that defining the protein dynamic transition as the temperature onset of mean square displacement can cause. Doster suggests that the drop of the elastic intensity (normalized by low temperature), which approximate the intermediate scattering function at the resolution time, to the 1/e of the low temperature value can be a better definition of temperature onset of the transition for any given time window. The advantage of it would be that the elastic intensity is a direct experimental value and is not influenced by the models and assumptions which are inevitable for other values like finding the displacement. Seems inspired by Gotze work[70], he tries to reduce the use of α and β-processes, and talk about first and second processes mostly. He counts three onsets of the mean square displacements in respect to temperature. One is related to the fast fluctuation of hydrogen bond (in the β process), which gives the increased amplitude above the glass transition, independently of the resolution of the instrument. The second one, which varies with the time resolution, is related to the long collective displacements. The third one, which is independent of the solution and shows up even in dehydrated proteins and bellow the glass temperature, is related to the side-chain rotations.

Sow-Hsin Chen's View

In 2005,2006 and 2007 a number of papers was published by Chen et al. about the fragile to strong dynamic crossover (structural transition) in the confined water at temperature 220K. Some of them where investigating, either by quasielastic neutron scattering[2, 71, 72] or computer molecular dynamic simulations[73], the hydration water layer around proteins and biomolecules. Here we follow the most relevant and influential one as related to our discussion[2]. In this paper they consider the shell water as the one single layer of water molecules covering the surface of the protein

and so they chose h (the ratio of water mass/ protein mass) around 0.3 and they performed other checks (differential scanning calorimetry) to check for absence of any bulk-like water. They used two samples for neutron scattering measurements, one with H2O water and one with heavy water (D2O) and then they subtracted the incoherent signal of protein hydrogen atoms. They covered the temperature range 180-270 K. The NIST center for neutron research with energy resolution of 0.8 μeV was their neutron source. The model they used for their analysis is the relaxing-cage model(RCM). In this model, the intermediate scattering function for translational dynamics of water (the rotation is disregarded for $Q < 1.1\text{Å}^{-1}$ according to [74]) is divided into two parts. The fast Gaussian in-cage vibrational relaxation, followed by a plateau, and a slow ($t > 1$ps) relaxation of the cage with a stretched exponential (Eq. (1.31) here, equation 1 in [2]).

$$F(Q,t) = F^S(Q,t)exp\left[-\left(\frac{t}{\tau_T(Q)}\right)^{\beta}\right] \tag{1.31}$$
$$where\ \tau_T(Q) \cong \tau_0(0.5Q)^{-\gamma}$$

where the $F^S(Q,t)$ stands for the fast vibrational dynamics of water molecule in the cage. It is calculated from simulations since it is not sensitive to temperature. $\tau_T(Q)$ is translational relaxation time, which is T and Q dependent and is specified by two other parameters (τ_0 and γ) which by stretch parameter β "are obtained by analysing simultaneously a group of nine quasi-elastic peaks at different Q values". The β value is 0.5. Then they obtain the average (translational) relaxation time by (Eq. (1.32))

$$\langle\tau_T\rangle = \frac{\tau_0\Gamma(1/\beta)}{\beta} \tag{1.32}$$

which is independent of Q.

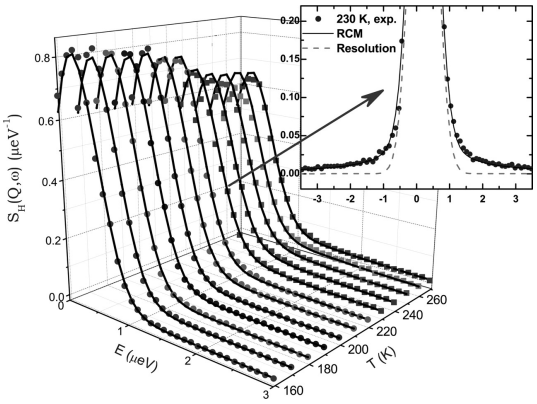

Figure 1.2: "Neutron Spectra and Their RCM Analyses. Measured QENS Spectra (Filled Symbols) and Their RCM Analysis Results (Solid Lines) at Q = 0.87 ΓΤΓÅ¯1 and at a Series of Temperatures Are Shown. (Inset) One Particular Spectrum at T = 230 K Is Singled out and Contrasted with the Resolution Function of the Instrument for This Q Value (Dashed Line)." [2]

The obtained average relaxation times show two different behaviours. The high temperatures behaviour match well with "Vogel-Fulcher-Tammann (VFT) law $\langle\tau_0\rangle = \tau_1 exp[DT_0/(T-T_0)]$", which describes fragile liquids, and for low temperatures, an Arrhenius law $\langle\tau_0\rangle = \tau_1 exp[E_A/k_BT]$ was found which describes strong liquid [4] . The intercept of the two is found to be at T_L =220K (Fig. 1.3). Also mean square displacement (using Gaussian approximation) and $\beta\gamma$ vs temperature changes are provided which show changes in 220K (Fig. 1.3). Graphs of the dynamic structure factor vs energy are provided for different temperatures. In fig.2 of the paper, specifically, the neutron spectra and RCM fits are provided. Though the fitting in the maximums doesn't look very precise as can be seen in (Fig. 1.2).

1.4 ET and FDT Application

Cellular and biological functions require energy and electron transfer (ET) is a key underlying step. The fascinating wide range of distances and time intervals that

[4] T_0 is the temperature in which the fragile liquid correlation length diverges (=176K in the paper), and E_A is the activation energy (=3.13 kcal/mol in the paper)

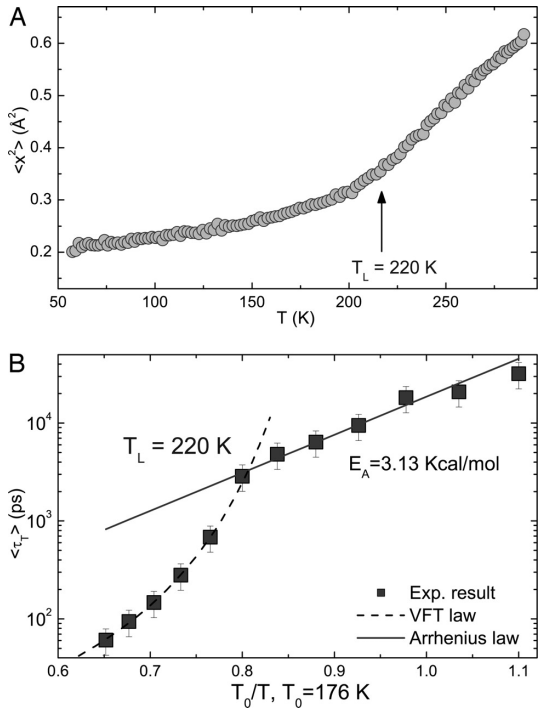

Figure 1.3: "Evidence for the Dynamic Transition. (A) The Temperature Dependence of the Mean-Squared Atomic Displacement of the Hydrogen Atom at 2-Ns Time Scale Measured by An Elastic Scan with Resolution of 0.8μeV. (B) Temperature Dependence of the Average Translational Relaxation Times Plotted in $\log(\langle\tau_T\rangle)$ vs. T_0/T,Where T_0 Is the Ideal Glass Transition Temperature. Here, There Is a Clear and Abrupt Transition From a VogelFulcherTammann Law at High Temperatures to An Arrhenius Law at Low Temperatures, with the Fitted Crossover Temperature $T_L = 220$ K and the Activation Energy $E_A = 3.13$ Kcal/mol Extracted From the Arrhenius Part Indicated in the Figure." [2]

biological ETs occur in and studies of the efficiency of the process have been the focus of many studies [75, 76, 77, 78, 79, 80, 81]. One of the earliest was the work of De Vault and Chance [82] helping the realization of quantum mechanical tunneling as the physical mechanism behind many ET reactions. In this case the focus was on the light-induced oxidation of cytochrome in Chromatium based on its insensitivity to temperature for low temperatures.

Modern theories of electron transfer assign the energy gap X between the donor and acceptor energy levels to the electron-transfer reaction coordinate.[3, 83, 84, 85]

For the half reaction changing the oxidation state of the system, the energy gap $\Delta E(\mathbf{q})$ is between the electronic states of the oxidized and reduced states.[15] The free energy surface is defined by tracing out the entire manifold of the nuclear degrees of freedom $\mathbf{q}$ while restraining the energy gap to a given value X

$$e^{-F(X)/(k_{\mathrm{B}}T)} \propto \langle \delta \left(X - \Delta E(\mathbf{q}) \right) \rangle \tag{1.33}$$

For electron transfer in solution, one considers the one-electron states of the donor and acceptor and the instantaneous (fluctuating) energy gap X between them as the reaction coordinate. Thermal fluctuations reduce this gap to zero in the activated state of an electron transfer reaction (radiationless transition). The same energy gap comes in resonance with the radiation photon in spectroscopy of charge-transfer transitions (Figure 1.4a).[86] One observes charge-transfer absorption or emission bands with the maxima corresponding to the average excitation energies $\langle X \rangle_i$. The separation between the maxima is the spectroscopic Stokes shift,[4, 87] which can be used to quantify the reorganization energy labelled as λ^{St} (Fig. 1.4b).

Please note that in general $G = F + pV$ which connects the Helmholtz free energy and Gibss energy with the work done at constant presure p which is negligible for most problems in condensed mater,[88] and so here they are used interchangeably.

If $P_i(\hbar\omega)$ is the probability of absorbing ($i = 1$) or emitting ($i = 2$) a photon with the energy $X = \hbar\omega$, the free energy surfaces of electron are constructed to compliment this picture in terms of the free energy (reversible work) required to achieve a given value of X: $G_i(X) = G_0^i - k_{\mathrm{B}}T \ln[P_i(X)]$ (Fig. 1.4c), where G_0^i is the free energy at the minimum. The separation between the minima of the free-energy surfaces then becomes equal to $2\lambda^{\mathrm{St}}$. One additionally can define the reorganization energy from the curvature of the free energy surface at the minimum, $\partial^2 G_i(X)/\partial X^2|_{X_{0i}}$, which can be related to the variance of the reaction coordinate X according to the standard

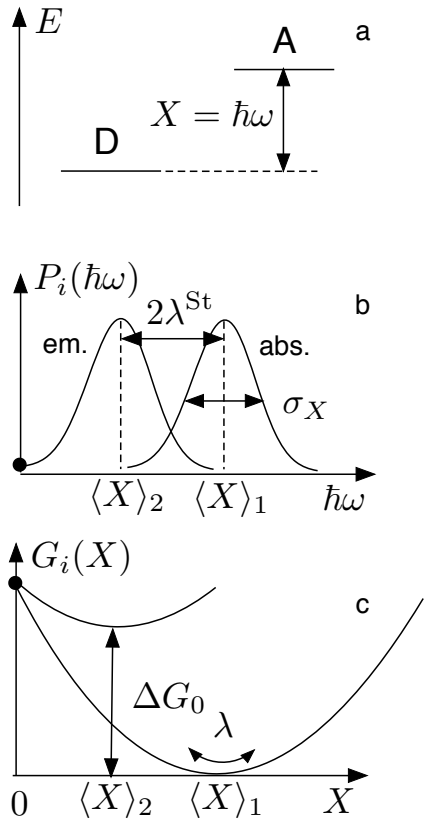

Figure 1.4: (a) Reaction Coordinate $X = \hbar\omega$ for Solution Electron Transfer Between the Donor (D) and Acceptor (A).[3] (b)Probability Densities for Absorbing (abs.) and Eemitting (em.) a Photon in a Charge-Transfer Optical Transition; $\langle X\rangle_i$ Stand for the Average Transition Energies. The Separation Between the Peaks of Optical Transitions Represents the Stokes Shift and the Corresponding Reorganization Energy λ^{St}. (c) The Free Energy Surfaces of Electron Transfer $G_i(X) = G_0^i - k_{\mathrm{B}}T\ln[P_i(X)]$ Following From the Optical Transition Probabilities $P_i(X)$. The Reorganization Energy λ Defines the Curvature of the Free Energy Surface Near the Bottom (Shown by the Double Arrow).It Also Provides the Measure of Inhomogeneous Broadening of the Optical Charge-Transfer Band[4] ($\sigma_X^2 = \langle(\delta X)^2\rangle = 2k_{\mathrm{B}}T\lambda$ in (b) and in Eq (1.34)). The Filled Dots in (b) and (c) Indicate, Respectively, $P_2(0)$ and the Crossing Point of $G_i(X)$ Representing the Transition State, $X = 0$, Of the Electron-Transfer Reaction.

rules of statistical mechanics[89, 85, 90]

$$\lambda = \langle(\delta X)^2\rangle/(2k_{\mathrm{B}}T) \tag{1.34}$$

A schematic of the free energy surfaces for half ET is presented in figure 1.5.

The Marcus theory of electron transfer[76] defines the free energy barrier for electron transfer, $\Delta G^{\dagger}$, in terms of the reorganization energy $\lambda^{\mathrm{St}} = \lambda$ and the reaction free energy ΔG_0

$$\Delta G^{\dagger} = \frac{(\lambda + \Delta G_0)^2}{4\lambda} \tag{1.35}$$

Returning to the picture of optical transitions, the variance reorganization energy λ determines the Gaussian width of the energy-gap fluctuations or the inhomogenoues width of a single vibronic optical line.[91] As mentioned above, in the Marcus picture one has $\lambda^{\mathrm{St}} = \lambda$, which is a specific case of a general result, namely FDT.[92] This phenomenology changes for protein electron transfer in solution, where one finds[90, 93] $\lambda \gg \lambda^{\mathrm{St}}$.

A generic Gaussian distribution of the reaction coordinate X results in the parabolic free energy surface[83, 94, 90]

$$G_i(X) = G_0^i + \frac{(X - \langle X\rangle_i)^2}{4\lambda} \tag{1.36}$$

where $i = \mathrm{Ox}, \mathrm{Red}$.

We can apply the condition of crossing at zero energy gap, $G_{\mathrm{Red}}(0) = G_{\mathrm{Ox}}(0)$, to obtain the average values

$$\begin{aligned} \langle X\rangle_{\mathrm{Ox}} &= -\lambda^{\mathrm{St}} - (\lambda/\lambda^{\mathrm{St}})\Delta G_0 \\ \langle X\rangle_{\mathrm{Red}} &= \lambda^{\mathrm{St}} - (\lambda/\lambda^{\mathrm{St}})\Delta G_0 \end{aligned} \tag{1.37}$$

where $\Delta G_0 = G_0^{\mathrm{Red}} - G_0^{\mathrm{Ox}}$ is the reaction free energy. The Stokes-shift reorganization energy from these equations is half of the separation between the minima of the

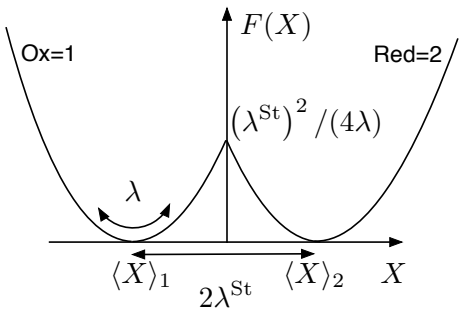

Figure 1.5: Schematic Representation of the Free Energy Surfaces for Half Electron Transfer, $Ox + e^- \rightarrow Red$. The Oxidized ($Ox = 1$) and Reduced ($Red = 2$) States Are Characterized by Approximately Parabolic Free Energy Surfaces Along the Energy Gap Reaction Coordinate X, with the Minima at $\langle X\rangle_1$ and $\langle X\rangle_2$. The Separation Between the Minima Is Twice the Stokes-Shift Reorganization Energy λ^{St}. The Curvatures of the Parabolas Produce the Reorganization Energy λ Related to the Variance of X: $\lambda = \langle \delta X^2\rangle/(2k_BT)$. The Activation Barrier of a Half Reaction Is Determined by Crossing of Two Parabolas at $X = 0$ And Is Given by Eq (5.2) At Zero Reaction Free Energy.

crossing parabolas

$$\lambda^{St} = \tfrac{1}{2}\left|\langle X\rangle_{Red} - \langle X\rangle_{Ox}\right| \tag{1.38}$$

The activation barrier for the cathodic process is the free energy difference between the activated state, $G_{Ox}(0)$, and the free energy at the minimum, G_0^{Ox}: $\Delta G^\dagger = G_{Ox}(0) - G_0^{Ox}$. One gets from eqs (1.36) and (1.37)

$$\Delta G^\dagger = \frac{(\lambda^r + \Delta G_0)^2}{4\lambda^r} \tag{1.39}$$

where λ^r is the effective reorganization energy given by eq (1.40)

$$\lambda^r = \frac{(\lambda^{St})^2}{\lambda} \tag{1.40}$$

For reactions involving small values of ΔG_0, typical for biology,[79] the reorganization energy becomes the most important factor determining the reaction barrier. While the electrochemistry of cytochrome c would be the subject of chapter 4, the elaboration on the breaking FDT, namely $\lambda^{St} \neq \lambda$, the use of fluctuation dissipation relation to define the effective temperature, the role of effective temperature to understand the rate of ET, and returning to the FDT regime at low temperatures are

provided in chapter 5. Cytochromes are proteins with heme and they are structurally very similar. In this work we chose cytochrome c because the experimental data for electrochemistry of it was available in the literature.

1.5 Charge Interaction

The last part of this work is about the screening of Coulomb charges inside liquid dielectrics. Here the derivation of the main equation, which is followed for the theory development and simulation calculation, is provided. Starting from definition of free energy one can write

$$\begin{aligned} &\Delta F \\ &\quad = F_Y - F_X = -\frac{1}{\beta} ln \frac{Q_Y}{Q_X} \\ &\quad = -\frac{1}{\beta} ln \{ \frac{\int\int d\vec{p}^N d\vec{r}^N exp[-\beta H_Y]}{\int\int d\vec{p}^N d\vec{r}^N exp[-\beta H_X]} \} \end{aligned} \tag{1.41}$$

now by inserting $1 = exp[+\beta H_X] exp[-\beta H_X]$ in the numerator

$$\begin{aligned} &\Delta F \\ &\quad = -\frac{1}{\beta} ln \{ \frac{\int\int d\vec{p}^N d\vec{r}^N exp[-\beta H_Y] exp[+\beta H_X] exp[-\beta H_X]}{\int\int d\vec{p}^N d\vec{r}^N exp[-\beta H_X]} \} \\ &\quad = -\frac{1}{\beta} ln \langle exp[-\beta (H_Y - H_X)] \rangle \end{aligned} \tag{1.42}$$

If one have two charges in a liquid, $H_Y - H_X$ can be replaced by $q_1\phi_1 + q_2\phi_2$, and one gets

$$\Delta F = -\frac{1}{\beta} ln \langle exp[-\beta (q_1\phi_1 + q_2\phi_2)] \rangle \tag{1.43}$$

where

$$\phi_1 = \phi_{s1} + \frac{q_2}{2R} \quad \& \quad \phi_2 = \phi_{s2} + \frac{q_1}{2R} \tag{1.44}$$

here R is the distance between two charges and ϕ_{si} is electrostatic potential created by the dielectric at the position of charges $q_i, i = 1, 2$.

Now by writing the cumulants, showing only first two non-zero terms one could write

$$\begin{aligned}
&\Delta F \\
&\quad \simeq \langle q_1\phi_1 + q_2\phi_2\rangle - \frac{\beta}{2}\langle[\delta(q_1\phi_1 + q_2\phi_2)]^2\rangle + ... \\
&\quad \simeq \langle \frac{q_1q_2}{R} + q_1\phi_{s1} + q_2\phi_{s2}\rangle - \frac{\beta}{2}\langle(0 + 0 + q_1\delta\phi_{s1} + q_2\delta\phi_{s2})^2\rangle + ... \\
&\quad \simeq \frac{q_1q_2}{R} + q_1\langle\phi_{s1}\rangle + q_2\langle\phi_{s2}\rangle - \frac{\beta}{2}({q_1}^2\langle\delta{\phi_{s1}}^2\rangle + {q_2}^2\langle\delta{\phi_{s2}}^2\rangle + 2{q_1}^2{q_2}^2\langle\delta\phi_{s1}\delta\phi_{s2}\rangle) + ...
\end{aligned} \tag{1.45}$$

for interaction free energy of the two charges in the realm of linear response one finally gets

$$\Delta F - G_{s1} - G_{s2} = q_1q_2(\frac{1}{R} - \beta\langle\delta\phi_{s1}\delta\phi_{s2}\rangle) \tag{1.46}$$

where the G_{si} is the energy of solvation for the charge q_i.

Chapter 2

DYNAMICAL AND ORIENTATIONAL STRUCTURAL CROSSOVERS IN LOW-TEMPERATURE GLYCEROL

This material was published in Physical Review E (journal) 94(1), p.012616 (2016 July 22).

2.1 Summary

Mean square displacements of hydrogen atoms in glass-forming materials and proteins, as reported by incoherent elastic neutron scattering, show kinks in their temperature dependence. This crossover, known as the dynamical transition, connects two approximately linear regimes. It is often assigned to the dynamical freezing of subsets of molecular modes at the point of equality between their corresponding relaxation times and the instrumental observation window. The origin of the dynamical transition in glass-forming glycerol is studied here by extensive molecular dynamics simulations. We find the dynamical transition to occur for both the center of mass translations and the molecular rotations at the same temperature, insensitive to changes of the observation window. Both the translational and rotational dynamics of glycerol show a dynamic crossover from the structural to a secondary relaxation at the temperature of the dynamical transition. A significant and discontinuous increase in the orientational Kirkwood factor and in the dielectric constant is observed in the same range of temperatures. No indication is found of a true thermodynamic transition to an ordered low-temperature phase. We therefore suggest that all observed crossovers are dynamic in character. The increase in the dielectric constant is related to the dynamic freezing of dipolar domains on the time-scale of simulations.

2.2 Introduction

Displacements of atoms and molecules induced by thermal agitation generally increase with temperature. A linear growth of the mean-squared displacement (MSD) with increasing temperature is predicted by the Nyquist (fluctuation-dissipation) theorem [92, 95]. The MSD is experimentally extracted from either the intermediate scattering function of the neutron scattering experiment [96] or from the fraction of recoilless γ-ray emission of the ^{57}Fe nucleus in the Mössbauer experiment [80, 97]. The Nyquist theorem was found to be violated for a number of glass-forming materials, where a kink in the MSD vs. temperature is often observed at the laboratory glass transition [98]. More complex behavior, with several kinks [99, 100, 101], was observed for proteins in partially hydrated powders or in the polycrystalline form [102, 103].

A typical temperature dependence of the protein MSD starts with the linear increase in accord with the Nyquist theorem and the corresponding vibrational density of states [103, 104]. It is followed by one or two low-temperature crossovers and, finally, with a much stronger increase above the temperature of the dynamical transition $T_d \sim 200 - 250$ K [105]. This latter temperature depends on a number of factors, including the resolution of the spectrometer, i.e., effectively the time period over which the atomic displacements are recorded [106, 107]. This phenomenology has attracted significant attention since enhanced flexibility and, therefore, the ability to perform biological function can develop at $T > T_d$ [108].

A somewhat unexpected observation came recently from Capaccioli *et al* [5], who presented two key observations based on the analysis of a large database of neutron scattering data accumulated so far: (i) the MSD measured in 50:50 lysozyme-glycerol mixture can be nearly seamlessly overlaid with corresponding measurements for the

pure glycerol and (ii) there are two crossover temperatures common to lysozyme-glycerol and glycerol systems, at $T_d \simeq 210$ and 276 K.

The first observation is significant for assigning the modes of the protein-solvent system responsible for the protein's extended flexibility at high temperatures. High protein flexibility is required for its biological action [109, 110, 80], and this perspective connects protein function with specific physical modes and fluctuations of the protein-solvent system [93]. Frauenfelder and co-workers suggested that the solvent mode coupled to the protein atomic displacements has to be attributed to the hydration shell [111, 112]. They also noted that this mode is decoupled from the α-relaxation of the bulk solvent (structural or collective relaxation with the longest relaxation time and usually connected to the liquid viscosity). The relaxation time of the hydration shell is both faster than α-relaxation and is Arrhenius, with the activation energy usually smaller than that of α-relaxation. Taken together, these features point to its β-character in the established classification of glass science [113, 114]. Since secondary β-relaxation processes exist also in the bulk solvent, the fluctuations localized in the hydration shell of the protein are classified as β_h-relaxation and are expected to carry the dynamics distinct from the bulk [115]. The dynamical transition then occurs when the β_h-relaxation of the hydration shell slows sufficiently down, with lowering temperature, to become longer than the instrumental time-scale (dynamical freezing) [116, 117].

The observation of a near-equivalence of MSDs recorded by neutron scattering in lysozyme-glycerol and pure glycerol systems puts under question the hydration-shell hypothesis, or at least the part of it attributing β-relaxation specifically to the shell, in contrast to a faster relaxation mode of the bulk (of presumably β-character). The question posed by this observation is whether the modes of the solvent coupled with protein flexibility are hydration-shell specific or generic to the bulk material.

Furthermore, since the dynamical transition is a general phenomenon common to glass-forming materials, including molecular liquids and biopolymers [98], the question here is what are the modes that experience dynamical freezing at T_d and whether the instrumental resolution must necessarily be a part of the explanation. Addressing some of these mechanistic questions is a goal of this study.

In order to avoid the complexities of protein solutions, we address these basic questions by focusing solely on bulk glycerol, for which we report here extensive molecular dynamics (MD) simulations. The temperature dependence of hydrogen MSDs is analyzed in terms of separate contributions of the center of mass translations and rotations relative to the center of mass of the molecule. Both translational and rotational MSDs show a crossover at the same temperature $T_d \sim 275$ K consistent with experimental data. The temperature of translational and rotational dynamical transitions does not change when the observation time is significantly altered. We also find that the same temperature characterizes the dynamic crossover from α to β relaxation as measured by glycerol's diffusivity and rotational dynamics.

The consistent picture arising from our observations is that a structural crossover occurs in glycerol at $\sim 250 - 275$ K, which affects both the MSDs and relaxation times. However, there is no indication from our data that this crossover should be identified with a true thermodynamic transition. We therefore suggest that all observed crossovers are dynamical in character. In particular, the structural crossover to a low-temperature state of glycerol, characterized by long-ranged dipolar correlations, becomes possible because these collective correlations cannot relax on the limited observation time. The dynamical transition in the MSD recorded by neutron scattering is not the result of crossing of the time-scale of single-particle translational/rotational diffusion with the observation time-scale, but rather the crossing of the latter with the time-scale of multi-body relaxation of polarized domains. A corresponding significant

increase in the orientational Kirkwood factor and the jump in the dielectric constant at low temperatures are caused, in our simulations, by the crossing of the relaxation time of dipolar domains and the observation (simulation) time. This phenomenology is similar to that of relaxor ferroelectrics where dynamic freezing of ferroelectric domains is responsible for the high dielectric constant of the low-temperature phase [118].

2.3 Incoherent Neutron Scattering

The experimental MSDs are extracted from incoherent elastic neutron scattering. The reported signals are affected by the instrumental resolution function convoluting with the self-dynamic structure factor $S_s(q,\omega)$, for which we assume the scattering momentum $\mathbf{q}$ directed along the x-axis of the laboratory frame. The function $S_s(q,\omega)$ is the time Fourier transform of the self-intermediate scattering function

$$I(q,t) = N^{-1}\sum_j \langle e^{iq\Delta x_j(t)}\rangle, \tag{2.1}$$

where $\Delta x_j = x_j(t) - x_j(0)$ is the displacement of a hydrogen atom and the sum runs over N hydrogen atoms in the system; $\langle \dots \rangle$ denotes an ensemble average.

In what follows we will consider all hydrogens in the system identical, although we will separate two groups of hydrogens of glycerol: 3 hydroxyl hydrogens and 5 hydrogens bonded to carbon atoms. Correspondingly, experimental results for partially deuterated glycerol [119] $C_3H_5(OD)_3$ (g-d3) and $C_3D_5(OH)_3$ (g-d5) will be analyzed by considering the corresponding groups of hydrogen atoms not substituted by deuteration.

The intensity of the elastic scattering function at $\omega = 0$ gives access to the MSD [96, 119]. The corresponding function $S_s(q,\omega=0,\Delta\omega)$, depending on the resolution window of the spectrometer $\Delta\omega$, can be approximated by $I(q,t_r) \simeq S_s(q,\omega=0,\Delta\omega)$,

where the resolution time t_r is related to the resolution window of the spectrometer. According to Doster *et al* [120], the connection is $t_r/\mathrm{ps} = 1.09/\Gamma(\mathrm{meV})$, where Γ is the width at half maximum of the resolution function.

The intermediate scattering function in Eq. (2.1) can be estimated in the Gaussian approximation [121], which leads to

$$-\ln\left[I(q,t)\right] \simeq q^2\langle(\delta x)^2\rangle - q^2\langle\delta x(t)\delta x(0)\rangle. \tag{2.2}$$

If the time autocorrelation function $\langle\delta x(t)\delta x(0)\rangle$, $\delta x(t) = x(t) - \langle x\rangle$ decays sufficiently to zero on the resolution time t_r, the second term in Eq. (2.2) disappears and one gets an estimate of the mean square fluctuation (MSF) $\langle(\delta x)^2\rangle$ from the linear slope of $-\ln[I(q,t_r)]$ vs q^2 [119, 122]. Otherwise one obtains half of the MSD $(1/2)\langle\Delta x(t_r)^2\rangle$ from the slope of $-\ln[I(q,t_r)]$ vs q^2.

The data presented here were obtained from extensive MD simulations of glycerol described by the OPLS-AA force field [123] as is explained in section A.1. Our main purpose in the analysis of the intermediate scattering function is to extract the relative contributions to the observed MSD arising from center of mass translations and molecular rotations relative to the center of mass. The question that we address here is whether the dynamical transition, if observed, occurs at the same temperature for these two modes. In addition to general mechanistic insights that such an analysis can produce, this question is relevant to testing the idea of dynamical freezing of a subset of molecular motions as the reason for the experimentally observed kink in the dependence of the MSD on temperature [102, 105, 103, 106], identified with T_d. If the kink is caused by reaching the equality between the relaxation time and the instrumental observation window [106], the dynamical transition temperature should be different for translations and rotations having their distinct relaxation times, unless they happen to be close. This is not what we observe from our simulations: the

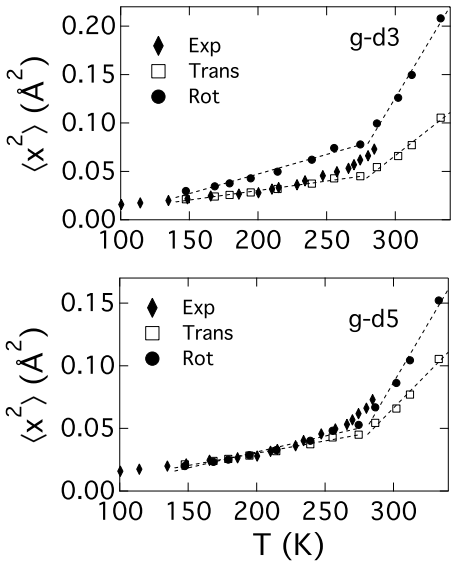

Figure 2.1: $\langle x^2 \rangle = \langle \Delta x(t_r)^2 \rangle$ for g-d5 (Upper Panel) and g-d3 (Lower Panel) Deuterated Glycerol. The Experimental Data Obtained From IN13 Spectrometer for Correspondingly Deuterated Glycerol [5] Are Compared to MD Simulations. The Simulated MSDs Are Separated into Displacement of the Glycerol Center of Mass (‘‘Trans”) and the Displacements of Hydrogens Relative to the Center of Mass (‘‘Rot”). The Dashed Lines Are the Linear Regressions Drawn Through the Corresponding Points From MD Simulations.

dynamical transition temperatures are the same for rotations and translations when calculated from fitting the intermediate scattering function to Eq. (2.2) (Fig. 2.1).

The separation of the center of mass translations and rotations relative to the center of mass assumes the factorization of the intermediate scattering function into the translational, $I_T(q,t)$, and rotational, $I_R(q,t)$, components

$$I(q,t) = I_T(q,t) I_R(q,t). \tag{2.3}$$

We therefore calculated $I_T(q,t)$ and $I_R(q,t)$ separately and produced the linear fits of the corresponding functions vs q^2 with $t_r = 25$ ps for both g-d3 and g-d5 liquids. No deuteration was actually performed in simulations and only the corresponding groups of hydrogen atoms were selected to produce the intermediate scattering functions.

The accuracy of translation/rotation factorization in Eq. (2.3) was tested previ-

ously and is usually found to hold [124, 125, 126]. Indeed, one expects this separation to be accurate in the Gaussian limit since translations and rotations carry different symmetry. If one separates $\Delta x(t) = \Delta x_c(t) + \Delta x_R(t)$ into the center of mass displacement $\Delta x_c(t)$ and the rotation relative to the center of mass $\Delta x_R(t)$, the MSD becomes the sum of two self terms and the translational-rotational cross term

$$\langle \Delta x(t)^2 \rangle = \langle \Delta x_c(t)^2 \rangle + \langle \Delta x_R(t)^2 \rangle + 2\langle \Delta x_c(t) \Delta x_R(t) \rangle. \tag{2.4}$$

Figure 2.2 shows an example of the analysis of the three correlation components in Eq. (2.4) from MD simulations. The translational and rotational components of the MSD are close in magnitude, while the cross-correlation is negative and is much smaller.

The translational and rotational MSDs are shown separately in Fig. 2.1 to indicate the common point of the kink at $T_d \sim 275$ K. The same temperature of the dynamical transition is reported experimentally [119, 5]. However, the absolute values of MSDs from experiment (closed diamonds in Fig. 2.1) are below the simulation results, which is easy to see from the plot since the overall MSD follows from adding up the translational and rotational components (Eq. (2.4)). The most probable explanation of this discrepancy is that fitting the experimental neutron scattering data in a limited range q-values used in the measurements [119] allows one to probe only a limited subset of motions [127, 128], presumably the translational diffusion. Indeed, the agreement between simulations and experiment for the center of mass MSD is quite good. We also note that the agreement between the calculated coefficient of self-diffusion of glycerol and the results of measurements by NMR [8] is also reasonable (Fig. 2.6 below).

The time dependence of MSDs shown in Fig. 2.2 also helps to understand the physical origin of MSDs recorded by neutron scattering. Both the translational and rotational components of the MSDs are characterized by two distinct regimes: a fast (~ 1 ps) growth due to ballistic motions in the liquid's cage (localized diffusion

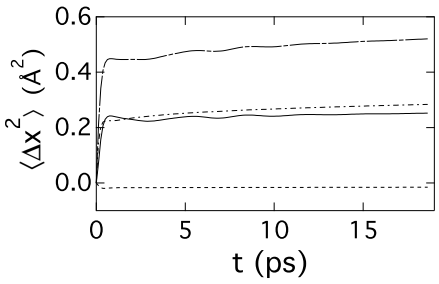

Figure 2.2: $\langle \Delta x(t)^2 \rangle$ vs Time at $T = 250$ K. The Overall MSD (Long-Dashed Line) Is Separated into the Center of Mass (Solid Line), Rotational (Dash-Dotted Line), and Cross (Dashed Line) Components (Eq. (2.4)).

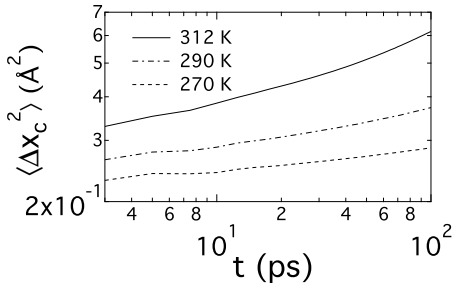

Figure 2.3: Center of Mass MSD, $\langle \Delta x_c(t)^2 \rangle$, Of Glycerol at Different Temperatures Indicated in the Plot.

[129]), followed by a much slower, long-range diffusion with $\langle \Delta x(t)^2 \rangle \propto t$ (see Fig. 2.3 for a log-log plot). The main observation here is that most of the MSD on the resolution time-scale $t_r \sim 25$ ps is caused by the ballistic displacement associated with a secondary relaxation and not by the diffusional motion associated with the primary relaxation process. This conclusion holds both below and above T_d (Figs. 2.2 and 2.3). The increase of the observation window from 25 ps to 135 ps makes the time spent by the particle on the linear, diffusional portion of the MSD longer (Fig. 2.2) and thus increases the slope of the high temperature part of the MSD curve (Fig. 2.4). It is important to realize that fast cage dynamics, resulting in the main portion of the observed MSD, are much faster than the resolution time t_r and in fact become even faster with lowering temperature because of a greater rigidity of the

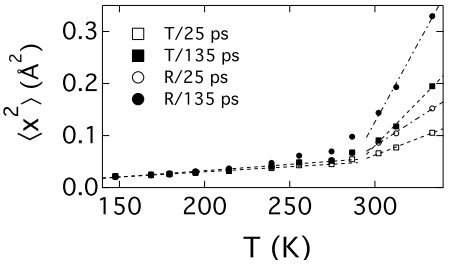

Figure 2.4: $\langle x^2 \rangle = \langle \Delta x(t_r)^2 \rangle$ for g-d5 Measured on $t_r = 25$ ps (open points) and $t_r = 135$ ps (Closed Points). The Center of Mass $\langle \Delta x_c^2 \rangle$ ("T", Squares) and Rotational $\langle \Delta x_R^2 \rangle$ ("R", Circles) Contributions Are Shown Separately. The Dashed and Dash-Dotted Lines Are Linear Regressions Drawn Through the Low-Temperature and High-Temperature Points.

low-temperature glycerol. It is the amplitude of the ballistic displacement which gets larger with increasing temperature, resulting in the observed temperature dependence of the MSD. The crossing of the resolution time of the spectrometer (25 ps) and the relaxation time of these ballistic motions never occurs (also se below) and, therefore, the kink in the MSD vs temperature cannot be attributed to the finite resolution time.

The change of the form of the MSD vs T with the changing observation window t_r is shown in Fig. 2.4. It adds additional evidence to the suggestion that the kink in the MSD's temperature dependence is not caused by the equality between the relaxation time and the observation window. While the high-temperature portion of the MSD has a steeper slope for a higher t_r, in agreement with experiment [5], the temperature of the dynamical transition T_d has little sensitivity to t_r. In addition, the equality between the dynamical transition temperatures for the translational and rotational MSDs is preserved between $t_r = 25$ ps and $t_r = 135$ ps. If one assumes that the consistency in T_d for $t_r = 25$ ps shown in Fig. 2.1 is a mere coincidence, it is hard to see how it can be preserved at $t_r = 135$ ps. One has to accept the conclusion that the kink in the MSD is not related to the observation window [122, 130] and,

instead, should be attributed to the softening of the liquid cage, with increasing temperature, in which a glycerol molecule finds itself for a relatively short time of ~ 1 ps. The rattling inside the cage is followed by an escape and the onset of long-range diffusion, but this component simply adds to the main displacement achieved by the ballistic cage rattling. The next question is whether structural distinctions of the entire liquid producing the difference between the low-temperature rigid cage and the high-temperature soft cage can be identified.

2.4 Dynamic Crossover

An explanation alternative to the instrumental resolution effect for the appearance of the kink in the proton MSD involves the dynamic crossover, i.e., a corresponding kink in the dependence of the system relaxation time on the inverse temperature [131]. This phenomenology, known as the fragile-to-strong transition in glass science [113], represents the crossover from the structural α-relaxation at high temperatures above the crossover to a secondary β-relaxation at low temperature below the crossover. Correspondingly, the activation barrier of the high-temperature α-relaxation is higher than the activation barrier of the low-temperature β-relaxation. We show below that this phenomenon is not connected to the kink in the MSD reported by neutron scattering and, at least in our simulations, has a trivial explanation of slower dynamics exceeding in its relaxation time the observation window (simulation time in the case of MD).

The problem of dynamic crossover in confined water has been extensively studied [132, 128, 133] and it has been established that the temperature of the dynamic crossover of confined water is generally consistent with T_d of proteins [131, 134]. The temperature T_d was also found to be independent of the protein hydration level [134, 130, 135] even though the relaxation times themselves are strongly affected by

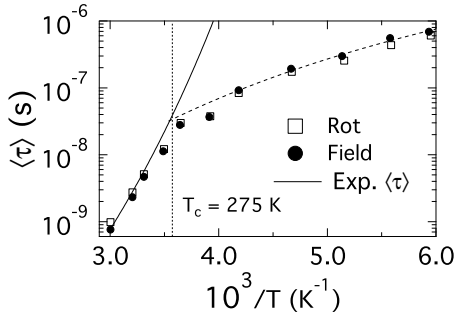

Figure 2.5: Average Relaxation Time $\langle\tau\rangle$ Obtained From Rotational Correlation Function ("rot")And From the Electric Field Correlation Function ("field") (Analysis of 2.5 ns of NVE MD Simulations, Section A.1). The Solid Line Refers to the Average Relaxation Time [6] Obtained by Fitting the Dielectric Loss Spectrum to the Cole-Davidson Function [7]. The Dashed Line Is a Regression Drawn Through the MD Points Obtained From the Electric Field Correlation Function. T_c (Dotted Line) Indicates the Crossover Temperature.

hydration. This latter observation points to the connection between T_d and some sort of structural change in confined water.

The dynamic crossover results for water are necessarily limited to confined systems since bulk water is unstable to nucleation below $\simeq 243$ K [136, 133]. Since our present simulations apply to bulk glycerol, it would be of significant interest to establish a phenomenology similar to that found for confined water for a material available in bulk phase both in simulations and in the laboratory experiment.

It is useful to start off with an estimate of how the dynamic crossover in the relaxation time can potentially affect the MSD measured on the resolution time t_r. This can be illustrated for the rotational MSD, which can be rewritten in terms of the rotational MSF $\langle(\delta x_R)^2\rangle = \langle x_R^2\rangle - \langle x_R\rangle^2$ and the normalized autocorrelation function of rotations $\phi_R(t)$

$$\langle \Delta x_R(t)^2\rangle = 2\langle(\delta x_R)^2\rangle\left[1-\phi_R(t)\right], \tag{2.5}$$

where

$$\phi_R(t) = \langle(\delta x_R)^2\rangle^{-1}\langle\delta x_R(t)\delta x_R(0)\rangle. \tag{2.6}$$

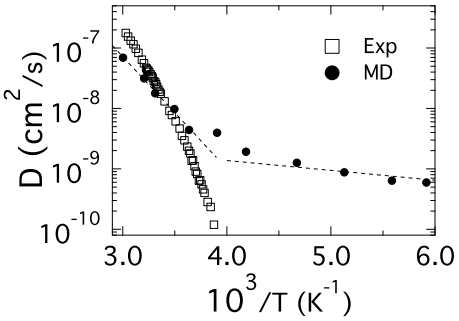

Figure 2.6: Diffusion Coefficients Recorded Experimentally by NMR ("Exp", [8]) and Obtained from the Simulations ("MD").The Dashed Line Is a Regression Drawn Through the MD Points.

The generic form of $\phi_R(t)$ is an initial ballistic (Gaussian) decay, followed by exponential collective relaxation: $\phi_R(t) = A_g \exp[-(t/\tau_g)^2] + (1 - A_g) \exp[-t/\tau_R]$ (or, alternatively, multi-exponential or stretched exponential term) [95]. In the entire temperature range studied for glycerol we find that t_r falls between the time of ballistic relaxation τ_g and the time of collective exponential relaxation τ_R: $\tau_g \ll t_r \ll \tau_R$. One therefore gets

$$\langle \Delta x_R(t)^2 \rangle \simeq 2\langle (\delta x_R)^2 \rangle \left[A_g + (1 - A_g)(t_r/\tau_R) \right]. \tag{2.7}$$

The relaxation time is not expected to affect the MSD when $t_r \ll \tau_R$, but can affect faster relaxing systems when $t_r \simeq \tau_R$ [137]. At $t_r \ll \tau_R$, the magnitude of the MSD is mostly determined by the amplitude of the Gaussian component of the relaxation dynamics, in agreement with the arguments presented in relation to Figs. 2.2 and 2.3. Therefore, if the dynamic crossover and the kink of the MSD occur at the same temperature [134] one has to relate this coincidence to a structural change and not to a direct effect of the relaxation time on the MSD. The hypothesis that the crossover in the relaxation time affects the MSD is, therefore, not supported by our simulation results.

The results for the average rotational relaxation time for all protons in glycerol

are shown in Fig. 2.5. It is calculated by integrating the time correlation function

$$\langle \tau_X \rangle = \int_0^\infty \phi_X(t) dt, \tag{2.8}$$

where $X = R$ corresponds to the normalized time correlation function in Eq. (2.6). These results are shown by the open points in Fig. 2.5.

We have additionally calculated the time correlation function $\phi_E(t) \propto \langle \delta\mathbf{E}(t) \cdot \delta\mathbf{E}(0) \rangle$ based on the dynamic variable of the electric field produced by the rest of the glycerol liquid at the center of mass of a given target molecule ($\mathbf{X} = \mathbf{E}$). The microscopic electric field $\mathbf{E}(t)$ is therefore a fluctuating local field producing a torque on the glycerol's dipole moment. The results for the average relaxation times obtained from the corresponding time correlation functions through Eq. (2.8) are shown by the closed points in Fig. 2.5. There is a good agreement between τ_R and τ_E suggesting that the electric field fluctuations are caused by molecular rotations, as one would anticipate from the standard Debye model of dielectric relaxation [138, 6].

The average relaxation times from MD simulations are compared in Fig. 2.5 with the average relaxation time calculated from the Cole-Davidson fit of glycerol's loss spectrum reported by broad-band dielectric spectroscopy [7] (solid line). There is a very good agreement between the simulations and experimental dielectric data at high temperatures, suggesting that the adopted force field [123] (see section A.1) is well parametrized for glycerol rotations. There is a less satisfactory agreement between the diffusion coefficient calculated from MD and measured by NMR (Fig. 2.6). Differences between quasi-elastic neutron scattering (QENS) and NMR/viscosity data for glycerol self-diffusion have been documented in the past [139, 129] and might contribute to the discrepancy.

The dynamic crossover occurs in the range of temperatures when the α-relaxation time becomes comparable to the length of the simulation trajectory $\tau_{\rm sim} \simeq 50$ ns. In

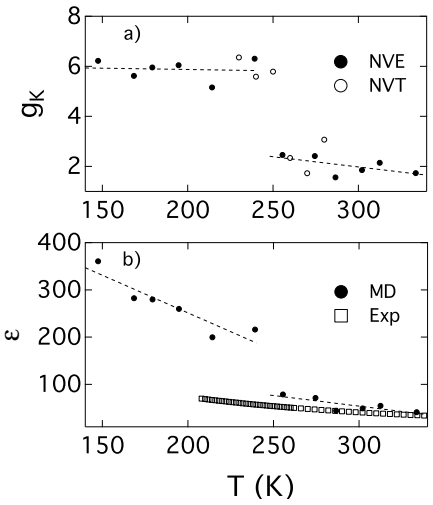

Figure 2.7: The Kirkwood Factor (a) and Dielectric Constant (b) Of Glycerol Calculated From MD (Circles)And Measured in Bulk Samples Experimentally [9] (Squares). The Dashed Lines Are Linear Fits to the Corresponding Subsets of Data to Guide the Eye. The Kirkwood Factors in (a)Were Obtained Both in NVE and NVT Separate Simulation Runs.

fact, the time window $\tau_{\rm calc}$ on which the time correlation function $\phi_X(t)$ is calculated from the simulation trajectories is always shorter, $\tau_{\rm calc} < \tau_{\rm sim}$. We therefore stop observing the slow relaxation in simulations when the α-relaxation time becomes longer than $\tau_{\rm calc}$. The relative weight of the fast relaxation in $\langle\tau\rangle$ increases and we observe this as a dynamical crossover.

What our data do not seem to address is why the kinks in the rotational and translational MSDs and the corresponding dynamical crossovers in the rotational relaxation times and translational diffusion (Figs. 2.5 and 2.6) all occur in the same range of temperatures. A possible scenario to explain this coincidence might include a structural transition resulting in a drop of the configurational entropy [140]. According to the general arguments based on the Adam-Gibbs relation [113], this would result in a much slower main relaxation process, which would sharply disappear from the observation window of our numerical experiment. While our results presented below do support alteration of glycerol's orientational structure, we do not have a

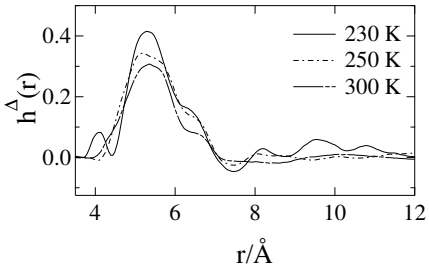

Figure 2.8: Projection of the Pair Distribution Function of Glycerol on the Orientational Invariant $\Delta(1,2) = (\hat{\mathbf{e}}_1 \cdot \hat{\mathbf{e}}_2)$ Calculated From MD Simulations at Different Temperatures.

direct evidence for a discontinuous change in the configurational entropy.

In order to identify possible structural changes, we have looked at the temperature dependence of the Kirkwood factor reflecting orientational correlations in the liquid

$$g_{\mathrm{K}} = \sum_m \langle \hat{\mathbf{e}}_\ell \cdot \hat{\mathbf{e}}_m \rangle. \tag{2.9}$$

Here, $\hat{\mathbf{e}}_m$ are the unit vectors of molecular dipoles (4.6 D in the force field used in our simulations). The Kirkwood factor was in turn used in the Kirkwood-Onsager relation [138] to calculate the dielectric constant $\epsilon(T)$ (the glycerol force field is non-polarizable and the refractive index is equal to unity). The results of these calculations are shown in Fig. 2.7.

The Kirkwood factor shows a discontinuous increase at $T < 250$ K, which results in the corresponding increase of the dielectric constant calculated from MD simulations. The increase in g_{K} is caused by the emergence of long-range orientational correlations of glycerol dipoles at low temperatures, as is illustrated in Fig. 2.8. We show there the projection of the pair correlation function of glycerol $h(r, \hat{\mathbf{e}}_1, \hat{\mathbf{e}}_2)$, depending on the distance r between two molecules and their orientations $\hat{\mathbf{e}}_1$ and $\hat{\mathbf{e}}_2$, on the rotational invariant of the scalar product between the unit vectors of the dipole

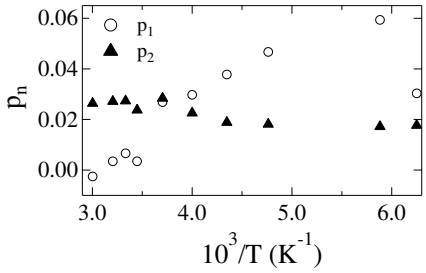

Figure 2.9: Orientational Order Parameters p_1 and p_2 in Eq. (2.11) Calculated From MD Trajectories at Different Temperatures.

moments $\Delta(1,2) = (\hat{\mathbf{e}}_1 \cdot \hat{\mathbf{e}}_2)$. The corresponding pair distribution function [95]

$$h^{\Delta}(r) = \int h(r, \hat{\mathbf{e}}_1, \hat{\mathbf{e}}_2)\Delta(1,2)\frac{d\omega_1 d\omega_2}{(8\pi)^2} \tag{2.10}$$

at different temperatures in shown in Fig. 2.8.

It is clear that a long-range oscillatory pattern, reflecting preferential parallel alignments of the dipoles, appears at low temperatures. The dipolar alignments are responsible for an increase in the low-temperature Kirkwood factor, $g_{\mathrm{K}} = 1 + \rho \int h^{\Delta}(r) d\mathbf{r}$, ρ is the number density. Despite these long-range orientational correlations, the low-temperature phase does not show any specific orientational order, as confirmed by calculations of the first and second orientational order parameters [141, 142] (Fig. 2.9) as explained below. No translational order is observed either: the radial pair distribution functions are nearly identical at low and high temperatures (Fig. 2.10). We therefore can conclude that the low-temperature phase is a disordered liquid.

The orientational order can be detected by orientational order parameters typically defined for liquid crystals [142]. The order parameter p_n is the average nth order Legendre polynomial $P_n(\hat{\mathbf{e}} \cdot \hat{\mathbf{n}})$

$$p_n = N_m^{-1} \sum_{\ell} \langle P_n(\hat{\mathbf{e}}_\ell \cdot \hat{\mathbf{n}}) \rangle \tag{2.11}$$

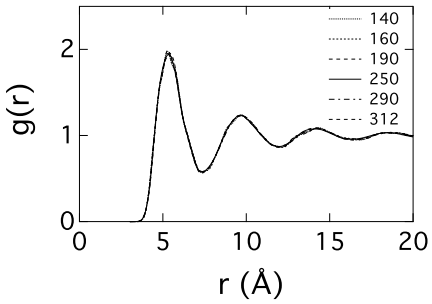

Figure 2.10: Pair Distribution Functions $g(r)$ Of the Center of Mass of Glycerol Calculated at the Temperatures Indicated in the Plot. The Calculated Functions Nearly Coincide on the Scale of the Plot.

relative to the liquid director $\hat{\mathbf{n}}$; N_m is the number of molecules in the liquid. The director is identified as the eigenvector corresponding to the largest eigenvalue of the tensor

$$Q_{\alpha\beta} = (2N_m)^{-1} \sum_{\ell} \left(3\,\hat{e}_{\ell,\alpha}\hat{e}_{\ell,\beta} - \delta_{\alpha\beta}\right), \tag{2.12}$$

where α and β are the Cartesian projections and $\delta_{\alpha\beta}$ is the Kronecker delta function. The results of calculations for the first and second order parameters ($n = 1, 2$) are shown in Fig. 2.9. No orientational order can be identified at low temperatures from these calculations.

The jump in the simulated dielectric constant is in stark disagreement with the linear dielectric experiment [9] where no discontinuities were observed (squares in Fig. 2.7b). The results of simulations are in fair agreement with experiment at high temperatures, but the increase in the Kirkwood factor at lower temperatures (Fig. 2.7a) makes the dielectric constant much higher than observations. Since the crossover temperature for the dielectric constant is roughly consistent with the kinks in the rotational and translational MSDs, we conclude that restricting the observation window not only makes changes to the observable relaxation dynamics, but also does not allow certain orientational correlations to relax. As a result, we observe a long-range

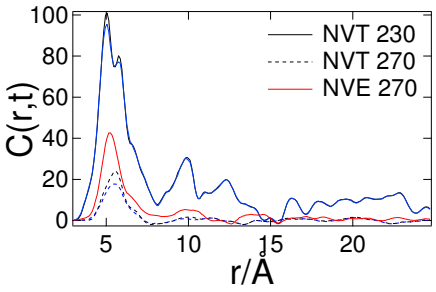

Figure 2.11: $C(r,t)$ at $t = 2.5$ ps (black lines) and $t = 2.5$ ns (Blue Lines)Calculated From NVT Simulations of Glycerol at Different Temperatures Indicated in the Plot. The Red Line Indicates NVE Simulation at 270 K.

orientational order frozen on the observation time-scale. This implies that both the low-temperature Kirkwood factor and the corresponding dielectric constant shown in Fig. 2.7 are non-equilibrium quantities. A similar, about five times compared to the bulk (Fig. 9 in Ref. 143), increase in the dielectric constant was observed for ultrathin films of glycerol obtained by vapor deposition [144]. Subsequent combined dielectric and calorimetry measurements have suggested the existence of rigid polar clusters, which relax as a whole, with an enhanced cluster dipole moment [143]. There is also recent evidence of an unrelaxed orientational order in organic glasses obtained by surface deposition [145].

The existence of highly correlated clusters should be seen in the heterogeneity of binary correlations expressed in terms of fourth-order correlation functions [146]. In order to test this hypothesis, we made the next step of calculating the distance- and time-dependent correlations between binary dipolar orientational correlations expressed through the instantaneous Kirkwood factors. Specifically, the quantity

$$c_\ell(t) = \sum_{m \neq \ell} \hat{\mathbf{e}}_\ell(t) \cdot \hat{\mathbf{e}}_m(t) \tag{2.13}$$

was constructed at each point of the simulation trajectory to reflect the instantaneous binary correlations of the chosen dipole moment ℓ with all remaining dipoles in the

liquid. Obviously, one has $\langle c_\ell(t)\rangle = g_K - 1$. We then constructed the distance- and time-dependent correlation between the local binary correlations as follows

$$C(r,t) = \frac{V}{N_m^2}\sum_{\ell,k}\langle c_\ell(0)c_k(t)\delta\left(\mathbf{r}-\mathbf{r}_\ell(0)+\mathbf{r}_k(t)\right)\rangle, \tag{2.14}$$

where the average is taken along the simulation trajectory and V is the liquid volume. The normalization of $C(r,0)$ relates it to the Kirkwood factor

$$V^{-1}\int C(r,0)d\mathbf{r} = (5/3)g_K^2 - 2g_K + 1. \tag{2.15}$$

Similarly to $h^{\Delta}(r)$ in Fig. 2.8, but significantly more pronounced, we observe the rise of long-range heterogeneous correlations at low temperatures (Fig. 2.11). The appearance of such correlations, exceeding the range of local order in the density distribution function (Fig. 2.10), signifies the spatial orientational heterogeneity of the low-temperature glycerol.

2.5 Discussion and Implications for the Protein Dynamical Transition

We obtained here, by computer simulations, both a kink in the temperature dependence of the MSD (dynamical transition) and the dynamical crossovers in the relaxation times. Both effects have been observed experimentally and a link between them has been suggested through some sort of structural transition in the liquid [131, 133, 135]. The answer to the ongoing discussion of whether a purely dynamical crossover or a structural transition explains the data might be that both are present. However, in contrast to the scenarios involving thermodynamic liquid-liquid transitions, both the structural and relaxation time crossovers have a dynamic origin. The structural crossover is caused by the inability of certain structural correlations to relax on the observation window. There is nothing in our data that connects the appearance of such structural correlations to a thermodynamic transition between

two phases of a bulk material. This distinction becomes, however, less loaded with physical meaning in the low-temperature state. When the relaxation time of the "orientationally correlated liquid" becomes much longer than any conceivable experimental time, one has to distinguish this state of the material as an "orientationally correlated glass", with all relevant properties distinct from the "ordinary" glass. One arrives at polyamorphism of the glass state [113] caused by long-ranged orientational correlations.

The observation of an increase in the dielectric constant of glycerol below the dynamical transition, here by simulations and for vapor deposited glasses experimentally [144, 143], adds a structural component to the standard picture of ergodicity breaking of glass science. The standard paradigm is that the glass does not have the ability to relax, but maintains the structure of the liquid. This is indeed true for the positional structure of the glycerol molecules. However, the inability of dipolar orientations to relax causes orientational heterogeneity represented by correlated dipolar clusters, which do not relax on the observation time-scale. The long-sought growth of the structural order of glass-formers on approach to the laboratory glass transition might be, therefore, best discovered by experiments probing the heterogeneity of orientational multipolar correlations.

Chapter 3

ERGODICITY BREAKING OF IRON DISPLACEMENT IN HEME PROTEINS

This material was published in Soft Matter (journal) 13(44), pp.8188-8201 (2017).

3.1 Summary

We present a model of the dynamical transition of atomic displacements in proteins. Increased mean-square displacement at higher temperatures is caused by the softening of the force constant for atomic/molecular displacements by electrostatic and van der Waals forces from the protein-water thermal bath. Displacement softening passes through a nonergodic dynamical transition when the relaxation time of the force-force correlation function enters, with increasing temperature, the instrumental observation window. Two crossover temperatures are identified. The lower crossover, presently connected to the glass transition, is related to the dynamical unfreezing of rotations of water molecules within nanodomains polarized by charged surface residues of the protein. The higher crossover temperature, usually assigned to the dynamical transition, marks the onset of water translations. All crossovers are ergodicity breaking transitions depending on the corresponding observation windows. Allowing stretched exponential relaxation of the protein-water thermal bath significantly improves the theory-experiment agreement when applied to solid protein samples studied by Mössbauer spectroscopy.

3.2 Introduction

Atomic displacements in proteins are viewed as a gauge of the overall flexibility of macromolecules.[147] Displacements of the hydrogen atoms are reported by

neutron scattering,[148] and mean-square displacements (B-factors) of all atoms are known from X-ray crystallography. Neutron scattering reports ensemble averages of scattering from many hydrogen atoms of a single protein.[148, 96, 109, 149] In contrast, Mössbauer spectroscopy often probes the displacement of a single atom in the protein,[150, 80] which is the heme iron in this study focused on cytochrome c (Cyt-c) and myoglobin proteins.

The temperature dependence of atomic displacements from both neutron scattering and Mössbauer spectroscopy shows a number of crossovers. They are marked by changes in the slope of atomic mean-square displacement vs temperature,[75, 102] deviating from expectations from the fluctuation-dissipation theorem.[92, 104] This problem has attracted significant attention in the literature.[96, 117, 80, 151, 152, 153, 154] The accumulation of the data over several decades of studies, combined with their recent refinements through the comparison of the results obtained on spectrometers with different resolution,[106, 5, 155, 156] have lead to a convergent phenomenological picture.

Two low-temperature crossovers are now identified (Fig. 3.1). The higher-temperature crossover T_d, originally assigned to the protein dynamical transition,[102, 151] depends on the observation window of the spectrometer[117, 106, 5, 155] and shifts to lower temperatures when the resolution is increased (a longer observation time τ_r in Fig. 3.1). The lower crossover temperature, $T_g \simeq 170 - 180$ K, is independent of the observation window (in the range of resolution windows available to spectroscopy) and is assigned to the glass transition of the protein hydration shell.[102, 155, 151, 5]

All motions, rotations and translations, in the hydration shell (except for cage rattling) terminate at the lower temperature T_g. While this interpretation is consistent with the basic phenomenology of glass science, it does not address the question of how the structure and dynamics of the hydration shell affect atoms inside the protein, the

heme iron for Mössbauer spectroscopy. The basic question here is whether the observations can be fully related to stiffening of the hydration shell at lower temperatures, thus reducing elastic deformations of the protein,[157] or there are some long-range forces acting on the heme, which are reduced in their fluctuations when the hydration shell dynamically freezes. It is possible that no simple answer to this question can be obtained in the case of neutron scattering since there are several classes of motions of protein hydrogens: cage rattling, methyl rotations, and jumps between cages.[101] To avoid these complications, we focus here on a single heavy atom, heme iron, probed by Mössbauer spectroscopy on the resolution time $\tau_r = 142$ ns.

The question addressed here is what are the physical mechanisms propagating fluctuations of the protein-water interface to an internal atom within the protein.[158, 159] This question, also relevant to how enzymes work,[93] was addressed by the electro-elastic model of the protein,[160, 161] where both the effect of the viscoelastic deformation and the effect of the long-range forces acting on the heme iron were considered. The main conclusion of that theoretical work was the recognition of the two-step nature of the crossover in the mean-square fluctuation (MSF) of the heme iron. The low-temperature crossover, $T_g \simeq 170 - 180$ K, was assigned to an enhancement of viscoelastic deformations above the glass transition of the protein-water interface.[160] The increment in the MSF at T_g was, however, insignificant, as confirmed below based on new molecular dynamics (MD) simulations. It was, therefore, concluded that altering elastic stiffening is not sufficient to describe the rise of the MSF above T_d and long-range forces need to be involved.

The iron MSF significantly increases when electrostatic forces acting on the iron are included.[160] The dynamical transition and the corresponding enhancement of the MSF are promoted by ergodicity breaking when the longest relaxation time crosses the instrumental time.[162, 116, 117, 106] The equation for the MSF resulting from

this perspective involves the MSF from local vibrations of the heme $\langle \delta x^2 \rangle_{\rm vib}$ and the global softening of the entire heme motions through the long-ranged forces acting on it. This second component enters the denominator of Eq. (3.1) through the variance of the force acting on heme's iron $\langle \delta F^2 \rangle_r$

$$\langle \delta x^2 \rangle_r = \frac{\langle \delta x^2 \rangle_{\rm vib}}{1 - \beta^2 \langle \delta F^2 \rangle_r \langle \delta x^2 \rangle_{\rm vib}}, \tag{3.1}$$

where $\beta = 1/(k_{\rm B}T)$ is the inverse temperature. Equation (3.1) was originally derived in Ref. [160] and is briefly re-derived in the discussion presented below.

The subscript "r" in the angular brackets, $\langle \dots \rangle_r$, indicates that the average is constrained by the observation window τ_r. Correspondingly, the fluctuations of the long-range forces are mostly frozen at low temperatures when $\langle \delta F^2 \rangle_r$ is low, yielding $\langle \delta x^2 \rangle \simeq \langle \delta x^2 \rangle_{\rm vib}$. Since the relaxation time of the long-range forces $\tau(T)$ depends on temperature according to the Arrhenius law, it shortens with increasing temperature, ultimately reaching the point[160, 163, 164, 152] $\tau_r \simeq \tau(T_d)$, at which the high-temperature crossover occurs. Fluctuations of the long-range forces become dynamically unfrozen at this temperature, leading to an increase of both $\langle \delta F^2 \rangle_r$ and $\langle \delta x^2 \rangle_r$.

In this chapter, we present new extensive simulations of Cyt-c in solution at different temperatures. The goal is to assert the role of long-range forces in achieving the softening of atomic displacements at high temperatures (Eq. (3.1)). We consider the entire heme as a separate unit experiencing the force from the surrounding thermal bath. This coarse graining allows us to focus on the long-time relaxation of the force-force correlation function relevant for the long observation time, $\tau_r = 142$ ns, of the Mössbauer experiment. We find that the longest relaxation time $\tau(T)$ follows the Arrhenius law with the activation barrier characteristic of a secondary relaxation process (β-relaxation of glass science[165]). We therefore support the proposal advanced by

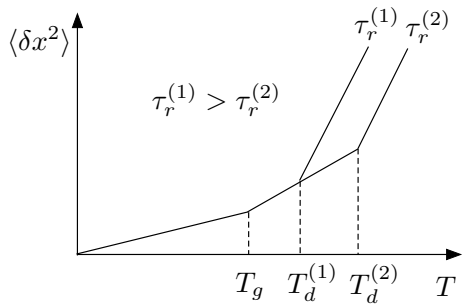

Figure 3.1: Schematic Representation of Two Crossovers in the Temperature Dependence of the Mean-Square Fluctuation (MSF) $\langle \delta x^2 \rangle$. The Lower Crossover, T_g, Is Independent of the Instrumental Resolution Window and Corresponds to the Glass Transition of the Protein-Water Interface. The Upper Crossover (Dynamical Transition), T_d, Does Depend on the Observation Window and Is Related to the Entrance of the Relaxation Time of the Force Acting on the Coarse-Grained Unit (Residue, Cofactor, etc.)Into the Resolution Window of the Experiment. The Temperature T_d Shifts to the Lower Value when the Observation Time Is Increased.

Frauenfelder and co-workers[117, 107] that the higher-temperature crossover is caused by ergodicity breaking when the relaxation time of the secondary process characterizing the protein-water interface enters the experimental observation window. This relaxation process effects the heme iron through the combination of non-polar (van der Waals) and polar (electrostatic) forces.

Our focus on the protein in solution has a limited applicability to experiments done with solid samples. Nevertheless, computer simulations produce results close to observations for the reduced state of Cyt-c. The length of simulations is also insufficient to sample the dynamics on the time-scale of $\tau_r = 142$ ns. In addition, the solution setup does not reproduce highly stretched dynamics observed in protein powders.[101, 166, 152] We find that the agreement between theory and experiment[13] is much improved when stretched exponential dynamics from dielectric spectroscopy for powder samples[28] are used in our model.

Despite limitations of our simulations in application to experimental data, there is one significant advantage of the solution setup. Experiments done with solid samples

cannot claim that the observed phenomenology directly applies to solutions. The similarity between our simulations and such experiments gives credit to the idea that dynamical transition, caused by ergodicity breaking, is a general phenomenon relevant to physiological conditions. From a more fundamental perspective, ergodicity breaking is broadly applicable to enzymetic activity at physiological conditions and is described by a formalism carrying significant similarities with the problem of dynamical transition of atomic displacements.[93] We discuss the connection between ergodicity breaking of atomic displacements with similar phenomenology for reactions of electron transfer in proteins at the end of this chapter.

3.3 Formalism

The standard definition adopted for the fraction of recoiless absorption of the γ-photon in Mössbauer spectroscopy is through the average

$$f(k) = \left|\left\langle e^{ikx}\right\rangle_{\mathrm{r}}\right|^2. \tag{3.2}$$

The average $\langle \dots \rangle_r$ is over the statistical configurations of the system accessible on a given time resolution of the experiment specified through the observation (resolution) time τ_r. Further, k is the wavevector aligned with the x-axis of the laboratory frame and x is the displacement of the heme iron.

The average over the stochastic variable of iron displacement x can be represented by an ensemble average with the free energy $F_r(x)$

$$\left\langle e^{ikx}\right\rangle_{\mathrm{r}} = \int dx e^{ikx-\beta F_r(x)}. \tag{3.3}$$

The free energy $F_r(x)$ is distinct from the usual thermodynamic free energy in two regards. First, it is a partial free energy corresponding to the reversible work performed by all degrees of freedom of the system at a fixed displacement x.

Therefore, $F_r(x)$ is analogous to the Landau functional of the thermodynamic order parameter.[167] There is another distinction of $F_r(x)$ from the thermodynamic free energy specified by the subscript "r". This free energy is defined by sampling the constrained part of the phase space Γ_r which can be accessed on the resolution time τ_r. The definition of $F_r(x)$ should thus include two constraints: (i) a fixed value x and (ii) a restricted phase space available to the system. Both constraints are mathematically realized by the following equation[168, 169, 93]

$$e^{-\beta F_r(x)} = \int_{\Gamma_r} d\Gamma \delta\left(x - \hat{\mathbf{x}} \cdot \mathbf{q}\right) e^{-\beta H}. \tag{3.4}$$

Here, $\hat{\mathbf{x}}$ is the unit vector along the x-axis and $\mathbf{q}$ is the iron's displacement vector. The restriction of the phase space is realized as a dynamical constraint on the frequencies over which the correlation functions appearing in the response functions are integrated.[93] A simple cutoff, $\omega > \omega_r = \tau_r^{-1}$, is used in the statistical averages below.

We will next consider the displacement of the iron as composed of the displacement of the heme's center of mass and the normal-mode vibrations relative to the center of mass. The Hamiltonian in Eq. (3.4) can therefore be separated into a linear term involving the external force $\mathbf{F}$ acting on the heme from the protein-water thermal bath and the Hamiltonian H_{vib} of intra-heme vibrations

$$H(\mathbf{q}) = H(0) - \mathbf{q} \cdot \mathbf{F} + H_{\text{vib}}. \tag{3.5}$$

By expanding the iron's displacement $\mathbf{q}$ in the normal-mode vibrations $\mathbf{Q}_\alpha$, we can re-write the free energy $F_r(x)$ in the form

$$\begin{aligned} e^{-\beta F_r(x) + \beta H(0)} = & \int d\mathbf{q} \delta\left(x - \hat{\mathbf{x}} \cdot \mathbf{q}\right) \langle e^{\beta \mathbf{q} \cdot \mathbf{F}} \rangle_B \\ & \int \prod_\alpha d\mathbf{Q}_\alpha \delta\left(\mathbf{q} - \sum_\alpha \hat{\mathbf{e}}_\alpha \frac{Q_\alpha}{\sqrt{m}}\right) e^{-\beta H_{\text{vib}}}, \end{aligned} \tag{3.6}$$

where m is the mass of the iron atom and the dimensionless vectors $\hat{\mathbf{e}}_\alpha$ represent the unitary transformation from the Cartesian coordinates to the normal modes Q_α.[170] Further, the average $\langle \dots \rangle_B$ is over the fluctuations of the classical protein-water thermal bath which creates movements of the heme as a whole. It is reasonable to anticipate that these relatively large-scale fluctuations follow the Gaussian statistics with the force variance $\sigma_F^2 = \langle (\delta \mathbf{F})^2 \rangle$, $\delta \mathbf{F} = \mathbf{F} - \langle \mathbf{F} \rangle$. The average over such fluctuations in Eq. (3.6) then becomes

$$\langle e^{\beta \mathbf{q} \cdot \mathbf{F}} \rangle_B = e^{(\beta q \sigma_F)^2/2}. \tag{3.7}$$

In addition, the integral over the normal modes in Eq. (3.6) is a Gaussian integral such that

$$\int \prod_\alpha d\mathbf{Q}_\alpha \delta \left(\mathbf{q} - \frac{1}{\sqrt{m}} \sum_\alpha \hat{\mathbf{e}}_\alpha Q_\alpha \right) e^{-\beta H_{\text{vib}}} = e^{-q^2/(2\sigma_{\text{vib}}^2)}, \tag{3.8}$$

where the variance due to intramolecular vibrations is

$$\sigma_{\text{vib}}^2 = \frac{\hbar}{6m} \sum_\alpha \hat{e}_\alpha^2 \frac{2\bar{n}_\alpha + 1}{\omega_\alpha}. \tag{3.9}$$

Here, $\bar{n}_\alpha$ is the average occupation number of the normal mode α with the frequency ω_α. By substituting Eqs. (3.7) and (3.8) into Eq. (3.6), one obtains the harmonic free energy function[160]

$$\beta F_r(x) = H(0) + \frac{x^2}{2\sigma^2} \tag{3.10}$$

with the variance

$$\sigma^2 = \frac{\sigma_{\text{vib}}^2}{1 - (\beta \sigma_F \sigma_{\text{vib}})^2}. \tag{3.11}$$

The basic result of this derivation is straightforward: adding Gaussian fluctuations of the heme's center of mass to intramolecular vibrations of the heme leads to the softening of the force constant of the harmonic free energy $F(x)$.[158] Combining this result with Eqs. (3.2) and (3.3), one obtains the Gaussian form for the recoiless

fraction

$$f(k) = e^{-k^2\langle \delta x^2 \rangle_r} \tag{3.12}$$

with $\langle \delta x^2 \rangle_r$ given by Eq. (3.1) in which $\langle \delta x^2 \rangle_{\rm vib} = \sigma^2_{\rm vib}$.

The subscript "r" in $\langle \delta F^2 \rangle_r$ specifies that the average over the stochastic fluctuations of the force $\mathbf{F}$ acting on the heme from the thermal bath is understood in the spirit of the dynamically restricted average over a dynamically accessible subspace of the system Γ_r, as specified in Eq. (3.4). In practical terms, this implies that only frequencies greater than $\omega_r = \tau_r^{-1}$ can contribute to the observables. The effective variance can therefore be calculated as[117, 93]

$$\langle \delta F^2 \rangle_r = \int_{\omega_r}^{\infty} (d\omega/\pi) C_F(\omega). \tag{3.13}$$

Here, $C_F(\omega)$ is the Fourier transform of the time auto-correlation function

$$C_F(t) = \langle \delta\mathbf{F}(t) \cdot \delta\mathbf{F}(0) \rangle, \tag{3.14}$$

where $\delta\mathbf{F}(t) = \mathbf{F}(t) - \langle \mathbf{F} \rangle$.

3.4 Results

We performed MD simulations of Cyt-c in oxidized (Ox) and reduced (Red) states at temperatures in the range 280–360 K as shown in Fig. 3.2 and in Fig. S1 in the ESI†. Additional simulations of the Ox state were done in the temperature range of 120–240 K. The simulation protocol is described elsewhere[171] and in more detail in the appendix A. Briefly, the system size involved 101440 atoms and the total of 33231 TIP3P water molecules. The production runs were 250 ns long for 280 K and above and 135 ns long for the lower temperatures. The overall length of the simulation trajectories was 4.7 μs produced with the NAMD software package.[172]

The total force acting on the heme, $\mathbf{F}_H$, was calculated from MD trajectories. This procedure averages out the short-time fluctuation of the forces caused by internal

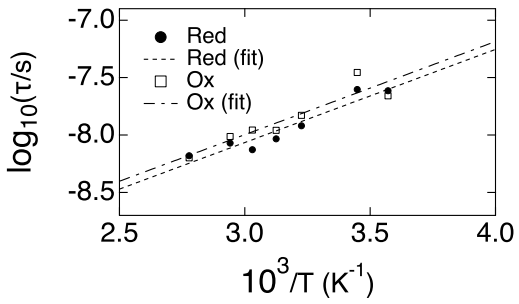

Figure 3.2: Long Relaxation Time of the Force-Force Autocorrelation Function of the Total Force Acting on the Heme Vs $1/T$. The Results of MD Simulations for the Reduced (Red, Filled Circles) and Oxidized (Ox, Open Squares)Are Fitted to Arrhenius Linear Functions with the Slopes $E_{\rm Red}/k_B = E_{\rm Ox}/k_B = 1868$ K.

vibrations and allows us to focus on the long-time dynamics, produced by the bath, and its potential effect on the observable displacement of the iron. We found that the force-force time correlation function calculated for the iron atom is dominated by intramolecular vibration and is oscillatory (Fig. A.10). The long-time dynamics is hard to extract from that correlation function, which is the reason for our focus on the overall force acting on the heme. However, this overall force needs rescaling when applied to the individual iron atom. Assuming that the heme moves as a rigid body, our re-scaling is given by the ratio of the iron mass $m = 56$ g/mol and the mass of the heme $M = 614$ g/mol

$$\mathbf{F} = \frac{m}{M}\mathbf{F}_H. \tag{3.15}$$

This rigid-body re-scaling can obviously apply only to the slowest dynamical components of the force. In contrast, the correlation function $C_F(t)$ calculated from simulations shows a number of time-scales, from sub-picoseconds, to long-time dynamics on the time-scale of 6–25 ns ($T \simeq 300$ K). While the slowest relaxation process usually constitutes about half of the amplitude of the time correlation function, Eq. (3.15) does not discriminate between the slow and fast dynamics. It is therefore clear that

our estimate of the overall amplitude of the force acting on heme's iron is good only up to some effective coefficient accounting for an imperfect rigidity of the heme. Elastic deformations of the heme shifting its center of mass are effectively disregarded in the re-scaling assuming the rigid-body motions. With these uncertainties in mind, we estimate $\langle \delta F^2 \rangle_r$ in Eq. (3.1) from the following equation

$$\langle \delta F^2 \rangle_r = f_{\rm ne}(T)(m/M)^2 \langle \delta F_H^2 \rangle. \tag{3.16}$$

The nonergodicity parameter $f_{\rm ne}(T)$ here comes from the dynamic restriction imposed on the integral over the frequencies in Eq. (3.13). Assuming that only the slowest component in the relaxation of the force can potentially enter the observation window, $\tau_r = 142$ ns, we can write[93] $f_{\rm ne}(T)$ in the form corresponding to exponential relaxation of $C_F(t)$ in Eq. (3.14) (see below the discussion of non-exponential, stretched dynamics)

$$f_{\rm ne}(T) = (2/\pi)\cot^{-1}\left[\tau(T)/\tau_r\right]. \tag{3.17}$$

In this equation, $\tau(T)$ is the relaxation time of the slowest component of $C_F(t)$. A similar expression, accounting for the finite resolution of the spectrometer, was used in the past for the integrated elastic intensity.[173]

It is clear from Eq. (3.17) that the nonergodicity parameter is equal to unity when $\tau(T) \ll \tau_r$ and the fluctuations of the force are ergodic. In the opposite limit of slow fluctuations, $\tau(T) \gg \tau_r$, the force fluctuations are dynamically frozen on the observation time and do not contribute to the softening of iron's displacement, $f_{\rm ne} \to 0$. This corresponds to low temperatures when intra-heme vibrations dominate. The crossover temperature T_d is reached at $\tau_r \simeq \tau(T_d)$.

The long-decay relaxation times $\tau(T)$ are shown in Fig. 3.2. The activation barrier of this relaxation time, $E_a/k_{\rm B} \simeq 1900$ K, is below the typical values for the α-relaxation of condensed materials, thus pointing to a localized (secondary) relaxation

process of the protein-water interface.[117, 166] In fact, the secondary β-relaxation of confined[174] and protein hydration[175] water observed below $T \simeq 228$ K is characterized by a higher activation energy, $\simeq 5340$ K. At high temperatures, comparable to the range studied here, the activation energy is lower even for the α-relaxation and is in the range ~ 1560 K[176] (see below). Still, the force-force correlation function projects the motions of both protein and a large number of hydration water molecules on a single collective coordinate of the overall force acting on the heme. The corresponding relaxation cannot be attributed to a single component. Experimental evidence for such collective dynamics is insufficient, but relatively low activation barriers are not uncommon for the collective Stokes-shift dynamics of optical dyes.[177, 178] An activation barrier of $E_a/k_{\rm B} \simeq 1660$ K was recently reported for the slow relaxation component of the Stokes-shift dynamics characterizing the protein-water interface.[178] When the optical dye is approximated by a dipole, the optical spectral shift reflects the local electric field at the dipole moment of the dye. There must be, therefore, a good match between the Stokes-shift measurements and at least the electrostatic component of the force-force correlation function considered here.

The long-decay relaxation time $\tau(T)$ was determined in the range of temperatures $280 \leq T \leq 360$ K, where our simulations demonstrate sufficient convergence. The Arrhenius fits of the simulation data (lines in Fig. 3.2) are then extrapolated to lower temperature where the experimental Mössbauer data are available. These extrapolated relaxation times are used in Eq. (3.17) to calculate the nonergodicity factor in Eq. (3.16). This extrapolation is obviously an approximation and we cannot exclude that the activation energy for the relaxation time grows at lower temperatures.

Calculations of displacements of the heme iron based on Eqs. (3.1), (3.16), and (3.17) are shown in two panels of Fig. 3.3. The experimental results[10] are reasonably reproduced by our calculations in the Red state of the protein without any

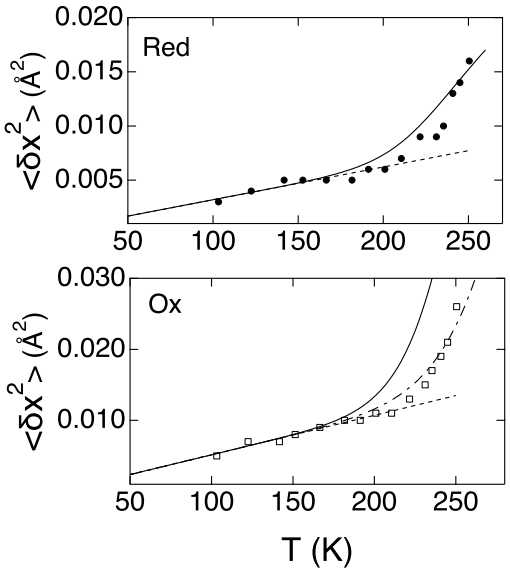

Figure 3.3: $\langle \delta x^2 \rangle$ for Reduced (Red, Upper Panel) and Oxidized (Ox, Lower Panel) States of Cyt-c. The Points Are Experimental Data[10] And the Solid Lines Are Calculations According to Eqs. (3.1), (3.16), and (3.17). The Dashed Lines Are Low-Temperature Interpolations of the Experimental Data. The Dashed-Dotted Line in the Lower Panel Is Based on Multiplying the Relaxation Time $\tau(T)$ for the Ox State with the Constant Coefficient Equal to 2.65.

additional fitting. The shift of the crossover temperature to a higher value in the Ox state observed experimentally would imply, in our model, slower dynamics of the force or a larger value of $\langle \delta F_H^2 \rangle$. While a larger value of $\langle \delta F_H^2 \rangle$ is indeed observed (Table 3.1), its overall result is insufficient to explain the shift of the experimental crossover temperature. The experimental results are recovered by multiplying $\tau(T)$ from simulations by a factor of 2.65. While this factor is obviously arbitrary, the need for a correction might be related to our insufficient sampling of the long-time dynamics, extrapolation of the high-temperature relaxation times to lower temperatures, and the assumption of exponential dynamics not supported by measurements with protein powders[101, 166, 152] (see below).

Despite some difficulties with the long-time dynamics in the Cyt-Ox state, the

Table 3.1: Separation of $\langle \delta F_H^2 \rangle$ (nN^2) into the Electrostatic (El.) and Non-Polar (vdW) Components and the Splitting into the Protein (Prot.) and Water Contributions ($T = 320$ K).

Redox State	El.	vdW	Prot.	Water	Total
Red	8.86	23.17	9.60	3.12	14.52
Ox	16.62	12.65	19.34	2.87[a]	17.05[a]

[a] The contribution of the first hydration layer to the force variance is 2.39 nN^2, the total force variance from the first hydration shell and protein combined is 16.7 nN^2.

short-time dynamics produced by simulations are consistent with experiment. This is confirmed by the calculation of the vibrational density of states

$$D(\omega) = \sum_{\alpha=1}^{3N} (\hat{\mathbf{e}}_\alpha \cdot \hat{\mathbf{x}})^2 \delta(\omega - \omega_\alpha), \tag{3.18}$$

where $\hat{\mathbf{e}}_\alpha$, as above in Eq. (3.6), are expansion coefficients for the linear transformation from the Cartesian displacement of the Fe atom to normal coordinates Q_α in Eq. (3.6). The normalization of the density of states adopted in producing the experimental data shown in Fig. 3.4 requires[170]

$$\int_0^\infty D(\omega) d\omega = 1. \tag{3.19}$$

With this normalization, the density of states from simulations was computed from the velocity-velocity autocorrelation function (see appendix A for more detail) and displayed in Fig. 3.4. While the overall shape of the density of states is reproduced, there is a nearly uniform shift toward low frequencies relative to experiment.[11, 12] This shift might be related to the expansion of the protein at $T = 300$ K, at which simulations were performed, compared to the experimental temperature of $T = 68$ K.

Table 3.1 shows the splitting of the variance of the force acting on the heme into electrostatic and van der Waals (vdW) components and, additionally, into the components from the water and protein parts of the thermal bath. Note that the components do not add to the total force variance because of cross-correlations. The splitting into

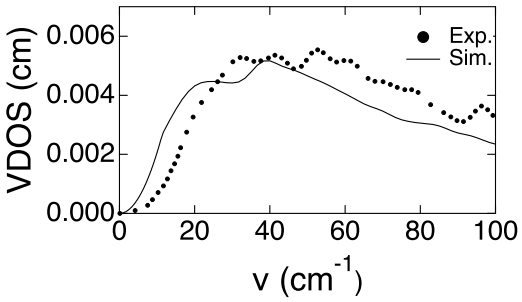

Figure 3.4: Experimental (Exp.,[11, 12] $T = 68$ K) and Simulation (Sim., $T = 300$ K)Vibrational Density of States for Cyt-Ox ($\bar{\nu} = \omega/(2\pi c)$, c Is the Speed of Light). Simulations Were Done for 1 ns in the NVE Ensemble with Non-Rigid Protons and 0.25 fs Integration Step (Configurations Saved Every 1 fs).

components indicates that vdW interactions and electrostatics contribute comparable magnitudes to the force variance. The softening of iron vibrations cannot therefore be fully attributed to electrostatics (dielectric effect[179, 117, 107]). It cannot be attributed to the hydration shell[107] either and is in fact a combined effect of protein and water, with the dominant contribution from the protein. The water contribution can be further diminished in solid samples used in neutron scattering or Mössbauer spectroscopy. However, the force variance arising from the protein and first hydration layer combined is only slightly below the overall force of the thermal bath (footnote in Table 3.1).

The separation of the force variance between protein and water allows us to comment on the idea of "slaving" of the protein dynamics by water suggested by Frauenfelder and co-workers.[179, 111, 117] The "slaving" phenomenology implies the equality of the enthalpy of activation for a relaxation process in the protein with the enthalpy of activation for the structural relaxation of bulk water (α-relaxation). When plotted in the Arrhenius coordinates ($-\ln[\tau]$ vs $1/T$) the two plots are then parallel.

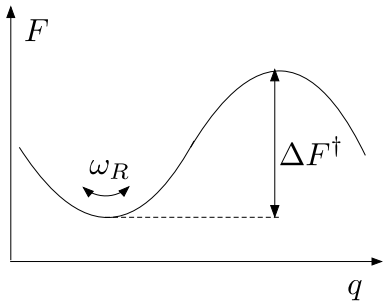

Figure 3.5: Activated Kinetics in the Kramers'Friction Dominated Limit. The Characteristic Frequency of Vibrations in the Well Is Given by $\omega_R = \omega_0^2/\zeta$ For An Overdamped Harmonic Oscillator with the Eigenfrequency ω_0 and Friction with the Medium ζ; $\Delta F^\dagger$ Is the Free Energy of Activation Along the Reaction Coordinate q.

The origin of this phenomenology is easy to appreciate within the framework of Kramers' activated kinetics dominated by friction with the thermal bath (Fig. 3.5). The rate constant of an activated process $\propto \omega_R \exp[-\beta\Delta F^\dagger]$ is the product of an effective frequency in the reactant well ω_R with the Boltzmann factor $\exp[-\beta\Delta F^\dagger]$ involving the free energy of activation $\Delta F^\dagger$. If the motions along the reaction coordinate are represented by an overdamped harmonic oscillator with the frequency ω_0 and the friction coefficient ζ, the direct solution of the Langevin equation leads to the relaxation frequency $\omega_R = \omega_0^2/\zeta$. Therefore, "slaving" appears when most of energy dissipation occurs to the water part of the thermal bath (which has a higher heat capacity than the protein[180]). In that case, the temperature dependence of $\zeta(T)$, and of the corresponding relaxation process in water, would determine the temperature dependence of the relaxation rate in the protein, which is only shifted to lower rates due to an additional activation barrier $\Delta F^\dagger$ (assuming $\Delta F^\dagger$ is temperature-independent). This is the "slaving" scenario.

While there are reported instances when this phenomenology is correct,[166, 181] one can argue that energy dissipation for a localized process occurs to the protein hydration shell, which possesses its own relaxation spectrum. Indeed, Frauenfelder and co-workers[117] argued that localized processes in the protein have to be "slaved"

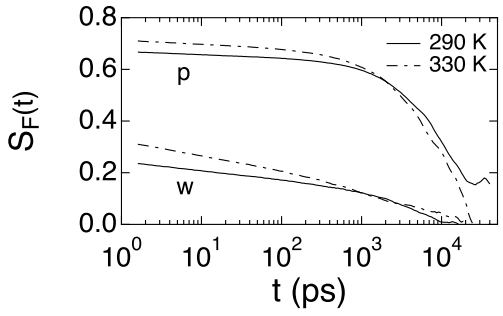

Figure 3.6: Normalized Force-Force Correlation Function $S_F(t) = C_F(t)/C_F(0)$ for the Protein (p) and Water (w) Components at the Temperatures Indicated in the Plot. The Fraction of the Fast Ballistic Decay Increases with Lowering Temperature Since the System Becomes More Rigid Overall. This Results in a Lower Starting Point of the Slow Component.

to the relaxation of the hydration layer. Consistently with that notion, relaxation processes related to protein function are often characterized by the activation barrier much lower than those for α-relaxation of bulk water (Fig. 3.2). For instance, the Stokes shift dynamics directly related to the redox activity of Cyt-c show the activation barrier of its relaxation time $E_a/k_{\rm B} \simeq 840$ K.[15] This is much lower than ~ 1560 K (increasing to ~ 6400 K upon cooling) from diffusivity and viscosity of water (α-relaxation).[176] The idea of "slaving" to β-relaxation of the hydration shell is less useful, and is harder to prove, since relaxation of the shell is mostly inaccessible experimentally. Our simulation results allow us such a test since the dynamics of both the hydration layer and of the heme's iron are available.

In application to Mössbauer experiment, our data do not support "slaving". Only $\sim 20\%$ of the force variance acting on heme's iron comes from from hydration water (Table 3.1). This also implies that the dynamics should be biomolecule-specific.[182] In this scenario, "slaving" would be only possible if the protein dynamics followed the dynamics of water. The results of simulations do not support this conjecture: the dynamics of $S_F(t) = C_F(t)/C_F(0)$ are distinctly different for the protein and its

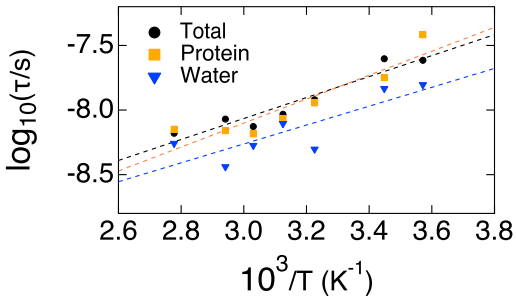

Figure 3.7: Long Relaxation Time of the Force-Force Autocorrelation Function of the Force Acting on the Heme Vs $1/T$ (Black Circles) for Reduced Cyt-C. Also Shown Are the Relaxation Times for the Force on the Heme Produced by the Protein (Squares) and by Water (Triangles).Fits to Arrhenius Linear Functions Are Shown by the Dashed Lines.

hydration water (Fig. 3.6). The dynamics of water is on average significantly faster (a larger drop from the initial value $S_F(0) = 1$, not resolved in Fig. 3.6), and the slow dynamics of the protein and water are not consistent either. Nevertheless, the temperature dependence of the relaxation time of the force-force correlation function is consistent between the protein and water components (Fig. 3.7). The enthalpies of activation for the protein and water relaxation are, therefore, close in magnitude, in a general accord with the "slaving" phenomenology. The origin of this effect can be traced to coupled fluctuations of the protein and hydration water,[183, 184, 185, 186, 187] without invoking the dominant role of water in the dynamics.

Water is a faster subsystem producing a shorter relaxation time of $C_F(t)$. One therefore anticipates that the temperatures of ergodicity breaking should separate for the water and protein components of the thermal bath.[188] This indeed happens, as is illustrated in Fig. 3.8 for the reduced state of Cyt-c. The rise of $\langle \delta x^2 \rangle$ due to water occurs at $\simeq 150$ K, while the transition temperature for the protein is $\simeq 200$ K. The water's onset is hard to disentangle because the force produced by water on the heme is relatively low. One might expect that the water-related transition is better resolved

in neutron scattering experiments[188] since a large number of protons located close to the interface potentially contribute to the signal. Overall, this calculation clearly points to a nonergodic origin of the dynamical transition, as we stress again below when considering the separation of rotational and translational motions of water in the hydration shell.

3.5 Stretched Relaxation

Difficulties with reproducing ergodicity breaking of Cyt-Ox (Fig. 3.3 lower panel) might be related to a limited applicability of the results obtained for solutions to dynamics in protein powders and crystals studied experimentally. In addition to the obvious uncertainty of extrapolating the high-temperature simulation results to lower temperatures, the dynamics of hydration water can be qualitatively different in those environments compared to solutions. The relaxation of hydration water in powders was associated by Ngai and co-workers[155, 152] with the general phenomenology of confined water in water-containing glass-formers. The ν-process characterizing such dynamics is highly stretched, with a very slow decay of the high frequency tail of the loss function: $\epsilon'' \propto \omega^{-\gamma}$ for the dielectric loss[189, 28] and $\chi''(\omega) \propto \omega^{-\gamma}$ for the neutron scattering loss.[101] A low value of stretching exponent, $\gamma \simeq 0.2$, is observed in both cases.

The ν-process observed in lysozyme and myoglobin powders by dielectric spectroscopy was identified to cause the dynamical transition in neutron scattering.[181] We can therefore use the corresponding relaxation time $\tau(T)$ reported from dielectric measurements to explain Mössbauer data for met-myoglobin[13] (oxidized form of myoglobin). Before we do that, we have to extend the nonergodicity parameter obtained in Eq. (3.17) for exponential relaxation to stretched exponential relaxation. Cole-Cole function was used to fit the dielectric data.[28] We therefore can re-write

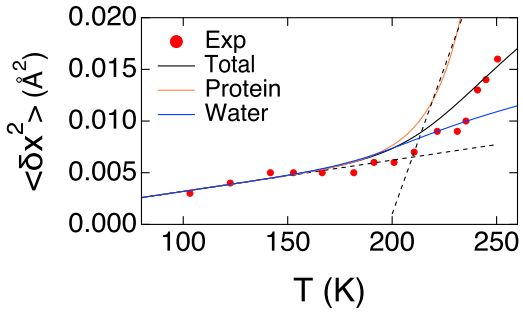

Figure 3.8: $\langle \delta x^2 \rangle$ For the Reduced State of Cyt-C. The Points Are Experimental Data[10] And the Solid Lines Are Calculations According to Eqs. (3.1), (3.16), and (3.17).The Calculations Are Done for the Total Force-Force Correlation Function (Black) and for Its Components from the Protein (Orange) and Water (blue).The Dashed Lines Refer to the Low-Temperature Linear Fit of the Experimental Data and to the High-Temperature Linear Fit of the Iron Displacement Produced by the Protein.

the nonergodicity parameter $f_{\rm ne}(T)$ as follows

$$f_{\rm ne}(T) = \frac{2}{\pi} \int_{\tau(T)/\tau_r}^{\infty} \frac{d\omega}{\omega} {\rm Im} \left[(1 + (i\omega)^{\gamma})^{-1} \right], \tag{3.20}$$

where γ is the stretching exponent of the Cole-Cole function. At $\gamma = 1$, Eq. (3.20) transforms to Eq. (3.17). This nonergodicity factor can be used in the following form for the force variance

$$\beta \langle \delta F^2 \rangle_r = A f_{\rm ne}(T) \tag{3.21}$$

where, according to the standard prescription of the fluctuation-dissipation theorem, the amplitude A is held constant. The use of this form along with $\gamma = 0.25$ and the experimental $\tau(T)$ (see Fig. A.6 in appendix A) in Eq. (3.20) produce the MSF of myoglobin shown by the solid line in Fig. 3.9. The fit requires $\langle \delta F^2 \rangle \simeq 0.1$ nN^2 at $T = 300$ K, which is roughly consistent with $\langle \delta F^2 \rangle \simeq 0.14$ nN^2 for Cyt-Ox in Table 3.1 when Eq. (3.15) is applied. The quality of the fit is significantly reduced with $\gamma = 1$ (Fig. A.13 in appendix A), which testifies to the need of applying stretched relaxation to describe ergodicity breaking in protein powders.

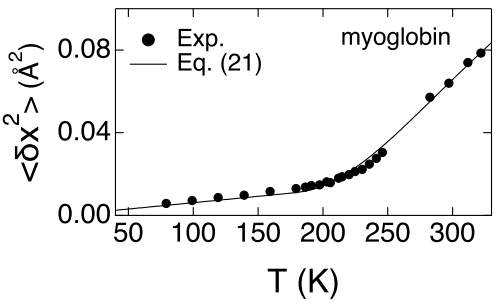

Figure 3.9: MSF of Heme Iron in Oxidized Myoglobin. Points Indicate Experimental Results,[13] Solid Line Refers to the Fit to Eqs. (3.1) and (3.16) with the Nonergodicity Factor $f_{\rm ne}(T)$ Determined From Stretched Dynamics According to Eq. (3.20).The Nonergodic Force Variance Is Determined According to Eq. (3.21) with the Fitting Constant $A = 2.5$ nN/Å (Corresponds to $\langle \delta F^2 \rangle = 0.1$ nN^2 at $T = 300$ K).

We note here that a somewhat analogous procedure employing a frequency filter to the loss spectrum was used by Frauenfelder and co-workers.[117] Their empirical approach was to apply the normalized dielectric loss spectrum of myoglobin embedded in poly(vynal)alcohol to the entire recoilless fraction of the Mössbauer effect $f(k)$ in Eq. (3.2). Our approach is clearly different as it applies the constraint imposed by the observation window to the force variance in the denominator of Eq. (3.1). The physical reason for using the dielectric loss is not clear and is in fact inconsistent with our results showing that nonpolar (vdW) forces significantly contribute to the force variance (Table 3.1).

3.6 Glass Transition

The lower crossover temperature T_g of the protein MSF represents the glass transition of the hydration shell.[152] It was previously identified with the onset of translational diffusion of the water molecules in the shell.[190] However, glass science requires one to pay attention not only to translations, but also to molecular rotations. There are a number of reasons for that. First, the configurational entropy of fragile glass-

formers is mostly rotational[191] (e.g., the heat capacities of supercooled ethanol and its plastic crystal are nearly identical[192]). Reducing the configurational entropy is required for reaching the glass transition[193] and, therefore, the rotational configuration space has to be strongly constrained close to T_g. Second, the temperature dependence of the dielectric relaxation time can be superimposed with the relaxation time from viscosity[165] and with the diffusion coefficient. Therefore, both rotations and translations are expected to dynamically freeze near T_g.

The density of water in the hydration shell is enhanced compared to the bulk,[194, 195] and shell water, being heterogeneous and more disordered than the bulk,[196, 187] is close in physical properties to a mixture of low-density and high-density amorphous ice as observed on samples with low hydration level.[197, 198] Note, however, that ice-like water has been also observed in the hydration layers of anti-freeze proteins in particular.[154] Nevertheless, the positional structure of the hydration shell (pair distribution function) mostly does not change with cooling, and there is no structural transition associated with crossing the temperature T_d.[199] Compared to the positional structure and translational dynamics,[200, 201] there is much less experimental and computational evidence on orientational correlations and rotational dynamics of water in the hydration shell. The lack of experimental evidence on the orientational structure, in contrast to orientational dynamics, is particularly notable. When dynamics are concerned, the single-particle rotational dynamics are slowed down by a factor of 2–4, as is seen by NMR[202] and computer simulations.[203] Collective relaxation probed by Stokes shift of optical dyes are much slower, in the range of sub- to nanonoseconds,[204, 205, 206] pointing to a significantly slower collective response of water dipoles[207] compared to single-molecule rotations. A relatively small retardation factor of single-particle rotations in hydration layers compared to the bulk can in fact be misleading since the distribution of rotational times considerably widens in

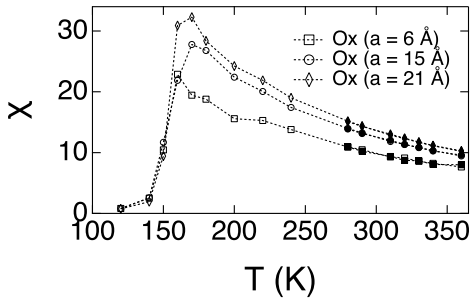

Figure 3.10: The Dipolar Susceptibility of the Hydration Shell Water Calculated From MD Simulations According to Eq. (3.22)For Shells of Thickness a Around Cyt-Ox (Open Points) and Cyt-Red (Filled Points) at Different Temperatures (Some Red and Ox Points Coincide on the Scale of the Plot). The Dotted Lines Connect the Points to Guide the Eye.

hydration layers such that a single average relaxation time is a poor representation of the dynamical heterogeneity of the hydration layer.[208, 209]

The fact that the collective response of the shell dipole is quite different from single-particle MSF is illustrated in Fig. 3.10, which shows the dipole moment variance for hydration shells of Cyt-Ox and Cyt-Red with varying temperature and thickness of the shell. More specifically, we present the dimensionless variance of the shell dipole moment defined analogously to the dielectric susceptibility of bulk dielectrics

$$\chi(a) = [3k_{\mathrm{B}}Tv_w N_w(a)]^{-1}\langle \delta\mathbf{M}(a)^2\rangle. \tag{3.22}$$

Here, v_w is the volume of a single water molecule (effective diameter 2.87 Å[210]) and $N_w(a)$ is the number of water molecules in the shell of thickness a measured from the van der Waals surface of the protein; $\mathbf{M}(a)$ is the total dipole moment of the water molecules in the shell, $\delta\mathbf{M}(a) = \mathbf{M}(a) - \langle\mathbf{M}(a)\rangle$.

The susceptibility shown in Fig. 3.10 represents the statistics of collective fluctuations of the entire dipole moment of the hydration shell. The main qualitative difference between $\langle\delta x^2\rangle(T)$ for the single-particle atomic displacements and fluctuations of

the collective shell dipole is that the latter clearly violates the fluctuation dissipation theorem,[92] which predicts $\langle \delta \mathbf{M}(a)^2 \rangle \propto T$. From the perspective of the fluctuation-dissipation theorem, $\chi(a)$ should be temperature-independent. The phenomenology of susceptibility decaying with temperature, in violation of the fluctuation-dissipation theorem,[9] is shared by most polar liquids.[6] However, the decay of $\chi(a)$ with increasing T is much stronger for the hydration layer than for the bulk liquid.[9]

In contrast to homogeneous liquids, the protein hydration shells are heterogeneous and highly frustrated.[207] This is because polarized interfacial water has to follow a nearly uniform mosaic of positive and negative surface residues. Surface charges provide pinning sites for the interfacial waters,[211] and the local electric field orients water dipoles into polarized domains. These domains are mutually frustrated by the altering sign of the charged residue since the dipoles at the domain boundaries can take either of the alternative orientations. This new physics, quite distinct from bulk polar liquids, connects hydration shells to relaxor ferroelectrics, where mutual frustration of dipolar crystalline cells breaks the material into ferroelectric nanodomains at the glass transition reached above the Curie point.[118] Despite strong interactions, the water molecules in the shell stay in the fluid state, but with the collective fluctuations of the shell dipole slowed down compared to the bulk (hundreds of picoseconds to tens of nanoseconds for the slow relaxation tail[212, 207, 209]). The relaxation time of the dipole moment of the first hydration layer, $\approx 1 - 10$ ns,[207] is in the same time range as the relaxation of elastics deformations of the protein's shape.[213] One can therefore anticipate that the protein and water dynamics are coupled on this long time-scale because of coupled elastic and water domain fluctuations, as was indeed suggested by Careri and co-workers long time ago.[214]

The phenomenology of relaxor ferroelectrics suggests that the dipolar response of the shell is determined by reorienting the polarized domains, instead of predom-

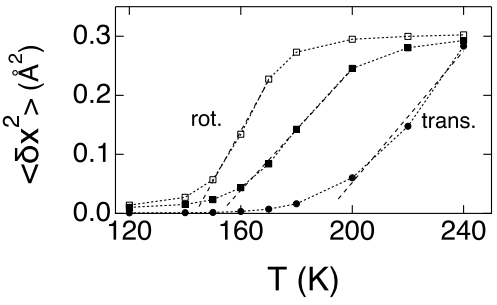

Figure 3.11: Center of Mass MSF (Trans., Circles) and the MSF Due to Molecular Rotations (Rot., Squares) of Water Molecules Within the Hydration Shell 6 Å Thick Around the Ox Cyt-C. The Center of Mass Translations and Molecular Rotations Are Calculated within the Time-Window of 100 Ps (Filled Points) and 1 ns (Open Points). The MSFs For Center-Of-Mass Translations Are Reduced by a Factor of 40 to Bring Them to the Same Scale with the Results for Rotations. The Dashed Lines Are Linear Fits Through Subsets of Points to Illustrate Differences in the Onset Temperatures ($T_{\rm rot}(1\ {\rm ns}) = 144$ K, $T_{\rm rot}(100\ {\rm ps}) = 152$ K, and $T_{\rm tr}(100\ {\rm ps}) = 191$ K.The Dotted Lines Connecting the Points Are Drawn to Guide the Eye.

inantly single-particle rotations found in bulk polar liquids.[215] This interpretation is supported by nanosecond time-scales characterizing the dynamic susceptibility of the shell $\chi(\omega, a)$[207] (Fig. A.12 in the appendix A). This picture does not contradict to the dynamic (fluid) nature of the hydration shell in which water can diffuse along the surface visiting a residue per $\simeq 11$ ps.[216] Moving from a positive to a negative residue can be accompanied with a dipole flip, still preserving the domain structure, which requires much longer times to be altered. The dipole flip of a water molecule moving to a neighboring residue will also produce a short relaxation time for single-particle rotations.[202, 203] Overall, the domains freeze in below T_g, remaining fluid above T_g.

A sharp drop of $\chi(a)$ at about $\simeq 145$ K signals reaching the glass transition on the time scale of MD simulations (Fig. 3.10). This T_g is somewhat lower than experimental $T_g \simeq 170$ K from calorimetry of concentrated solutions of Cyt-c.[217] The glass transition of the hydration shell prevents elastic motions of the protein,

making a hydrated protein harder at low temperatures than the dry one.[157] One wonders if rotations and translations of water molecules in the shell terminate at the same temperature. Figure 3.11 shows that this is not the case (see appendix A for the details of calculations). The glass transition for $\chi(a)$ coincides with freezing of water rotations. The onset temperature depends on the observation window (cf. filled to open squares in Fig. 3.11), consistent with ergodicity breaking at the transition. On the contrary, the onset of water translations occurs at a higher temperature, $\simeq 190$ K. A similar phenomenology was recently reported from neutron scattering of protein's hydration shell,[108] where the onset of water's translations also followed the onset of rotations. The temperature of translational onset is close to T_d, as was noted in the past.[218] Similar findings are reported in a recent study of rotational dynamics of a spin probe located in the hydration shell of lysozyme by electron spin echo spectroscopy.[219] The authors report two crossover temperatures, 130 K and 160 K, within the resolution window of 100 ns. This technique is sensitive to rotations of the spin probe only, but one can anticipate that enhanced translations of the surrounding waters at the higher crossover temperature can also enhance the rotations of the spin probe.

A crude estimate of the "dielectric constant" of the shell might be relevant here. If, for the sake of an estimate, one adopts the connection between the dielectric constant and the susceptibility of bulk dielectrics, $\epsilon(a) = 1+4\pi\chi(a)$, then the inspection of Fig. 3.10 suggests $\epsilon(a) \simeq 407$ at $T = 170$ K and $a = 21$ Å. This very high dielectric constant is consistent with recent dielectric spectroscopy of protein powders,[220, 28] reporting high dielectric increments $\Delta\epsilon \simeq 10^2 - 10^4$ for the relaxation process reaching 1-10 μs at the room temperature. Given the temperature dependence of this relaxation process, it appears likely that it is responsible for glass transition of hydrated protein samples.[166] The drop of χ at T_g seen in Fig. 3.10, and a similar behavior observed

previously in simulations of lysozyme,[207] suggests a possible connection between high $\Delta\epsilon$ and polarized domains formed in the hydration shell.

3.7 Onset of Protein Functionality

Equation (3.1) offers a natural explanation of the extended flexibility of proteins at high temperatures in terms of the force constant assigned to a cofactor or residue in the folded protein.[157] According to Eq. (3.1), softening of the protein matrix due to collective agitation of the protein-water thermal bath reduces the vibrational force constant $\kappa_{\rm vib} = (\beta\langle\delta x^2\rangle_{\rm vib})^{-1}$ by the magnitude

$$\kappa_b = \beta\langle\delta F^2\rangle_r. \tag{3.23}$$

The total force constant $\kappa = (\beta\langle\delta x^2\rangle)^{-1}$ becomes

$$\kappa = \kappa_{\rm vib} - \kappa_b. \tag{3.24}$$

Using Eq. (3.24), Fig. 3.12 shows $\kappa_b(T)$ for Cyt-c (Ox) and myoglobin (Figs. 3.3 and 3.9). We have additionally included the results from neutron scattering of lysozyme (Lys) in 50:50 glycerol-D_2O solution (h = 0.83 g D_2O/g Lys),[14] which display a crossover temperature at $\simeq$ 180 K. All these data point to a rise of κ_b at T_d to a nearly constant value (except for Cyt-Ox) charactering the protein flexibility at GHz frequencies. The Young's moduli of the hydrated protein fall with increasing temperature[221, 157] in a fashion consistent with κ_b in Fig. 3.12.

The notion of protein dynamics as proxy for enzymatic activity has been actively discussed in the recent literature.[222, 154, 223] One has to clearly distinguish flexibility,[180] i.e. the ability to sample a large number of conformations, from the actual dynamics, i.e. the time-scales involved in usually dissipative decay of correlation functions. Whether flexibility and activity must accompany each other for slow

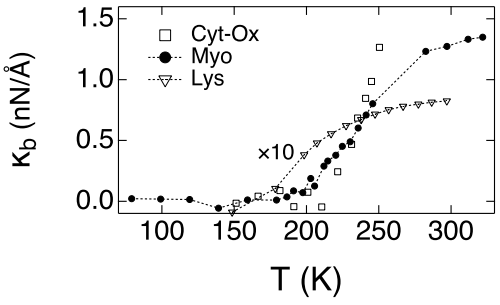

Figure 3.12: Force Constant of the Protein-Water Medium $\kappa_b = \beta\langle\delta F^2\rangle_r$ Calculated from $\kappa(T)$ and $\kappa_{\rm vib}(T)$ According to Eq. (3.24). Points Indicate the Experimental Results for Cyt-c (Ox),[10] Myoglobin (Myo),[13] and for Lysozyme Dissolved in 50:50 Glycerol-D_2O Solvent at $h = 0.83$ g D_2O/g Lys.[14] The Results for Lysozyme Are Multiplied by a Factor of 10 to Bring Them to the Scale of the Plot. The Dotted Lines Connecting the Points Are Drawn to Guide the Eye.

(in milliseconds) enzymetic reactions remains to be seen,[224] but there is one class of enzyme reactions where protein configurational space has to be dynamically restricted for the reaction to occur.[93] This is the process of protein electron transport essential to production of all energy in biology,[225] either through photosynthesis or through mitochondrial respiration.[79]

The fluctuation-dissipation theorem connects fluctuations to response to an external perturbation.[92] In this framework, high flexibility implies high solvation,[226] or trapping, energy. Electrons in biological energy chains have to perform many tunneling steps within a narrow energy window consistent with the energy input from food or light. In order to accomplish vectorial electron transport, energy chains have to avoid deep energy traps. Therefore, large conformational motions producing asymmetries in solvation energies between the initial and final tunneling states have to be dynamically frozen on the reaction time.[93]

This phenomenology is consistent with what we have found here for the dynamical transition of atomic displacements. The role of the force constant in Eq. (3.23) is

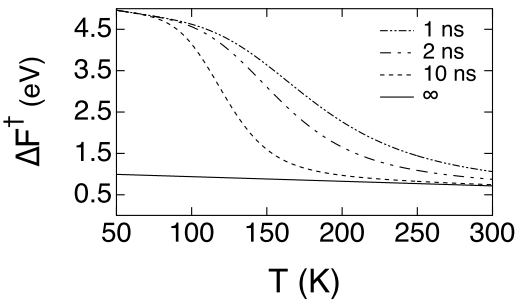

Figure 3.13: $\Delta F^{\dagger}$ Given by Eq. (3.26) vs T Calculated from MD Simulations (~ 250 ns of Simulations at Each Temperature[15]). The Legend Indicate the Reaction Times $\tau_r = k_R^{-1}$.Deviations From the Thermodynamic Behavior, $k_R = 0$ (Specified as An Infinite Observation Time, "∞"),Are Determined by the Nonergodic Factor $f_{\rm ne}(T)$ (Eq. (3.17)) Calculated from τ_r and the Relaxation Time[15] $\tau_X(T)$(s) = $\exp[-23.8+835/T]$. The Reorganization Energies From Long Simulation Trajectories Are Approximated by Linear Functions of Temperature: $\lambda^{\rm St}(T) = 1.71 - 0.0015 \times T$ eV, $\lambda(T) = 4.19 - 0.00446 \times T$ eV (T Is in K).

played by the reorganization energy λ determined through the variance of the donor-acceptor energy gap X used to gauge the progress of the reaction.[225, 85, 227, 93] The reorganization energy is determined through the variance of X by the equation inspired by the fluctuation-dissipation theorem (cf. to Eq. (3.23))

$$\lambda(k_R) = \beta \langle \delta X^2 \rangle_r / 2. \tag{3.25}$$

Here, $\langle \delta X^2 \rangle_r = \langle \delta X^2 \rangle f_{\rm ne}(T)$ depends on the observation window through the nonergodicity factor $f_{\rm ne}(T)$ (Eq. (3.17)) multiplying the thermodynamic ($\tau_r \to \infty$) variance $\langle \delta X^2 \rangle$. The only difference of this problem from our discussion of iron's MSF is that one has to replace the relaxation time of the force $\tau(T)$ with the relaxation time $\tau_X(T)$ of the Stokes-shift correlation function[228] $C_X(t) = \langle \delta X(t) \delta X(0) \rangle$. The role of the observation window is now played by the reaction time $\tau_r = k_R^{-1}$ given in terms of the reaction rate constant k_R.[229]

The reorganization energy $\lambda(k_R)$ quantifies the depth of the trap created for a charge by the protein-water thermal bath. The amount of energy to de-trap the elec-

tron and bring it back to the tunneling configuration specifies the activation barrier $\Delta F^{\dagger}$. It is given in terms of two energy parameters:[93] the difference of first moments of X in the initial and final states, known as the Stokes-shift reorganization energy $\lambda^{\rm St}$, and the second moment of X specified by $\lambda(k_R)$

$$\Delta F^{\dagger} = (\lambda^{\rm St})^2/[4\lambda(k_R)]. \tag{3.26}$$

The parameter $\lambda^{\rm St}$ specifies the energy difference between two states of the protein (Red and Ox in the case of Cyt-c). It does not reach its thermodynamic value because of the inability of the protein to sample its entire phase space on the reaction time.[93] Instead of reaching, through a conformational change, two thermodynamic minima of stability (for Red and Ox states), the protein gets trapped in an intermediate local minimum. The time separation $k_R^{-1} \ll \tau_{\rm conf}$ between the reaction time and the time of the conformational transition $\tau_{\rm conf}$ constrains the available configuration space thus producing the glassy statistics and dynamics of the protein.[230, 231] A relatively small value of $\lambda^{\rm St}$ follows, such that the condition $\lambda^{\rm St} \ll \lambda(k_R)$ keeps the reaction barrier in Eq. (3.26) relatively low. The reorganization energy $\lambda(k_R)$ in the denominator in Eq. (3.26) is, however, directly affected by nonergodic freezing of a subset of degrees of freedom, which can lead to a significant increase of the reaction barrier at low temperatures and to the termination of the protein function.

This perspective is illustrated in Fig. 3.13 showing the effect of the observation window on $\Delta F^{\dagger}(T)$. The input parameters to the results shown in Fig. 3.13 are $\lambda^{\rm St}(T)$ and $\lambda(T)$ taken from simulation trajectories ($\simeq 250$ ns) and the Stokes-shift relaxation time $\tau_X(T)$ calculated for Cyt-c.[15] As the temperature decreases, the relaxation time $\tau_X(T)$ leaves the observation window, $\tau_r = k_R^{-1}$, and $\lambda(k_R)$ drops. The activation barrier grows at low temperatures (see Eq. (3.26)) and the reaction slows down due to ergodicity breaking qualitatively consistent with the dynamical transi-

tion for the atomic MSF (at faster rates, such as those involved in primary events of photosynthesis, λ^{St} becomes affected by k_R and the picture changes again[232]). The overlap of the time-scales probed by the neutron scattering and Mössbauer spectroscopy with the typical reaction times of protein electron transfer suggests that the fluctuations of the protein-water thermal bath responsible for the high-temperature part of the displacement curve are the same as those involved in activating redox activity of proteins. We come back to the biological function of the protein and its termination at low temperatures in chapter 5.

Chapter 4

THEORY AND ELECTROCHEMISTRY OF CYTOCHROME C

This material was published in the Journal of Physical Chemistry B 121(19), pp.4958-4967 (2017 May 9).

4.1 Summary

Extensive simulations of cytochrome c in solution are performed to address the apparent contradiction between large reorganization energies of protein electron transfer typically reported by atomistic simulations and much smaller values produced by protein electrochemistry. The two sets of data are reconciled by deriving the activation barrier for electrochemical reaction in terms of an effective reorganization energy composed of half the Stokes shift (characterizing the medium polarization in response to electron transfer) and the variance reorganization energy (characterizing the breadth of electrostatic fluctuations). This effective reorganization energy is much smaller than each of the two components contributing to it and is fully consistent with electrochemical measurements. Calculations in the range of temperatures between 280 and 360 K combine long classical molecular dynamics simulations with quantum calculation of the protein active site. The results agree with the Arrhenius plots for the reaction rates and with cyclic voltammetry of cytochrome c immobilized on self-assembled monolayers. Small effective reorganization energy, and the resulting small activation barrier, is a general phenomenology of protein electron transfer allowing fast electron transport within biological energy chains.

4.2 Introduction

Redox proteins participate in metabolic redox reactions of biology and in photosynthetic and respiratory energy chains responsible for the cross-membrane electron transport. The conditions of operation of redox proteins within energy chains require some design trade-offs to accommodate both the small reaction free energies and the need to place bulky cofactors in the chain at sufficiently long distances. The overall rate of protein electron transfer is the product of the Boltzmann factor describing the activation barrier and the electron coupling (tunneling probability) decaying exponentially with the distance between the donor and acceptor.[77, 78, 81]

It is often assumed that proteins provide a nonpolar environment for electron transfer, blocking the access of highly polar water to the active sites. This view is supported by the low dielectric constant of protein powders ($\sim 2-5$[233, 89]) and the low magnitude of the screening factor (effective dielectric constant[225]) required in the Coulomb law to screen the interaction between the charges. However, hydration of the protein causes ionization of the surface groups and their increased mobility.[96] As a result, any active site of a hydrated protein is surrounded by a nearly uniform density of surface charges[234] maintaining the stability of the folded protein in solution and allowing its solubility in water.[235] While these charges mostly do not affect the electrostatic screening inside the protein, their motions, caused by thermally activated elastic deformations of the protein, produce a significant electrostatic noise at the protein active site.[90] It is this electrostatic noise that affects the electronic energy levels of the donor and acceptor, bringing them into resonance for electron tunneling.[76]

As we saw in section 1.4 the reorganization energy in the Marcus equation (eq (1.35)) is both the measure of the change in the distribution of charges (polariza-

tion) in the medium caused by transferring the electron (nominator in eq (1.35)) and the measure of the breadth of electrostatic fluctuations caused by thermal agitation (denominator in eq (1.35)).[89, 90] The Boltzmann factor $\exp[-\Delta G^{\dagger}/(k_{\mathrm{B}}T)]$ then becomes a Gaussian distribution of the variable ΔG_0 with the mean $-\lambda$ and the variance $2k_{\mathrm{B}}T\lambda$.

Given that a hydrated protein is a soft medium possessing a large density of charge at the protein-water interface, it is hardly a surprise that atomistic computer simulations consistently show large reorganization energies for electron transfer, $\lambda \simeq 1-2$ eV,[236, 237, 238, 227] or even higher[232, 239] when the simulation trajectories are sufficiently long. More surprising was the realization that the reorganization energy characterizing the fluctuations of the energy levels (thermal agitation) was distinct from the reorganization energy characterizing their shift upon electron transfer (medium polarization).[232]. We know from section 1.4 , that the former is λ and the later is λ^{St}.

The typical phenomenology of electrostatic fluctuations at active sites of proteins as calculated from atomistic simulations is the inequality[232, 90] $\lambda \gg \lambda^{\mathrm{St}}$. The reason for this result can be traced to the non-Boltzmann (non-ergodic) sampling of the phase-space available to the protein on the reaction time-scale,[93] polarizability of the active site,[84, 171] or the combination of both these factors and/or some other reasons not yet identified. This phenomenology, as well as some analytic models allowing non-Gaussian fluctuations affecting electron transfer,[84, 240, 241] provides an extension of the standard Gaussian picture of the Marcus model,[83] which stipulates[85] $\lambda^{\mathrm{St}} = \lambda$. At least some of these extensions[84] require non-parabolic free energy surfaces. Since our simulations do not provide sufficient sampling to distinguish such features, the phenomenology of equal-curvature parabolas[93] is used here. Specifically, the variance reorganization energies in the oxidized and reduced states are considered

to be equal (given by λ) and distinct from λ^{St}. This phenomenological approach allows us to accommodate both the non-Boltzmann (non-equilibrium) sampling and polarizability effects (requiring non-parabolic free energy surfaces[84]) in terms of only two reorganization parameters, λ and λ^{St}.

Large values of the reorganization energies appearing in simulations come in direct contradiction to often small, in the range $0.3 - 0.6$ eV[17, 18, 242, 16, 243, 244, 245] (or even smaller, < 0.25 eV[246, 247]), values of the reorganization energy reported by electrochemistry of redox proteins. Since electrostatics is not much sensitive to the details of force fields employed by atomistic simulations, the problem cannot be simply related to still existing deficiencies of the atomistic force-field models. As one can see from section 1.4, the reorganization energy reported by electrochemistry of proteins is an effective "reaction" (superscript "r") reorganization energy combining two reorganization energies typically reported by simulations(1.40)

The notion that proteins are characterized by the condition $\lambda \gg \lambda^{\mathrm{St}}$ explains why relatively small values of λ^r are reported by electrochemical measurements. Please note that λ^r in the form of eq (1.40) is a direct consequence of the parabolic shape of the free energy surfaces of electron transfer. One comes back to the standard Marcus picture with $\lambda^r = \lambda = \lambda^{\mathrm{St}}$ when $\lambda^{\mathrm{St}} = \lambda$.

In order to show the consistency of our theoretical model with experimental data, we have performed extensive simulations of a much studied[248, 249] heme protein cytochrome c (Cyt-c, wild type from horse). We show that the temperature dependence of the reaction reorganization energy $\lambda^r(T)$ is consistent with the Arrhenius plots for electrochemical rates obtained from cyclic voltammetry.[16] We also show that the distribution of the energy levels (density of states) of the oxidized heme, caused by thermal agitation of the bath, is consistent with the corresponding distribution obtained by taking the derivative of the cathodic current with the overpotential,

$di_c/d\eta$. The cathodic current i_c is obtained from cyclic voltammetry after correction for mass transport.[250, 17, 18, 251] We report an overall good agreement between experiment[16, 252, 243, 17] and the combined application of the analytic theory and computer simulations.[93, 171]

Producing reliable values of reorganization parameters of Cyt-c has required the combination of long trajectories of classical molecular dynamics (MD) simulations with quantum calculations of the heme's active site. Since long simulation times are required for the convergence of the reorganization energies, our quantum calculations are based on Warshel's empirical valence-bond method,[253, 254] which involves diagonalizing the quantum Hamiltonian, affected by fluctuating electrostatics, along the MD trajectory.[237, 171] This specific form of a general QM/MM methodology[255] allows one to combine long trajectories required for sufficient sampling of electrostatic fluctuations with a large number, $M \simeq 100$, of excited quantum states of the active site. These excited states are coupled to the fluctuating electrostatic field through a set of transition dipoles and thus allow us to account for the polarizability of the active site and the corresponding deformation of the electronic density in response to the medium fluctuations.[84, 237, 171] This part of the calculation formalism turns out to be very essential for achieving low values of λ^r consistent with experiment.

4.3 Methods

4.3.1 Eelectron Transfer

In the case of electrode electron transfer, the energy gap involving one-electron states is between the fluctuating energy level of the oxidized reactant in solution ϵ_{Ox} and the energy level in the metal ϵ (cathodic process, Fig. 4.1).[22] Correspondingly, we replace $i = \{1, 2\}$ for solution electron transfer with $i = \{\mathrm{Ox}, \mathrm{Red}\}$ for electrode

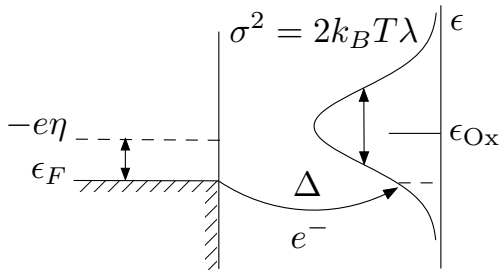

Figure 4.1: Schematics of Cathode Electron Transfer From the Fermi Energy Level ϵ_F, Corresponding to the Equilibrium Electrode Potential, to An Oxidized Reactant with the Average Energy ϵ_{Ox}. Electron Transfer Predominantly Occurs From ϵ_FTo a Nonequilibrium Energy Level in Resonance with. The Electrode-Reactant Electronic Coupling Δ Characterizes the Tunneling Probability (Eq (4.3)). The Nonequilibrium Energy Level Is a Part of a Gaussian Manifold with the Variance $\sigma^2 = 2k_BT\lambda$ Specifying the Reorganization Energy λ (Eq (1.34)). The Overpotential η Shifts the Electrode Chemical Potential as $\mu = \epsilon_F - e\eta$.

reactions. While full description of the problem in terms of finite-temperature distribution of the electrons in the metal is possible,[256, 257, 258, 259, 260] we first simplify the discussion by considering electron transfer to a single level corresponding to the chemical potential of the electrons in the metal $\mu = \epsilon_F - e\eta$. It is modified by the overpotential η (e is the elementary charge) from the Fermi energy ϵ_F consistent with the equilibrium potential at the electrode (Fig. 4.1).

In this picture, the initial state of the system with the electron in the metal is $E_{\mathrm{g}}^{\mathrm{Ox}} + \mu$, where $E_{\mathrm{g}}^{\mathrm{Ox}}$ is the ground state of the oxidized state of the reactant. The final state, before any relaxation of the nuclear subsystem has occurred, is the ground quantum state in the reduced state $E_{\mathrm{g}}^{\mathrm{Red}}$. Both energies refer to the same nuclear configuration of the thermal bath. The electron-transfer reaction coordinate, monitoring the transition to the activation state $X = 0$, is the energy gap between the initial and final states[3, 85]

$$X = E_{\mathrm{g}}^{\mathrm{Ox}} - E_{\mathrm{g}}^{\mathrm{Red}} + \mu \tag{4.1}$$

Since the reduction and oxidation rates are equal at $\eta = 0$, $e\eta = \Delta G_0$ for the electrochemical discharge. One therefore gets for the barrier of electrochemical electron

transfer

$$\Delta G^{\dagger} = \frac{(\lambda^r + e\eta)^2}{4\lambda^r} \tag{4.2}$$

The significant result of this derivation is that accepting two equal-curvature parabolas, even with the variance reorganization energy distinct from the Stokes reorganization energy, does not alter the basic Marcus result[76] for the dependence of the activation barrier on the reaction free energy. The two reorganization energies, λ and λ^{St}, combine into an effective reorganization energy λ^r (eq (1.40)), which is the only parameter that can be reported from experiments altering either the reaction free energy (solution reactions) or the electrode overpotential (electrochemical kinetics). In contrast, spectroscopy of charge-transfer bands allows one to distinguish between λ^{St} and λ.[87, 261] The former parameter determines the spectroscopic Stokes shift, while the latter yields the inhomogeneous broadening of the spectral lines (Fig. 1.4b).[91, 262, 4]

The arguments presented here can be extended to the calculation of the rate of non-adiabatic electron transfer, which involves summation of the Golden Rule transitions to all energy levels of the metal below the chemical potential μ. The resulting cathodic rate is[256, 263, 264, 265]

$$k_c(\eta) = \frac{\Delta}{\hbar}\mathrm{erfc}\left(\frac{\lambda^r + e\eta}{\sqrt{4k_BT\lambda^r}}\right) \tag{4.3}$$

where $\mathrm{erfc}(x)$ is the complimentary error function and $\Delta = \pi\rho_F V^2$ is the electronic coupling between the redox species and the electrode. It is given in terms of the coupling V between the reactant and the individual energy state in the metal and the density of states ρ_F of the conduction electrons at the Fermi level.[266, 257, 259]

The derivative of the rate over the overpotential, $dk_c/d\eta$, is thus proportional to the "density of states" of the oxidized energy level in the medium

$$P_c(\eta) \propto \exp\left[-\frac{(\lambda^r + e\eta)^2}{4k_BT\lambda^r}\right] \tag{4.4}$$

This distribution is distinct from the corresponding distribution along the reaction coordinate $P_{\mathrm{Ox}}(X) \propto \exp[-\beta G_{\mathrm{Ox}}(X)]$ (Figure A.2). The function $P_c(\eta)$ is a measure of the probability $P_{\mathrm{Ox}}(0)$ to reach the activated state $X = 0$ when the average $\langle X \rangle_{\mathrm{Ox}} = -\lambda^{\mathrm{St}} - (e\eta)(\lambda/\lambda^{\mathrm{St}})$ is varied by applying the overpotential. The distribution function $P_c(\eta)$ is directly accessible from cyclic voltamemtry upon correction for mass transport.[250]

Solvent dynamics can potentially affect the preexponential factor of the rate constant.[267, 268, 269, 270] The rate constant of electron transfer between the electrode and an adsorbed reactant, not affected by diffusion, is given by the following relation[271, 272, 273]

$$k_c^s(\eta) = (1+g)^{-1} k_c(\eta) \tag{4.5}$$

with the nonadiabatic rate constant $k_c(\eta)$ according eq (4.3). The factor in front of it, correcting for the solvent dynamics, is given by the relation

$$g = \frac{\Delta\langle\tau\rangle}{\hbar} \frac{4k_B T \lambda^r}{(\lambda^r + e\eta)^2} \tag{4.6}$$

The theory leading to eq (4.5) is the result of applying the Sumi-Marcus[268] formalism to electrode kinetics.[273] The analytical expressions in eqs (4.5) and (4.6) are obtained under the assumption of a sufficiently low overpotential such that $\lambda^r + e\eta \gg k_B T$.[273] Further, $\langle\tau\rangle$ is the characteristic time of the Stokes-shift dynamics of the energy gap X specified through the energy gap autocorrelation function[274]

$$C_X(t) = \langle \delta X(t) \delta X(0) \rangle \tag{4.7}$$

where $\delta X(t) = X(t) - \langle X \rangle$ and $\langle\tau\rangle$ is defined as the integral of the normalized time correlation function (average solvation time[228])

$$\langle\tau\rangle = \int_0^\infty dt C_X(t)/C_X(0) \tag{4.8}$$

The relaxation times in the range $\langle\tau\rangle \simeq 300 - 900$ ps[275, 204, 276, 277] were determined from MD simulations (Figure A.5 and Table A.3). These Stokes-shift relaxation times were used in eq (4.6) to estimate the effect of the solvent dynamics on $k_c^s(0)$. It was found to be negligible for the experimental data considered below.

4.3.2 Simulations and Data Analysis

. The NMR solution structure of horse heart cytochrome c (PDB 1GIW) was adopted as the starting configuration for the classical MD simulations. The simulations were done with NAMD software suite, [172] with the trajectory length of $\geq$ 250 ns for each temperature and oxidation state (overall $\geq$ 4 μs of MD simulations). The classical MD simulations were followed by empirical valence-bond calculations[253, 254] performed for the quantum center including the heme, histidine, methionine, and two cysteine amino acids (Fig. 4.2 and A.2.1) following the protocol developed in the past.[171] The electrostatic potential of the bath $\phi(\mathbf{r})$ acting on the quantum center was expanded around the potential $\phi_{\rm Fe}$ at the heme iron up to the dipolar operator. This expansion leads to a set of transition dipoles $\boldsymbol{\mu}_{jk}^i$ in the matrix of the quantum center Hamiltonian[237, 171]

$$H_{jk}^i = \left(E_j^i + Q^i\phi_{\rm Fe}\right)\delta_{jk} - \boldsymbol{\mu}_{jk}^i \cdot \mathbf{E}_b \tag{4.9}$$

Here, E_j^i is the energy of jth state in either $i =$ Ox or $i =$ Red states and Q^i is the total charge of the quantum center. The excited states j and k are coupled through the electric field of the thermal bath $\mathbf{E}_b$ multiplying transition dipoles $\boldsymbol{\mu}_{jk}^i$ in eq (4.9). Physically, this term in the Hamiltonian represents the polarization of the heme by the medium field through a non-zero polarizability α_j^i of state j, which is given in terms of the transition dipoles as

$$\alpha_j^i = 2\sum_{k\neq j} \left|\boldsymbol{\mu}_{jk}^i\right|^2 / \Delta E_{jk} \tag{4.10}$$

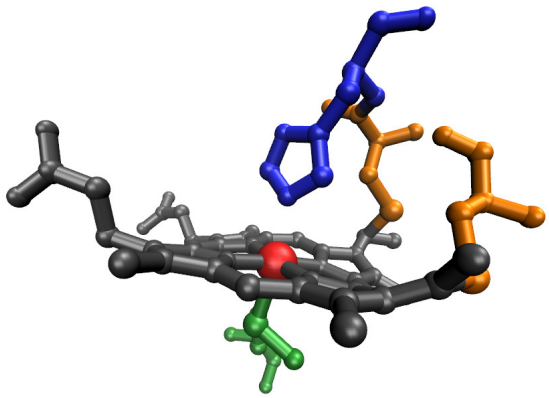

Figure 4.2: Quantum Center of Cyt-C Used in the Calculations to Compute the Hamiltonian Matrix in Eq (4.9). It Includes the Heme (Gray, with Fe Colored Red), Histidine (Blue), Methionine (Green), and Two Cysteine (Orange) Amino Acids.

where $\Delta E_{jk} = E_k - E_j$.

The quantum states $j = 0, \ldots, M$ include the ground state of the quantum center, $j = 0$, and a number of its excited states produced here by ZINDO/S calculations for the oxidized (Ox, $Q = -1$) and reduced (Red, $Q = -2$) states. The number of states $M = 100$ was chosen to converge the polarizability of the quantum center. Decreasing the number of states M makes the quantum center less polarizable and eventually brings the system back to the Marcus formulation with $\lambda^{\mathrm{St}} \simeq \lambda$.[171] Additional details of the simulation protocol and of the quantum calculations are given in appendix A.

A polarizable quantum center carrying the polarizability $\boldsymbol{\alpha}^i$ gives rise to the polarization free energy $-(1/2)\mathbf{E}_b \cdot \boldsymbol{\alpha}^i \cdot \mathbf{E}_b$. On the other hand, the free energy (reversible work) invested in creating a fluctuation in the medium scales quadratically with the field,[278, 84, 279] $(\chi/2)\mathbf{E}_b^2$. The sum of this term and the polarization free energy lowers the force constant for the medium fluctuation from χ to $\simeq (\chi - \alpha^i)$, $\alpha^i = \frac{1}{3}\mathrm{Tr}[\boldsymbol{\alpha}^i]$. When projected on the reaction coordinate of electron transfer X, less free energy invested in an electrostatic medium fluctuation implies lower curvature

of the corresponding parabola $G_i(X)$ and a higher reorganization energy λ.[84] This physical picture is consistent with our simulations.

The Hamiltonian matrix in eq (4.9) is diagonalized at each instantaneous value of the potential ϕ_{Fe} and the electric field $\mathbf{E}_b$ along the simulation trajectory to produce the minimum eigenvalues $E_{\mathrm{g}}^{\mathrm{Ox/Red}}$ corresponding to the quantum ground state in either oxidized or reduced states of the active site. They are used in eq (4.1) to produce the trajectory of the fluctuating variable X. The probability distributions of X calculated in the oxidized and reduced states yield the free energy surfaces of the half reaction $G_i(X)$ (Figure A.2).

The reorganization energies λ^{St} and λ are obtained from, correspondingly, the first and second moments of the variable X. The former is defined in terms of the average energy gap $\langle X\rangle_i$ in the Red and Ox states according to eq (1.38). The latter is given through the variance, $\lambda_i = \langle(\delta X)^2\rangle_i/(2k_{\mathrm{B}}T)$, $i = \mathrm{Ox}, \mathrm{Red}$. Significantly longer simulations are required to converge λ_i compared to λ^{St} (Figure A.1). We find λ_{Ox} and λ_{Red} slightly different even after 250 ns of simulations (Fig. 4.3 and Table A.2.2). The values of λ used for the kinetic analysis were therefore obtained by taking the mean of the values in the corresponding redox states, $\lambda = (\lambda_{\mathrm{Ox}}+\lambda_{\mathrm{Red}})/2$ (black circles in Fig. 4.3).

A separate issue is the potential impact of the polarizability of the protein-water solvent on the reorganization energies calculated from simulations. Dielectric continuum models predict that the reorganization energy is proportional to the Pekar factor $c_0 = n_D^{-2} - \epsilon_s^{-1}$,[76] which implies a drop by a factor of about n_D^{-2} in going from a non-polarizable solvent to a polarizable solvent with the refractive index n_D (assuming a high static dielectric constant ϵ_s). This perspective would suggest that the reorganization energies obtained by computer simulations in non-polarizable solvents (TIP3P water in this study) would need to be scaled down to account for the polar-

izability effects. Recently this problem has been addressed by computer simulations and liquid-state theories.[280, 281]

It turns out that microscopic solvation models do not support re-scaling of the reorganization energy according to the rules stipulated by dielectric continuum models. In contrast to those predictions, λ stays nearly constant with increasing n_D^2, or even slightly increases (for polarizable water models), instead of the predicted drop. Given these new results and previous simulations and calculations of the effects of the solvent polarizability on electron transfer,[282, 283] it is reasonable to suggest that the reorganization parameters obtained from the present simulations do not need further re-scaling. A good agreement with experimental results demonstrated below is another indication that our calculation formalism is robust.

We also note that electron transfer in redox proteins is typically accompanied by small structural changes of the active site[284] and, correspondingly, low reorganization energy of active site vibrations. Estimated values range from $0.05 - 0.09$ eV for Fe-porphins[285] to $0.10 - 0.14$ eV for Zn-porphyrins[286] to $\simeq 0.1$ eV in azurins.[287] This internal reorganization energy is generally split between quantum and classical vibrations. The reorganization energy related to quantum vibrations affects the rates in the Marcus inverted region of electron transfer,[288] which is not typically reached in either the electrochemical experiment or at the typical conditions of redox reactions in biological energy chains. Therefore, only the classical part of the internal reorganization energy can potentially affect these reactions. While the splitting of the reorganization energy between the classical and quantum modes is not known for Cyt-c, the classical part of the internal reorganization energy, remaining after subtracting the quantum component, is expected to be small, within the simulation uncertainties. We therefore do not include the internal reorganization energy in our calculations of the electrode kinetics.

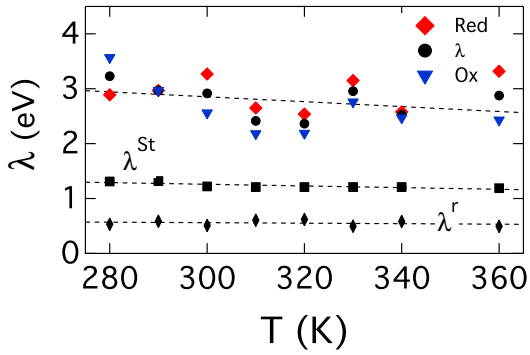

Figure 4.3: Temperature Dependence of Reorganization Energies From QM/MD Simulations. Shown Separately Are the Variance Reorganization Energies λ_i (Eq (1.34)) in the Reduced (Red Diamonds) and Oxidized (Blue Triangles) States of Cyt-C and Their Mean Values (Black Circles). Squares Refer to the Stokes-Shift Reorganization Energy λ^{St} (Eq (1.38)) and Black Diamonds Refer to the Reaction Reorganization Energy λ^r (Eq (1.40)). The Dashed Lines Are Linear Regressions Through the Simulation Points (the Upper Dashed Line Is a Linear Regression Through the Mean Values $\lambda(T)$).

4.4 Results

The results of QM/MD simulations for the reorganization energies as functions of temperature are shown in Figure 4.3. The corresponding values at $T = 300$ K, estimated from linear regressions of the simulation data, are listed in Table 4.1. As expected, both reorganization energies, λ^{St} and λ, are fairly large and consistent with a large density of charge and polar groups surrounding the active site of a redox protein. A relatively small value of the reaction reorganization energy λ^r (eq (1.40)) is achieved due to $\lambda \gg \lambda^{\mathrm{St}}$. As we already pointed out, this inequality in the case of Cyt-c is the consequence of a high polarizability of the active site allowing its electronic density to deform in response to the fluctuations of the thermal bath. Reducing the polarizability by either using fixed partial atomic charges (zero polarizability) or a small number of quantum states when diagonalizing the quantum Hamiltonian produce $\lambda^{\mathrm{St}} \simeq \lambda \simeq 1.3-1.6$ eV consistent with the standard Marcus picture of a single reorganization energy characterizing electron transfer.[171] However, these values of

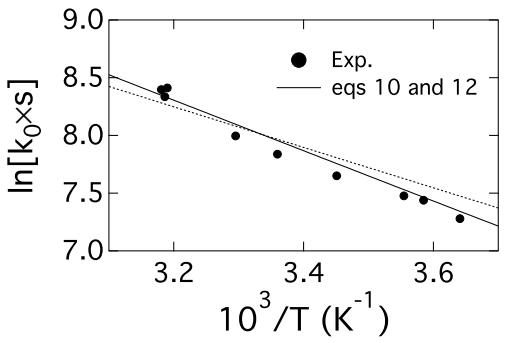

Figure 4.4: Rate Constant $k_0 = k_c(0)$ (Eq (4.3)) at $\eta = 0$ for Horse Cyt-c on the Gold Electrode Modified with PyC_{11}/C_{10} Self-Assembled Monolayer[16] (Points, Exp.). The Solid Line Shows the Calculations Based on Eqs (4.3) and (4.5),Which Give Identical Results. The Electron Coupling $\Delta = 2 \times 10^{-9}$ eVIs Used to Reproduce the Experimental Data. The Temperature-Dependent Reorganization Energy $\lambda^r(T)$ from Figure 4.3 Was Used in Eqs (4.3) and (4.5).The Dotted Line Shows the Result of Neglecting the Temperature Dependence $\lambda^r(T)$ and Putting $\lambda^r = \lambda^r(300\ \mathrm{K})$.

the reorganization energy are too high to describe the experimental electrochemical data, as we show below.

Not only the reorganization energy itself, but also its temperature dependence is reduced for λ^r compared to λ^{St} and λ. We list in Table 4.1 the entropies of reorganization

$$S_\lambda = -\left(\partial\lambda/\partial T\right)_V \tag{4.11}$$

at constant volume consistent with the NVT ensemble used in the simulations (see A.2.1). All reorganization energies are decaying functions with increasing temperature, as is expected from studies of electron-transfer reactions in polar liquids.[289, 290]

The decay of the reorganization energy with increasing temperature is related to structural fluctuations in polar liquids producing changes in both orientations of the liquid dipoles and their positions (density fluctuations). While changes in orientations are mostly driven by redistributing the thermal energy (energy driven), the density rearrangements require local repacking of the liquid against repulsive molecular cores

Table 4.1: Reorganization Parameters of Cyt-c at $T = 300$ K (eV).[a]

Parameter	λ	λ^{St}	λ^{r}
λ	2.85	1.26	0.56
TS_{λ}	1.34	0.45	0.14

[a]The Parameters in the Table Are Calculated From Linear Interpolations of the MD Data in the Range of Temperatures From 280 K to 360 K (Fig. 4.3).

(entropy driven). The difference in the character of fluctuations, energy-driven for rotations and entropy-driven for translations, projects on different effects of temperature on the corresponding components in the reorganization energy. The reorganization energy arising from molecular rotations is nearly temperature-independent, while the reorganization energy arising from density fluctuations decays approximately hyperbolically with increasing temperature. The overall dependence of the reorganization energy on temperature is hyperbolic,[289] as proven experimentally[291, 290] for systems with $\lambda^{\mathrm{St}} \simeq \lambda$. Figure 4.3 shows that the general rule of the reorganization energy decaying with increasing temperature extends to redox proteins with $\lambda \gg \lambda^{\mathrm{St}}$.

The largest entropy S_{λ} is observed for the variance reorganization energy λ, with $TS_{\lambda}/\lambda \simeq 0.5$ consistent with typical values observed for electron transfer in polar molecular liquids.[289] In contrast, the temperature variation of λ^{r} is significantly reduced, by an order of magnitude, due to the mutual cancellation of the corresponding temperature effects on λ^{St} and λ. This cancellation achieves a significant robustness of operation and insensitivity of the enzyme to the variations of thermodynamic conditions.[77] Consistently, a very small reaction entropy was recently reported for electrochemistry of immobilized myoglobin.[292]

The magnitude of λ^{r}, and its temperature dependence, are fully consistent with the experimental data. Figure 4.4 shows the temperature variation of $k_0 = k_c(0)$ measured for horse Cyt-c[16] immobilized on a self-assembled monolayer (SAM) on

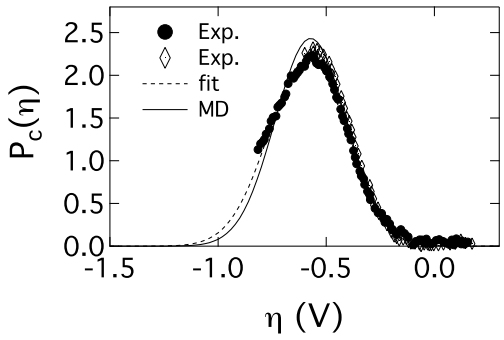

Figure 4.5: Normalized Probability Density $P_c(\eta)$ (Eq (4.4)) Obtained From Experiment with Tuna (Filled Circles[17]) and Horse (Diamonds[18])Cyt-C and From MD Simulations (Solid Line).The Experimental Results Were Collected at $T = 273$ K From Voltammograms with the Electrode Coated with the $OH-(CH_2)_{11}SH$ ω-Hydroxyalkenthiol.The MD Value of the Reorganization Energy $\lambda^r = 0.57$ eV Was Obtained by Extrapolating the Results Shown in Figure 4.3 to 273 K.The Dashed Line Is the Gaussian Fit Through the Filled Circles.

a metal electrode.[256, 293, 294] Immobilization is achieved by linking the heme of Cyt-C to terminal pyridine group of the PyC_{11}/C_{10} monolayer. The application of the non-adiabatic electron-transfer rate requires the unknown parameter Δ in eq (4.3), which does not affect the slope of the Arrhenius plot ($\ln k_0$ vs $1/T$), but causes its vertical shift. The value of Δ was adjusted to fit the experimental data (points in Fig. 4.4). A good agreement of the Arrhenius slope with experiment suggests that λ^r, and its temperature dependence, are reliably reproduced by the simulations. Neglecting the temperature dependence of λ^r results in a lower slope (dotted line), in accord with the positive sign of S_λ in Table 4.1 affecting the enthalpy of activation according to the relation

$$\Delta H^\dagger \simeq \frac{\lambda + TS_\lambda}{4} \tag{4.12}$$

The estimate of the solvent dynamic effect,[267, 269, 270] with the relaxation time $\langle\tau\rangle \simeq 300 - 900$ ps obtained from simulations (see A.2.1), shows that the term in the denominator in eq (4.5), containing $g \propto \langle\tau\rangle$ (eq (4.6)), can be neglected for this

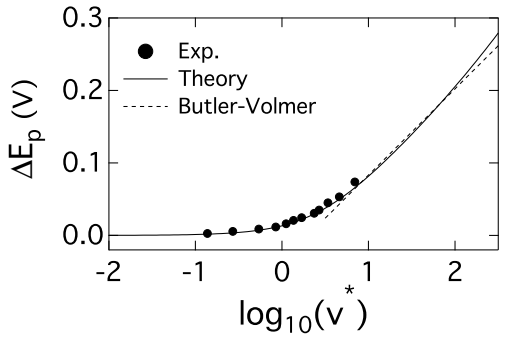

Figure 4.6: Shift of the Cathodic Peak Potential ΔE_p Vs the Scan Rate $\log_{10}(v^*)$, $v^* = ev/(k_{\rm B}Tk_c(0))$. The Points Are Experimental Data[16]And the Solid Line Is the Calculations[19, 20] Performed with $\lambda^r = 0.56$ eV and $\Delta = 2 \times 10^{-9}$ eV at $T = 298$ K. The Dashed Line Indicates Laviron's[21] Irreversible Reaction Limit with the Slope $2.3k_BT/(\alpha e)$And with the Transfer Coefficient $\alpha = 0.5$ (Butler-Volmer Kinetics[22]).

reaction ($g \simeq 4 \times 10^{-4}$).

An independent test of our results is provided by voltammetry of horse Cyt-c performed[17] on an electrode coated with ω-hydroxyalkenthiol SAM of a thickness comparable to the one used to produce data shown in Figure 4.4.[16] In these experiments, the derivative of the diffusion-corrected[250] electrode current $di_c/d\eta$ was recorded (points in Fig. 4.5). As mentioned above, this derivative is proportional to the probability density $P_c(\eta)$ along the overpotential coordinate (eq (4.4)). The probability density based on our MD simulations (solid line in Fig. 4.5) is in good agreement with experiment without any additional fitting. The value of $\lambda^r \simeq 0.57$ eV used in the analysis is consistent with $\lambda^r \simeq 0.58 \pm 0.04$ eV reported previously[18, 242] (native rat Cyt-c in Ref. 242).

Our results are also consistent with the reported cyclic voltammograms[16] without additional fitting (Fig. 4.6). The calculations were performed by applying the rate constant as given by eq (4.3) to kinetic equations describing redox adsorbates (see A.2.1).[19, 20] The reorganization energy λ^r for the analysis is taken from our MD data and $\Delta = 2 \times 10^{-9}$ eV is the fitting parameter from the Arrhenius plot shown

in Figure 4.4. The calculations are consistent with the expected limiting behavior for fully irreversible reactions where Laviron's solution[21] for the Butler-Volmer kinetics predicts the linear plot with the slope $2.3k_BT/(\alpha e)$ (dashed line in Figure 4.6 for the transfer coefficient $\alpha = 0.5$).

Chapter 5

TERMINATION OF BIOLOGICAL FUNCTION AT LOW TEMPERATURES: GLASS OR STRUCTURAL TRANSITION?

This material was published in the Journal of Physical Chemistry Letters 9(9), pp.2359-2366 (2018 Apr 19).

5.1 Summary

Energy of life is produced by electron transfer in energy chains of respiration or photosynthesis. A small input of free energy available to biology puts significant restrictions on how much free energy can be lost in each electron-transfer reaction. We advocate the view that breaking ergodicity, leading to violation of the fluctuation-dissipation theorem (FDT), is how proteins achieve high reaction rates without sacrificing the reaction free energy. Here we show that a significant level of nonergodicity, represented by a large extent of the configurational temperature over the kinetic temperature, is maintained in the entire physiological range for the cytochrome c electron transfer protein. The protein returns to the state consistent with the FDT below the crossover temperature close to the temperature of the protein glass transition. This crossover leads to a sharp increase in the activation barrier of electron transfer and is displayed by a kink in the Arrhenius plot for the reaction rate constant.

5.2 Introduction

Life exists in a very narrow range of temperatures and the question of what happens when the temperature is lowered seems to be irrelevant for biological function. However, in particular in the field of physiological energy flow,[79] lowering temper-

ature has offered significant insights into the basic physical mechanisms behind the high-temperature phenomena. The classical experiments by de Vault and Chance[82] showed that the rate of protein electron transfer becomes temperature-independent below ~ 150 K, which helped to realize that electron tunneling is the physical mechanism behind biological electron transport.[81] Likewise, lowering temperature in Mössbauer spectroscopy of myoglobin allowed Parak and Formaneck[75] to observe a kink in the temperature dependence of iron displacement in the heme cofactor. This result came in violation of the fluctuation-dissipation theorem (FDT)[92] and of an even earlier result known as the Nyquist theorem.[295] Here, we continue along this path of enquiry by employing large-scale molecular dynamics (MD) simulations to drive cytochrome c (Cyt-c) protein below its glass transition to interrogate the effect of lowering temperature on the activation barrier of protein electron transfer. We show that the violation of the FDT first pointed out by Parak and Formaneck[75, 80] is a fundamental principle allowing proteins to achieve fast reaction rates without sacrificing the reaction free energy.

The FDT is a set of relations connecting the response of a macroscopic variable X to a weak perturbation with thermal fluctuations of the same variable.[92] Specifically, if a weak step perturbation F is introduced at time $t = 0$, the change $\Delta X(t) = \chi(t)F$ is represented by the product of the linear response function $\chi(t)$ and F. The total change $\Delta X(\infty)$ obtained at $t \to \infty$ is related to the variance $\langle \delta X^2 \rangle$ caused by thermal agitation at equilibrium:[92] $k_{\mathrm{B}} T \chi(\infty) = \langle \delta X^2 \rangle$ (angular brackets refer to an equilibrium ensemble average).

The general framework of the FDT applies to solvation of charge by polar liquids and is typically ascribed to the linear response approximation for solvation,[296] with the most famous result given by the Born equation for polar solvation. This framework is also commonly applied to enzymology[297, 298] and, more specifically, to probably

the simplest reaction catalyzed by proteins, the reaction of electron transfer.[76, 79] No bonds are formed or broken during electron transfer, which allows one to reduce the problem to the language of nonequlibrium solvation and the fluctuation-dissipation relations. This connection was achieved by Marcus,[278] who, following Onsager's idea of microscopic reversibility,[299] defined the free energy required to bring the donor and acceptor in the resonance configuration for electron tunneling. This formalism has lead to now widely accepted picture of equal-curvature crossing parabolas (Fig. 1.5). The collective variable $X = \Delta E(\mathbf{q})$, depending on the system's nuclear coordinates $\mathbf{q}$, is the energy gap between the initial and final electronic states[3] and the activation barrier is the free energy required to climb from the parabola's bottom to $X = 0$ at the crossing point (tunneling configuration).

5.3 Discussion and Results

While providing a general and widely applicable view of activated processes in polar materials, the Marcus picture is too limited when applied to protein electron transfer. The difficulty is the need for a large in magnitude and negative reaction free energy,[76] $\Delta G_0 \simeq -\lambda$, to accomplish sufficiently fast near-activationless electron transfer often observed in primary events of photosynthesis and energy chains of respiration.[300, 301] The proposal that proteins might provide a weakly polar environment for redox active sites[288] has been mostly refuted by a large number of recent MD simulations[227] and by comparison of simulations with experiment[232, 302, 15] (with potential exceptions of active sites buried deep inside the membrane-bound proteins[303, 227]). As our simulations below also indicate, the typical reorganization energy of protein electron transfer, $\simeq 1$ eV, is not much different from the standard expectations for organic donor-acceptor complexes in solution[304, 305] and ligand-protected (e.g., $\lambda \simeq 1$ eV for cobaltocene[306]) redox metal ions (up to three

times higher reorganization energies are found for transition metal aqua ions[307]). Such relatively high values of the reorganization energy for protein electron transfer require significant losses of free energy for an energy chain operating at low activation barriers. On the other hand, rather small input free energy, $|\Delta G_0| \simeq 1$ eV, is typically available to biology, either through the photon energy or the redox potential of organic molecules.[79] Since this input needs to be utilized in a large number of electron-transfer steps, energy complexes of biology must have developed non-Marcusian mechanisms of operation to avoid wasteful conversion of free energy to heat.

Nonlinear solvation, going beyond the linear response approximation of the Marcus picture and the FDT, does not seem to have a significant chance to operate in the soft environment of an active site subjected to screening by mobile waters and ionic clouds.[83, 296] We have alternatively suggested that energetic efficiency of biology exceeding the predictions of the standard models is achieved by eliminating ergodicity,[232] i.e., by incomplete sampling of the space of available configurations. This hypothesis leads to a number of verifiable predictions.[93] Most directly, ergodicity breaking, common to glass science, leads to the violation of the FDT with the consequence that the thermal variance of an observable property $\langle \delta X^2 \rangle / (k_{\mathrm{B}} T)$ exceeds the linear susceptibility $\chi(\infty)$. To characterize this distinction, one introduces an effective (fictive[308]) temperature of a glassy system $T_{\mathrm{eff}} \propto \langle \delta X^2 \rangle / \chi(\infty)$.[309, 310, 311, 312] In the case of electron transfer, this definition translates to the following relation[93]

$$\frac{T_{\mathrm{eff}}}{T} = \frac{\lambda}{\lambda^{\mathrm{St}}} \tag{5.1}$$

Here, T_{eff} is the effective temperature characterizing the configurational manifold of the thermal bath of the reaction site (protein and the surrounding solvent for protein

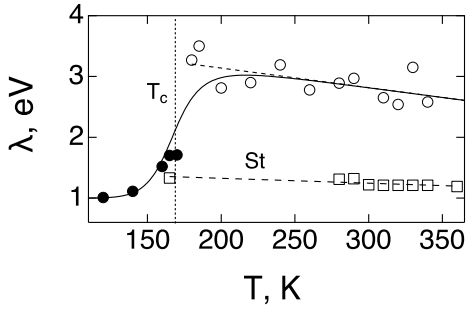

Figure 5.1: Temperature Dependence of the Reorganization Energies Calculated From the First and Second Moments of the Reaction Coordinate, λ^{St} (Marked as "St", Open Squares) and λ (Circles). We Find $\lambda \gg \lambda^{\mathrm{St}}$ at High Temperatures (Open Circles),In Violation of the Fluctuation-Dissipation Theorem, and the Return to $\lambda^{\mathrm{St}} \simeq \lambda$ Anticipated by the FDT Below the Crossover Temperature $T_c \simeq 170$ K (Filled Circles). The Results for λRefer to the Oxidized State of Cyt-C, and Both Oxidized and Reduced States Were Simulated to Produce λ^{St}. The Solid Curve Is the Fit to Eq (5.6) Assuming Ergodicity Breaking with the Arrhenius Relaxation Time $\tau_X = \tau_0 \exp[E_X/(k_{\mathrm{B}}T)]$. The Activation Energy $E_X/k_{\mathrm{B}} = 1725$ K Was Obtained from MD Simulations (Fig. A.14) and $\tau_0/\tau_{\mathrm{obs}} = 10^{-6}$ WasAdopted Based on the Length of the Simulation Trajectories. The Dashed Lines Are the Linear Regressions Through the Simulation Points.

electron transfer) and T is the standard kinetic temperature.

The right-hand side of eq (5.1) involves two reorganization energies, λ^{St} and λ. The former is the analog of the linear susceptibility $\chi(\infty)$ of the FDT. It is equal to half of the separation between the mean values of the energy gap X in two electron-transfer states[313, 314] (the Stokes shift[87])(equation (1.38) and figure 1.5). The second reorganization energy is λ (eqauation (1.34) and Figure 1.5).

In the thermodynamic limit of ergodic sampling described by the FDT, $T_{\mathrm{eff}} = T$ and $\lambda^{\mathrm{St}} = \lambda$, as required by the standard theory.[76] When ergodicity is broken, one gets[310] $T_{\mathrm{eff}} > T$ and the reorganization energy from the curvature exceeds that from the shift between the parabolas' minima. As is easy to appreciate from Figure 1.5, this scenario leads to the drop of the activation barrier compared to the standard theory. The activation barrier with zero reaction free energy becomes

$$\Delta F^{\dagger} = \lambda^{r}/4 = \left(\lambda^{\mathrm{St}}\right)^{2}/(4\lambda) = \left(\lambda^{\mathrm{St}}/4\right)\left(T/T_{\mathrm{eff}}\right) \tag{5.2}$$

The effective "reaction" reorganization energy λ^r is the only parameter that enters the activation barrier, which for a non-zero reaction free energy ΔG_0 still carries the form of the Marcus theory[93] (check equations (1.36) and (1.39)). What is different from the standard theory is that $\lambda^r = (\lambda^{\rm St})^2/\lambda$ loses its simple meaning of a linear solvation free energy and becomes a composite parameter given by eq (5.2). In the case of Cyt-c at 300 K we obtain from MD simulations: $\lambda \simeq 2.9$ eV, $\lambda^{\rm St} \simeq 1.3$ and $T_{\rm eff}/T \simeq 2.3$. The resulting $\lambda^r \simeq 0.57$ eV is in close agreement[15] with the values reported from electrochemistry of proteins attached to monolayer-coated electrodes,[17, 18, 242] $\lambda^r \simeq 0.58 \pm 0.04$ eV. This result is slightly below $\lambda^r \simeq 0.7$ eV from solution rates measured vs the reaction driving force (Marcus inverted parabola) for cytochrome c proteins modified through the attachment of Ru-based electron donors.[307] No direct comparison to electrochemistry can, however, be conducted because reorganization of Ru-chromophore significantly affects the energetics.[315]

Mechanisms to lower reaction barriers had to be sought after by natural selection. Our theoretical framework presents a potential realization of this selection pressure through a physically robust mechanism. The practical question is whether proteins can serve as media allowing ergodicity breaking and what are the magnitudes of barrier depression that can be achieved.

The main result of this study is shown in Figure 5.1. It presents the analysis of extensive (> 5.6 μs) MD simulations of Cyt-c (PBD 1GIW and 1AKK) in two redox states at a number of temperature from above the room temperature ($T_{\rm H} = 360$ K) to low temperatures ($T_{\rm L} = 120$ K) below the glass transition of the protein at $T_g \simeq (170 - 180)$ K.[100] The main observation from these data is that

$$T_{\rm eff} \gg T \tag{5.3}$$

at physiological temperatures, where $\lambda(T)$ is a slightly dropping function of tempera-

ture, as expected.[289] The high-temperature behavior, where the FDT is clearly violated, is followed by a sharp return to the FDT expectations, $T_{\text{eff}} \simeq T$, at a crossover temperature T_c not too far from T_g. The question addressed by this report is what are the mechanisms contributing to this unusual phenomenology. The simulation protocol for the MD simulations presented here was described previously[171, 15] and is discussed in more detail in appendix A. It is important to note that while $T_{\text{eff}} \gg T$ is often found for the electrostatics of protein active sites in agreement with experimentally reported kinetics of electron transfer,[232, 302] Cyt-c is a somewhat special case. We found, in agreement with previous simulations,[237, 227] that $\lambda \simeq \lambda^{\text{St}}$ when the heme is represented by partial atomic charges and no polarizability of the active site is included. The condition $\lambda \gg \lambda^{\text{St}}$ is achieved by allowing polarizability of the active site modeled here by QM/MD calculations described in previous publication[171] and in section A.2.1. The polarizability of Cyt-c significantly exceeds what a similar formalism finds for iron-sulfur clusters in bacterial complex I, where still $T_{\text{eff}}/T \approx 3-6$ was reported.[316]

One first has to stress that the ratio $T_{\text{eff}}/T > 2$ is significantly higher for proteins than for bulk glass-formers,[311] but close to the results obtained by pulling DNA hairpins with optical tweezers.[312] The DNA experiments represent a driven system, while protein electrostatics is intrinsically non-equilibrium. There are, therefore, some unique properties of the biomolecule-water thermal bath that allow a very substantial deviation from the FDT for the charge-potential conjugate variables and a correspondingly large depression of the activation barrier related to electrostatics at the active site.

The first question to ask in connection with a sharp drop of λ at T_c is whether one can identify some other properties, related either to the protein or to its hydration shell, which show similarly strong alterations around T_c. We could not identify protein

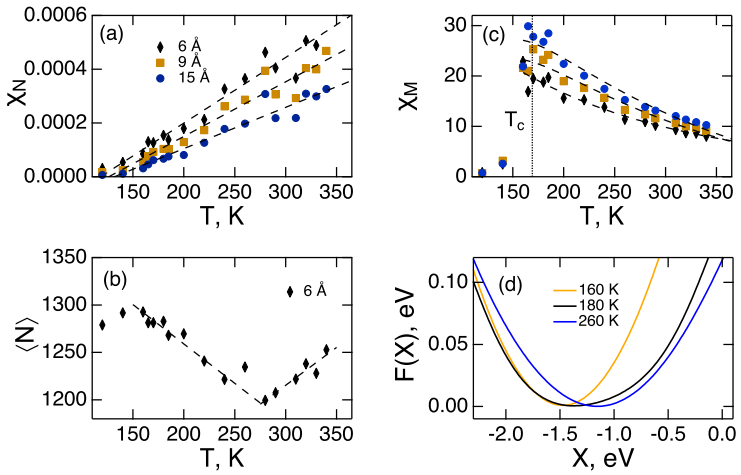

Figure 5.2: (a) Compressibility of Hydration Shells $\chi_N(a)$ (Eq (5.4)). (b) Average Number of Water Molecules in the Shell of Thickness $a = 6$ Å. (c) Dipolar Susceptibility $\chi_M(a)$ (Eq (3.22)). (d) Free Energy Surfaces of Oxidized Cyt-C (Eq (1.33)), $F(X) = F_1(X)$. The Free Energy Surfaces Have Been Shifted to the Common Level $F(\langle X\rangle_1) = 0$.The Dashed Lines Drawn Through the Points in (a)-(c) Are Fits to Guide the Eye and the Vertical Dotted Line in (c)Is Drawn at the Temperature $T_c \simeq 170$ K Also Shown in Figure 5.1.

properties showing a crossover, but a number of crossovers for the hydration shell were found by the present simulations.

We first focus on whether the orientational or density manifold of the hydration shell shows an unusual behavior. Figure 5.2a presents the compressibility of the hydration layers of different thickness a measured from the protein's van der Waals surface. The compressibility is calculated as the variance relative to the average number of hydration waters in the shell of thickness a[317, 318, 207]

$$\chi_N(a) = \langle \delta N(a)^2 \rangle / \langle N(a) \rangle \tag{5.4}$$

The resulting functions $\chi_N(a)$, calculated for $a = 6, 9, 15$ Å, are all approximately proportional to the kinetic temperature T, as expected from the FDT (Fig. 5.2a). No discontinuity is seen at T_c, even though a curious dependence is found for the average number of waters, as is shown in Figure 5.2b. The average $\langle N(a) \rangle$ is seen to go through a minimum at $T \simeq 270$ K. It is also reflected by a slight bump of $\chi_N(T)$

at the same temperature. The origin of this behavior is not clear since TIP3P force field used in the simulations does not display the density maximum consistent with the properties of water. The compressibility of the hydration shell is also higher for thinner shells, despite a typically higher density of the hydration water compared to the bulk.[195] This observation indicates that the network of water hydrogen bonds is broken in the hydration shell (see also below), which is more disordered than the bulk[196, 187] and has a higher compressibility.

The temperature dependence of the orientational manifold of the hydration water is distinctly different from its density. Figure 5.2c shows the dipole moment susceptibility[207] provided by equation (3.22). The dimensionless dipolar susceptibility is defined in analogy with the dielectric susceptibility of bulk dielectrics.[319] It is normalized with the average number of waters in the shell $\langle N(a)\rangle$. The temperature dependence of $\chi_M(a)$ is peculiar in two regards: (i) it violates the FDT even at high temperatures (similarly to $\lambda(T)$ in Figure 5.1), increasing with lowering temperature in contrast to the anticipated decrease, and (ii) it shows a sharp drop to nearly zero at a temperature consistent with the drop of λ at T_c (vertical dotted line in Figure 5.2c). The violation of the temperature dependence predicted by the FDT for the variance of the bulk dipole moment is displayed by many polar liquids,[9] but the temperature slope of $\chi_M(a)$ for the hydration shells far exceeds that for bulk liquids. A similar observation was previously made for the lysozyme protein,[207] and this behavior of $\chi_M(T)$ might universally apply to the protein hydration shells.

The question raised by the unusual temperature dependence of $\chi_M(T)$ is whether the hydration shell is en route to a dipolar ordered phase interrupted by the glass transition, similarly to the phenomenology found for relaxor ferroelectrics.[118] We have analyzed orientational order of the interfacial dipoles in terms of two lowest order parameters, $p_l = \langle P_l(\cos\theta)\rangle$, $l = 1, 2$, of the water dipoles forming angle θ with the

closest normal direction to the van der Waals surface of the protein[207] ($P_l(x)$ is the Legendre polynomial of order l). The preferential alignment of water molecules in the interface corresponds to their hydrogens pointing toward the protein surface (either dangling OH bonds[320, 321] or hydrogen bonds with the protein, Figure A.18). This alignment, which is further tested with a separate order parameter[322] p_{21} sensitive to dangling bonds (Fig. A.19), is enhanced when the temperature is lowered (Fig. A.17). Nevertheless, there is no distinguishable structural transition in the ordering of dipoles in the interface. Still, the free energy surfaces of electron transfer presented in Figure 5.2d indicate a bimodal behavior near T_c.

The details of the free energy calculation formalism are given in the section A.2.1. Briefly, we employ Warshel's valence-bond approach,[253, 254] in which the quantum-mechanical Hamiltonian of the heme with ligating amino acids is diagonalized at each simulation frame along the MD trajectory.[237, 171] The energies produced by diagonalizing the oxidized and reduced states of Cyt-c form the energy gap $X = \Delta E(\mathbf{q})$. The reorganization energy λ in the oxidized state is shown in Figure 5.1 and the free energy surfaces for the oxidized state of Cyt-c at different temperatures are shown in Figure 5.2d. They show a distinct shift of the minimum around T_c, with the overall shape near T_c suggestive of a bimodal distribution (similarly to Landau's free energy functionals of an order parameter[167]). In search of a possible structural transition[153] of water in the protein-water interface, we have examined the temperature effect on the distribution functions $P(Q)$ of the tetrahedral order parameter Q of hydration water.

The tetrahedral order parameter[24, 25]

$$Q = 1 - \tfrac{3}{8} \sum_{i=1}^{3} \sum_{j=i+1}^{4} \left(\cos\theta_{ij} + 1/3\right)^2 \tag{5.5}$$

is defined by the angle θ_{ij} formed by a target molecule with its four nearest neigh-

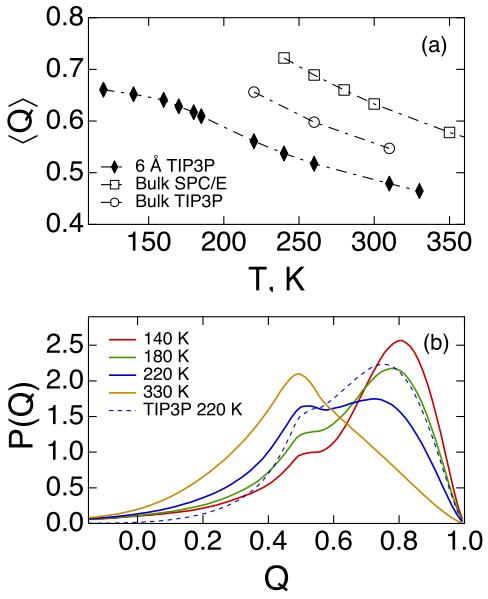

Figure 5.3: (a) $\langle Q \rangle$ vs T for the Hydration Waters within the Shell of Thickness $a = 6$ Å Around Cyt-C in the Oxidized Form (Filled Diamonds). Also Shown Are $\langle Q \rangle$-Values for Bulk SPC/E Water[23] (Open Squares) and TIP3P Water (Open Circles). (b) Distribution Functions of the Tetrahedral Order Parameter[24, 25] (Eq (5.5)) In the Hydration Shell of Oxidized Cyt-C ($a = 6$ Å) At Different Temperatures. The Dashed Line Refers to Bulk TIP3P Water.

bors i and j. Tetrahedral ice-like structure yields $\langle Q \rangle = 1$ and $\langle Q \rangle = 0$ describes the state of orientational disorder. We find that $\langle Q \rangle$ of the hydration shell increases monotonically with lowering temperature (Fig. 5.3a) in parallel to bulk SPC/E[23] and TIP3P water, but below both of them. Consistently with compressibility $\chi_N(a)$ of hydration shells (Fig. 5.2a), lower $\langle Q \rangle$ values indicate higher disorder of hydration water compared to the bulk.[196, 187] The distributions $P(Q)$ shown in Figure 5.3b rather closely follow the behavior observed in the bulk[25] (dashed line), developing a bimodal distribution consistent with more ordered hydration water at low temperatures (also see Fig. A.15). The disturbance of the tetrahedral order imposed by the protein is marginal[323] and, overall, we see little evidence of a structural transition of the hydration shell around the crossover temperature. We therefore favor the glass transition (dynamical freezing) interpretation of the crossover in both λ and χ_M. The

two-state shape of $F(X) = F_1(X)$ near the crossover temperature (Fig. 5.2d) likely reflects changes in the bimodal distribution of Q shown in Figure 5.3b.

In the glass transition scenario, thermal motions of the medium, leading to fluctuations of the electron-transfer energy gap X, become dynamically frozen when the relaxation time $\tau_X(T)$ of the collective coordinate $X(t)$ becomes comparable with the observation time $\tau_{\rm obs}$, which is the length of the simulation trajectory in our case. In turn, the relaxation time $\tau_X(T)$ is associated with the Stokes-shift dynamics[87] and is found from the corresponding Stokes-shift time correlation function $C_X(t) = \langle \delta X(t) \delta X(0) \rangle$, $\delta X(t) = X(t) - \langle X \rangle$. The nonergodic reorganization energy becomes a sum of the low-temperature component λ_f produced by fast vibrational and ballistic motions of the medium and the component λ_s related to collective medium fluctuations with the relaxation time $\tau_X(T)$. The slow component λ_s is multiplied by the nonergodicity factor accounting for dynamical freezing[93](also look at Eq. (3.17))

$$\lambda(T) = \lambda_f + (2\lambda_s/\pi) \cot^{-1} \left[\tau_X(T)/\tau_{\rm obs} \right] \tag{5.6}$$

Slow collective modes of the protein-water interface, producing $\lambda_s > \lambda_f$, are related to elastic deformations of the protein's shape. Such elastic deformations, covering a broad range of time-scales,[324] shift the positions of polar and ionized surface residues, thus resulting in a significant electrostatic noise at the protein's active site reflected by λ_s. Modeling elastic protein fluctuations does not necessarily require atomistic simulations and can be accomplished even with mechanical elastic-network models for protein fluctuations.[161] Global elastic modes shifting surface charges are coupled to polarized domains of hydration water at the protein-water interface, also enhancing the magnitude of electrostatic fluctuations. The dynamics of interfacial water, coupled to the surface residues,[184] are highly stretched[325] and involve time-scales significantly exceeding those of bulk water.[324] The interfacial electro-

statics couples to the polarizability of the heme through the electrostatic field, thus leading to a higher value of the reorganization energy.[171]

The complex dynamics of the protein-water interface are reduced in eq (5.6) to an effective Debye process. Such reduction is not always possible and complex (stretched-exponential) dynamics are required to describe ergodicity breaking of heme's iron displacements.[46] For the Debye process, relative values of $\tau_X(T)$ and $\tau_{\rm obs}$ are sufficient to account for nonergodicity. The results of MD simulations for $\tau_X(T)$ were fitted to the Arrhenius law $\tau_X = \tau_0 \exp[E_X/(k_{\rm B}T)]$ yielding $E_X/k_{\rm B} \simeq 1725$ K (Fig. A.14). This relaxation time was then used in eq (5.6) to produce the solid line in Figure 5.1 based on the low-temperature value λ_f and the high-temperature linear interpolation of the simulation points (upper dashed line in Figure 5.1). The crossover temperature $T_c \simeq 170$ K (vertical dotted line in Figure 5.1) is determined as the mean point $\lambda(T_c) = (\lambda_s + \lambda_f)/2$. We reach an overall consistency of this procedure, and the hypothesis of dynamical freezing, with the simulation data.

The data accumulated in this study present the following general picture of kinetically and energetically efficient operation of redox enzymes. The folded state of the protein, strongly coupled with the surrounding hydration water, exists in a nonergodic state similar to a quenched and ageing glass.[326] The resulting incomplete sampling of the phase space leads to a separation of the configurational effective temperature $T_{\rm eff}$ from the kinetic temperature T, eq (5.1). In contrast to bulk glass formers, where the excess of $T_{\rm eff}$ over T is very minor, this ratio can be very significant, $T_{\rm eff}/T \simeq 2-6$, when judged from $\lambda^{\rm St}$ and λ.[232, 93] The excess amplitude of fluctuations, leading to large magnitudes of λ, is provided by coupled fluctuations of the protein-water interface.[232] The time-scale of these fluctuations is on the scale from hundreds of picoseconds to nanoseconds to microseconds.[324] The Stokes-shift relaxation time follows the Arrhenius temperature dependence with the activation

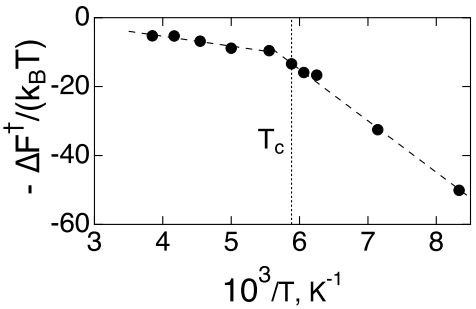

Figure 5.4: Arrhenius Plot of $-\Delta F^{\dagger}/(k_{\rm B}T)$ vs $1/T$ for the Reaction of Electrode Reduction of Cyt-C. Points Represent the Activation Barriers Calculated as $\Delta F^{\dagger} = F(0) - F(\langle X \rangle_1)$ From the Free Energy Surfaces Calculated at Different Temperatures From MD Trajectories. The Dashed Lines Are Linear Interpolations Between the Points. The Vertical Dotted Line Indicates the Crossover Temperature T_c Shown in Figure 5.1.

barrier $E_X/k_{\rm B} \simeq 2 \times 10^3$ K consistent with β-type relaxation of the protein hydration shell.[117]

Coupled protein-water fluctuations can be dynamically frozen by either choosing a reaction window τ_r significantly below τ_X, or by lowering temperature and thus driving $\tau_X(T)$ out of the observation window. The former mechanism is accomplished for fast primary reactions of bacterial photosynthesis,[301, 232] where the reaction time is $\tau_r \simeq 3 - 10$ ps. The latter mechanism is explored by us in this chapter for protein electron transfer. We have previously shown that the same mechanism applies to the dynamical transition in proteins,[75] when lowering temperature drives the dynamics of heme's iron displacements out of the observation window.[46] When the collective modes of the protein-water interface, allowing nonergodic sampling of configurations, freeze in, only fast ballistic modes of the thermal bath drive thermal fluctuations. The reaction kinetics returns at this point to the expectations of the FDT. In the framework of electron-transfer kinetics, this regime corresponds to equality of two reorganization energies, $\lambda^{\rm St} \simeq \lambda$, as we indeed observe in MD simulations (Fig. 5.1).

An observable consequence of the sharp return of the protein to the ergodic behavior at lower temperatures should be displayed as a crossover in the Arrhenius plot for

the reaction rate. This is illustrated in Figure 5.4 where we calculated the activation barrier of electron transfer as the free energy required to reach the activated state $X = 0$, $\Delta F^{\dagger} = F(0) - F(\langle X \rangle_1)$. The free energy surfaces at different temperature were obtained from MD simulations according to eq (1.33). The sharp drop of λ at T_c is accompanied by an increase in the slope of the Arrhenius plot (the activation energy vs $1/T$ is shown in Figure A.16).

Crossovers in Arrhenius plots are far from unusual for photosynthetic systems.[327, 328, 329] The earliest examples are the classical experiments by de Vault and Chance,[82] where flattening of the Arrhenius plot for electron transfer from reduced Cyt-c to the primary reaction center donor at low temperatures was reported. It is therefore important to stress that many of these reactions involve the reaction free energy, with its own temperature dependence,[232] and are often close to activationless[300] or electron-transfer inverted regimes, when intramolecular vibrations become significant, particularly at low temperatures.[288] In contrast, Figure 5.4 shows activated kinetics in the normal regime of electron transfer, not affected by quantum intramolecular vibrations and for a half (electrode) reaction with no driving force (zero overpotential for electrochemistry). The activation barrier, and its increase at lower temperatures, are solely the result of two reorganization energies in eq (5.2).

Chapter 6

SCREENING OF COULOMB INTERACTIONS IN LIQUID DIELECTRICS

This material was published in arXiv:1807.07242 (2018 Jul 19).

6.1 Summary

The interaction of charges in dielectric materials is screened by the dielectric constant of the bulk dielectric. In dielectric theories, screening is assigned to the surface charge appearing from preferential orientations of dipoles along the local field in the interface. For liquid dielectrics, such interfacial orientations are affected by the interfacial structure characterized by a separate interfacial dielectric susceptibility. We argue that dielectric properties of polar liquids should be characterized by two distinct susceptibilities responsible for local response (solvation) and long-range response (dielectric screening). We develop a microscopic model of screening showing that the standard bulk dielectric constant is responsible for screening at large distances. The potential of mean force between ions in polar liquids becomes oscillatory at short distances. Oscillations arise from the coupling of the collective longitudinal excitations of the dipoles in the bulk with the interfacial structure of the liquid around the solutes.

6.2 Introduction

The material formulation of the Coulomb law suggests that the potential energy of two charges, q_1 and q_2, placed in a dielectric material with the dielectric constant

ϵ should be determined from the equation

$$U = \frac{q_1 q_2}{\epsilon R}. \tag{6.1}$$

The dielectric is then said to screen the interaction between two charges placed at distance R, lowering the interaction energy from its vacuum value $q_1 q_2/R$ to a value ϵ times smaller. While the language of interaction energy is often used in electrostatics, U^{MF} is in fact a potential of mean force (PMF), a free energy, as is now well understood[330, 331, 332, 333, 334, 335] and will also become clear from the discussion presented below.

Dielectric screening is assigned in theories of dielectrics to the surface charge created at the dividing dielectric surface. For instance, when an ion with the charge q is introduced in the dielectric, the surface charge of an opposite sign is placed at the cavity expelled by the ion from the dielectric material (Fig. 6.1). Maxwell thought of the surface charge as the result of deformation of the entire material made of positively and negatively charged fluids neutralizing each other.[336] The external field then deforms the material by pulling and pushing the oppositely charged liquid in opposite directions and creating opposite charges at the closest dividing surface. This view might still apply to an ionic crystal, but needs revision when molecular polar materials are concerned. The current view of interfacial dielectric polarization of polar molecular materials is that molecular dipoles are oriented by the field and predominantly point their oppositely charged ends toward the external charges. Even though they move randomly by thermal agitation, a large fraction of molecules arrives at the interface oriented along the field thus producing an overall surface charge density of the sign opposite to the sign of the external charge.[337]

The mathematics build around this picture assigns the surface charge density σ to the projection of the polarization density $\mathbf{P}$ of the material onto the unit vector

$\hat{\mathbf{n}}$ normal to the dividing surface and pointing outward from the dielectric[338] :$\sigma = P_n = \hat{\mathbf{n}} \cdot \mathbf{P}$ (Fig. 6.1). The surface charge density at the cavity surrounding the charge q_1 is then $\sigma_1 = -(q_1/S)(1-\epsilon^{-1})$, where $S = 4\pi a^2$ is the surface area of the cavity with the radius a. The electrostatic potential of charge q_1 and the potential of the opposite charge distributed over the cavity surface add up to $\phi_1 = q_1/(\epsilon r)$ at any $r > a$. This electrostatic potential then interacts with the charge q_2 with the energy $U = q_2\phi_1$, thus recovering Eq. (6.1). Importantly, the electrostatic potential in the medium is a small number produced by a nearly complete compensation of two large numbers of opposite sign: the vacuum potential and the potential of the surface charges. This mathematics of the problem puts a significant demand on theoretical formulations, which should incorporate this compensatory effect before any approximations have been introduced.

This textbook consideration, and corresponding more elaborate derivations,[339] make a case for a proposal that screening of charges in the bulk of a dipolar dielectric is in fact a surface phenomenon dictated by the orientational structure of dipoles in the interface. If this assumption is correct, then the statistics of material's dipoles pointing their opposite ends to the ion cannot be determined solely by bulk properties of the material and should be a function of the interfacial structure as well. While Maxwell's notion of bulk deformation still applies to ionic lattices, the focus on the interface seems to be particularly important for liquid dielectrics which respond to inserting a solute by altering their interfacial structure, both in terms of the dipolar orientations and interfacial density. The goal of this article is to investigate physical consequences of this proposition and to develop a mathematical formalism to correct Eq. (6.1). Our focus here is on liquid dielectrics which, according to the picture of interfacial polarization, can build global dielectric screening through changes in the interfacial structure. We show below that, in agreement with standard expectations,

the bulk dielectric constant and not interfacial structure ultimately determines the long-distance screening of charges. The interfacial structure affects screening at short distances only.

The fact that the surface charge density can be significantly modified in polar liquids compared to the standard prescriptions of dielectric theories can be established by numerical simulations of microscopic interfaces. One needs, in accord with the standard rules, obtain the statistical average of normal projection of the polarization density $\langle P_n \rangle$. It can be calculated from the fluctuation relation[339, 340]

$$\langle P_n \rangle = -\beta \langle \delta P_n \delta U^C \rangle, \tag{6.2}$$

where δU^C is the fluctuation of the Coulomb interaction between the charge and the polar medium and $\beta = (k_{\mathrm{B}}T)^{-1}$ is the inverse temperature. This fluctuation formula was indeed evaluated from molecular dynamics (MD) trajectories obtained for a model nonpolar Kihara solute and corresponding solutes carrying ionic charges.[340] The result of this calculation was the effective dielectric constant of the interface $\epsilon_{\mathrm{int}} \simeq 9$ for $a = 5$ Å. The result is obviously much lower that the dielectric constant of bulk water (TIP3P water with $\epsilon \simeq 97$ in the simulations). A low value of an effective dielectric constant around $\epsilon \simeq 5$ has long been suggested to explain ionic mobility[341] and in fact was successfully used to calculate ionic activity coefficients.[342] We stress that essentially equal interface dielectric constants were found for both neutral and ionic solutes with $a = 5$ Å,[340] suggesting that ϵ_{int} lower than the bulk value can potentially apply not only to ions.

The question we address here is what is the dielectric constant that should be used in Eq. (6.1) at distances of the nanometer scale. We develop an analytical theory of microscopic screening by a polar liquid and perform molecular dynamics simulations of model solutes in SPC/E water. The main result of the proposed theory is the

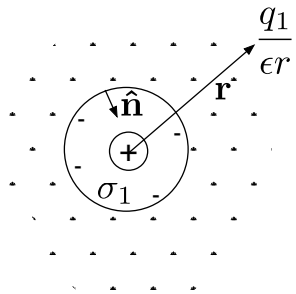

Figure 6.1: Schematic Representation of Screening of Charge q_1 by the Dielectric with the Dielectric Constant ϵ. The Electrostatic Potentials Produced by the Charge q_1 and the Oppositely Charged Surface Charge Density σ_1 Add Up to $q_1/(\epsilon r)$ Inside the Dielectric.

fluctuation relation for the screening between the charges in the dielectric and the corresponding perturbation theory formulated in terms of microscopic pair correlation functions. It casts the screening of charges by a polar liquid in terms of the structure factor of the longitudinal collective excitations of the liquid dipoles. The exact result of this consideration is the following relation

$$U(R) = \frac{q_1 q_2}{\epsilon R} - q_1 q_2 \sum_n I^{(n)}(R). \tag{6.3}$$

Here, the first summand is the standard dielectric result in Eq. (6.1). The second summand is the sum over all longitudinal collective excitations of the liquid represented by the poles of the corresponding longitudinal structure factor. These excitations of the bulk liquid dielectric are coupled to the interfacial structure of the solutes to create oscillations of the PMF around the long-distance dielectric result given by Eq. (6.1). In contrast to screening by free charges in plasmas, where plasmon excitation are quasiparticles with the lifetime significantly exceeding the oscillation period, longitudinal excitations in polar liquids (dipolarons[343, 344, 215, 345, 346]) are overdamped. The qualitative outcome of the theory is that their overall effect is represented by exponentially decaying oscillations with the decay length Λ and the oscillation wavevector $k_{\max}$ given by the first maximum of the polarization structure

factor

$$\sum_n I^{(n)}(R) \propto e^{-R/\Lambda} \cos\left(k_{\max} R\right). \tag{6.4}$$

Most simulations of the PMF between ions in solution have been performed for small ions typically used as electrolytes.[347, 333, 348] The effect of the molecular structure of water on ion pairing is clearly seen in energetic stabilization of contact and solvent-separated ion-pair configurations. The well-defined molecular structure of water around small ions is expected to alter at a nanometer cross-over length-scale,[349, 350] asymptotically approaching the structure at flat interface. While this cross-over is usually understood in terms of changes in the density profile and shell compressibility,[318] the electrostatic interfacial properties are affected as well.[351, 26] As an example of a dramatic crossover in electrostatic properties, we show in Fig. 6.2 the change of the variance of the solvent field E_s at the center of a spherical solute with the solute size. Applying the linear response approximation, one anticipates that the variance of the solvent field scales as inverse cube[351] of the solute radius R_0

$$\sigma_E^2 = \beta\sigma^3 \langle (\delta E_s)^2 \rangle_0 \propto (\sigma/R_0)^3, \tag{6.5}$$

where the solvent diameter σ is used to produce the dimensionless quantity σ_E^2. For solute radii below $\simeq 1$ nm, the molecular dynamics (MD) simulations[26] show the power law $\sigma_E^2 \propto R_0^{-\delta}$ with $\delta = 3.8$ consistent with this expectation. In contrast, there is a sharp cross-over in scaling at $R_0 \simeq 1$ nm, when the exponent changes to $\delta = 0.1$, i.e., essentially no decay of σ_E^2 with the growing solute size. These results are reported here based on previously produced trajectories[26] for Kihara solutes[352, 353] of varying size. This model solute combines a hard-sphere core with the radius $r_{\rm HS}$ with a Lennard-Jones layer of thickness σ_{0s} at the surface (see the discussion of the simulation protocol below and, in particular, the interaction potential in Eq. (6.30)). The radii reported in Fig. 6.2, $R_0 = r_{\rm HS} + \sigma_{0s}$, are altered by changing $r_{\rm HS}$.

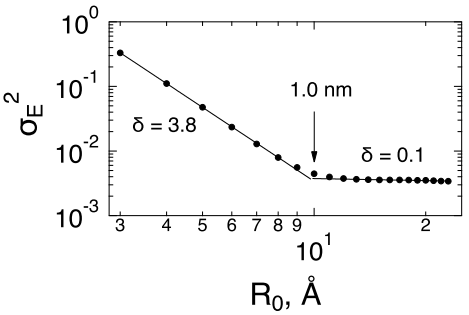

Figure 6.2: Variance of the Electric Field of SPC/E Water at the Center of a Set of Non-Polar Kihara Solutes with Varying Size R_0.The Dashed Lines Show the Fitting of the Data with the Power Law $\sigma_E^2 \propto R_0^{-\delta}$. The Resulting Values of δ for Smaller and Larger Solutes Are Indicated in the Plot. The Simulations[26] Are Done for the Kihara Solutes of Varying Size with the Solute-Solvent Interaction Energy $\epsilon_{\rm LJ} = 0.65$ kJ/mol [Eq. (6.30)].

The slowing down of the decay of the field variance with increasing solute size is caused by softening of the interface,[349] thus allowing stronger fluctuations compensating for an increased size. This crossover does not rule out further crossovers as the size of the solute increases, as we anticipate, but cannot prove with the present computational capabilities. Independently of the long-distance asymptote of σ_E^2, the appearance of a soft, fluctuating interface raises the question of its coupling with the bulk dipolaron excitations responsible for oscillations in electrostatic screening[346] [Eqs. (6.3) and (6.4)]. For small ions, screening is mostly driven by dielectric laws[331] and the structure of the hydration shell is insignificant except at the contact configuration.[333] One wonders how extending the size of the solute and changing the density of the hydration layer affect this outcome. Here we report new simulations of the Kihara solutes in SPC/E water[26] to address these questions. We study how dipolaron excitations in the bulk couple to the interfacial structure and how does this coupling affect oscillations of microscopic dielectric screening. We find that increasing density of the hydration layer, by increasing the solute-solvent attraction, significantly amplifies the PMF oscillations. On the other hand, increasing the

size of the solute, beyond the cross-over region in Fig. 6.2, reduces the oscillations amplitude and leads to a faster approach to the dielectric limit. In other words, softening of the nanometer-scale interface leads to a faster approach to the continuum limit for ionic screening.

6.3 Fluctuation Relations

We now consider two charges, q_1 and q_2, at the distance R immersed in a polar material. Each charge is represented by a repulsive sphere with the radius a defined more precisely below. The total free energy of this system of charges is the sum of their gas-phase interaction energy and the free energy of polarizing the dielectric F_s

$$F = \frac{q_1 q_2}{R} + F_s. \tag{6.6}$$

For the latter, we will use the linear response approximation.[354, 355] It allows one to represent F_s as either half of the average interaction energy between the charges and the polar medium or in terms of the variance of the interaction energy. In the latter approach, one obtains

$$F_s = -(\beta/2)\langle(\delta u_q)^2\rangle, \tag{6.7}$$

where $\delta u_q = u_q - \langle u_q\rangle$ and the interaction energy u_q between the charges and the dielectric is given in terms of the electrostatic potentials ϕ_{si} created by the dielectric at the positions of charges q_i, $i = 1, 2$

$$u_q = q_1\phi_{s1} + q_2\phi_{s2}. \tag{6.8}$$

The variance of u_q splits into self terms, representing solvation free energies of individual charges, and the cross term modifying their interaction due to the screening by the polar material. Combining the cross terms with the gas-phase interaction

energy, we obtain (Eq. (1.46)) the following formula for the screened interaction energy between the charges[356]

$$U(R) = q_1 q_2 \left[R^{-1} - \beta \langle \delta\phi_{s1} \delta\phi_{s2} \rangle \right]. \tag{6.9}$$

Equation (6.9) is the starting point for our theoretical development. We first note that in the linear response approximation the ensemble averages $\langle \dots \rangle$ in the above equations do not depend on the charge state of the ions. The averages can be taken either for the dielectric in equilibrium with the full charges q_i, or at $q_i = 0$, or for any charge state in between.[357] Previous studies[354, 355, 358, 340] have shown that this approximation is satisfied exceptionally well when the ionic radius a is sufficiently large to avoid strong interactions between the charges and the dipoles of the medium. We will assume first that this approximation holds and show below that it is indeed satisfied when tested against numerical simulations. For the rest of our discussion we put $q_1 = q_2 = e$, where e is the elementary charge.

Before we proceed to the formal theory, it is useful to anticipate the result when the standard dielectric theory applies. It is easy to see that Eq. (6.1) is recovered when one assumes for the potential cross correlation

$$\beta \langle \delta\phi_{s1} \delta\phi_{s2} \rangle = 4\pi \chi^L R^{-1}, \tag{6.10}$$

where $4\pi\chi^L = 1 - \epsilon^{-1}$ is the longitudinal susceptibility of a polar material.[215] According to the standard expectation of the theory of polar liquids,[359] spherical ions interact with the longitudinal polarization of a dipolar liquid with the susceptibility χ^L in the macroscopic limit of long-wavelength polarization excitations. The theory, therefore, must be able to produce this limit when only the long-ranged macroscopic polarization of the medium is accounted for. The formalism developed next satisfies this expectation.

6.4 Perturbation Theory

If the average $\langle \dots \rangle$ in Eq. (6.9) is treated as an ensemble average over the configurations of a polar liquid around two uncharged cavities with the radii a, the calculation of the cross correlation becomes a standard perturbation problem of liquid state theories.[360] One can write the cross correlation in terms of the solute-solvent and solvent-solvent distribution functions as follows

$$\begin{aligned} \langle \delta\phi_{s1}\delta\phi_{s2}\rangle &= \rho \int d1 \phi_{s1}(1)\phi_{s2}(1) g_{0s}(r_1) \\ &+ \rho^2 \int d1 d2 \phi_{s1}(1)\phi_{s2}(2) g_{0s}(r_1) g_{0s}(r_2) h_{ss}(1,2), \end{aligned} \tag{6.11}$$

where $\rho = N/V$ is the number density of a polar liquid and

$$\phi_s(1) = -\frac{\mathbf{m}_1 \cdot \hat{\mathbf{r}}_\mathbf{1}}{r_1^2} \tag{6.12}$$

is the electrostatic potential of liquid's dipole $\mathbf{m}_1$ at the position $\mathbf{r}_1$ in the liquid, $\hat{\mathbf{r}}_1 = \mathbf{r}_1/r_1$. The positions and orientations of the liquid dipoles are combined into single indexes such as $(1) = (\mathbf{r}, \boldsymbol{\omega}_1)$ and $d1 = d\mathbf{r}d\boldsymbol{\omega}_1/(4\pi)$. We note also that $\langle \phi_s \rangle = 0$ when no preferential orientations of liquid's dipoles is anticipated around an uncharged repulsive core of the solute. Further, the Kirkwood superposition approximation[360, 361] has been applied to the second summand in Eq. (6.11) to represent the three-particle solute-solvent-solvent distribution function as the product of the solute-solvent pair distribution function $g_{0s}(r)$ and the solvent-solvent pair correlation function $h_{ss}(12)$. The latter depends on both the distance between two molecules in the liquid r_{12} and their orientations $\boldsymbol{\omega}_1$ and $\boldsymbol{\omega}_2$.

One can use Fourier transform to re-write Eq. (6.11) in reciprocal space. The transformation to reciprocal space allows one to eliminate the space convolution in the second summand in Eq. (6.11) and present the result in terms of k-space structure factors describing collective fluctuations in the liquid. The details of the derivation

are given in the A.3.2 and the result of this derivation is the sum of two terms, $I_1(R)$ and $I_2(R)$, representing the corresponding summands in Eq. (6.11) as one-dimensional k-integrals

$$I(R) = \beta\langle\delta\phi_{s1}\delta\phi_{s2}\rangle = I_1(R) + I_2(R), \tag{6.13}$$

where

$$\begin{aligned} I_1(R) &= \frac{6y}{\pi}\int_0^\infty dk f_{0s}(k) j_0(kR) \\ I_2(R) &= \frac{6y}{\pi}\int_0^\infty dk f_{0s}(k)^2 j_0(kR)\left[S^L(k) - 1\right]. \end{aligned} \tag{6.14}$$

Here, $j_n(x)$ is the spherical Bessel function of nth order[362] and $f_{0s}(k)$ appears as a result of Fourier transforming $\phi_s(1)g_{0s}(r_1)$. It is given by the relation

$$f_{0s}(k) = k\int_0^\infty dr j_1(kr) g_{0s}(r), \tag{6.15}$$

which is a special case of the Hankel transform.[363] Further, $S^L(k)$ in Eq. (6.14) is the longitudinal structure factor of a polar liquid,[215, 364] which describes correlated fluctuation of the reciprocal-space polarization density projected on the direction of the wavevector $\hat{\mathbf{k}} = \mathbf{k}/k$

$$\tilde{P}^L(\mathbf{k}) = \sum_j (\mathbf{m}_j \cdot \hat{\mathbf{k}})\, e^{i\mathbf{k}\cdot\mathbf{r}_j}, \tag{6.16}$$

where the sum runs over all dipoles $\mathbf{m}_j$ in the liquid with their positions at $\mathbf{r}_j$. The structure factor is a scaled variance of this collective variable given as

$$S^L(k) = \frac{3}{Nm^2}\langle\tilde{P}^L(\mathbf{k})\tilde{P}^L(-\mathbf{k})\rangle. \tag{6.17}$$

The long-wavelength limit of the structure factor is related to the longitudinal susceptibility of a dielectric through the dimensionless density of dipoles in the liquid $y = (4\pi/9)\beta m^2\rho$ by the following relation

$$3yS^L(0) = 4\pi\chi^L. \tag{6.18}$$

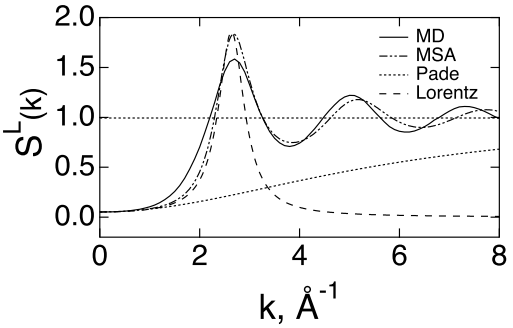

Figure 6.3: $S^L(k)$ For SPC/E Water at $T = 300$ K From Molecular Dynamics Simulations (MD)And From the MSA Solution for Dipolar Hard Spheres[27] in Eq. (6.26) (MSA). The Dotted Line Refers to the Padé Form in Eq. (6.23) ($\Lambda = 0.17$ Å) and The Dashed Line Marks the Lorentz Approximation [Eq. (6.24)]. The Horizontal Dotted Line Marks the $k \to \infty$ Limit $S^L(\infty) \to 1$.

The opposite limit of $S^L(k)$ at $k \to \infty$ corresponds to disappearance of correlations between different dipoles in the liquid, which leads to $S^L(\infty) = 1$. Both limits are illustrated in Fig. 6.3 for SPC/E water from our simulations discussed in more detail below.

Equations (6.13) and (6.14) is a formally exact solution for the electrostatic potential cross-correlation within the limits of the linear response approximation and the Kirkwood anzatz[361] for the triple solute-solvent-solvent correlation function. The first summand in Eq. (6.13), $I_1(R)$, describes fluctuations of the potential at two ions produced by rotations and translations of a single molecule in the liquid. The second term, $I_2(R)$, corresponds to correlated thermal motions of two molecules. The interaction of a liquid dipole with the first charge is propagated through the liquid dipole-dipole correlations to the second charge. The function $f_{0s}(k)$ reflects the local structure of the liquid around each solute thus coupling the screening fluctuations of the bulk with the interfacial structure. It has an important property of $f_{0s}(0) = 1$ (see below) and scales at large k as $\exp[ika]$. This latter property allows one to convert $I_i(R)$ into the residue integrals in the complex k-space. The integral $I_1(R)$ is

calculated exactly as $I_1(R) = 3y/R$ if only the pole at $k = 0$ is accounted for. The same applies to the $k = 0$ pole of $I_2(R)$. Given that we assume $R > 2a$, the $k = 0$ pole produces the result $I_2^{(0)}(R) = (3y/R)(S^L(0)-1)$. The rest of the contour integral in the complex k-space is given by residues of $S^L(k) - 1$ at complex poles k_n. The final result is

$$I(R) = R^{-1}\left(1 - \epsilon^{-1}\right) + \sum_n I^{(n)}(R). \tag{6.19}$$

This form can be substituted to Eq. (6.9) with the result for the interaction of two ions given by Eq. (6.3).

A significant advantage of the result in Eq. (6.3) is that it incorporates the cancellation of two large terms from the gas-phase Coulomb interaction of the charges and its screening by surface charges of the dielectric as the zero-order term, thus avoiding errors from incorporating approximations into each of the components. The corrections to the continuum limit arise from longitudinal collective excitations in the polar liquid coupled to the interfacial structure of each solute. This is a physically attractive picture, which might extend beyond the derivation presented here. We explore physical consequences of it in terms of an analytical solution when the poles of the longitudinal structure factor can be well defined.

Before we turn to this next step, it is useful to identify the approximations made in deriving Eq. (6.19). First, we have assumed that there is no specific orientational structure of the solvent dipoles around a nonpolar solute carrying zero charge. This is a reasonable approximation in most cases, although water dipoles attend preferential orientations around nonpolar solutes.[365] This pattern, also found for SPC/E water employed here, tends to diminish when more accurate force fields are used.[366] Second, the structure factor $S^L(k)$ in Eq. (6.14) refers to the reference system, which is the polar liquid with inserted nonpolar repulsive cores of the solutes. Since the dielectric constant is affected by solution compared to the bulk, particularly

for electrolytes,[347] the ability to use the structure factor for bulk liquid needs to be tested. We in fact have done this test in our simulations discussed below and have shown that at the concentrations used in our calculations the bulk and solution structure factors are nearly identical (Fig. A.24). We have also tested the sensitivity of the sum over the poles, the second summand in Eq. (6.19), to the dielectric constant and found it relatively low. The use of the bulk structure factor $S^L(k)$ in Eq. (6.14) is therefore justified and we now proceed to using our analytical approximation to calculate the sum over the dipolaron excitations in the liquid.

6.5 Analytical Solution

In order to study the behavior of $f_{0s}(k)$ in Eq. (6.15), we will follow here the procedure analogous to that adopted in the perturbation theory of nonpolar (Lennard-Jones) fluids. The theory of nonpolar fluids[367] starts with the observation that the Boltzmann factor, $e(r) = \exp[-\beta u(r)]$, of the intermolecular liquid potential $u(r)$ changes sharply over a short range of distances. This allows one to formulate a perturbation theory in terms of short-ranged "blip functions". Following this general framework, we consider the Boltzmann factor of the reference solute-solvent interaction potential $u_{0s}(r)$, which is mostly repulsive and is responsible for the formation of the solute cavity with the radius a. The corresponding Boltzmann function, $e_{0s}(r) = \exp[-\beta u_{0s}(r)]$, of the solute-solvent distance r, changes between zero inside the repulsive core of the solute and unity inside the liquid. Figure 6.4 shows $e_{0s}(r)$ calculated for the solute-water isotropic interaction potential given in the Kihara form[352] [Eq. (6.30)] and used in our numerical simulations discussed below. A sharp growth of $e_{0s}(r)$ implies that one can approximate its derivative by a delta-function:[361] $e'_{0s}(r) \simeq \delta(r-a)$, which also provides the definition of the cavity radius a as the position of the maximum of e'_{0s}.

We now re-write Eq. (6.15) in the form involving the derivative of the ion-liquid distribution function

$$f_{0s}(k) = \int_0^\infty dr j_0(kr) g'_{0s}(r). \tag{6.20}$$

From this equation, one gets at $k = 0$ the following boundary condition $f_{0s}(0) = g_{0s}(\infty) - g_{0s}(0) = 1$. We next note that $g_{0s}(r) = e_{0s}(r)y_{0s}(r)$, where $y_{0s}(r)$ is a smooth function.[361] One therefore can put

$$g'_{0s}(r) \simeq e'_{0s}(r)y_{0s}(r). \tag{6.21}$$

Figure 6.4 compares $e'_{0s}(r)$ with $g'_{0s}(r)$ obtained from MD simulations. One can see that $g'_{0s}(r)$ follows the shape of $e'_{0s}(r)$ at the lower value of the solute-solvent Lennard-Jones attraction energy ϵ_{LJ}, thus suggesting that $y(r)$ is nearly constant in the range of r-values where the spikes of these functions occur. As the attraction increases and the interface becomes more structured, the peak of $g'_{0s}(r)$ shifts to larger distances. Nevertheless, the approximation of $g'_{0s}(r)$ with a positive and negative blips turns out to be quite accurate for modeling $f_{0s}(k)$ at all parameters studied here.

Given that e'_{0s} involves positive and negative blips (Fig. 6.4), it can be represented by a sum of delta-functions positioned at $r = a$ and $r = b$ and carrying positive and negative amplitudes. This transforms $f_{0s}(r)$ to the form

$$f_{0s}(k) = cj_0(ka) + (1 - c)j_0(kb), \tag{6.22}$$

where b is the position of the negative blip and the coefficients in front of the spherical Bessel functions are chosen to satisfy the condition $f_{0s}(0) = 1$. The fit of this function to $f_{0s}(k)$ obtained by numerical integration in Eq. (6.20) is given in the subsection A.3.2. For our discussion here we only need to know that $f_{0s}(k)^2$ in the integral $I_2(R)$ in Eq. (6.14) scales at most as $e^{\pm 2ibk}$ and can perform the residue integration under the assumption $R > 2b$.

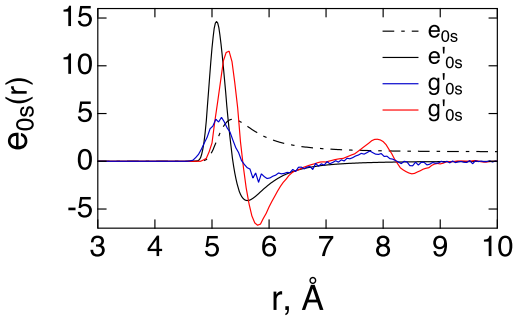

Figure 6.4: Boltzmann Factor $e_{0s}(r)$ and Its Derivative $e'_{0s}(r)$For the Kihara Potential Describing the Solute-Solvent Isotropic Interaction. $g'_{0s}(r)$Obtained From Molecular Dynamics Simulations Are Shown at $\epsilon_{\rm LJ} = 0.65$ kJ/mol (Blue) and 3.7 kJ/mol (Red). The Position of the Positive Spike of $e'_{0s}(r)$ Defines the Cavity Radius a, Which Is Very Close to $R_0 = r_{\rm HS} + \sigma_{0s} = 5$ Å for the Kihara Solutes Studied Here [Eq. (6.30)].

The positions of singularities of $S^L(k)$ in the complex k-plane are generally unknown and we resort here to two approximations. We first apply the Ornstein-Zernike approximate based on the known expansion of $S^L(k)$ at low wavevectors.[361] According to the Ornstein-Zernike equation, $S^L(k) = \left[1 + (\rho/3)c^L(k)\right]^{-1}$, where $c^L(k)$ is the direct correlation function propagating the longitudinal polarization through the liquid.[27, 361] The expansion $c^L(k)$ in powers of k results in a vanishing linear term such that $S^L(k)^{-1}$ becomes a linear function of k^2. One therefore can approximate $S^L(k)$ with the Padé form as

$$S^L(k) = \frac{S^L(0) + \Lambda^2 k^2}{1 + \Lambda^2 k^2}, \tag{6.23}$$

where $\Lambda = 0.17$ Å is found from the slope of $S^L(k)^{-1}$ vs k^2 for SPC/E water (Fig. A.25). This representation of $S^L(k)$ is not very reliable (Fig. 6.3). A better approximation can be reached in terms of the Lorenzian function with the maximum coinciding with the $k_{\rm max}$ of the simulated $S^L(k)$. Since $S^L(k)$ has to be a symmetric function of k, $S^L(k) = S^L(-k)$, the following functionality yields a more reasonable

approximation (Fig. 6.3)

$$S^L(k) = \tfrac{1}{2} S^L(0) \left[\frac{k_{\max}^2 + \kappa^2}{(k - k_{\max})^2 + \kappa^2} + \frac{k_{\max}^2 + \kappa^2}{(k + k_{\max})^2 + \kappa^2} \right] \tag{6.24}$$

This function has two poles in the upper-half k-plane: $k_1 = k_{\max} + i\kappa$ and $k_2 = -k_{\max} + i\kappa$. The sum over these poles results in

$$\begin{aligned} \sum_n I^{(n)}(R) = & \frac{k_{\max}^2 + \kappa^2}{2\kappa R} \left(1 - \frac{1}{\epsilon} \right) \\ & \operatorname{Im} \sum_{n=1,2} k_n^{-1} f_{0s}(k_n)^2 e^{iRk_n}. \end{aligned} \tag{6.25}$$

The overdamped dipolar excitations in the polar liquid produce an exponential decaying screening, not unlike the Debye-Hückel screening by plasmon excitations in electrolytes [Eq. (6.4)]. The fitting of Eq. (6.24) to the simulation data produces $k_{\max} = 2.6$ Å^{-1} and the screening length $\Lambda = \kappa^{-1} = 3.2$ Å, both consistent with the diameter of the water molecule $\sigma \simeq 2.8 - 2.9$ Å ($2\pi/k_{\max} = 2.4$ Å).

The mean-spherical approximation (MSA) for dipolar fluids[27] provides a next step for improving the analytical solution. This exact solution of the Ornstein-Zernike equation with the MSA closure yields the longitudinal structure factor in terms of the Baxter solution[368, 361] $Q(k, \xi^L)$ of the Percus-Yevick closure for the fluid of hard spheres

$$S^L(k) = \left| Q(\kappa^L k, \xi^L) \right|^{-2}. \tag{6.26}$$

Here, the longitudinal polarity parameters is found from the $k = 0$ value of the structure factor by solving the equation[27]

$$S^L(0) = \frac{(1 - 2\xi^L)^4}{(1 + 4\xi^L)^2}. \tag{6.27}$$

In addition, an empirical factor κ^L is introduced to provide the best fit of the analytical function to the results of simulations. This slight correction is required to reproduce a more open structure of water compared to closely packed simple fluids and results

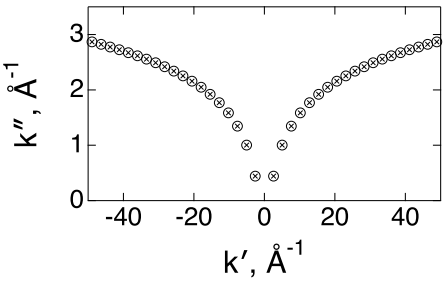

Figure 6.5: Poles $k_n = k'_n + ik''_n$ of the MSA Longitudinal Structure Factor [Eq. (6.26)] In the Upper Half-Plane of the Complex k-Plane: $\left|Q(\kappa k_n, \xi^L)\right|^2 = 0$. The Pole Closest to the Real Axis Is: $k_1 = 2.61 + 0.44i$, Å^{-1}.

in $\kappa^L = 0.85$ for SPC/E water studied here (Fig. 6.3). Similar scaling is required for other force fields of water when fitted to the Baxter function in Eq. (6.26). We found $\kappa^L = 0.95$[283] and $\kappa^L = 0.93$[280] for TIP3P[369] and SWM4-DP[370] water, respectively. The comparison of $S^L(k)$ for the SPC/E and TIP3P water models is shown in Fig. A.24.

The analytical form given by Eq. (6.26) results in a large number of poles $k_n = \pm k'_n \pm ik''_n$ in the complex k-plane (Fig. 6.5). The pole closest to the real axis has its imaginary part corresponding to the correlation length $\Lambda \simeq (k''_1)^{-1} = 2.26$ Å, reasonably close to the Lorentzian fitting. Further, the pole $I^{(n)}$ in Eq. (6.25) becomes

$$I^{(n)}(R) = \frac{6y}{R}\mathrm{Re}\left[\frac{f_{0s}(k_n)^2}{k_n c'_n}e^{ik_nR}\right], \tag{6.28}$$

where $c'_n = (\rho/3)dc^L/dk|_{k=k_n}$.

The numerical summation over the poles shown in Fig. 6.5 is compared to both the Lorentz approximation [Eq. (6.25)] and to direct integration in Fig. 6.6. The latter is done by combining the integral $I(R)$ in Eq. (6.13) and (6.14) with the Coulomb interaction energy to obtain an integral representation for the PMF

$$U(R) = \frac{6ye^2}{\pi}\int_0^\infty dk f_{0s}(k)^2 j_0(kR)\left[(3y)^{-1} - S^L(k)\right]. \tag{6.29}$$

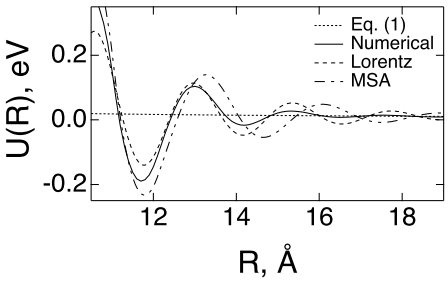

Figure 6.6: Direct Integration in Eq. (6.29) (Solid Line) Compared to the Lorentzian Approximation in Eq. (6.25) (Dashed Line) and to the Summation Over the Poles of $S^L(k)$ Produced by the MSA (Fig. 6.5) (Dash-Dotted Line).The Calculations Are Done for Two Spheres with the Radii 5 Å at Varying Distance R Between Their Centers. The Structure Factor for the SPC/E Water From Simulations (Fig. 6.3) Is Used in Numerical Integration. The Corresponding Fits to the Lorentz and the MSA Solutions Are Displayed in Fig. 6.3.The Dotted Line Shows the Dielectric Result [Eq. (6.1)].

It turns out that the simplest Lorentzian form captures the main features of the PMF, and it is even superior to the summation of poles produced by the MSA approximation. The resulting PMF shows oscillations around the continuum solution thus producing over- and under-screening at different distances due to the molecular nature of the polar liquid.[330, 331] The oscillations of the interaction energy are, however, mostly within $\sim 5 - 9k_{\mathrm{B}}T$ consistent with many previous simulations of ion pairing in force-field water.[347, 333, 348, 371] We now turn to direct MD simulations of the potential cross-correlation in Eq. (6.9).

6.6 Numerical Simulations

Numerical MD simulations employed two solutes placed in the simulation box containing 7408 SPC/E[29] water molecules. The solute-solvent interaction potential was given by the isotropic Kihara potential,[352, 353] which combines the hard-sphere repulsion characterized by the repulsion radius r_{HS} with a Lennard-Jones layer of the

thickness σ_{0s} and the attraction energy $\epsilon_{\rm LJ}$

$$u_{0s}(r) = 4\epsilon_{\rm LJ}\left[\left(\frac{\sigma_{0s}}{r - r_{\rm HS}}\right)^{12} - \left(\frac{\sigma_{0s}}{r - r_{\rm HS}}\right)^{6}\right] . \tag{6.30}$$

The MD trajectories were produced with the NAMD simulation package[172] supplemented with a separate script developed to calculate the force between the Kihara solute and SPC/E water. The parameters used for the Kihara potential in this set of simulations were $r_{\rm HS} = 2$ Å, $\sigma_{0s} = 3$ Å, and $\epsilon_{\rm LJ} = 3.7$ kJ/mol. We additionally analyzed the trajectories obtained previously,[26] which involved the variation of $r_{\rm HS}$ to produce the results shown in Fig. 6.2 and for the analysis presented below. We have also analyzed simulation data with changing solute-solvent attraction energy $\epsilon_{\rm LJ}$. Two values of this parameter, $\epsilon_{\rm LJ} = 0.65$ kJ/mol and $\epsilon_{\rm LJ} = 20$ kJ/mol, were used in the analysis. The former attraction energy is close to the interaction energy of the water molecules in the bulk, and it models a hydrophobic solute which does not produce a strong pull on the waters in the hydration shell.[353] The value $\epsilon_{\rm LJ} = 3.7$ kJ/mol mostly studied here is more consistent with a hydrophilic solute. Finally, the attraction at $\epsilon_{\rm LJ} = 20$ kJ/mol is so strong that it breaks water's structure and results in the condensation of the first hydration layer at the solute surface. The resulting layering is seen as a gap of zero solute-solvent pair distribution between the first and second hydration layers (Fig. A.22).

One of the advantages of using nonpolar solutes for the calculation of the dipolar screening is that one avoids the Coulomb interactions between the charged solutes and their images in the replicas of the simulation cell, which are unavoidable in any finite-size simulations.[332] The cross-correlations (Eq. (6.13)) were calculated at a number of configurations with the distance between two Kihara solutes altered in the range $10 \leq R \leq 20$ Å. However, the ability to use the non-ionic solutes to calculate screening between ions is based on the linear response approximation, which assumes

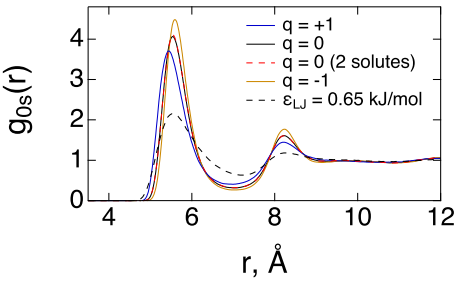

Figure 6.7: Solute-Solvent Density Distribution Functions $g_{0s}(r)$ Calculated From MD Simulations of Neutral ($q = 0$) and Charged ($q = \pm 1$) Single Kihara Solutes in SPC/E Water ($r_{\rm HS} = 2$ Å).Also Shown Is the Distribution Function for a Single Solute in the Box Containing Two Kihara Solutes Separated by the Distance of $R = 20$ Å.The Results Shown by the Solid Lines Refer to $\epsilon_{\rm LJ} = 3.7$ kJ/mol, While the Dashed Line Refers to $\epsilon_{\rm LJ} = 0.65$ kJ/mol.

that the solvent structure remains intact for all charge state of the ion, from zero charge to the highest charge considered in this framework. In order to test this assumption we have additionally simulated single Kihara solutes in SPC/E water in neutral and charged states. For the charged solutes, the charge $q = \pm 1$ was placed at the center of the Kihara sphere. Figure 6.7 shows that the pair solute-solvent distribution functions obtained for all three states are very close, in support of the linear response assumption. Further, the solute-solvent density profiles in the simulation box with two solutes are identical to single-solute distribution at sufficiently large separations between two spheres (Fig. 6.7, the two lines are identical on the scale of the plot). The solute-solvent density profile is in fact more strongly affected by the magnitude of the Lennard-Jones energy $\epsilon_{\rm LJ}$ in Eq. (6.30) than by the charge state in the range of radii considered here. The dashed line in Fig. 6.7 shows $g_{0s}(r)$ at $\epsilon_{\rm LJ} = 0.65$ kJ/mol, with a clearly less structured interface.

The results of calculations of $I(R)$ in Eq. (6.13) need to be combined with the direct Coulomb interaction in Eq. (6.9) to obtain the screened PMF. We found, in agreement with previous results,[356] that this approach leads to the $R \to \infty$ asymp-

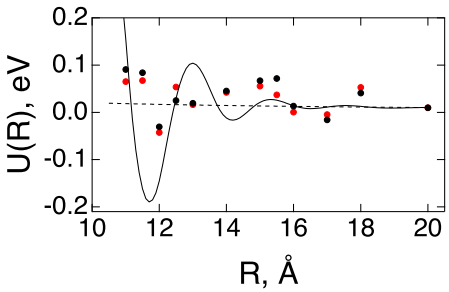

Figure 6.8: Results of MD Simulation for Two Neutral Kihara Solutes Placed at Different Distances R.Black Points Refer to Electrostatic Potential Created by Water's Partial Atomic Charges and the Red Points Indicate the Electrostaic Potential Created by the Water's Point Dipoles. The Solid Line Is the Result of Numerical Integration in Eq. (6.29)And the Dashed Line Is the Dielectric Result in Eq. (6.1).

tote shifted from zero. The reason is that the Ewald potential $\phi_{\mathrm{E}}(R)$ is shifted from the Coulomb potential.[356] The simulation results (black points in Fig. 6.8) were therefore shifted vertically to fit the analytical model (Eq. (6.29), solid line) at the largest distance studied here. We have additionally performed calculations replacing the atomic charges at the water molecules with point dipoles. These results (red points in Fig. 6.8) are very close to the charge-based calculations thus justifying the use of the dipolar density field to represent water in the analytical theory.

We next address the question of the effect of the solute size and the density of the hydration layer on the oscillatory screening behavior of the PMF. Figure 6.9 shows the calculations performed according to Eq. (6.29) with the solute-water pair distribution functions of Kihara solutes of increasing size. A clear pattern of decreasing amplitude of the screening oscillations is seen for larger solutes. The oscillations essentially disappear beyond the size crossover shown in Fig. 6.2. Increasing the density of the hydration shell produces an opposite effect. We achieve denser hydration layers by significantly increasing the solute-solvent Lennard-Jones attraction (the lower panel in Fig. 6.9). The value $\epsilon_{\mathrm{LJ}} = 20$ kJ/mol used to illustrate this point is somewhat

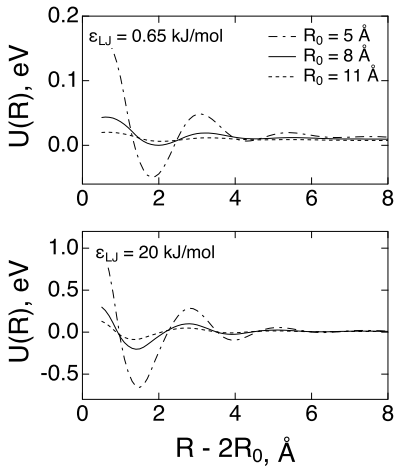

Figure 6.9: $U(R)$ From Eq. (6.29) with $S^L(k)$ for SPC/EWater and $f_{0s}(k)$ Calculated From Solute-Water Distribution Functions of Kihara Solutes with Changing Size R_0. The Results for Two Magnitudes of the Solute-Solvent Lenard-Jones Energy $\epsilon_{\rm LJ}$ Are Shown.

unrealistic, leading to a collapse of the first hydration shell and layering between the first and second shells (see examples of the solute-solvent distribution function in Fig. A.22). However, this calculation produces an about order-of-magnitude increase in the amplitude of oscillations, indicating that oscillatory pattern of screening is caused by coupling of the bulk dipolarons to the interfacial structure. Increasing the structure of the hydration shell enhances the amplitude of oscillations.

6.7 Discussion

The textbook picture of screening of electrostatic fields in dielectrics goes back to Maxwell[336] and considers a slab of dielectric placed in an external field E_0. The external field induces bulk strain leading to surface charges. They in turn produce an internal electric field E_s opposing (screening) the external field (Fig. 6.10). The Maxwell field $E = E_0 - E_s$ is the result of near cancelation between these two fields leading to E_0 reduced by ϵ. This picture silently assumes that the dielectric is a solid and can sustain bulk stress. The dielectric constant, related to material's ability to

develop this bulk stress in response to an external field, is a bulk material property.

This simple picture is bound to fail and needs to be changed for liquid dielectrics since liquids do not sustain bulk stress and any surface charge must be a surface phenomenon. Since the dielectric constant is still a bulk material property reported by the dielectric experiment, dielectric screening needs to be described in a language disconnected from surface charges. The main question here is whether polarization of the interface and the corresponding interfacial susceptibility, which enter the local polarity response (e.g., for ion solvation), are related to dielectric screening at large (on molecular scale) distances. Not unexpected, our results show that the local response of the liquid interface is mostly unrelated to the long-distance screening. The latter is achieved in liquids by mutual correlations of the liquid dipoles in the bulk and not by the field of the surface charges. The cartoon shown in Fig. 6.10 does not apply to liquid dielectrics, even at the qualitative level.

A significant consequence of this perspective is that the bulk dielectric constant reported by the dielectric experiment applies to long-distance dielectric screening, but a local interfacial susceptibility has to be used for solvation. In practical terms, polar liquids must be characterized by at least two susceptibilities describing the surface and bulk responses separately. The model solutes dissolved in the force-field water studied here provide a convincing example: their interfacial dielectric constant obtained from Eq. (6.2) is $\simeq 9$,[340] but the dielectric constant entering the long-distance screening is $\simeq 71$. The analytical theory presented here can be extended to liquids confined in the slab geometry since this extension is achieved at $R_0 \to \infty$ while keeping the thickness of the liquid between two solutes constant. The parameters of the theory still remain the same: the density distribution function of the interface and the bulk structure factor.

We find that the dielectric limit of the Coulomb law in Eq. (6.1) is reached at

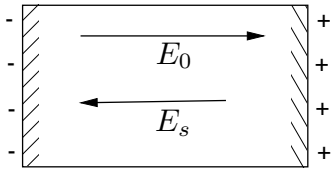

Figure 6.10: Schematics of Dielectric Screening in Solid Dielectrics: the External Field Causes a Bulk Stress in the Sample, Resulting in Surface Charges. The External Field E_0 Is Compensated by the Field of the Surface Charges E_s to Yield the Screened Maxwell Field $E = E_0 - E_s$.Liquid Dielectrics Do Not Support Bulk Stress and Corresponding Surface Charges Must Be An Interfacial Property Not Directly Related to the Bulk Dielectric Constant.

long distances between the solutes, but the granularity of the polar liquid shows itself over $\simeq 0.5 - 1$ nm into the bulk in the form of oscillations around the dielectric solution. These oscillations are linked to the overdamped excitations in the polar liquid (dipolarons[215]) represented by the poles of the longitudinal structure factor of dipolar polarization density.[372] The excitation with the longest length of decay causes the first peak of the structure factor and is mostly sufficient to reproduce the oscillatory screening calculated by numerical integration. We therefore conclude that dipolaron excitation responsible for the first peak in the structure factor is the main cause of the oscillatory dielectric screening and of the corresponding PMF in ion pairs. It is important to stress that previous reports of oscillatory PMF have been limited to small ions typically employed as supporting electrolytes.[331, 347, 333, 348] Here we show that similar oscillations develop for dielectric screening between large solutes with the diameter of $\simeq 1$ nm.

The simulation protocol employed here is based on the fluctuation relation for the dielectric screening involving the correlation of electrostatic potential produced by the polar liquid at two solutes [Eq. (6.9)]. The advantage of this formalism is that it does not require integrating the force between the solutes over distances.[348, 335] One therefore can directly calculate the screening between groups belonging to a well-defined structure (such as a protein[316]). Since the approach is based on linear

response, one has the freedom to either remove the charges from the corresponding groups or keep them if needed. Nevertheless, dielectric screening is still a challenging task for simulations since subtraction of two large terms prone to numerical errors is involved. A significant advantage of the theoretical approach summarized in Eq. (6.3) is that subtraction of two largest contributions to the PMF is achieved in the continuum limit and only microscopic corrections linked to damped dipolaron excitations need a separate calculation.

Chapter 7

CONCLUSION

In first chapter we talked about glycerol crossovers and dynamics. We saw that the thermodynamic transformation is not at work to create dipolar domains. The conclusion that no thermodynamic transformation is at work in creating dipolar domains does not make our observations less "interesting". In particular, this scenario is relevant to the role of dynamics and structure of protein's hydration shells in the protein function. About anything related to the protein structure and function has to be described as metastable. Protein itself is unstable to either hydrolysis or association, both bringing it to a thermodynamically more stable state [373]. The function of proteins as enzymes catalyzing specific biochemical reactions is even more affected by the notion of a finite "observation window" [93]. This idea implies that any dynamical or structural information related to the protein itself or to its hydration shell has to be considered from the perspective of a finite observation window provided by the reaction rate, i.e., the characteristic time on which the reactants climb the activation barrier separating them from the products. A dynamic process slower than the rate becomes dynamically frozen and does not contribute to the fluctuation spectrum of the bath driving the reaction.

The ability of the solvent to preserve a specific structure distinct from its thermodynamic state on a given observation window immediately implies that an enzymetic reaction will "see" different solvents, with potentially dramatically different properties (such as polarity), depending on the reaction rate. Figure 2.7 provides a dramatic confirmation of this possibility showing the ability of glycerol to possess a very high dielectric constant due to its inability to relax its long-range orientational correlations

on a given observation window. A related example, with a similar phenomenology, is the appearance of polarized (ferroelectric) domains in the hydration shells of proteins observed on the time-scale of simulations [207]. Similarly to our present results for glycerol, these domains might well equilibrate to zero overall dipole on longer time-scales, but a non-zero net dipole of the shell will be recorded by any kinetic process occurring faster than the domain relaxation dynamics.

Bulk glycerol studied by linear dielectric spectroscopy does not display the features indicative of domain formation. There is a general agreement that linear dielectric spectroscopy does not directly probe heterogeneity of a bulk material [6]. However, it might still be illuminating to ask why the relaxation of oriented domains in the bulk is not observed by dielectric spectroscopy. One possible answer to this is that the lifetime of a domain is smaller than its rotational relaxation time. The domains dissolve before there is a chance to probe their rotational relaxation. Increasing the lifetime of domains, as potentially achieved by surface vapor deposition [144, 143], might create conditions for observing the large dipole of the correlated domain.

The identification of the MSD crossover with the cage dynamics, in the combination with nearly identical behavior of MSD of glycerol and lysozyme-glycerol [5], puts under question the need for a special β_h relaxation process of the hydration shell [111, 112, 117] to explain these data. It appears that fast secondary relaxation of bulk glycerol (β_f in the standard classification of glass science [165, 374, 375]) is sufficient to describe the glycerol-protein system. It does not necessarily mean that the same situation repeats itself for a hydrated protein or other hydrated molecules [137], or applies equally well to the Mössbauer experiment with a much longer resolution time of $t_r \simeq 140$ ns [80]. Some experimental data indeed claim the existence of independent relaxation processes of the protein hydration shells with significantly slower relaxation times [205, 376]. The resolution of this claim, however, depends on the wa-

ter mode probed by the observations. There is a relatively insignificant slowing down of water's single-molecule rotational dynamics in hydration shells [377]. An attempt to find a separate dynamic process in density fluctuations (translations) probed by depolarized light scattering resulted in the realization that cross protein-water correlations, instead of a separate dynamic process, can explain the data [378]. However, the collective variable of the shell dipole moment can be characterized as a separate dynamic process, which is both significantly slower and is spatially extended into the bulk [379]. From a general perspective, a strong perturbation of the forces existing in the bulk is required for a new dynamic process to appear. If a significant alteration of the hydrogen-bond network is achieved in the solvation layer, one can expect a separate dynamic process to show up. The extent of such network perturbation is where the distinction between glycerol and water might be found.

The model presented in chapter 3, assigns atomic displacements in the protein to two factors: (i) high-frequency vibrations within the subunit (residue, cofactor, etc.) and (ii) fluctuations in the position of the subunit caused by thermal fluctuations of the entire protein and its hydration shell. The second component enters the observable MSF in terms of the variance of the force applied to the center of mass of the subunit (denominator in Eq. (3.1)). This equation can be alternatively viewed as softening of a stiff vibrational force constant by the protein-water thermal bath (Eq. (3.24)). Since the variance of the force depends on the observation window, softening of vibrations is achieved at the temperature above T_d allowing the long-time relaxation of the force autocorrelation function to remain within the observation window. An experimental link to this picture is provided by inelastic x-ray scattering[380, 381, 382] recording softening of the protein phonon-like modes representing global vibrations. In line with the common observations of the dynamical transition, softening of the protein phonon modes is strongly suppressed in dry samples.[381] Similar phenomenology is

provided by the temperature dependence of the protein boson peak[221, 383] reflecting the density of protein collective vibrations on the length-scale of a few nanometers and THz frequency.[384, 385, 386] For instance, the frequency of the boson peak for myoglobin falls from ~ 32 cm^{-1} to ~ 16 cm^{-1} when the temperature is raised from 170 to 295 K.[221]

The forces produced by the protein-water thermal bath at internal sites inside the protein are strongly affected by the structure and dynamics of the hydration shell.[160, 158, 159] Shell dipoles cluster in nanodomains pinned by charged surface residues. Dynamical freezing of these nanodomains occurs at the glass transition of the hydration shell corresponding to the lower crossover temperature T_g (Fig. 3.1). Rotations of water molecules in the shell dynamically freeze at this temperature. Translations dynamically freeze at a higher temperature close to T_d. Therefore, the existence of two crossover temperatures in the dynamical transition of proteins reflects two separate ergodicity breaking crossovers for rotations and translations of hydration water (Fig. 3.11).

The entrance of the relaxation time into the resolution window, resulting in the dynamical transition of a specific relaxation mode, is often considered to be a "trivial" effect, in contrast to an anticipated true structural transition.[102, 387] However, this ergodicity breaking allows protein-driven reactions to proceed without being trapped into deep solvation wells. The link between flexibility and solvation, and thus the ability to produce traps, has been under-appreciated in the literature on enzymatic activity. As an illuminating example, protein electron transfer occurs in dynamically quenched proteins where ergodicity breaking impedes the development of deep solvation traps along the electron-transport chain.

Effective (reaction) reorganization energy λ^r (eq (1.40)), combining the Stokes-shift and variance reorganization energies, controls the activation barrier of electrode

electron transfer. The resulting low activation barrier is consistent with the values obtained from cyclic voltammograms. The low value of λ^r is specific to metalloproteins in solution. Here, we have not directly simulated the protein attached to the electrode and instead applied the results for the protein solution to interfacial electron transfer.

The effect of temperature on the activation barrier is significantly reduced compared to the standard models due to the compensation of individual temperature dependencies of λ and λ^{St} in λ^r. This result implies a robust operation of the redox enzyme, little affected by the alteration of temperature.

Redox enzymes act to lower the activation barrier for electron transfer. When the reaction free energy is low, lower barrier implies minimizing the reorganization energy (eq (1.39)). It has been long anticipated that redox proteins should have evolved mechanisms to achieve this goal. However, traditional thinking in terms of a non-polar environment provided by the protein and producing low solvation energy turned out, with the help of atomistic simulations, to be inconsistent with a wet and covered with charges and polar groups environment of a typical redox site. The mechanisms which evolved in such a heterogenous environment appear to be different from the standard thinking of the Marcus model considering polarization of a homogeneous solvent in response to re-localizing the electron.

The heterogeneous protein-water thermal bath is capable of producing the spectrum of fluctuations deviating from the rules of the Gibbs ensemble by the fact of being trapped in non-equilibrium states on the time-scale of the reaction.[93] While this mechanism operates for a number of proteins, Cyt-c appears to be more stable and rigid than many other proteins, thus disallowing a large number of trap states. Polarizability of the active site is involved in this case. It achieves the same result of an intense electrostatic noise effectively lowing the barrier for electron transfer. It ap-

pears that different mechanisms are involved with different proteins, all reaching the same goal of minimizing the reaction reorganization energy through large-amplitude interfacial noise. The principle of a noisy protein-water interface, also washing out small differences in thermodynamic conditions and effects of insignificant mutations, might be a general principle by which energy chains of biology achieve low activation barriers for physiological electron transport.

The perspective presented here offers a potential explanation for the evolutionary pressure preserving large protein complexes to drive electron transport in biological energy chains. Obviously, redox chemistry can be accomplished by much smaller molecules, such as organic donor-acceptor complexes employed in photoinduced electron transfer.[304] However, the Stokes-shift dynamics of small molecules, leading to electron transfer, are extremely fast in water,[388] with most of the Stokes shift accumulated at sub-picosecond times. This is the case of $\tau_X \ll \tau_r$, when ergodic conditions are fulfilled and no rate increase due to reaction nonergodicity can be achieved. In contrast, for large protein complexes, a significant portion of the Stokes shift is associated with much longer time-scales, in the nanosecond to microsecond domain.[324] These large complexes, due to a combination of properties not fully understood and distinct from bulk glass formers,[311] allow highly nonergodic sampling of the reaction coordinate, thus leading to the configurational temperature much exceeding the kinetic temperature (eqs (5.1) and (5.3)). The interested reader can refer to author's published research[45][47][46][15][389][390][391].

[1] Paul W Fenimore, Hans Frauenfelder, BH McMahon, and RD Young. Bulk-solvent and hydration-shell fluctuations, similar to α-and β-fluctuations in glasses, control protein motions and functions. *Proceedings of the National Academy of Sciences of the United States of America*, 101(40):14408–14413, 2004.

[2] S-H Chen, Li Liu, Emiliano Fratini, Piero Baglioni, Antonio Faraone, and Eugene Mamontov. Observation of fragile-to-strong dynamic crossover in protein hydration water. *Proceedings of the National Academy of Sciences*, 103(24): 9012–9016, 2006.

[3] Arieh Warshel. Dynamics of reactions in polar solvents. Semiclassical trajectory studies of electron-transfer and proton-transfer reactions. *J. Phys. Chem.*, 86 (12):2218–2224, 1982.

[4] M. L. Horng, J. A. Gardecki, A. Papazyan, and M. Maroncelli. Subpicosecond measurements of polar solvation dynamics: Coumarin-153 revisited. *J. Phys. Chem.*, 99:17311–17337, 1995.

[5] S Capaccioli, K L Ngai, S Ancherbak, and A Paciaroni. Evidence of Coexistence of Change of Caged Dynamics at Tgand the Dynamic Transition at Tdin Solvated Proteins. *J. Phys. Chem. B*, 116(6):1745–1757, 2012.

[6] Ranko Richert. Supercooled liquids and glasses by dielectric relaxation spectroscopy. *Adv. Chem. Phys.*, 156:101–195, 2015.

[7] N. Menon, K. P. O'Brien, P. K. Dixon, L. Wu, S. R. Nagel, B. D. Williams, and J. P. Carini. Wide-frequency dielectric susceptibility measurements in glycerol. *J. Non-Crystal. Solids*, 141:61–65, 1992.

[8] Bo Chen, E E Sigmund, and W P Halperin. Stokes-Einstein Relation in Supercooled Aqueous Solutions of Glycerol. *Phys. Rev. Lett.*, 96(14):145502, 2006.

[9] D. V. Matyushov and R. Richert. Communication: Temperature derivative of the dielectric constant gives access to multipoint correlations in polar liquids. *J. Chem. Phys.*, 144:041102, 2016.

[10] E. N. Frolov, R. Gvosdev, V. I. Goldanskii, and F. G. Parak. Difference in the dynamics of oxidized and reduced cytochrome c measured by mössbauer spectroscopy. *J. Biol. Inorg. Chem.*, 2:710–713, 1997.

[11] B. M. Leu, Y. Zhang, L. Bu, J. E. Straub, J. Zhao, W. Sturhahn, E. E. Alp, and J. T. Sage. Resilience of the iron environment in heme proteins. *Biophys. J.*, 95:5874–5889, 2008.

[12] B M Leu and J T Sage. Stiffness, resilience, compressibility. *Hyperfine Interactions*, 237:87, 2016.

[13] F. G. Parak and K. Achterhold. Protein dynamics on different timescales. *J. Phys. Chem. Solids*, 66:2257–2262, 2005.

[14] A. Paciaroni, S. Cinelli, and G. Onori. Effect of environment on the protein dynamical transition: A neutron scattering study. *Biophys. J.*, 83:1157–1164, 2002.

[15] S. Seyedi, M. M. M. Waskasi, and D. V. Matyushov. Theory and electrochemistry of cytochrome *c*. *J. Phys. Chem. B*, 121:4958–4967, 2017.

[16] Hongjun Yue, D. Khoshtariya, D. H. Waldeck, J. Grochol, P. Hildebrandt, and D. H. Murgida. On the electron transfer mechanism between cytochrome *c* and metal electrodes. Evidence for dynamic control at short distances. *J. Phys. Chem. B*, 110(40):19906–19913, 2006. doi: 10.1021/jp0620670.

[17] S Terrettaz, J Cheng, and C J Miller. Kinetic parameters for cytochrome *c* via insulated electrode voltammetry. *J. Am. Chem. Soc.*, 118(33):7857–7858, 1996.

[18] J Cheng, S Terrettaz, J I Blankman, C J Miller, B Dangi, and R D Guiles. Electrochemical comparison of heme proteins by insulated electrode voltammetry. *Israel J. Chem.*, 37(2-3):259–266, 1997.

[19] T M Nahir, R A Clark, and E F Bowden. Linear-sweep voltammetry of irreversible electron transfer in surface-confined species using the Marcus theory. *Anal. Chem.*, 66(15):2595–2598, 1994.

[20] Michael J. Honeychurch. Effect of electron-transfer rate and reorganization energy on the cyclic voltammetric response of redox adsorbates. *Langmuir*, 15 (15):5158–5163, 07 1999.

[21] E. Laviron. General expression of the linear potential sweep voltammogram in the case of diffusionless electrochemical system. *J. Electroanal. Chem.*, 101: 19–28, 1979.

[22] A. J. Bard and L. R. Faulkner. *Electrochemical Methods. Fundamentals and Applications*. Wiley, New York, 1980.

[23] Cui Zhang and Giulia Galli. Dipolar correlations in liquid water. *J. Chem. Phys.*, 141(8):084504–6, 2014.

[24] P L Chau and A J Hardwick. A new order parameter for tetrahedral configurations. *Mol. Phys.*, 93(3):511–518, 1998.

[25] J. R. Errington and P. G. Debenedetti. Relationship between structural order and the anomalies of liquid water. *Nature*, 409:318–321, 2001.

[26] D. R. Martin, A. D. Friesen, and D. V. Matyushov. Electric field inside a "Rossky cavity" in uniformly polarized water. *J. Chem. Phys.*, 135:084514, 2011.

[27] M. S. Wertheim. Exact solution of the mean spherical model for fluids of hard spheres with permanent electric dipole moments. *J. Chem. Phys.*, 55:4291–4298, 1971.

[28] Masahiro Nakanishi and Alexei P Sokolov. Protein dynamics in a broad frequency range: Dielectric spectroscopy studies. *J. Non-Cryst. Solids*, 407:478–485, 2014.

[29] H. J. C. Berendsen, J. R. Grigera, and T. P. Straatsma. The missing term in effective pair potentials. *J. Phys. Chem.*, 91:6269, 1987.

[30] D. N. LeBard and D. V. Matyushov. Redox entropy of plastocyanin: Developing a microscopic view of mesoscopic solvation. *J. Chem. Phys.*, 128:155106, 2008.

[31] Albert Einstein. On the motion of small particles suspended in liquids at rest required by the molecular-kinetic theory of heat. *Annalen der physik*, 17:549–560, 1905.

[32] Rep Kubo. The fluctuation-dissipation theorem. *Reports on progress in physics*, 29(1):255.

[33] Dmitry V Matyushov. Fluctuation relations, effective temperature, and ageing of enzymes: The case of protein electron transfer. *Journal of Molecular Liquids*. "submitted".

[34] Federico Corberi, Eugenio Lippiello, and Marco Zannetti. Fluctuation dissipation relations far from equilibrium. *Journal of Statistical Mechanics: Theory and Experiment*, 2007(07):P07002, 2007.

[35] A Puglisi, A Sarracino, and A Vulpiani. Temperature in and out of equilibrium: A review of concepts, tools and attempts. *Physics Reports*, 2017.

[36] Leticia F Cugliandolo. The effective temperature. *Journal of Physics A: Mathematical and Theoretical*, 44(48):483001, 2011.

[37] SF Edwards. The role of entropy in the specification of a powder. In *Granular Matter*, pages 121–140. Springer, 1994.

[38] PC Hohenberg and Boris I Shraiman. Chaotic behavior of an extended system. *Physica D: Nonlinear Phenomena*, 37(1-3):109–115, 1989.

[39] Leticia F Cugliandolo, Jorge Kurchan, and Luca Peliti. Energy flow, partial equilibration, and effective temperatures in systems with slow dynamics. *Physical Review E*, 55(4):3898, 1997.

[40] Jean-Philippe Bouchaud. Weak ergodicity breaking and aging in disordered systems. *Journal de Physique I*, 2(9):1705–1713, 1992.

[41] Leticia F Cugliandolo and Jorge Kurchan. Analytical solution of the off-equilibrium dynamics of a long-range spin-glass model. *Physical Review Letters*, 71(1):173, 1993.

[42] Kumiko Hayashi and Mitsunori Takano. Violation of the fluctuation-dissipation theorem in a protein system. *Biophysical journal*, 93(3):895–901, 2007.

[43] A Crisanti and F Ritort. Violation of the fluctuation–dissipation theorem in glassy systems: basic notions and the numerical evidence. *Journal of Physics A: Mathematical and General*, 36(21):R181, 2003.

[44] Leticia F Cugliandolo and Jorge Kurchan. The out-of-equilibrium dynamics of the sherrington–kirkpatrick model. *Journal of Physics A: Mathematical and Theoretical*, 41(32):324018, 2008.

[45] Salman Seyedi, Daniel R Martin, and Dmitry V Matyushov. Dynamical and orientational structural crossovers in low-temperature glycerol. *Physical Review E*, 94(1):012616, 2016.

[46] S. Seyedi and D. V. Matyushov. Ergodicity breaking of iron displacement in heme proteins. *Soft Matter*, 13:8188–8201, 2017.

[47] Salman S Seyedi and Dmitry V Matyushov. Termination of biological function at low temperatures: Glass or structural transition? *The journal of physical chemistry letters*, 2018.

[48] New Jersey) L. Van Hove(Institute for Advanced Study, Prinsceton. Van-Hove_TimeSpace_Correlations.pdf. *Phys. Rev. Lett.*, 95:249–262, 1954.

[49] Gordon Leslie Squires. *Introduction to the theory of thermal neutron scattering*. Cambridge university press, 1978.

[50] H Keller and PG Debrunner. Evidence for conformational and diffusional mean square displacements in frozen aqueous solution of oxymyoglobin. *Physical Review Letters*, 45(1):68, 1980.

[51] F Parak, EW Knapp, and D Kucheida. Protein dynamics: Mössbauer spectroscopy on deoxymyoglobin crystals. *Journal of molecular biology*, 161(1): 177–194, 1982.

[52] Wolfgang Doster, Stephen Cusack, and Winfried Petry. Dynamical transition of myoglobin revealed by inelastic neutron scattering. 1989.

[53] Hans Frauenfelder, Stephen G Sligar, and Peter G Wolynes. The energy landscapes and motions of proteins. *Science*, 254(5038):1598–1603, 1991.

[54] Paul W Fenimore, Hans Frauenfelder, Benjamin H McMahon, and Fritz G Parak. Slaving: solvent fluctuations dominate protein dynamics and functions. *Proceedings of the National Academy of Sciences*, 99(25):16047–16051, 2002.

[55] Hans Frauenfelder, Guo Chen, Joel Berendzen, Paul W Fenimore, Helén Jansson, Benjamin H McMahon, Izabela R Stroe, Jan Swenson, and Robert D Young. A unified model of protein dynamics. *Proceedings of the National Academy of Sciences*, 106(13):5129–5134, 2009.

[56] Robert D Young, Hans Frauenfelder, and Paul W Fenimore. Mössbauer effect in proteins. *Physical review letters*, 107(15):158102, 2011.

[57] Salvatore Magazù, Federica Migliardo, and Antonio Benedetto. Elastic incoherent neutron scattering operating by varying instrumental energy resolution: principle, simulations, and experiments of the resolution elastic neutron scattering (rens). *Review of Scientific Instruments*, 82(10):105115, 2011.

[58] Torsten Becker, Jennifer A Hayward, John L Finney, Roy M Daniel, and Jeremy C Smith. Neutron frequency windows and the protein dynamical transition. *Biophysical journal*, 87(3):1436–1444, 2004.

[59] Salvatore Magazu, Federica Migliardo, and Antonio Benedetto. Puzzle of protein dynamical transition. *The Journal of Physical Chemistry B*, 115(24):7736–7743, 2011.

[60] Paul W Fenimore, Hans Frauenfelder, Salvatore Magazù, Benjamin H McMahon, Ferenc Mezei, Federica Migliardo, Robert D Young, and Izabela Stroe. Concepts and problems in protein dynamics. *Chemical Physics*, 424:2–6, 2013.

[61] WOLFGANG Doster, ANTON Bachleitner, RAINER Dunau, MANFRED Hiebl, and E Lüscher. Thermal properties of water in myoglobin crystals and solutions at subzero temperatures. *Biophysical journal*, 50(2):213, 1986.

[62] W Doster, S Cusack, and W Petry. Dynamic instability of liquidlike motions in a globular protein observed by inelastic neutron scattering. *Physical review letters*, 65(8):1080, 1990.

[63] Thomas Kleinert, Wolfgang Doster, Harald Leyser, Winfried Petry, Veronika Schwarz, and Marcus Settles. Solvent composition and viscosity effects on the kinetics of co binding to horse myoglobin. *Biochemistry*, 37(2):717–733, 1998.

[64] H Lichtenegger, W Doster, Th Kleinert, A Birk, B Sepiol, and G Vogl. Heme-solvent coupling: a mössbauer study of myoglobin in sucrose. *Biophysical journal*, 76(1):414–422, 1999.

[65] Wolfgang Doster and Marcus Settles. Protein–water displacement distributions. *Biochimica et Biophysica Acta (BBA)-Proteins and Proteomics*, 1749(2):173–186, 2005.

[66] Wolfgang Doster. The dynamical transition of proteins, concepts and misconceptions. *European Biophysics Journal*, 37(5):591–602, 2008.

[67] Wolfgang Doster. The protein-solvent glass transition. *Biochimica et Biophysica Acta (BBA)-Proteins and Proteomics*, 1804(1):3–14, 2010.

[68] Wolfgang Doster, Sebastian Busch, Ana M Gaspar, M-S Appavou, Joachim Wuttke, and Hugo Scheer. Dynamical transition of protein-hydration water. *Physical review letters*, 104(9):098101, 2010.

[69] Wolfgang Doster. The two-step scenario of the protein dynamical transition. *Journal of Non-Crystalline Solids*, 357(2):622–628, 2011.

[70] Wolfgang Götze. *Complex Dynamics of Glass-Forming Liquids: A Mode-Coupling Theory: A Mode-Coupling Theory*, volume 143. Oxford University Press, 2008.

[71] S-H Chen, Li Liu, Xiangqiang Chu, Yang Zhang, Emiliano Fratini, Piero Baglioni, Antonio Faraone, and Eugene Mamontov. Experimental evidence of fragile-to-strong dynamic crossover in dna hydration water. *The Journal of chemical physics*, 125(17):171103, 2006.

[72] Xiang-qiang Chu, Emiliano Fratini, Piero Baglioni, Antonio Faraone, and Sow-Hsin Chen. Observation of a dynamic crossover in rna hydration water which triggers a dynamic transition in the biopolymer. *Physical Review E*, 77(1): 011908, 2008.

[73] Pradeep Kumar, Z Yan, L Xu, MG Mazza, SV Buldyrev, S-H Chen, S Sastry, and HE Stanley. Glass transition in biomolecules and the liquid-liquid critical point of water. *Physical review letters*, 97(17):177802, 2006.

[74] SH Chen, C Liao, F Sciortino, P Gallo, and P Tartaglia. Model for single-particle dynamics in supercooled water. *Physical Review E*, 59(6):6708, 1999.

[75] F. Parak and H. Formanek. Untersuchung des schwingungsanteils und des kristallgitterfehleranteils des temperaturfaktors in myoglobin durch vergleich von miissbauerabsorptionsmessungen mit riintgenstrukturdaten. *Acta Crystallogr. A*, 27:573, 1971.

[76] R. A. Marcus and N. Sutin. Electron transfer in chemistry and biology. *Biochim. Biophys. Acta*, 811:265–322, 1985.

[77] C. C. Page, C. C. Moser, X. X. Chen, and P. L. Dutton. Natural engineering principles of electron tunneling in biological oxidation-reduction. *Nature*, 402: 47–52, 1999.

[78] H. B. Gray and J. R. Winkler. Long-range electron transfer. *Proc. Natl. Acad. Sci.*, 102:3534–3539, 2005.

[79] D. G. Nicholls and S. J. Ferguson. *Bioenergetics 3*. Academic Press, London, 2002.

[80] F. G. Parak. Physical aspects of protein dynamics. *Rep. Prog. Phys.*, 66:103–129, 2003.

[81] Spiros S. Skourtis, David H. Waldeck, and David N. Beratan. Fluctuations in biological and bioinspired electron-transfer reactions. *Annu. Rev. Phys. Chem.*, 61(1):461–485, 2010. doi: 10.1146/annurev.physchem.012809.103436.

[82] D. de Vault and B. Chance. Studies of phosynthesis using a pulsed laser. i. Temperature dependence of cytochrome oxidation rate in Chromatium. Evidence for tunneling. *Biophys. J.*, 6:825, 1966.

[83] R. A. Kuharski, J. S. Bader, D. Chandler, M. Sprik, M. L. Klein, and R. W. Impey. Molecular model for aqueous ferrous-ferric electron transfer. *J. Chem. Phys.*, 89:3248–3257, 1988.

[84] D. W. Small, D. V. Matyushov, and G. A. Voth. The theory of electron transfer: What may be missing? *J. Am. Chem. Soc.*, 125:7470–7478, 2003.

[85] J. Blumberger and M. Sprik. Quantum vs classical electron transfer energy as reaction coordinate for the aqueous Ru^{2+}/Ru^{3+} redox reaction. *Theor. Chem. Acc.*, 115:113–126, 2006.

[86] R. A. Marcus. Relation between charge transfer absorption and fluorescence spectra and the inverted region. *J. Phys. Chem.*, 93:3078–3086, 1989.

[87] L. Reynolds, J. A. Gardecki, S. J. V. Frankland, and M. Maroncelli. Dipole solvation in nondipolar solvents: Experimental studies of reorganization energies and solvation dynamics. *J. Phys. Chem.*, 100:10337–10354, 1996.

[88] Morteza M Waskasi, Marshall D Newton, and Dmitry V Matyushov. Impact of temperature and non-gaussian statistics on electron transfer in donor–bridge–acceptor molecules. *The Journal of Physical Chemistry B*, 121(12):2665–2676, 2017.

[89] T Simonson. Electrostatics and dynamics of proteins. *Reports on Progress in Physics*, 66:737–787, 2003.

[90] D. V. Matyushov. Protein electron transfer: Dynamics and statistics. *J. Chem. Phys.*, 139:025102, 2013.

[91] S. Mukamel. *Principles of Nonlinear Optical Spectroscopy.* Oxford University Press, New York, 1995.

[92] R. Kubo. The fluctuation-dissipation theorem. *Rep. Prog. Phys.*, 29:255–284, 1966.

[93] Dmitry V Matyushov. Protein electron transfer: is biology (thermo)dynamic? *J. Phys.: Condens. Matter*, 27(47):473001, 2015.

[94] Marc T M Koper. Combining experiment and theory for understanding electrocatalysis. *J. Electroanal. Chem.*, 574(2):375–386, 2005.

[95] J. P. Hansen and I. R. McDonald. *Theory of Simple Liquids.* Academic Press, Amsterdam, 2003.

[96] F. Gabel, D. Bicout, U. Lehnert, M. Tehei, M. Weik, and G Zaccai. Protein dynamics studied by neutron scattering. *Quat. Rev. Biophys.*, 35:327–367, 2002.

[97] Robert D. Young, Hans Frauenfelder, and Paul W. Fenimore. Mössbauer effect in proteins. *Phys. Rev. Lett.*, 107:158102–, 10 2011.

[98] C. A. Angell. Formation of glasses from liquids and biopolymers. *Science*, 267: 1924–1935, 1995.

[99] J H Roh, V N Novikov, R B Gregory, J E Curtis, Z Chowdhuri, and A P Sokolov. Onsets of Anharmonicity in Protein Dynamics. *Phys. Rev. Lett.*, 95 (3):038101, 2005.

[100] S. Khodadadi, A. Malkovskiy, A. Kisliuk, and A. P. Sokolov. A broad glass transition in hydrated proteins. *Biochim. Biophys. Acta*, 1804:15–19, 2010.

[101] Liang Hong, Nikolai Smolin, Benjamin Lindner, Alexei P. Sokolov, and Jeremy C. Smith. Three classes of motion in the dynamic neutron-scattering susceptibility of a globular protein. *Phys. Rev. Lett.*, 107(14):148102, 2011.

[102] W. Doster, S. Cusack, and W. Petry. Dynamic transition of myoglobin revealed by inelastic neutron scattering. *Nature*, 337:754, 1989.

[103] G. Zaccai. How soft is a protein? a protein dynamics force constant measured by neutron scattering. *Science*, 288:1604–1607, 2000.

[104] K. Achterhold, C. Keppler, A. Ostermann, U. van Bürck, W. Sturhahn, E. E. Alp, and F. G. Parak. Vibrational dynamics of myoglobin determined by the phonon-assisted Mössbauer effect. *Phys. Rev. E*, 65:051916, 2002.

[105] W. Doster. The dynamical transition of proteins, concepts and misconceptions. *Eur. Biophys. J.*, 37:591, 2008.

[106] Salvatore Magazù, Federica Migliardo, and Antonio Benedetto. Puzzle of Protein Dynamical Transition. *J. Phys. Chem. B*, 115:7736–7743, 2011.

[107] Paul W Fenimore, Hans Frauenfelder, Salvatore Magazù, Benjamin H McMahon, Ferenc Mezei, Federica Migliardo, Robert D Young, and Izabela Stroe. Concepts and problems in protein dynamics. *Chem. Phys.*, 424:2–6, 2013.

[108] Giorgio Schirò, Yann Fichou, François-Xavier Gallat, Kathleen Wood, Frank Gabel, Martine Moulin, Michael Härtlein, Matthias Heyden, Jacques-Philippe Colletier, Andrea Orecchini, Alessandro Paciaroni, Joachim Wuttke, Douglas J Tobias, and Martin Weik. Translational diffusion of hydration water correlates with functional motions in folded and intrinsically disordered proteins. *Nat. Comm.*, 6:6490, 2015.

[109] J. C. Smith. Protein dynamics: comparison of simulations with inelastic neutron scattering experiments. *Quat. Rev. Biophys.*, 24:227, 1991.

[110] G. Zaccai. Proteins as nano-machines: dynamics–function relations studied by neutron scattering. *J. Phys.: Condens. Matter*, 15:S1673–S1682, 2003.

[111] P. W. Fenimore, H. Frauenfelder, B. H. McMahon, and R. D. Young. Bulk-solvent and hydration-shell fluctuations, similar to α and β-fluctuations in glasses, control protein motion and functions. *Proc. Natl. Acad. Sci. USA*, 101:14408–14413, 2004.

[112] Vassiliy Lubchenko, Peter G Wolynes, and Hans Frauenfelder. Mosaic Energy Landscapes of Liquids and the Control of Protein Conformational Dynamics by Glass-Forming Solvents. *J. Phys. Chem. B*, 109(15):7488–7499, 2005.

[113] C. A. Angell, K. L. Ngai, G. B. McKenna, and S. W. Martin. Relaxation in glassforming liquids and amorphous solids. *J. Appl. Phys.*, 88:3113, 2000.

[114] E. Donth. *The Glass Transition: Relaxation Dynamics in Liquids and Disordered Materials*. Springer, Berlin, 2001.

[115] G. Chen, P. W. Fenimore, H. Frauenfelder, F. Mezei, J. Swenson, and R. D. Young. Protein fluctuations explored by inelastic neutron scattering and dielectric spectroscopy. *Phil. Mag.*, 88:33, 2008.

[116] S. Khodadadi, S. Pawlus, J. H. Roh, V. Garcia Sakai, E. Mamontov, and A. P. Sokolov. The origin of the dynamic transition in proteins. *J. Chem. Phys.*, 128 (19):195106, 2008.

[117] H. Frauenfelder, G. Chen, J. Berendzen, P. W. Fenimore, H. Jansson, B. H. McMahon, I. R. Stroe, J. Swenson, and R. D. Young. A unified model of protein dynamics. *Proc. Natl. Acad. Sci. USA*, 106:5129–5134, 2009.

[118] G. A. Samara. The relaxational properties of compositionally disordered abo_3 porovsketes. *J. Phys.: Condens. Matter*, 15:R367–R411, 2003.

[119] J. Wuttke, W Petry, G. Coddens, and F Fujara. Fast dynamics of glass-forming glycerol. *Phys. Rev. E*, 52(4):4026–4034, 1995.

[120] W Doster, M Diehl, R Gebhardt, R E Lechner, and J Pieper. TOF-elastic resolution spectroscopy: time domain analysis of weakly scattering (biological) samples. *Chem. Phys.*, 292(2-3):487–494, 2003.

[121] Zheng Yi, Yinglong Miao, Jerome Baudry, Nitin Jain, and Jeremy C Smith. Derivation of Mean-Square Displacements for Protein Dynamics from Elastic Incoherent Neutron Scattering. *J. Phys. Chem. B*, 116(16):5028–5036, 2012.

[122] Giorgio Schirò, Francesca Natali, and Antonio Cupane. Physical Origin of Anharmonic Dynamics in Proteins: New Insights From Resolution-Dependent Neutron Scattering on Homomeric Polypeptides. *Phys. Rev. Lett.*, 109(12): 128102, 2012.

[123] Carl Caleman, Paul J van Maaren, Minyan Hong, Jochen S Hub, Luciano T Costa, and David van der Spoel. Force Field Benchmark of Organic Liquids: Density, Enthalpy of Vaporization, Heat Capacities, Surface Tension, Isothermal Compressibility, Volumetric Expansion Coefficient, and Dielectric Constant. *J. Chem. Theory Comp.*, 8(1):61–74, 2012.

[124] J. Teixeira, M.-C. Bellissent-Funel, S. H. Chen, and A. J. Dianoux. Experimental determination of the nature of diffusive motions of water molecules at low temperatures. *Phys. Rev. A*, 31(3):1913–1917, 1985.

[125] S H Chen, P Gallo, F Sciortino, and P Tartaglia. Molecular-dynamics study of incoherent quasielastic neutron-scattering spectra of supercooled water. *Phys. Rev. E*, 56:4231–4243, 1997.

[126] Li Liu, Antonio Faraone, and Sow-Hsin Chen. Model for the rotational contribution to quasielastic neutron scattering spectra from supercooled water. *Phys. Rev. E*, 65(4):041506, 2002.

[127] S H Chen, C Liao, F Sciortino, P Gallo, and P Tartaglia. Model for single-particle dynamics in supercooled water. *Phys. Rev. E*, 59(6):6708–6714, 1999.

[128] L. Liu, S.-H. Chen, A. Faraone, C.-W. Yen, and C.-Y. Mou. Pressure dependence of fragile-to-strong transition and possible second critical point in supercooled confined water. *Phys. Rev. Lett.*, 95:117802, 2005.

[129] Eugene Mamontov. Diffusion in confinement as a microscopic relaxation mechanism in glass-forming liquids. *Chem. Phys. Lett.*, 530:55–60, 3 2012.

[130] Margarita Fomina, Giorgio Schirò, and Antonio Cupane. Hydration dependence of myoglobin dynamics studied with elastic neutron scattering, differential scanning calorimetry and broadband dielectric spectroscopy. *Biophysical Chemistry*, 185:25–31, 2014.

[131] S.-H. Chen, L. Liu, E. Fratini, P. Baglioni, and E. Mamontov. Observation of fragile-to-strong dynamic crossover in protein hydration water. *Proc. Natl. Acad. Sci.*, 103:9012–9016, 2006.

[132] J.-M. Zanotti, M.-C. Bellissent-Funel, and S.-H. Chen. Experimental evidence of a liquid-liquid transition in interfacial water. *Europhys. Lett.*, 71:91, 2005.

[133] Antonio Cupane, Margarita Fomina, Irina Piazza, Judith Peters, and Giorgio Schirò. Experimental Evidence for a Liquid-Liquid Crossover in Deeply Cooled Confined Water. *Phys. Rev. Lett.*, 113(21):215701, 2014.

[134] Giorgio Schirò, Margarita Fomina, and Antonio Cupane. Communication: Protein dynamical transition vs. liquid-liquid phase transition in protein hydration water. *J. Chem. Phys.*, 139(12):121102, 2013.

[135] Francesco Mallamace, Carmelo Corsaro, Domenico Mallamace, Sebastiano Vasi, Cirino Vasi, H Eugene Stanley, and Sow-Hsin Chen. Some thermodynamical aspects of protein hydration water. *J. Chem. Phys.*, 142(21):215103, 2015.

[136] F. Mallamace, M. Broccio, C. Corsaro, A. Faraone, U. Wanderlingh, L. Liu, C.-Y. Mou, and S. H. Chen. The fragile-to-strong dynamic crossover transition in confined water: nuclear magnetic resonance results. *J. Chem. Phys.*, 124: 161102, 2006.

[137] Marion Jasnin, Lambert van Eijck, Michael Marek Koza, Judith Peters, Cedric Laguri, Hugues Lortat-Jacob, and Giuseppe Zaccai. Dynamics of heparan sulfate explored by neutron scattering. *Phys. Chem. Chem. Phys.*, 12(14):3360–3362, 2010.

[138] H. Fröhlich. *Theory of dielectrics*. Oxford University Press, Oxford, 1958.

[139] G. J. Cuello, F J Bermejo, R Fayos, R Fernandez-Perea, A Criado, F Trouw, C Tam, H Schober, E Enciso, and N G Almarza. Anharmonic dynamics in crystalline, glassy, and supercooled-liquid glycerol: A case study on the onset of relaxational behavior. *Phys. Rev. B*, 57(14):8254–8263, 1998.

[140] D. V. Matyushov and C. A. Angell. Gaussian excitations model for glass-former dynamics and thermodynamics. *J. Chem. Phys.*, 126:094501, 2007.

[141] G. Ayton and G. N. Patey. Ferroelectric order in model discotic nematic liquid crystals. *Phys. Rev. Lett.*, 76:239, 1996.

[142] G. Vertogen and W. H. de Jeu. *Thermotropic Liquid Cristals, Fundamentals*. Springer-Verlag, Berlin, 1988.

[143] A Kasina, T Putzeys, and M Wübbenhorst. Dielectric and specific heat relaxations in vapor deposited glycerol. *J. Chem. Phys.*, 143(24):244504, 2015.

[144] Simona Capponi, Simone Napolitano, and Michael Wübbenhorst. Supercooled liquids with enhanced orientational order. *Nat. Comm.*, 3:1233, 2012.

[145] Shakeel S Dalal, Diane M Walters, Ivan Lyubimov, Juan J de Pablo, and M D Ediger. Tunable molecular orientation and elevated thermal stability of vapor-deposited organic semiconductors. *Proc. Natl. Acad. Sci. USA*, 112(14):4227–4232, 2015.

[146] Ludovic Berthier and Giulio Biroli. Theoretical perspective on the glass transition and amorphous materials. *Rev. Mod. Phys.*, 83(2):587–645, 2011.

[147] Hans Frauenfelder, Stephen G. Sligar, and Peter G. Wolynes. The energy landscapes and motions of proteins. *Science*, 254:1598–1603, 1991.

[148] S. W. Lovesey. *Theory of neutron scattering from condensed matter*, volume 1. Clarendon Press, Oxford, 1984.

[149] Torsten Becker and Jeremy C Smith. Energy resolution and dynamical heterogeneity effects on elastic incoherent neutron scattering from molecular systems. *Phys. Rev. E*, 67(2):558–8, 2003.

[150] H. Frauenfelder, F. Parak, and R. D. Young. Conformational substates in proteins. *Ann. Rev. Biophys. Biophys. Chem.*, 17:451, 1998.

[151] W. Doster. The protein-solvent glass transition. *Biochim. Biophys. Acta*, 1804: 3–14, 2010.

[152] K L Ngai, S Capaccioli, and A Paciaroni. Dynamics of hydrated proteins and bio-protectants: Caged dynamics, β-relaxation, and α-relaxation. *Biochim. Biophys. Acta (BBA) - General Subjects*, 1861(1):3553–3563, 2017.

[153] G Schirò and A Cupane. Anharmonic activations in proteins and peptide model systems and their connection with supercooled water thermodynamics. *Il Nuovo Cimento*, 39 C(3):305, 2016.

[154] Marie-Claire Bellissent-Funel, Ali Hassanali, Martina Havenith, Richard Henchman, Peter Pohl, Fabio Sterpone, David van der Spoel, Yao Xu, and Angel E García. Water determines the structure and dynamics of proteins. *Chem. Rev.*, 116(13):7673–7697, 2016.

[155] K L Ngai, S Capaccioli, and A Paciaroni. Change of caged dynamics at Tgin hydrated proteins: Trend of mean squared displacements after correcting for the methyl-group rotation contribution. *J. Chem. Phys.*, 138(23):235102–15, 2013.

[156] S Magazu, F Mezei, P Falus, B Farago, E Mamontov, M Russina, and Federica Migliardo. Protein dynamics as seen by (quasi) elastic neutron scattering. *Biochim. Biophys. Acta (BBA) - General Subjects*, 1861(1):3504–3512, 2017.

[157] Liang Hong, Dennis C Glass, Jonathan D Nickels, Stefania Perticaroli, Zheng Yi, Madhusudan Tyagi, Hugh O'Neill, Qiu Zhang, Alexei P Sokolov, and Jeremy C Smith. Elastic and Conformational Softness of a Globular Protein. *Phys. Rev. Lett.*, 110(2):028104–5, 2013.

[158] Liang Hong, Xiaolin Cheng, Dennis C Glass, and Jeremy C Smith. Surface Hydration Amplifies Single-Well Protein Atom Diffusion Propagating into the Macromolecular Core. *Phys. Rev. Lett.*, 108(23):238102–4, 2012.

[159] Kathleen Wood, François-Xavier Gallat, Renee Otten, Auke J van Heel, Mathilde Lethier, Lambert van Eijck, Martine Moulin, Michael Haertlein, Martin Weik, and Frans A A Mulder. Protein Surface and Core Dynamics Show Concerted Hydration-Dependent Activation. *Angew. Chem. Int. Ed.*, 52(2): 665–668, 2012.

[160] D. V. Matyushov and A. Y. Morozov. Electrostatics of the protein-water interface and the dynamical transition in proteins. *Phys. Rev. E*, 84:011908, 2011.

[161] D. R. Martin and D. V. Matyushov. Solvent-renormalized dissipative electroelastic network model of hydrated proteins. *J. Chem. Phys.*, 137:165101, 2012.

[162] Torsten Becker, Jennifer A Hayward, John L Finney, Roy M Daniel, and Jeremy C Smith. Neutron Frequency Windows and the Protein Dynamical Transition. *Biophys. J.*, 87(3):1436–1444, 2004.

[163] K L Ngai, S Capaccioli, S Ancherbak, and N Shinyashiki. Resolving the ambiguity of the dynamics of water and clarifying its role in hydrated proteins. *Phil. Mag.*, 91(13-15):1809–1835, 2011.

[164] D. V. Matyushov. Nanosecond Stokes shift dynamics, dynamical transition, and gigantic reorganization energy of hydrated heme proteins. *J. Phys. Chem. B*, 115:10715–10724, 2011.

[165] M. D. Ediger, C. A. Angell, and S. R. Nagel. Supercooled liquids and glasses. *J. Phys. Chem.*, 100:13200, 1996.

[166] S Khodadadi and A P Sokolov. Protein dynamics: from rattling in a cage to structural relaxation. *Soft Matter*, 11(25):4984–4998, 2015.

[167] L. D. Landau and E. M. Lifshits. *Statistical Physics*. Pergamon Press, New York, 1980.

[168] R. G. Palmer. Broken ergodicity. *Adv. Phys.*, 31:669–735, 1982.

[169] Andrea Crisanti and Felix Ritort. Violation of the fluctuation–dissipation theorem in glassy systems: basic notions and the numerical evidence. *J. Phys. A: Math. Gen.*, 36:R181–290, 2003.

[170] J T Sage, C Paxson, G R A Wyllie, W Sturhahn, S M Durbin, P M Champion, E E Alp, and W R Scheidt. Nuclear resonance vibrational spectroscopy of a protein active-site mimic. *J. Phys.: Cond. Matter*, 13(3):7707–7722, 2001.

[171] M. Dinpajooh, D. R. Martin, and D. V. Matyushov. Polarizability of the active site of cytochrome *c* reduces the activation barrier for electron transfer. *Sci. Rep.*, 6:28152, 2016.

[172] James C. Phillips, Rosemary Braun, Wei Wang, James Gumbart, Emad Tajkhorshid, Elizabeth Villa, Christophe Chipot, Robert D. Skeel, Laxmikant Kalé, and Klaus Schulten. Scalable molecular dynamics with NAMD. *J. Comput. Chem.*, 26(16):1781–1802, 2005. doi: 10.1002/jcc.20289.

[173] T. Springer. *Dynamics of solids and liquids by neutron scattering*, volume 3. Spriner, Berlin, 1977.

[174] J Swenson and S. Cerveny. Dynamics of deeply supercooled interfacial water. *J. Phys.: Condens. Matter*, 27(3):033102, 2014.

[175] M Vogel. Origins of Apparent Fragile-to-Strong Transitions of Protein Hydration Waters. *Phys. Rev. Lett.*, 101(22):225701, 2008.

[176] Amine Dehaoui, Bruno Issenmann, and Frédéric Caupin. Viscosity of deeply supercooled water and its coupling to molecular diffusion. *Proc. Natl. Acad. Sci. U.S.A.*, 112(39):12020–12025, September 2015.

[177] Corey W Meadows, Ryan Ou, and Judith P Klinman. Picosecond-Resolved Fluorescent Probes at Functionally Distinct Tryptophans within a Thermophilic Alcohol Dehydrogenase: Relationship of Temperature-Dependent Changes in Fluorescence to Catalysis. *J. Phys. Chem. B*, 118(23):6049–6061, 2014.

[178] Yangzhong Qin, Luyuan Zhang, Lijuan Wang, and Dongping Zhong. Observation of the Global Dynamic Collectivity of a Hydration Shell around Apomyoglobin. *J. Phys. Chem. Lett.*, 8(6):1124–1131, 2017.

[179] P. W. Fenimore, H. Frauenfelder, B. H. McMahon, and F. G. Parak. Slaving: Solvent fluctuations dominate protein dynamics and functions. *Proc. Natl. Acad. Sci.*, 99:16047–16051, 2002.

[180] Alan Cooper. Protein fluctuations and the thermodynamic uncertainty principle. *Prog. Biophys. Molec. Biol.*, 44(3):181–214, 1984.

[181] Sheila Khodadadi and Alexei P Sokolov. Atomistic details of protein dynamics and the role of hydration water. *Biochim. Biophys. Acta (BBA) - General Subjects*, 1861(1):3546–3552, 2017.

[182] S. Khodadadi, J. H. Roh, A. Kisliuk, E. Mamontov, M. Tyagi, S. A. Woodson, R. M. Briber, and A. P. Sokolov. Dynamics of biological macromolecules: Not a simple slaving by hydration water. *Biophys. J.*, 98:1321–1326, 2010.

[183] T. Li, A.A. Hassanali, Y.-T. Kao, D. Zhong, and S.J. Singer. Hydration dynamics and time scales of coupled water-protein fluctuations. *J. Am. Chem. Soc.*, 129(11):3376–3382, 2007.

[184] B. Halle and L. Nilsson. Does the dynamic stokes shift report on slow protein dynamics? *J. Phys. Chem. B*, 113:8210–8213, 2009.

[185] K E Furse and S A Corcelli. Molecular dynamics simulations of DNA solvation dynamics. *J. Phys. Chem. Lett.*, 1(12):1813–1820, 2010.

[186] D. R. Martin and D. V. Matyushov. Non-Gaussian statistics and nanosecond dynamics of electrostatic fluctuations affecting optical transitions in a green fluorescent protein. *J. Phys. Chem. B*, 116:10294–10300, 2012.

[187] Valeria Conti Nibali, Giovanna D'Angelo, Alessandro Paciaroni, Douglas J Tobias, and Mounir Tarek. On the coupling between the collective dynamics of proteins and their hydration water. *J. Phys. Chem. Lett.*, 5(7):1181–1186, 2014.

[188] Antonio Benedetto. Protein and hydration-water dynamics are decoupled: A new model connecting dynamics and biochemical function is required. *arXiv.org*, page arXiv:1705.03128, May 2017.

[189] Jonathan D Nickels, Victoria Garcia-Sakai, and Alexei P Sokolov. Dynamics in protein powders on the nanosecond–picosecond time scale are dominated by localized motions. *J. Phys. Chem. B*, 117(39):11548–11555, 2013.

[190] Jean-Marc Zanotti, Marie-Claire Bellissent-Funel, and Joseph Parello. Hydration-Coupled Dynamics in Proteins Studied by Neutron Scattering and NMR: The Case of the Typical EF-Hand Calcium-Binding Parvalbumin. *Biophys. J.*, 76(5):2390–2411, 1999.

[191] D. V. Matyushov. Configurational entropy of polar glass formers and the effect of electric field on glass transition. *J. Chem. Phys.*, 145:034504, 2016.

[192] B Kabtoul, R J Jiménez-Riobóo, and M A Ramos. Thermal and acoustic experiments on polymorphic ethanol. *Phil. Mag.*, 88(33-35):4197–4203, 2008.

[193] R. Richert and A. C. Angell. Dynamics of glass-forming liquids. V. On the link between molecular dynamics and configuration entropy. *J. Chem. Phys.*, 108: 9016, 1998.

[194] M Gerstein and C Chothia. Packing at the protein-water interface. *Proc. Natl. Acad. Sci. USA*, 93:10167–10172, 1996.

[195] D. I. Svergun, S. Richard, M. H. J. Koch, Z. Sayers, S. Kuprin, and G. Zaccai. Protein hydration in solution: Experimental observation by x-ray and neutron scattering. *Proc. Natl. Acad. Sci.*, 95:2267–2272, 1998.

[196] Adrien Lerbret, Alain Hédoux, Burkhard Annighöfer, and Marie-Claire Bellissent-Funel. Influence of pressure on the low-frequency vibrational modes of lysozyme and water: A complementary inelastic neutron scattering and molecular dynamics simulation study. *Proteins: Structure, Function, and Bioinformatics*, 81(2):326–340, 2012.

[197] J M Zanotti, M C Bellissent-Funel, and A I Kolesnikov. Phase transitions of interfacial water at 165 and 240K. Connections to bulk water physics and protein dynamics. *Eur. Phys. J.: Spec. Top.*, 141(1):227–233, 2007.

[198] A Paciaroni, A Orecchini, E Cornicchi, M Marconi, C Petrillo, M Haertlein, M Moulin, H Schober, M Tarek, and F Sacchetti. Fingerprints of amorphous icelike behavior in the vibrational density of states of protein hydration water. *Phys. Rev. Lett.*, 101(14):148104, 2008.

[199] Koji Yoshida, Aya Tashiro, and Toshio Yamaguchi. Thermal properties and hydration structure of poly-l-lysine, polyglycine, and lysozyme. *J. Mol. Liq.*, 217:57–61, 2016.

[200] V. A. Makarov, B. K. Andrews, P. E. Smith, and B. M. Pettitt. Residence times of water molecules in the hydration sites of myoglobin. *Biophys. J.*, 79: 2966–2974, 2000.

[201] Stefania Perticaroli, Lucia Comez, Marco Paolantoni, Paola Sassi, Laura Lupi, Daniele Fioretto, Alessandro Paciaroni, and Assunta Morresi. Broadband Depolarized Light Scattering Study of Diluted Protein Aqueous Solutions. *J. Phys. Chem. B*, 114(24):8262–8269, 2010.

[202] B. Halle. Protein hydration dynamics in solution: a critical survey. *Phil. Trans. R. Soc. Lond.*, 359:1207, 2004.

[203] Damien Laage, Thomas Elsaesser, and James T. Hynes. Perspective: Structure and ultrafast dynamics of biomolecular hydration shells. *Structural Dynamics*, 4(4):044018–15, 2017.

[204] X. J. Jordanides, M. J. Lang, X. Song, and G. R. Fleming. Solvation dynamics in protein environments studied by photon echo spectroscopy. *J. Phys. Chem. B*, 103:7995–8005, 1999.

[205] Samir Kumar Pal and Ahmed H. Zewail. Dynamics of water in biological recognition. *Chem. Rev.*, 104:2099, 2004.

[206] Paul Abbyad, Xinghua Shi, William Childs, Tim B. McAnaney, Bruce E. Cohen, and Steven G. Boxer. Measurement of solvation responses at multiple sites in a globular protein. *J. Phys. Chem. B*, 111(28):8269–8276, 2007.

[207] D. R. Martin and D. V. Matyushov. Dipolar nanodomains in protein hydration shells. *J. Phys. Chem. Lett.*, 6(3):407–412, 2015.

[208] Sayantan Mondal, Saumyak Mukherjee, and Biman Bagchi. Decomposition of total solvation energy into core, side-chains and water contributions: Role of cross correlations and protein conformational fluctuations in dynamics of hydration layer. *Chem. Phys. Lett.*, 683:29–37, 2017.

[209] Saumyak Mukherjee, Sayantan Mondal, and Biman Bagchi. Distinguishing dynamical features of water inside protein hydration layer: Distribution reveals what is hidden behind the average. *J. Chem. Phys.*, 147(2):024901–13, 2017.

[210] R. Schmid and D. V. Matyushov. Entropy of attractive forces and molecular nonsphericity in real liquids: A measure of structural ordering. *J. Phys. Chem.*, 99:2393, 1995.

[211] Francesco Pizzitutti, Massimo Marchi, Fabio Sterpone, and Peter J. Rossky. How protein surfaces induce anomalous dynamics of hydration water. *J. Phys. Chem. B*, 111(26):7584–7590, 2007. doi: 10.1021/jp0717185.

[212] A. D. Friesen and D. V. Matyushov. Surface polarity and nanoscale solvation. *J. Phys. Chem. Lett.*, 3:3685–3689, 2012.

[213] Mingyang Lu and Jianpeng Ma. The role of shape in determining molecular motions. *Biophys. J.*, 89:2395–2401, 2005.

[214] J A Rupley, E Gratton, and G. Careri. Water and globular proteins. *Tr. Biochem. Scie.*, 8(1):18–22, 1983.

[215] P. Madden and D. Kivelson. A consistent molecular treatment of dielectric phenomena. *Adv. Chem. Phys.*, 56:467–566, 1984.

[216] Adam Hospital, Michela Candotti, Josep Lluís Gelpí, and Modesto Orozco. The Multiple Roles of Waters in Protein Solvation. *J. Phys. Chem. B*, 121(15): 3636–3643, 2017.

[217] J. L. Green, J. Fan, and C. A. Angell. The protein-glass analogy: Some insights from homopeptide comparison. *J. Phys. Chem.*, 98:13780, 1994.

[218] M. Tarek and D. J. Tobias. Role of protein-water hydrogen bond dynamics in the protein dynamical transition. *Phys. Rev. Lett.*, 88:138101, 2002.

[219] Elena A Golysheva, Georgiy Yu Shevelev, and Sergei A Dzuba. Dynamical transition in molecular glasses and proteins observed by spin relaxation of nitroxide spin probes and labels. *J. Chem. Phys.*, 147(6):064501–10, 2017.

[220] Naoki Shinyashiki, Wataru Yamamoto, Ayame Yokoyama, Takeo Yoshinari, Shin Yagihara, Rio Kita, K L Ngai, and Simone Capaccioli. Glass Transitions in Aqueous Solutions of Protein (Bovine Serum Albumin). *J. Phys. Chem. B*, 113(43):14448–14456, 2009.

[221] Stefania Perticaroli, Jonathan D Nickels, Georg Ehlers, Hugh O'Neill, Qui Zhang, and Alexei P Sokolov. Secondary structure and rigidity in model proteins. *Soft Matter*, 9(40):9548–9556, 2013.

[222] Katherine A. Henzler-Wildman, Vu Thai, Ming Lei, Maria Ott, Magnus Wolf-Watz, Tim Fenn, Ed Pozharski, Mark A. Wilson, Gregory A. Petsko, Martin Karplus, Christian G. Hubner, and Dorothee Kern. Intrinsic motions along an enzymatic reaction trajectory. *Nature*, 450(7171):838–844, 2007.

[223] Robert Callender and R Brian Dyer. The Dynamical Nature of Enzymatic Catalysis. *Acc. Chem. Res.*, 48(2):407–413, 2015.

[224] Shina C. L. Kamerlin and Arieh Warshel. At the dawn of the 21st century: Is dynamics the missing link for understanding enzyme catalysis? *Proteins*, 78: 1339—1375, 2010.

[225] A. Warshel, P. K. Sharma, M. Kato, and W. W. Parson. Modeling electrostatic effects in proteins. *Biochim. Biophys. Acta*, 1764:1647–1676, 2006.

[226] G. Hummer, L. R. Pratt, and A. E. Garcia. Molecular theories and simulation of ions and polar molecules in water. *J. Phys. Chem. A*, 102:7885, 1998.

[227] Jochen Blumberger. Recent advances in the theory and molecular simulation of biological electron transfer reactions. *Chem. Rev.*, 115(20):11191–11238, 2015.

[228] M. Maroncelli. The dynamics of solvation in polar liquids. *J. Mol. Liq.*, 57: 1–37, 1993.

[229] D. V. Matyushov. Nonergodic activated kinetics in polar media. *J. Chem. Phys.*, 130:164522, 2009.

[230] Naoko Nakagawa and Michel Peyrard. The inherent structure landscape of a protein. *Proc. Natl. Acad. Sci. USA*, 103(14):5279–5284, 2006.

[231] Kumiko Hayashi and Mitsunori Takano. Violation of the Fluctuation-Dissipation Theorem in a Protein System. *Biophys. J.*, 93(3):895–901, 2007.

[232] D. N. LeBard and D. V. Matyushov. Protein-water electrostatics and principles of bioenergetics. *Phys. Chem. Chem. Phys.*, 12:15335–15348, 2010.

[233] R. B. Gregory. Protein hydration and glass transition behavior. In R. B. Gregory, editor, *Protein-solvent interactions*, page 191. Marcel Dekker, New York, 1995.

[234] D. J. Barlow and J. M. Thornton. Charge distribution in proteins. *Biopolymers*, 25:1717–1733, 1986.

[235] K. A. Dill. Dominant forces in protein folding. *Biochemistry*, 29:7133–7155, 1990.

[236] J. Blumberger and M. L. Klein. Reorganization free energies of long-range electron transfer in porphyrin-binding four-helix bundle protein. *J. Am. Chem. Soc.*, 128:13854–13867, 2006.

[237] Carlo Augusto Bortolotti, Andrea Amadei, Massimiliano Aschi, Marco Borsari, Stefano Corni, Marco Sola, and Isabella Daidone. The reversible opening of water channels in cytochrome *c* modulates the heme iron reduction potential. *J. Am. Chem. Soc.*, 134(33):13670–13678, 2012.

[238] Martin McCullagh and Gregory A Voth. Unraveling the Role of the Protein Environment for [FeFe]-Hydrogenase: A New Application of Coarse-Graining. *J. Phys. Chem. B*, 117(15):4062–4071, 2013.

[239] Alexander Heck, P Benjamin Woiczikowski, Tomas Kubar, Bernd Giese, Marcus Elstner, and Thomas B Steinbrecher. Charge Transfer in Model Peptides: Obtaining Marcus Parameters from Molecular Simulation. *J. Phys. Chem. B*, 116(7):2284–2293, 2012.

[240] D. V. Matyushov. Non-Gaussian statistics of binding/unbinding events and the energetics of electron transfer reactions. *Chem. Phys.*, 351:46–50, 2008.

[241] Rodolphe Vuilleumier, Kafui A Tay, Guillaume Jeanmairet, Daniel Borgis, and Anne Boutin. Extension of Marcus Picture for Electron Transfer Reactions with Large Solvation Changes. *J. Am. Chem. Soc.*, 134(4):2067–2074, 2012.

[242] J J Wei, Haiying Liu, K Niki, E. Margoliash, and D H Waldeck. Probing electron tunneling pathways: Electrochemical study of rat heart cytochrome *c* and its mutant on pyridine-terminated SAMs. *J. Phy. Chem. B*, 108(43):16912–16917, 2004.

[243] Damián Alvarez-Paggi, María A Castro, Verónica Tórtora, Laura Castro, Rafael Radi, and Daniel H Murgida. Electrostatically Driven Second-Sphere Ligand Switch between High and Low Reorganization Energy Forms of Native Cytochrome c. *J. Am. Chem. Soc.*, 135(11):4389–4397, 2013.

[244] Damián Alvarez-Paggi, Ulises Zitare, and Daniel H Murgida. The role of protein dynamics and thermal fluctuations in regulating cytochrome c/cytochrome c oxidase electron transfer. *Biochim. Biophys. Acta - Bioenergetics*, 1837(7):1196–1207, 2014.

[245] Roberto A S Luz and Frank N Crespilho. Gold nanoparticle-mediated electron transfer of cytochrome c on a self-assembled surface. *RSC Adv.*, 6(67):62585–62593, 2016.

[246] Qijin Chi, Jingdong Zhang, Jens E. T. Andersen, and Jens Ulstrup. Ordered assembly and controlled electron transfer of the blue copper protein azurin at gold (111) single-crystal substrates. *J. Phys. Chem. B*, 105(20):4669–4679, 2001.

[247] Lars J. C. Jeuken, James P. McEvoy, and Fraser A. Armstrong. Insights into gated electron-transfer kinetics at the electrodeprotein interface: A square wave voltammetry study of the blue copper protein azurin. *J. Phys. Chem. B*, 106 (9):2304–2313, 2002.

[248] M Fedurco. Redox reactions of heme-containing metalloproteins: dynamic effects of self-assembled monolayers on thermodynamics and kinetics of cytochrome *c* electron-transfer reactions. *Coord. Chem. Rev.*, 209(1):263–331, 2000.

[249] Jing Liu, Saumen Chakraborty, Parisa Hosseinzadeh, Yang Yu, Shiliang Tian, Igor Petrik, Ambika Bhagi, and Yi Lu. Metalloproteins Containing Cytochrome, Iron–Sulfur, or Copper Redox Centers. *Chem. Rev.*, 114(8):4366–4469, 2014.

[250] Anne M. Becka and Cary J. Miller. Electrochemistry at .omega.-hydroxy thiol coated electrodes. 3. Voltage independence of the electron tunneling barrier and measurements of redox kinetics at large overpotentials. *J. Phys. Chem.*, 96(6): 2657–2668, 1992. doi: 10.1021/j100185a049. URL `http://dx.doi.org/10.1021/j100185a049`.

[251] Milan Fedurco, Jan Augustynski, Chiara Indiani, Giulietta Smulevich, Marián Antalík, Mikuláš Bánó, Erik Sedlák, Mary C Glascock, and John H Dawson. Electrochemistry of Unfolded Cytochrome cin Neutral and Acidic Urea Solutions. *J. Am. Chem. Soc.*, 127(20):7638–7646, 2005.

[252] David H Waldeck and Dimitri E Khoshtariya. Fundamental Studies of Long- and Short-Range Electron Exchange Mechanisms between Electrodes and Proteins. In *Applications of Electrochemistry and Nanotechnology in Biology and Medicine I*, pages 105–238. Springer New York, New York, NY, July 2011.

[253] Arieh Warshel and Robert M. Weiss. An empirical valence bond approach for comparing reactions in solutions and in enzymes. *J. Am. Chem. Soc.*, 102(20): 6218–6226, 1980. doi: 10.1021/ja00540a008.

[254] A. Warshel. *Computer modeling of chemical reactions in enzymes and solutions.* Wiley Interscience, New York, 1991.

[255] T Kubař and M Elstner. A hybrid approach to simulation of electron transfer in complex molecular systems. *J. R. Soc. Interface*, 10(87):20130415, 2013.

[256] C. E. D. Chidsey. Free energy and temperature dependence of electron transfer at the metal-electrolyte interface. *Science*, 251:919–922, 1991.

[257] A. V. Gorodyskii, A. I. Karasevskii, and D. V. Matyushov. Adiabatic outer-sphere electron transfer through the metal-electrolyte interface. *J. Electroanal. Chem.*, 315:9–28, 1991.

[258] Jay B. Straus, August Calhoun, and Gregory A. Voth. Calculation of solvent free energies for heterogeneous electron transfer at the water–metal interface: Classical versus quantum behavior. *J. Chem. Phys.*, 102(1):529–539, 1995.

[259] W. Schmickler. *Interfacial Electrochemistry*. Oxford University Press, New York, 1996.

[260] Joost VandeVondele, Regla Ayala, Marialore Sulpizi, and Michiel Sprik. Redox free energies and one-electron energy levels in density functional theory based ab initio molecular dynamics. *J. Electroanal. Chem.*, 607(1-2):113–120, 2007.

[261] D. V. Matyushov and M. D. Newton. Understanding the optical band shape: Coumarin-153 steady-state spectroscopy. *J. Phys. Chem. A*, 105:8516–8532, 2001.

[262] Graham R. Fleming and Minhaeng Cho. Chromophore-solvent dynamics. *Annu. Rev. Phys. Chem.*, 47:109–134, 1996.

[263] N. S. Hush. Electron transfer in retrospect and prospect. 1: Adiabatic electrode processes. *J. Electroanal. Chem.*, 470:170–195, 1999.

[264] Agostino Migliore and Abraham Nitzan. On the evaluation of the marcus–hush–chidsey integral. *J. Electroanal. Chem.*, 671:99–101, 4 2012. doi: http://dx.doi.org/10.1016/j.jelechem.2012.02.026. URL `http://www.sciencedirect.com/science/article/pii/S1572665712000823`.

[265] Martin C Henstridge, Eduardo Laborda, Neil V Rees, and Richard G Compton. Marcus–Hush–Chidsey theory of electron transfer applied to voltammetry: A review. *Electrochim. Acta*, 84:12–20, 2012.

[266] W. Schmickler. A theory of adiabatic electron-transfer reactions. *J. Electroanal. Chem.*, 204:31–43, 1986.

[267] L. D. Zusman. Outer-sphere electron transfer in polar solvents. *Chem. Phys.*, 49:295–304, 1980.

[268] H. Sumi and R. A. Marcus. Dynamical effects in electron transfer reactions. *J. Chem. Phys*, 84:4894–4914, 1986.

[269] Ilya Rips and Joshua Jortner. Dynamic solvent effects on outer-sphere electron transfer. *J. Chem. Phys.*, 87(4):2090–2104, 1987.

[270] Yi Jing Yan, Massimo Sparpaglione, and Shaul Mukamel. Solvation dynamics in electron-transfer, isomerization, and nonlinear optical processes: a unified liouville-space theory. *J. Phys. Chem.*, 92(17):4842–4853, 1988. doi: 10.1021/j100328a010.

[271] John D Morgan and Peter G Wolynes. Adiabaticity of electron transfer at an electrode. *J. Phys. Chem.*, 91(4):874–883, 1987.

[272] Nalini Chakravarti and K L Sebastian. Electrochemical electron transfer: a diffusion-reaction equation approach. *Chem. Phys. Lett.*, 193(6):456–460, 1992.

[273] D.V. Matyushov. Potential-step transient response of an electrochemical system. *J. Electroanal. Chem.*, 367(1-2):1–6, 1994.

[274] G. van der Zwan and J. T. Hynes. Time-dependent fluorescence solvent shifts, dielectric friction, and nonequilibrium solvation in polar solvents. *J. Phys. Chem.*, 89:4181, 1985.

[275] Daniel W. Pierce and Steven G. Boxer. Dielectric relaxation in a protein matrix. *J. Phys. Chem.*, 96:5560–5566, 1992.

[276] S. Lampa-Pastirk and W. F. Beck. Polar solvation dynamics in zn(ii)-substituted cytochrome c: Diffusive sampling of the energy landscape in the hydrophobic core and solvent-contact layers. *J. Phys. Chem. B*, 108:16288–16294, 2004.

[277] Yangzhong Qin, Menghui Jia, Jin Yang, Dihao Wang, Lijuan Wang, Jianhua Xu, and Dongping Zhong. Molecular Origin of Ultrafast Water–Protein Coupled Interactions. *J. Phys. Chem. Lett.*, 7:4171–4177, 2016.

[278] R A Marcus. Electrostatic free energy and other properties of states having nonequilibrium polarization. I. *J. Chem. Phys.*, 24(5):979–989, 1956.

[279] Mohammadhasan Dinpajooh and D. V. Matyushov. Interfacial structural transition in hydration shells of a polarizable solute. *Phys. Rev. Lett.*, 114:207801, 2015.

[280] M. Dinpajooh, M. D. Newton, and D. V. Matyushov. Free energy functionals for polarization fluctuations: Pekar factor revisited. *J. Chem. Phys.*, 145:064504, 2017.

[281] Dmitry V Matyushov and Marshall D Newton. Solvent-Induced Shift of Spectral Lines in Polar-Polarizable Solvents. *J. Phys. Chem. A*, 121(11):2232–2240, 2017.

[282] S. Gupta and D. V. Matyushov. Solvent and solute polarizability effects on the reorganization energy of electron transfer. *J. Phys. Chem. A*, 108:2087–2096, 2004.

[283] A. A. Milischuk, D. V. Matyushov, and M. D. Newton. Activation entropy of electron transfer reactions. *Chem. Phys.*, 324:172–194, 2006.

[284] Weixia Liu, Jon N. Rumbley, S. Walter Englander, and A. Joshua Wand. Fast structural dynamics in reduced and oxidized cytochrome c. *Protein Science*, 18 (3):670–674, 2009.

[285] E. Sigfriddson, M. H. M. Olsson, and U. Ryde. A comparison of the inner-sphere reaorganization energies of cytochromes, iron-sulfur clusters, and blue copper proteins. *J. Phys. Chem. B*, 105:5546–5552, 2001.

[286] Xenia Amashukeli, Nadine E Gruhn, Dennis L Lichtenberger, Jay R Winkler, and Harry B Gray. Inner-Sphere Electron-Transfer Reorganization Energies of Zinc Porphyrins. *J. Am. Chem. Soc.*, 126(47):15566–15571, 2004.

[287] M. Cascella, A. Magistrato, I. Tavernelli, P. Carloni, and U. Rothlisberger. Role of protein frame and solvent for the redox properties of azurin from *Pseudomonas aeruginosa*. *Proc. Natl. Acad. Sci.*, 103:19641–19646, 2006.

[288] M. Bixon and J. Jortner. Electron transfer – from isolated molecules to biomolecules. *Adv. Chem. Phys.*, 106:35, 1999.

[289] P. K. Ghorai and D. V. Matyushov. Solvent reorganization entropy of electron transfer in polar solvents. *J. Phys. Chem. A*, 110:8857–8863, 2006.

[290] M. M. Waskasi, Gerdenis, A. L. Moore, T. A. Moore, D. Gust, and D. V. Matyushov. Marcus bell-shaped electron transfer kinetics observed in an arrhenius plot. *J. Am. Chem. Soc.*, 138(29):9251–9257, 2016.

[291] P. Vath, M. B. Zimmt, D. V. Matyushov, and G. A. Voth. A failure of continuum theory: Temperature dependence of the solvent reorganization energy of electron transfer in highly polar solvents. *J. Phys. Chem. B*, 103:9130–9140, 1999.

[292] Dimitri E Khoshtariya, Tinatin D Dolidze, Mikhael Shushanyan, and Rudi van Eldik. Long-range electron transfer with myoglobin immobilized at Au/mixed-SAM junctions: Mechanistic impact of the strong protein confinement. *J. Phys. Chem. B*, 118:692–706, 2014.

[293] John F Smalley, Sandra B Sachs, Christopher E D Chidsey, Stephen P Dudek, Hadley D Sikes, Stephen E Creager, C J Yu, Stephen W Feldberg, and Marshall D Newton. Interfacial Electron-Transfer Kinetics of Ferrocene through Oligophenyleneethynylene Bridges Attached to Gold Electrodes as Constituents of Self-Assembled Monolayers: Observation of a Nonmonotonic Distance Dependence. *J. Am. Chem. Soc.*, 126(44):14620–14630, 2004.

[294] Marshall D. Newton and John F. Smalley. Interfacial bridge-mediated electron transfer: mechanistic analysis based on electrochemical kinetics and theoretical modelling. *Phys. Chem. Chem. Phys.*, 9(5):555–572, 2007. doi: 10.1039/B611448B. URL `http://dx.doi.org/10.1039/B611448B`.

[295] H Nyquist. Thermal agitation of electric charge in conductors. *Phys. Rev.*, 32 (1):110–113, 1928.

[296] G. Hummer, L. R. Pratt, and A. E. Garcia. Free energy of ionic hydration. *J. Phys. Chem.*, 100:1206–1215, 1996.

[297] A. Warshel and W. W. Parson. Dynamics of biochemical and biophysical reactions: insight from computer simulations. *Quart. Rev. Biophys.*, 34:563, 2001.

[298] Sándor Volkán-Kacsó and Rudolph A Marcus. Theory of single-molecule controlled rotation experiments, predictions, tests, and comparison with stalling experiments in F 1-ATPase. *Proc. Natl. Acad. Sci. U.S.A.*, 113(43):12029–12034, 2016.

[299] L. Onsager and S. Machlup. Fluctuations and irreversible processes. *Phys. Rev.*, 91:1505–1512, 1953.

[300] G. R. Fleming, J. L. Martin, and J. Breton. Rates of primary electron transfer in photosynthetic reaction centers and their mechanistic implications. *Nature*, 333:190–192, 1988.

[301] A. J. Hoff and J. Deisenhofer. Photophysics of photosynthesis. *Phys. Rep.*, 287: 1–247, 1997.

[302] D. N. LeBard, D. R. Martin, S. Lin, N. W. Woodbury, and D. V. Matyushov. Protein dynamics to optimize and control bacterial photosynthesis. *Chem. Sci.*, 4:4127—4136, 2013.

[303] Varomyalin Tipmanee and Jochen Blumberger. Kinetics of the terminal electron transfer step in cytochrome *c* oxidase. *J. Phy. Chem. B*, 116(6):1876–1883, 2012.

[304] G L Closs and J R Miller. Intramolecular long-distance electron transfer in organic molecules. *Science*, 240(4851):440–447, 1988.

[305] P. F. Barbara, T. J. Meyer, and M. A. Ratner. Contemporary issues in electron transfer research. *J. Phys. Chem.*, 100:13148–13168, 1996.

[306] W R Fawcett and M Opallo. Possible experimental evidence for molecular solvation effects in simple heterogeneous electron-transfer reactions. *J. Phys. Chem.*, 96(7):2920–2924, 1992.

[307] Jay R Winkler and Harry B Gray. Electron flow through metalloproteins. *Chem. Rev.*, 114(7):3369–3380, 2014.

[308] C A Angell, K L Ngai, G B McKenna, P F McMillan, and S W Martin. Relaxation in glassforming liquids and amorphous solids. *J. Appl. Phys.*, 88(6): 3113–3157, 2000.

[309] Leticia F Cugliandolo, Jorge Kurchan, and Luca Peliti. Energy flow, partial equilibration, and effective temperatures in systems with slow dynamics. *Phys. Rev. E*, 55:3898–3914, 1997.

[310] Th. M. Nieuwenhuizen. Thermodynamics of the glassy state: Effective temperature as an additional system parameter. *Phys. Rev. Lett.*, 80(25):5580–5583, 1998.

[311] Tomás S. Grigera and N. E. Israeloff. Observation of fluctuation-dissipation-theorem violations in a structural glass. *Phys. Rev. Lett.*, 83(24):5038–5041, 12 1999. URL `https://link.aps.org/doi/10.1103/PhysRevLett.83.5038`.

[312] E. Dieterich, J. Camunas-Soler, M. Ribezzi-Crivellari, U. Seifert, and F. Ritort. Single-molecule measurement of the effective temperature in non-equilibrium steady states. *Nature Phys.*, 11:971–977, 2015. URL `http://dx.doi.org/10.1038/nphys3435`.

[313] I. Muegge, P. X. Qi, A. J. Wand, Z. T. Chu, and A. Warshel. The reorganization energy of cytochrome c revisited. *J. Phys. Chem. B*, 101:825–836, 1997.

[314] T. Simonson. Gaussian fluctuations and linear response in an electron transfer protein. *Proc. Natl. Acad. Sci.*, 99:6544–6549, 2002.

[315] J. Blumberger. Free energies for biological electron transfer from qm/mm calculation: method, application and critical assessment. *Phys. Chem. Chem. Phys.*, 10:5651–5667, 2008.

[316] D. R. Martin and D. V. Matyushov. Electron-transfer chain in respiratory complex I. *Sci. Rep.*, 7:5495, 2017.

[317] J. Mittal and G. Hummer. Static and dynamic correlations in water at hydrophobic interfaces. *Proc. Natl. Acad. Sci. USA*, 105:20130–20135, 2008.

[318] S. Sarupria and S. Garde. Quantifying water density fluctuations and compressibility of hydration shells of hydrophobic solutes and proteins. *Phys. Rev. Lett.*, 103:037803, 2009.

[319] C. J. F. Böttcher. *Theory of Electric Polarization*, volume 1. Elsevier, Amsterdam, 1973.

[320] Yousung Jung and R A Marcus. Protruding interfacial OH groups and 'on-water' heterogeneous catalysis. *J. Phys.: Condens. Matter*, 22(28):284117, 2010.

[321] Joel G Davis, Blake M Rankin, Kamil P Gierszal, and Dor Ben-Amotz. On the cooperative formation of non-hydrogen-bonded water at molecular hydrophobic interfaces. *Nat. Chem.*, 5:796—802, 2013.

[322] D. V. Matyushov. Electrophoretic mobility without charge driven by polarisation of the nanoparticle–water interface. *Mol. Phys.*, 112(15):2029—2039, 2014.

[323] Divya Nayar, Manish Agarwal, and Charusita Chakravarty. Comparison of tetrahedral order, liquid state anomalies, and hydration behavior of mTIP3P and TIP4P water models. *J. Chem. Theory Comput.*, 7(10):3354–3367, 2011.

[324] D. R. Martin and D. V. Matyushov. Communication: Microsecond dynamics of the protein and water affect electron transfer in a bacterial bc_1 complex. *J. Chem. Phys.*, 142:161101, 2015.

[325] Daniel R Martin, James E Forsmo, and Dmitry V Matyushov. Complex dynamics of water in protein confinement. *J. Phys. Chem. B*, pages acs.jpcb.7b10448–8, 2017.

[326] Giulio Biroli. A crash course on ageing. *J. Stat. Mech.*, (05):P05014, 2005.

[327] B. J. Hales. Temperature dependency of the rate of electron transport as a monitor of protein motion. *Biophys. J.*, 16:471, 1976.

[328] M. Volk, G. Aumeier, T. Langenbacher, R. Feick, A. Ogrodnik, and M.-E. Michel-Beyerle. Energetics and mechanism of primary charge separation in bacterial photosynthesis. a comparative study on reaction centers of rhodobacter sphaeroides and chloroflexus aurantiacus. *J. Phys. Chem. B*, 102(4):735–751, 1998.

[329] Q. Xu and M. R. Gunner. Temperature dependence of the free energy, enthalpy, and entropy of $p^+q_a^-$ charge recombination in *Rhodobacter sphaeroides* R-26 reaction centers. *J. Phys. Chem. B*, 104:8035–8043, 2000.

[330] Shawn E Huston and Peter J Rossky. Free energies of association for the sodium-dimethyl phosphate ion pair in aqueous solution. *J. Phys. Chem.*, 93(23):7888–7895, 1989.

[331] Alexander A. Rashin. Electrostatics of ion-ion interactions in solution. *J. Phys. Chem.*, 93(11):4664–4669, 1989. doi: 10.1021/j100348a051. URL `http://dx.doi.org/10.1021/j100348a051`.

[332] Joel S Bader and David Chandler. Computer simulation study of the mean forces between ferrous and ferric ions in water. *J. Phys. Chem.*, 96(15):6423–6427, 1992.

[333] Christopher J Fennell, Alan Bizjak, Vojko Vlachy, and Ken A Dill. Ion Pairing in Molecular Simulations of Aqueous Alkali Halide Solutions. *J. Phys. Chem. B*, 113(19):6782–6791, 2009.

[334] Yun Luo, Wei Jiang, Haibo Yu, Alexander D MacKerell, and Benoît Roux. Simulation study of ion pairing in concentrated aqueous salt solutions with a polarizable force field. *Farad. Disc.*, 160(21):135–149, 2013.

[335] Daniel Trzesniak, Anna-Pitschna E. Kunz, and Wilfred F. van Gunsteren. A comparison of methods to compute the potential of mean force. *ChemPhysChem*, 8(1):162–169, 2007. doi: 10.1002/cphc.200600527. URL `http://dx.doi.org/10.1002/cphc.200600527`.

[336] J. C. Maxwell. *A Treatise on Electricity and Magnetism*, volume 1. Dover Publications, New York, 1954, sec. 63.

[337] J. D. Jackson. *Classical Electrodynamics*. Wiley, New York, 1999.

[338] L. D. Landau and E. M. Lifshitz. *Electrodynamics of Continuous Media*. Pergamon, Oxford, 1984.

[339] D. V. Matyushov. Electrostatics of liquid interfaces. *J. Chem. Phys.*, 140: 224506, 2014.

[340] Mohammadhasan Dinpajooh and D. V. Matyushov. Dielectric constant of water in the interface. *J. Chem. Phys.*, 145:014504, 2016.

[341] P J Stiles, J B Hubbard, and R F Kayser. Dielectric saturation and dielectric friction in electrolyte solutions. *J. Chem. Phys.*, 77(12):6189–6196, 1982.

[342] Philip J Lenart, Arben Jusufi, and Athanassios Z Panagiotopoulos. Effective potentials for 1:1 electrolyte solutions incorporating dielectric saturation and repulsive hydration. *J. Chem. Phys.*, 126(4):044509–8, 2007.

[343] R Lobo. R. lobo, je robinson and s. rodriguez, j. chem. phys. 59, 5992 (1973). *J. Chem. Phys.*, 59:5992, 1973.

[344] EL Pollock and BJ Alder. Frequency-dependent dielectric response in polar liquids. *Physical Review Letters*, 46(14):950, 1981.

[345] Igor P Omelyan. Temperature behavior of the frequency-dependent dielectric constant for a stockmayer fluid. *Physics Letters A*, 216(1-5):211–216, 1996.

[346] Igor P Omelyan. Longitudinal wavevector-and frequency-dependent dielectric constant of the tip4p water model. *Molecular Physics*, 93(1):123–136, 1998.

[347] Sergei Gavryushov. Effective Interaction Potentials for Alkali and Alkaline Earth Metal Ions in SPC/E Water and Polarization Model of Hydrated Ions. *J. Phys. Chem. B*, 110(22):10888–10895, 2006.

[348] Eva Pluhařová, Ondrej Marsalek, Burkhard Schmidt, and Pavel Jungwirth. Ab Initio Molecular Dynamics Approach to a Quantitative Description of Ion Pairing in Water. *J. Phys. Chem. Lett.*, 4(23):4177–4181, 2013.

[349] D. Chandler. Interfaces and the driving force of hydrophobic assembly. *Nature*, 437:640–647, 2005.

[350] S. Rajamani, T. M. Truskett, and S. Garde. Hydrophobic hydration from small to large lengthscales: Understanding and manipulating the crossover. *Proc. Natl. Acad. Sci.*, 102:9475–9480, 2005.

[351] D. R. Martin and D. V. Matyushov. Electrostatic fluctuations in cavities within polar liquids and thermodynamics of polar solvation. *Phys. Rev. E*, 78:041206, 2008.

[352] T. Kihara. Intermolecular forces and equation of state of gases. *Adv. Chem. Phys.*, 1:267–307, 1958.

[353] A. D. Friesen and D. V. Matyushov. Local polarity excess at the interface of water with a nonpolar solute. *Chem. Phys. Lett.*, 511:256–261, 2011.

[354] G Hummer and A Szabo. Calculation of freeenergy differences from computer simulations of initial and final states. *J. Chem. Phys.*, 105:2004–2010, 1996.

[355] J. Åqvist and T. Hansson. On the validity of electrostatic linear response in polar solvents. *J. Phys. Chem.*, 100:9512–9521, 1996.

[356] F. Figueirido, G. S. Del Buono, and R. M. Levy. On finite-size effects in computer simulations using the Ewald potential. *J. Chem. Phys.*, 103:6133–6142, 1995.

[357] A. Milischuk and D. V. Matyushov. Dipole solvation: Nonlinear effects, density reorganization, and the breakdown of the Onsager saturation limit. *J. Phys. Chem. A*, 106:2146, 2002.

[358] Sowmianarayanan Rajamani, Tuhin Ghosh, and Shekhar Garde. Size dependent ion hydration, its asymmetry, and convergence to macroscopic behavior. *J. Chem. Phys.*, 120(9):4457–4466, 2004.

[359] J. S. Høye and G. Stell. Statistical mechanics of polar systems: Dielectric constant for dipolar fluids. *J. Chem. Phys.*, 61:562, 1974.

[360] C. G. Gray and K. E. Gubbins. *Theory of Molecular Liquids*. Clarendon Press, Oxford, 1984.

[361] J.-P. Hansen and I. R. McDonald. *Theory of Simple Liquids*. Academic Press, Amsterdam, 4 edition, 2013.

[362] M. Abramowitz and I. A. Stegun, editors. *Handbook of Mathematical Functions*. Dover, New York, 1972.

[363] G. Stell, G. N. Patey, and J. S. Høye. Dielectric constants of fluid models: Statistical mechanical theory and its quantitayive implementation. *Adv. Chem. Phys.*, 48:183–328, 1981.

[364] F. O. Raineri, H. Resat, and H. L. Friedman. Static longitudinal dielectric function of model molecular fluids. *J. Chem. Phys.*, 96:3068, 1992.

[365] C. Y. Lee, J. A. McCammon, and P. J. Rossky. The structure of liquid water at an extended hydrophobic surface. *J. Chem. Phys.*, 80:4448–4455, 1984.

[366] Richard C Remsing, Marcel D Baer, Gregory K Schenter, Christopher J Mundy, and John D Weeks. The Role of Broken Symmetry in Solvation of a Spherical Cavity in Classical and Quantum Water Models. *J. Phys. Chem. Lett.*, 5:2767–2774, 2014.

[367] H. C. Andersen, D. Chandler, and J. D. Weeks. Roles of repulsive and attractive forces in liquids: The equilibrium theory of classical fluids. *Adv. Chem. Phys.*, 34:105–155, 1976.

[368] R. J. Baxter. Ornstein-Zernicke relation and Percus-Yevick approximation for fluid mixtures. *J. Chem. Phys.*, 52:4559, 1970.

[369] William L. Jorgensen, Jayaraman Chandrasekhar, Jeffry D. Madura, Roger W. Impey, and Michael L. Klein. Comparison of simple potential functions for simulating liquid water. *J. Chem. Phys.*, 79(2):926–935, 1983.

[370] Guillaume Lamoureux and Benot Roux. Modeling induced polarization with classical Drude oscillators: Theory and molecular dynamics simulation algorithm. *J. Chem. Phys.*, 119(6):3025–3039, 2003.

[371] Elise Duboué-Dijon, Philip E Mason, Henry E Fischer, and Pavel Jungwirth. Hydration and ion pairing in aqueous mg2+ and zn2+ solutions: Force-field description aided by neutron scattering experiments and ab initio molecular dynamics simulations. *The Journal of Physical Chemistry B*, 122(13):3296–3306, 2017.

[372] D. Pines. *Elementary excitations in solids*. Perseus Books, 1999.

[373] Harold A. Scheraga. My 65 years in protein chemistry. *Quart. Rev. Biophys.*, 48(02):117–177, 2015.

[374] P. Lunkenheimer and A. Loidl. Dielectric spectroscopy of glass-forming materials: -relaxation and excess wing. *Chem. Phys.*, 284(1–2):205–219, 11 2002. doi: http://dx.doi.org/10.1016/S0301-0104(02)00549-9.

[375] P Lunkenheimer, U Schneider, R Brand, and A Loid. Glassy dynamics. *Contemporary Physics*, 41(1):15–36, 2010.

[376] Kankan Bhattacharyya. Nature of biological water: a femtosecond study. *Chem. Commun.*, (25):2848–2857, 2008. doi: 10.1039/B800278A.

[377] D. Laage, G. Stirnemann, F. Sterpone, R. Rey, and J. T. Hynes. Reorientation and allied dynamics in water and aqueous solutions. *Annu. Rev. Phys. Chem.*, 62:395–416, 2011.

[378] D. R. Martin and D. V. Matyushov. Hydration shells of proteins probed by depolarized light scattering and dielectric spectroscopy: Orientational structure is significant, positional structure is not. *J. Chem. Phys.*, 141:22D501, 2014.

[379] D. V. Matyushov. Dipolar response of hydrated proteins. *J. Chem. Phys.*, 136: 085102, 2012.

[380] Dazhi Liu, Xiang-qiang Chu, Marco Lagi, Yang Zhang, Emiliano Fratini, Piero Baglioni, Ahmet Alatas, Ayman Said, Ercan Alp, and Sow-Hsin Chen. Studies of Phononlike Low-Energy Excitations of Protein Molecules by Inelastic X-Ray Scattering. *Phys. Rev. Lett.*, 101(13):135501–4, 2008.

[381] Zhe Wang, Wei-Shan Chiang, Peisi Le, Emiliano Fratini, Mingda Li, Ahmet Alatas, Piero Baglioni, and Sow-Hsin Chen. One role of hydration water in proteins: key to the "softening" of short time intraprotein collective vibrations of a specific length scale. *Soft Matter*, 10(24):4298–4303, 2014.

[382] Utsab R Shrestha, Debsindhu Bhowmik, Kurt W Van Delinder, Eugene Mamontov, Hugh O'Neill, Qiu Zhang, Ahmet Alatas, and Xiang-qiang Chu. Collective Excitations in Protein as a Measure of Balance Between its Softness and Rigidity. *J. Phys. Chem. B*, 121(5):923–930, 2017.

[383] Anna V Frontzek, Serge V Strokov, Jan Peter Embs, and Sergey G Lushnikov. Does a Dry Protein Undergo a Glass Transition? *J. Phys. Chem. B*, 118(11): 2796–2802, 2014.

[384] E Duval, A Boukenter, and T Achibat. Vibrational dynamics and the structure of glasses. *J. Phys.: Cond. Matter*, 2:10227–10234, 1990.

[385] Mounir Tarek and Douglas J Tobias. Effects of solvent damping on side chain and backbone contributions to the protein boson peak. *J. Chem. Phys.*, 115(3): 1607–1612, 2001.

[386] Giorgio Schirò, Chiara Caronna, Francesca Natali, M. Marek Koza, and Antonio Cupane. The "protein dynamical transition"does not require the protein polypeptide chain. *J. Phys. Chem. Lett.*, 2(18):2275–2279, 2011. doi: 10.1021/jz200797g.

[387] Antonio Cupane, Margarita Fomina, Irina Piazza, Judith Peters, and Giorgio Schirò. Experimental Evidence for a Liquid-Liquid Crossover in Deeply Cooled Confined Water. *Phys. Rev. Lett.*, 113(21):215701–5, 2014.

[388] Ralph Jimenez, Graham R. Fleming, P. V. Kumar, and M. Maroncelli. Femtosecond solvation dynamics of water. *Nature*, 369:471, 1994.

[389] Salman S Seyedi and Dmitry V Matyushov. Protein dielectrophoresis in solution. *The Journal of Physical Chemistry B*, 122(39):9119–9127, 2018.

[390] Salman Seyedi and Dmitry V Matyushov. Dipolar susceptibility of protein hydration shells. *Chemical Physics Letters*, 2018.

[391] Salman Seyedi, Daniel R Martin, and Dmitry V Matyushov. Screening of coulomb interactions in liquid dielectrics. *arXiv preprint arXiv:1807.07242*, 2018.

[392] Carl Caleman, Paul J. van Maaren, Minyan Hong, Jochen S. Hub, Luciano T. Costa, and David van der Spoel. Force field benchmark of organic liquids: Density, enthalpy of vaporization, heat capacities, surface tension, isothermal compressibility, volumetric expansion coefficient, and dielectric constant. *J. Chem. Theory Comput.*, 8(1):61–74, 2012.

[393] Berk Hess, Carsten Kutzner, David van der Spoel, and Erik Lindahl. GROMACS 4: Algorithms for Highly Efficient, Load-Balanced, and Scalable Molecular Simulation. *Journal of Chemical Theory and Computation*, 4(3):435–447, March 2008.

[394] S. E. Feller and A. D. MacKerell. An improved empirical potential energy function for molecular simulations of phospholipids. *J. Phys. Chem. B*, 104: 7510–7515, 2000.

[395] Karol Kaszuba, Pekka A Postila, Oana Cramariuc, Marcin Sarewicz, Artur Osyczka, Ilpo Vattulainen, and Tomasz Róg. Parameterization of the prosthetic redox centers of the bacterial cytochrome bc 1 complex for atomistic molecular dynamics simulations. *Theor. Chem. Acc.*, 132(6):1–13, 2013.

[396] Jesse G Kleingardner and Kara L Bren. Biological significance and applications of heme *c* proteins and peptides. *Acc. Chem. Res.*, 48(7):1845–1852, 2015.

[397] Marcelo A. Martí, Luciana Capece, Alejandro Crespo, Fabio Doctorovich, and Dario A. Estrin. Nitric oxide interaction with cytochrome *c* and its relevance to guanylate cyclase. Why does the iron histidine bond break? *J. Am. Chem. Soc.*, 127(21):7721–7728, 06 2005. doi: 10.1021/ja042870c. URL `http://dx.doi.org/10.1021/ja042870c`.

[398] M. J. Frisch, G. W. Trucks, H. B. Schlegel, G. E. Scuseria, M. A. Robb, J. R. Cheeseman, G. Scalmani, V. Barone, B. Mennucci, G. A. Petersson, H. Nakatsuji, M. Caricato, X. Li, H. P. Hratchian, A. F. Izmaylov, J. Bloino, G. Zheng, J. L. Sonnenberg, M. Hada, M. Ehara, K. Toyota, R. Fukuda, J. Hasegawa, M. Ishida, T. Nakajima, Y. Honda, O. Kitao, H. Nakai, T. Vreven, Jr. Montgomery, J. A., J. E. Peralta, F. Ogliaro, M. Bearpark, J. J. Heyd, E. Brothers, K. N. Kudin, V. N. Staroverov, R. Kobayashi, J. Normand, K. Raghavachari, A. Rendell, J. C. Burant, S. S. Iyengar, J. Tomasi, M. Cossi, N. Rega, J. M. Millam, M. Klene, J. E. Knox, J. B. Cross, V. Bakken, C. Adamo, J. Jaramillo, R. Gomperts, R. E. Stratmann, O. Yazyev, A. J. Austin, R. Cammi, C. Pomelli, J. W. Ochterski, R. L. Martin, K. Morokuma, V. G. Zakrzewski, G. A. Voth, P. Salvador, J. J. Dannenberg, S. Dapprich, A. D. Daniels, Ö. Farkas, J. B. Foresman, J. V. Ortiz, J. Cioslowski, and D. J. Fox. Gaussian 09 Revision E.01, 2009.

[399] Michael C Zerner, Gilda H Loew, Robert F Kirchner, and Ulrich T Mueller-Westerhoff. An intermediate neglect of differential overlap technique for spectroscopy of transition-metal complexes. ferrocene. *Journal of the American Chemical Society*, 102(2):589–599, 1980.

APPENDIX A

SIMULATION AND ANALYSIS PROTOCOLS

A.1 Glycerol

Molecular dynamics (MD) simulations were performed for twelve different temperatures (147, 168, 179, 195, 214, 239, 255, 275, 287, 302, 312, 334 K) in a cubic box consisting of 1000 glycerol molecules using the OPLS-AA (Optimized Potentials for Liquid Simulation - All Atoms) force field [392] as a part of the Gromacs [393] simulation package. After the initial NPT and NVT equilibration runs, 50 ns trajectories were produced in the NVE ensemble with no constraints.

Each system was initialized with a 300 ps NVT run using a Nose-Hoover thermostat with H-bonds constrained, followed by a 300 ps run with no constraints. A 1-3 ns NVE run was followed to check for stability before performing 50 ns production runs for each temperature. The time step for all production runs was 0.5 fs, with all atoms (including hydrogens) allowed to move according to the OPLS-AA force field parameters. The group cutoff-scheme was used with an update time of 5 ns and a cutoff distance of 1.1 nm for the shifted Lennard-Jones and electrostatic interactions with a group list distance of 13 Å renewed every 10 simulation steps. Long-ranged electrostatic interactions were calculated with the particle mesh Ewald method. Additional NVT trajectories (tens of ns) were produced in order to compare the results between NVE and NVT ensembles (Fig. 2.7). NVT simulations, with the Verlet cutoff-scheme and a Nose-Hoover thermostat, were carried out for the following temperatures: 230, 240, 250, 260, 270, and 280 K. The typical trajectory length was 50 ns and all atoms were allowed to move.

A.2 Cytochrome C

A.2.1 Simulation Protocol

The simulation protocol has followed the previous simulations setup[171] and was used here to simulate the hydrated cytochrome c (Cyt-c) at a number of temperatures (from 120 K to 360 K) and in its oxidized and reduced states. The trajectories were produced with NAMD software program.[172] The CHARMM 27[394] force field was used. Particle mesh Ewald was used to handle the long-range electrostatics, with the cutoff distance of 12.0 Å. The time step of 2.0 fs was used for all simulations. No ions were used to neutralize the total charge of the simulation cell. It was found in previous simulations[186] that ions complicate the convergence of λ since they are not sufficiently screened and tend to bind to ionized surface residues. The analysis of implementing Ewald sums in the cell with uncompensated charge is discussed in the previous work where the computational model of Cyt-c was developed.[171] That analysis also included separate simulations of Cyt-c with the presence of electrolyte, with little effect on the results for the reorganization energies. The simulation cell carrying a net charge was used for the rest of simulations since it provides faster convergence of λ.

Separate NMR solution structures for the oxidized (PDB 1AKK) and reduced (PDB 1GIW) were used for the initial setup. The force field parameters and charges for the two oxidation states were taken from Kaszuba *et al.*[395] These force-field parameters were applied to produce classical MD trajectories used to calculate the classical electric field and electrostatic potential entering the quantum Hamiltonian (see below).

The procedure of solvating two structures followed several steps. First, crystallographic water molecules were taken from the 1YCC PDB file and added to the

1GIW cytochrome c structure (Red state). To assure that the protein was properly saturated with water, we performed a "soaking" procedure. It consisted of making a small sphere of water surrounding the protein with a total system size of 5497 atoms. From this structure, 150 ns simulations were performed. Finally, from the last frame of these longer simulations, a box (100.1Å×100.1Å× 100.1Å) consisting of a total of 101440 atoms was created and additional water molecules added to the total of 33231 molecules. This addition of water was followed by 20 ns NPT simulations allowing the newly created box to relax around the sphere. This NPT equilibration was followed by 10 ns NVT equilibration. The same sequence of steps was then applied to the 1AKK structure preceded by the alignment of the 1GIW and 1AKK structures. All force field parameters were applied using VMD's "psfgen" tool and TIP3P water molecules were added using VMD's "solvate" plugin [172].

Most electron-transfer cytochromes form 6-coordinated His-Fe-Met complex[396]. The Fe-His bond is, however, weaker than the Fe-Met bond and can break in some forms of cytochrome c [397]. The stretching frequency of the Fe-His bond in 6-coordinated cytochromes is[397] $\sim 220 - 240$ cm^{-1}. The breaking of the Fe–Nϵ bond was previously modeled by QM/MM simulations[397] and used in our modeling to construct a Morse potential

$$U(r) = D_e \left[1 - e^{-\gamma(r-r_e)}\right]^2 \tag{A.1}$$

with the well depth $D_e = 9.0$ kcal/mol, the well width $\gamma = 1.52$ Å^{-1}, and the equilibrium bond distance $r_e = 2.33$ Å.[171] The potential in eq (A.1) was applied to the simulations in the form of the force by utilizing NAMD tclForces functionality. We found, however, that the application of this potential does not strongly affect any properties that we have collected on the time-scale of simulations.

Test simulations were done with two different NMR structures, to which both Red

and Ox charge distributions of the heme were applied. We, however, found that small differences in protein structure do not yield noticeable changes in the electron-transfer activation parameters. It is the change in the charge distribution that is the main factor affecting the average energy gap for the half reaction (eq (4.1)). Either of the two structures can in fact be used in simulations of electron transfer in Cyt-c.

NVT simulations, 1 ns each, with the temperature increments of 1 K were used for cooling and heating from the initial temperature of 300 K. Production simulations of at least 250 ns in length were performed for Red and Ox oxidation states at $T \geq 280$ K and of 135 ns in length for the temperatures below 280 K.

Quantum calculations. A portion of Cyt-c was chosen as the quantum center (Figure 4.2) and was treated quantum mechanically, with the rest of the system treated at the classical atomistic level. The quantum center contained the heme, HIS, MET, and two CYS ligated amino acids. In all cases, hydrogen atoms were added to satisfy valency. The geometry of the quantum center was optimized by freezing all the atoms except the added hydrogens.[171]

The Hamiltonian matrix of the quantum center in the electrostatic field of the surrounding classical subsystem is provided in equation (4.9). GAUSSSIAN'09 [398] was used for all quantum calculations in vacuum (Red and Ox states) using the ZINDO/S method [399]. The charges of the Red (singlet) and Ox (doublet) quantum center were -2 and -1, respectively. The transition dipoles in the Hamiltonian matrix were used to calculate the polarizability tensor of the quantum center

$$\alpha_0^{\alpha\beta} = 2 \sum_{j>0} \frac{\mu_{0j}^{\alpha} \mu_{j0}^{\beta}}{E_j - E_0}, \tag{A.2}$$

The convergence of this parameter as a function of the number of states was used to determine $M = 100$ states in the Hamiltonian matrix. The polarizability change of the active sites $\Delta\alpha = \alpha_{\mathrm{Ox}} - \alpha_{\mathrm{Red}} = -30.8$ Å was found with this choice, $\alpha = \frac{1}{3}\mathrm{Tr}[\boldsymbol{\alpha}]$.

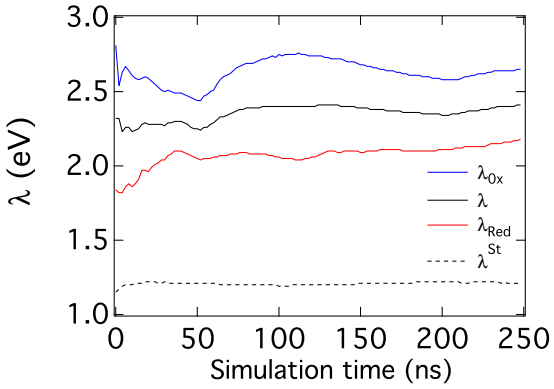

Figure A.1: Running Averages of the Reorganization Energies of the Oxidized (Ox) and Reduced (Red) States at $T = 310$ K. $\lambda = (\lambda^{\mathrm{Ox}} + \lambda^{\mathrm{Red}})/2$ Indicates Their Mean. λ^{St} Indicates the Running Average for the Stokes-Shift Reorganization Energy.

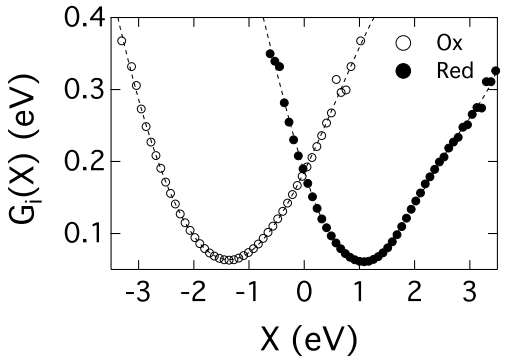

Figure A.2: Free Energies of Electron Transfer for the Oxidized (Ox) and Reduced (Red) States of Cyt-C Calculated From MD Simulations (Points) at $T = 300$ K.The Dashed Lines Are Interpolations Between the Points to Guide the Eye.

A.2.2 Data Analysis

The energy gap in the QM/MD simulations is defined as the difference between the lowest eigenvalues $E_g^{\mathrm{Ox/Red}}$ of the oxidized and reduced states (eq.(4.1)) obtained by diagonalizing the corresponding Hamiltonian matrices in Eq. (4.9)

The electrode chemical potential μ in eq.(4.1) is established by the condition of the free energies of electron transfer intercepting at $X = 0$.

Two reorganization energies of electron transfer, λ^{St} and λ, are considered here. Figure A.1 shows the running averages of λ_i and λ^{St} along the simulation trajectory. We also list values and the error estimates calculated as the standard deviation between averages within the trajectory blocks of 20 ns in length in table A.2.2 . These calculations most likely overestimate the errors since they include parts of the trajectory when sufficient convergence was not yet reached. However, they point out that the temperature variation of λ_1 and, in particular, its drop at the crossover temperature are well resolved by the present simulations. The free energy surfaces from simulations at $\eta = 0$ (overpotential (chapter 4)) are shown in Figure A.2.

Since our calculations do not include the chemical potential of the metal in eq (A.2), the calculated values of the reaction coordinate incorporate an unknown gas-phase shift ΔI

$$X_{\mathrm{MD}} = \Delta I + X \tag{A.3}$$

In order to determine this component, we turned to the temperature dependence of the minimum of the free energy surface in the oxidized state. In the idealized behavior of the Marcus theory, one expects $X_{\mathrm{min}} = -\lambda^{\mathrm{St}}$. Corrections to this idealized limit can always be present, and we assumed that they can be accommodated into a shift linear in temperature, $X_{\mathrm{min}}(T) = -\lambda^{\mathrm{St}}(T) + aT$, where $\lambda^{\mathrm{St}}(T) = 1.486$ eV $- 0.8 \times 10^{-3}$eV/K $\times\, T$ was found from MD simulations. We found that simulated minima follow the temperature dependence

$$X_{\mathrm{MD}} = \Delta I - \lambda^{\mathrm{St}}(T) + aT \tag{A.4}$$

very well. From these results we found $\Delta I = 2.52$ eV to be most consistent with the data. Figure A.3 shows the application of this shift to the Red and Ox free energy surfaces at $T = 165$ K. This constant offset was used to shift the energy gaps X_{MD} to obtain X.

Table A.1: Reorganization Energies (eV).[a]

T	λ^{St}	$\lambda_1(Ox)$	$\lambda_2(Red)$
120		1.01±0.04	
140		1.11±0.08	
160		1.52±0.18	
165	1.33	1.70±0.22	2.07
170		1.71±0.22	
180		3.27±0.68	
185		3.50±0.61	
200		2.81±0.34	
220		2.90±0.37	
240		3.19±0.32	
260		2.78±0.21	
280	1.31	2.89±0.28	3.70
290	1.32	2.97±0.70	2.97
310	1.21	2.65±0.32	2.18
320	1.21	2.54±0.23	2.19
330	1.21	3.15±0.35	2.76
340	1.21	2.58±0.22	2.47

[a]Errors in the Reorganization Energy From the Energy Gap Variance Are Estimated as the Standard Deviation Between Averages Calculated From 20 ns Blocks Along the MD Trajectory.

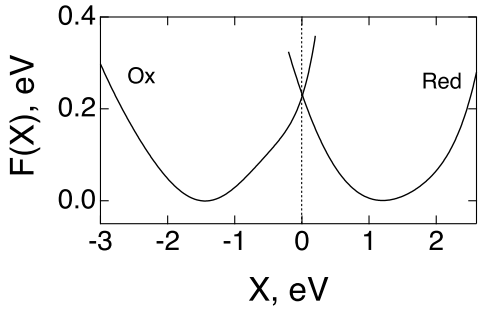

Figure A.3: Free Energy Surfaces of Electron Transfer for Ox and Red States of Cyt-C at $T = 165$ K.The Lines Are Interpolations Through the Histogram Points Obtained by Calculating X_{MD}Along the Simulation Trajectory Followed by the Horizontal Shift by $\Delta I = 2.52$ eV.

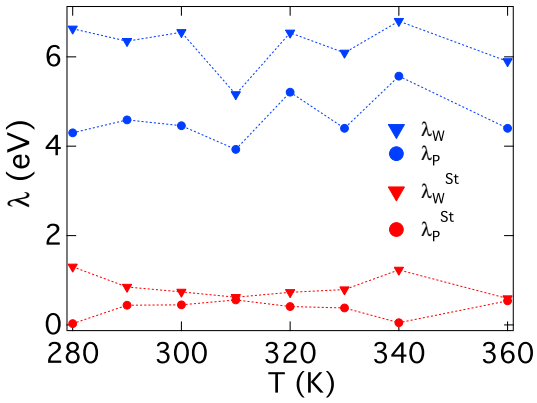

Figure A.4: Protein and Water Reorganization Energies in the Temperature Range From 280 to 360 K. Triangles Refer to Water and Circles Represent Protein. The Red Points Show the Simulation Results for the Stokes-Shift Reorganization Energy λ^{St} And the Blue Points Indicate the Variance Reorganization Energy λ.The Dotted Lines Connect the Points.

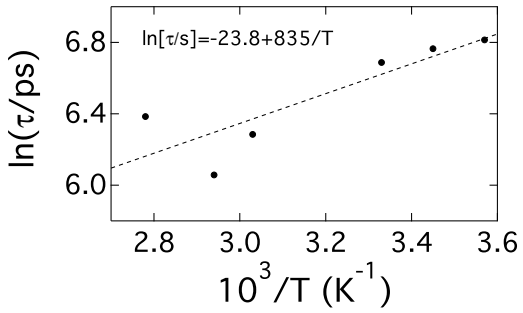

Figure A.5: Relaxation Time of the Stokes-Shift Dynamics (Eq (A.6)) as a Function of $1/T$.The Points Refer to the Simulation Data and the Straight Line Is the Linear Regression $\ln[\langle\tau(\mathrm{s})\rangle] = -23.8 + 835\mathrm{K}/T$.

Table A.2: Stokes Shift and Variance Reorganization Energies of Protein and Water Components of the Thermal Bath (eV).

	λ^{St}		λ	
T	protein	water	protein	water
280	0.03	1.3	4.3	6.6
290	0.44	0.85	4.6	6.3
300	0.45	0.74	4.5	6.5
310	0.55	0.62	3.9	5.2
320	0.41	0.73	5.2	6.5
330	0.38	0.79	4.4	6.1
340	0.055	1.23	5.6	6.8
360	0.54	0.59	4.4	5.9

The reorganization energy was additionally separated into the protein and water components. This was achieved by using the corresponding contributions for the electrostatic potential ϕ_{Fe} and the electrostatic field $\mathbf{E}_b$ in the Hamiltonian matrix in eq (4.9). These results are shown in Figure A.4 and listed in Table A.2. Note that λ_p (protein) and λ_w (water) do not add up to λ because the diagonalization of the Hamiltonian matrix within the empirical valence-bond formalism produces a generally non-linear functional of the electrostatic scalar (potential) and vector (electric field) fields of the medium.

A.2.3 Dynamics

Dynamics and Parameters Regarding Electrochemistry (Chapter 4)

The main dynamic function studied in Chapter 4 is the time auto-correlation function of the energy gap (Stokes-shift dynamics) $C_X(t) = \langle \delta X(t) \delta X(0) \rangle$. This correlation function calculated from MD trajectories in Red and Ox states of cytochrome c was fitted to five decaying exponential functions

$$S_2(t) = C_X(t)/C_X(0) = \sum_{n=1}^{5} A_n e^{-t/\tau_n} \tag{A.5}$$

with the fitting parameters listed in Table A.3 ($\sum_{i=1}^{5} A_i = 1$). The average relaxation times at different temperatures, also listed in Table A.3, are obtained according to the relation

$$\langle \tau \rangle = \sum_{n=1}^{5} A_n \tau_n \tag{A.6}$$

Calculation Protocols, MSF and Dynamics of the Susceptibility (Chapter 3)

The calculations of the force acting on the heme involved all atoms of the protein and water except the following atoms closest to the heme: SG on the SYS, SG on

Table A.3: Fitting Parameters for the Time Correlation Functions of the Energy Gap to the Sum of 5 Exponential Functions (Eq (A.5), Relaxation Times τ_n Are in ps). The Average Relaxation Time $\langle\tau\rangle$ Is Given by Eq (A.6).

T	A_1	A_2	A_3	A_4	A_5	τ_1	τ_2	τ_3	τ_4	τ_5	$\langle\tau\rangle$
						Red					
290	0.53	0.20	0.09	0.07	0.11	0.09	2.02	6166.55	22.98	240.53	573.90
300	0.616	0.170	0.001	0.14	0.07	0.13	4.82	2617.11	2623.93	103.58	376.71
310	0.60	0.20	0.06	0.09	0.05	0.09	1.37	3797.56	8.62	113.98	243.72
320	0.60	0.21	0.05	0.08	0.05	0.08	1.12	1224.03	6.91	79.07	69.90
330	0.57	0.18	0.07	0.10	0.08	0.09	1.66	1220.05	41.75	167.50	103.26
340	0.65	0.16	0.03	0.08	0.08	0.12	3.03	10000.0	81.05	1502.62	385.72
360	0.65	0.16	0.03	0.07	0.08	0.11	2.38	283.98	48.38	1027.16	92.03
						Ox					
290	0.53	0.17	0.12	0.13	0.06	0.08	1.29	10000.0	9.79	148.90	1160.12
300	0.48	0.17	0.15	0.13	0.07	0.1	1.90	7879.70	16.03	294.63	1228.29
310	0.60	0.20	0.06	0.09	0.05	0.09	1.37	3797.56	8.62	113.99	243.72
320	0.66	0.12	0.04	0.07	0.03	0.1	1.53	8764.37	14.40	282.57	397.37
330	0.64	0.19	0.09	0.05	0.03	0.13	3.97	10000.0	119.59	1206.51	969.43
340	0.57	0.16	0.09	0.11	0.07	0.09	1.46	5357.80	13.75	123.72	468.54
360	0.59	0.06	0.05	0.20	0.11	0.10	633.15	27.61	2.04	10000.0	1093.0

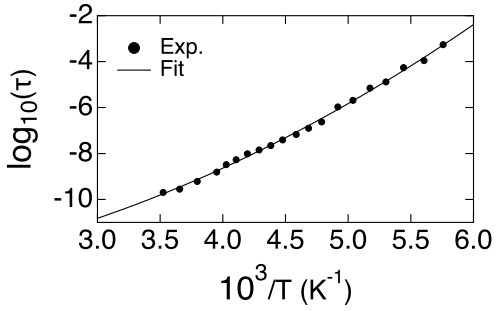

Figure A.6: Relaxation Time of the ν-ProcessReported From Broad Band Dielectric Spectroscopy of Hydrated Myoglobin Powders (Points, $h = 0.36$ g of Water/g of Prot.).[28] The Solid Line Is Regression Through the Points with the Equation: $\log_{10}[\tau(\text{ps})] = -1.5974 + 314348/T^2 - 17.757/T$.

the CYS and SD on the MET. For the force variance of the Ox state, the expected linear temperature scaling of $\langle \delta \mathbf{F}^2 \rangle$ was not followed for the variances obtained from 250 ns simulation trajectories. Therefore, the force variance was calculated from 50 ns segments and then averaged over 5 such values to obtain the data shown in Fig. A.13. These results were used to produce figure 3.3 in chapter 3.

Force acting on the heme The force autocorrelation function

$$C_F^a(t) = \langle \delta \mathbf{F}^a(t) \cdot \delta \mathbf{F}^a(0) \rangle \tag{A.7}$$

was calculated from MD trajectories in Red and Ox states of Cyt-C. The component $a = \text{El}, \text{Tot}$ here indicate either the electrostatic force or total force acting on the heme of Cyt-C. $\mathbf{F}^a(t)$ in this equation is therefore the sum of all forces acting on the atoms of the heme. The calculations of the autocorrelation function were done in the time interval from 0.2 ps to 10–40 ns by sliding the averaging window along the trajectory of 250 ns. The correlation function was fitted to five decaying exponents (Eq. (A.5)) with the fitting parameters listed in Tables A.4, A.5,A.6. The average relaxation time, also listed in the tables, was calculated according to the relation A.6.

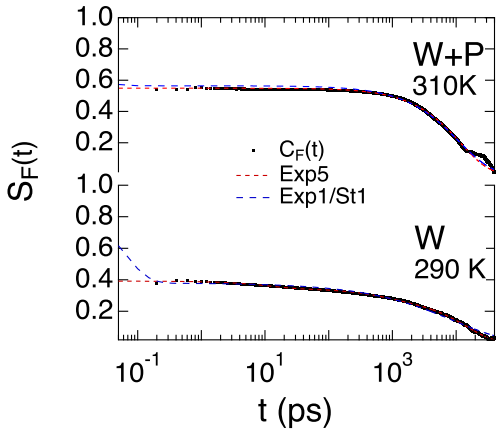

Figure A.7: Exp5 Represent Fitting with 5 Exponents (Eq. A.5), While Exp1/St1 Is when 1 Exponent and One Stretch Exponential Is Used for the Fitting (Eq. A.8).The Top Subsection Is $S_F(t)$ Of Force Coming From Water Plus Protein on the HEME for Red State at 310 K, While the Bottom Is From Water Molecules on HEME at 290 K for Red State.

The fitting process of 5 Exponents is only to have keep the same method for all the fittings and get the closest fits to the data. To illustrate that using another method would not change the general results, the stretch exponent (eq. A.8) is used to fit the data and the results is compared with the 5-exponents fitting. As one can see in (figs. A.7,A.8 and A.9), the results are not that different, (one would expect it, since the multi-exponential amplitudes are negligible for most of the parts, except for two major ones, one in very short drop and one for long-time dynamics(tens of ns range)).

$$S_F = C_F(t)/C_F(0) = A_1 e^{-t/\tau_1} + (1 - A_1) e^{-t/{\tau_2}^{\beta}} \tag{A.8}$$

The time of stretch fitting (fig. A.8) is obtained by eq. (A.9)

$$\tau = \Gamma(1 + \frac{1}{\beta}) * \tau_2 \tag{A.9}$$

here the Γ represents gamma function.

In contrast to $S_F(t)$ averaging over vibrations of the individual atoms in the heme,

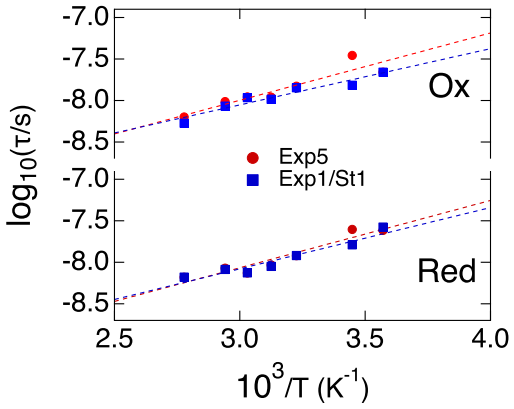

Figure A.8: Comparing the Results From Using Long-Time Component of 5 Exponents(Exp5) And the Results From Using Stretch Exponential (Eq. A.9)(Exp1/St1) for Ox State(Top) and Red State(Bottom).The Slope of the Fittings Are 1559 K for Ox and 1701 K for Red State for Stretch Exponential, and 1868 K for Using Long-Time Component of 5 Exponents .

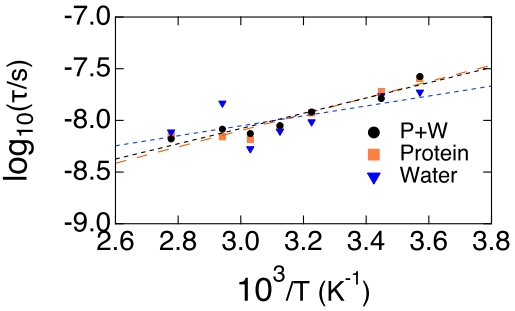

Figure A.9: Here the Results of Using Eq. (A.9) For Different Components of the Force Is Presented. The Slope of Fit to the Protein+water Is 1701 K, for the Protein Component Is 1819 K and for the Water Is 1108 K. The Fittings for Water Were Specially Poor. The Data Was Also Fitted with 3 Exponents and One Stretch, which Gave the Best Fits and the Resulting Slope where 1155 K (Not Shown in the Graph).

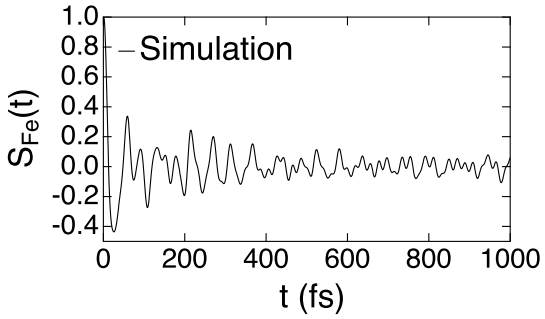

Figure A.10: Normalized Time Auto-Correlation Function of the Force Acting on the Fe Atom $S_{\mathrm{Fe}}(t) = C_{\mathrm{Fe}}(t)/C_{\mathrm{Fe}}(0)$, Where $C_{\mathrm{Fe}}(t) = \langle \delta\mathbf{F}_{\mathrm{Fe}}(t) \cdot \delta\mathbf{F}_{\mathrm{Fe}}(0) \rangle$.

the force-force time auto-correlation function of the force acting on the heme iron is highly oscillatory (Fig. A.10). This correlation function is difficult to analyze in terms on the long-time dynamics required for the dynamical transition and the force acting on the entire heme was chosen for that reason.

MSF of Cyt-C The modeling of the MSF of the heme iron requires calculating the overall force variance acting on the heme and the nonergodicity parameter $f_{\mathrm{ne}}(T)$ in Eq. (3.16) in the chapter 3. The variance of the total force acting on the heme depends on temperature. Based on the expectations from the fluctuation-dissipation theorem, we approximated the simulation results at different temperatures by a linear function, $\langle \delta F_H \rangle = cT$. The coefficient c for two oxidation states is $c_{\mathrm{Red}} = 0.018$ and $c_{\mathrm{Ox}} = 0.017$ $(\mathrm{eV/\AA})^2\mathrm{K}^{-1}$. The simulation points and the linear fit are shown in Fig. A.11

MSF of Hydration Shell The self intermediate scattering function (ISF) was calculated separately for translations and rotations of the water molecules in the hydration shell of Cyt-c. The translational ISF is

$$F_s(k,t) = N^{-1} \sum_j \left\langle e^{i\mathbf{k}\cdot\Delta\mathbf{r}_j(t)} \right\rangle , \tag{A.10}$$

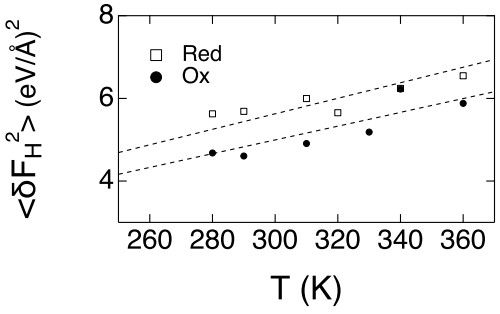

Figure A.11: Variance of the Force Acting on the Heme $\langle \delta F_H^2 \rangle$ Vs T. The Dashed Lines Are Regressions Through the Points, $\langle \delta F_H^2 \rangle = cT$.

where $\Delta\mathbf{r}(t) = \mathbf{r}_{\mathrm{O}}(t)\ \mathbf{r}_{\mathrm{O}}(0)$ for oxygen atoms counted within the shell 6 Å thick. A similar function was calculated replacing $\Delta\mathbf{r}(t)$ in Eq. (A.10) with $\Delta\mathbf{r}_{\text{O-H}}(t)$ for the vector connecting the oxygen and hydrogen atoms. For each function $-\ln(F_s(k,t))$ vs q^2 in the range of small q-values ($q < 0.13$ Å^{-1}) was fitted wit a linear function to produce the corresponding MSFs. $t = 100$ ps and $t = 1$ ns were used in the calculations shown in Fig. 3.11 of the chapter 3.

Dynamics of the susceptibility The calculations of the static dipolar susceptibility of the hydration shell are shown in Fig. 3.10 of the chapter 3. The dynamic version of the susceptibility function requires calculating the time correlation function of the shell dipole moment, $\langle \delta\mathbf{M}(t) \cdot \delta\mathbf{M}(0) \rangle$. The imaginary part of the frequency Fourier transform of the susceptibility is the loss function $\chi''(\omega)$. The results of calculations of this functions are shown in Fig. A.12. The calculations are performed for the water shell with the thickness of 6 Å around the van der Waals surface of the protein.

Vibrational density of states Vibrational density of states of the Fe atom in the heme was calculated from the velocity correlation function

$$Z(t) = \tfrac{1}{3}\langle \mathbf{v}_{\mathrm{Fe}} \cdot \mathbf{v}_{\mathrm{Fe}}(0) \rangle \tag{A.11}$$

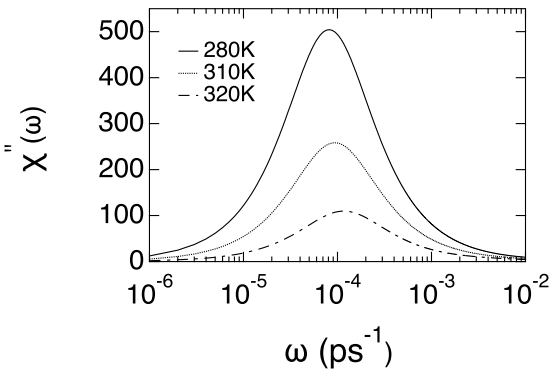

Figure A.12: $\chi''(\omega)$ for $T = 280$, 310 and 320 K. The Thickness of the Water Shell Is 6 Å.

It is connected to the vibrational density of states (VDOS) $D(\omega)$ by the relation (A.12)[11]

$$Z(t) = \frac{k_{\mathrm{B}}T}{2m_{\mathrm{Fe}}}\mathrm{Re}\int_{-\infty}^{\infty} D(\omega)e^{i\omega t}d\omega, \tag{A.12}$$

where m_{Fe} is the mass of the Fe atom.

The Fourier transform was calculated numerically by multiplying $Z(t)$ with a Gaussian function with FWHM = 1 meV. The resulting VDOS presented in the text was produced from 1 ns NVE simulation with non-rigid protons and 0.25 fs simulation step (1 fs saving frequency). Since the trajectory length limits the range of low frequencies, quadratic extrapolation to zero was applied below 10 cm^{-1}.

Analysis of Experimental Results

The relaxation time for myoglobin (Fig. 43.4 in the chapter 3) was taken from dielectric measurements of protein powders by Nakanishi and Sokolov.[28] The process named as "main" is highly stretched, with the high-frequency wing of the dielectric loss following the power law decay, $\epsilon'' \propto \omega^{-\alpha}$. The stretching exponent α changes from 0.24 at $T = 163$ K to 0.17 at $T = 143$ K (lysozyme). The dielectric loss was fitted to the Cole-Cole dispersion function with the resulting relaxation time shown

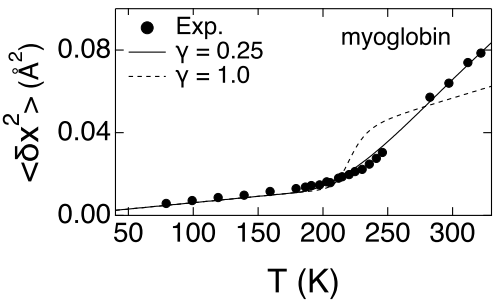

Figure A.13: MSF of Heme Iron in Oxidized Myoglobin. Points Indicate Experimental Results,[13]Solid Line Refers to the Fit to Eqs. (3.1) and (3.16) with the Nonergodicity Factor $f_{\rm ne}(T)$ Determined From Stretched Dynamics [Eq. (3.20) in the Chapter 3] With $\gamma = 0.25$ (Solid Line) and $\gamma = 1.0$ (Dashed Line). The Nonergodic Force Variance Is Determined as $\beta\langle\delta F^2\rangle_r = Af_{\rm ne}(T)$ With the Fitting Constant $A = 2.5$ nN/Å ($\gamma = 0.25$) and 1.53 nN/Å ($\gamma = 1.0$). The Relaxation Time $\tau(T)$ Is From the Broad Band Dielectric Spectroscopy of Hydrated Myoglobin Powders[28] as Shown in Fig. A.6

by points in Fig. A.13. These data, fitted to a function shown by the solid line in Fig. A.13, were used in producing the nonergodic variance of the force acting on the Fe atom in the heme of myoglobin.

Dynamics and Parameters (Chapter 5)

In chapter 5, as is also mentioned about chapter 4, the main dynamic function studied is the time auto-correlation function of the energy gap (Stokes-shift dynamics) $C_X(t) = \langle\delta X(t)\delta X(0)\rangle$. The normalized correlation function $S_X(t) = C_X(t)/C_X(0)$ calculated from MD trajectories in the oxidized states of cytochrome c was fitted to a sum of one decaying exponential function and a stretched exponential form

$$S_X(t) = A_E e^{-t/\tau_E} + (1 - A_E)e^{-(t/\tau)^\beta} \tag{A.13}$$

The average relaxation times at different temperatures are obtained according to

$$\langle\tau\rangle = A_E\tau_E + (1 - A_E)\tau\Gamma(1 + \beta^{-1}) \tag{A.14}$$

Table A.4: Total Time Correlation Function for Cyt-C (Red). The Relaxation Times Are in Ps. The Units of the Force Are eV/Å.

T	A_1	A_2	A_3	A_4	A_5	τ_1	τ_2	τ_3	τ_4	τ_5	$\langle\tau\rangle$	$\langle\delta\mathbf{F}_H^2\rangle$
280	0.518	0.045	0.002	0.012	0.423	24273	1228	0.008	0.005	0.008	12634	5.63
290	0.44	0.11	0.45	0.00	0.00	24929	2350	0.006	0.008	0.005	11240	5.69
310	0.527	0.021	0.036	0.009	0.406	12026	1228	0.008	0.010	0.005	6369	5.99
320	0.493	0.017	0.002	0.035	0.451	9259	50.40	0.009	0.007	0.01	4567	5.65
330	0.566	0.000	0.202	0.000	0.232	7444	0.026	0.009	0.020	0.008	4212	8.32
340	0.475	0.016	0.485	0.00	0.02	8501	62.65	0.009	0.62	0.01	4038	6.24
360	0.500	0.000	0.003	0.000	0.497	6603	0.009	0.008	0.006	0.007	3303	6.54

where $\Gamma(x)$ is the gamma-function.[362] The results of the fit of $\langle\tau\rangle(T)$ to the Arrhenius dependence are shown in Figure A.14.

The activation barrier was calculated as the free energy difference between the point at $X = 0$ and the bottom of the free energy surface at its minimum, $\Delta F^{\dagger} = F(0) - F(\langle X\rangle_1)$. The temperature dependence of the activation barrier for the Cyt-c reduction is shown in Figure A.16.

Table A.5: Electrostatic Component of the Force-Force Correlation Function for Cyt-C, Red. The Relaxation Times Are in Ps. The Units of the Force Are eV/Å.

T	A_1	A_2	A_3	A_4	A_5	τ_1	τ_2	τ_3	τ_4	τ_5	$\langle\tau\rangle$	$\langle\delta\mathbf{F}_H^2\rangle$
280	0.861	0.027	0.072	0.010	0.03	16229	4.733	0.002	0.4	0.05	13979	4.05
290	0.85	0.02	0.11	0.02	0.00	15443	35.34	0.07	2.940	0.06	13169	4.14
310	0.79	0.07	0.057	0.05	0.032	8333	0.038	0.03	0.1	77	6585	2.75
320	0.76	0.04	0.002	0.08	0.12	10529	1175	0.01	1.5	0.00	8038	3.45
330	0.81	0.03	0.00	0.01	0.14	7962	67.52	0.00	0.06	0.00	6483	3.73
340	0.77	0.06	0.13	0.02	0.02	10938	1081	0.077	2.98	8.12	8517	4.02
360	0.82	0.01	0.11	0.02	0.033	7837	45.2	0.00	4.52	0.585	6427	4.39

Table A.6: Total Force-Force Time Correlation Function for Cyt-C, Ox. The Relaxation Times Are in Ps. The Units of the Force Are eV/Å.

T	A_1	A_2	A_3	A_4	A_5	τ_1	τ_2	τ_3	τ_4	τ_5	$\langle\tau\rangle$	$\langle\delta\mathbf{F}_H^2\rangle$
280	0.580	0.168	0.002	0.028	0.373	21944	338.959	0.007	0.004	0.007	12730	7.09
290	0.15	0.41	0.43	0.008	0.0	35007	11053.6	0.004	29.39	0.008	9884	6.15
310	0.550	0.029	0.191	0.023	0.207	14854	78.834	0.002	0.158	0.004	8164	6.25
320	0.57	0.00	0.003	0.059	0.362	10973	0.007	0.009	0.733	0.01	6318	6.64
330	0.558	0.013	0.021	0.0	0.408	11047	198	0.004	0.005	0.007	6167	6.33
340	0.48	0.038	0.190	0.03	0.25	9712	149.6	0.003	0.183	0.004	4688	6.97
360	0.550	0.010	0.005	0.003	0.432	6331	0.250	10.0	0.005	0.009	3482	6.30

Table A.7: Electrostatic Component of the Force-Force Correlation Function for Cyt-C, Ox. The Relaxation Times Are in Ps. The Units of the Force Are eV/Å.

T	A_1	A_2	A_3	A_4	A_5	τ_1	τ_2	τ_3	τ_4	τ_5	$\langle\tau\rangle$	$\langle\delta\mathbf{F}_H^2\rangle$
280	0.87	0.00	0.00	0.024	0.10	16917	111.7	0.002	19.72	0.003	14697	4.99
290	0.9	0.02	0.04	0.045	0.00	12124	1.86	0.001	0.051	0.018	10912	6.01
310	0.81	0.08	0.08	0.02	0.01	16048	1451	0.00	0.78	0.7	13202	6.29
320	0.9	0.00	0.03	0.00	0.067	10553	0.327	0.00	0.01	0.00	9486	6.47
330	0.852	0.017	0.015	0.092	0.023	11171	164	7.68	0.060	1.076	9526	6.26
340	0.738	0.15	0.04	0.04	0.03	27377	1727	0.745	0.01	0.01	20461	6.97
360	0.861	0.002	0.11	0.03	0.0	7028	64.34	0.00	0.37	0.00	6054	6.30

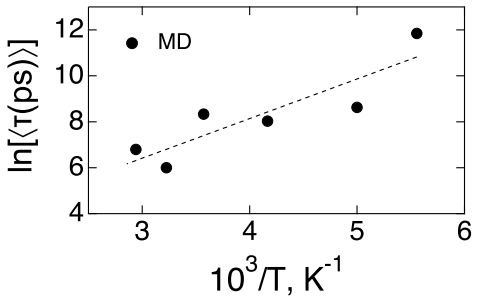

Figure A.14: Relaxation Time of the Stokes-Shift Dynamics (Eq (A.14))As a Function of $1/T$.The Points Refer to the Simulation Data for the Oxidized Form of Cyt-C and the Dashed Straight Line Is the Linear Regression $\ln[\langle\tau(\text{ps})\rangle] = 1.24 + 1725\text{K}/T$.

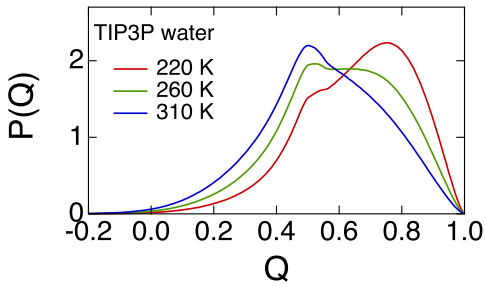

Figure A.15: Distribution $P(Q)$Of the Tetrahedral Order Parameter Q (Eq (5.5)) At Different Temperatures for TIP3P Water.

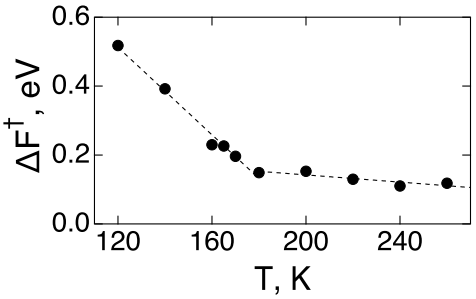

Figure A.16: Activation Barrier for the Reduction Reaction of Cyt-C Vs T. Points Are the Simulation Results and the Dashed Lines Are Linear Fits Through the High-Temperature and Low-Temperature Portions of the Data.

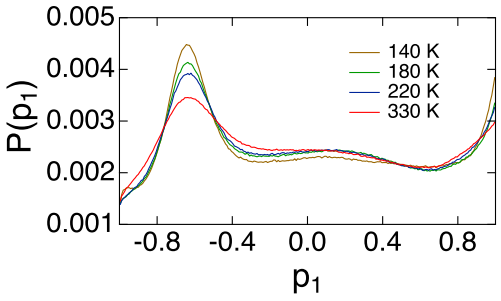

Figure A.17: Distribution Functions of the First-Order Orientational Order Parameter p_1 (Eq (A.15)) In the Hydration Shell of Oxidized Cyt-C ($a = 6$ Å)At Different Temperatures Indicated in the Plot. The Maximum of the Distribution Corresponds to the Angle 130°Between the Water Dipole Moment and the Normal to the Protein Surface.

A.2.4 Order Parameters of Hydration Water

The tetrahedral order parameter[24, 25, 23] is given by the equation (5.5). Figure (5.3a) shows the dependence of the average $\langle Q \rangle$ within the hydration shell of Cyt-c on temperature. As expected, there is a continuous increase of tetrahedral order of the hydration water with lowering temperature (Figure A.15). We also find that hydration water is less ordered than bulk SPC/E[23] and TIP3P water.

We have also calculated the first two, $l = 1, 2$ orientational order parameters of the water molecules in the protein's hydration shell

$$p_l = P_l(\hat{\mathbf{e}} \cdot \hat{\mathbf{n}}) \tag{A.15}$$

where $\hat{\mathbf{e}}$ is the unit vector of the water dipole moment chosen within the distance a from the protein surface and $\hat{\mathbf{n}}$ is the unit normal to the protein surface ($P_l(x)$ is the Legendre polynomial of order l). The calculation of the unit normal $\hat{\mathbf{n}}$ first involved the location of the protein atom closest to a given water molecule. Once the closest protein atom was located, the normal direction was determined along the vector connecting this atom to water's oxygen.

The distribution functions of p_1 at different temperatures are shown in Figure

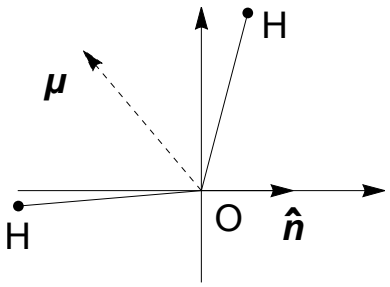

Figure A.18: Configuration of the Water Molecules Relative to the Normal to the Protein Surface $\hat{\mathbf{n}}$Corresponding to the Maximum of $P(p_1)$ in Figure A.17. $\boldsymbol{\mu}$ Shows the Direction of the Dipole Moment and the Lines Represent the OH Bonds.

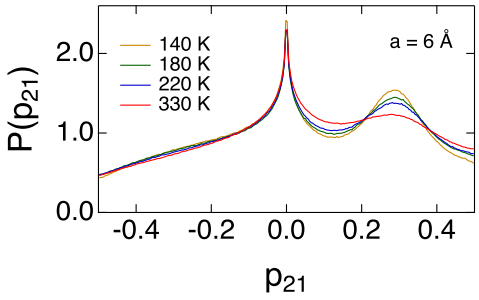

Figure A.19: Distribution Functions of the Orientational Order Parameter p_{21} (Eq (A.16))In the Hydration Shell of Oxidized Cyt-C (a = 6 Å)At Different Temperatures Indicated in the Plot. The Lower Maximum of the Distribution, Growing with Lowering Temperature, Corresponds to the Angle $\chi = 0°$Between the Plane of the Water Molecule and the Plane Containing the Normal and the Water Dipole Moment.

A.17. It is clear that there is a broad spread of dipolar orientations in the shell, with some preference for a radial orientation parallel or antiparallel to the local normal to the surface. The temperature variation of the distribution does not reveal, however, any discontinuous changes pointing to a structural transition in the hydration shell.

The maximum of the distribution $P(p_1)$, at the angle $\theta = 130°$ between $\hat{\mathbf{n}}$ and $\boldsymbol{\mu}$, corresponds to the configuration in which the water molecules in the interface point their hydrogens toward the protein surface (Figure A.18). Further identification of this preferential orientation is achieved by considering an additional order parameter appearing from the expansion of the interfacial distribution functions in rotational

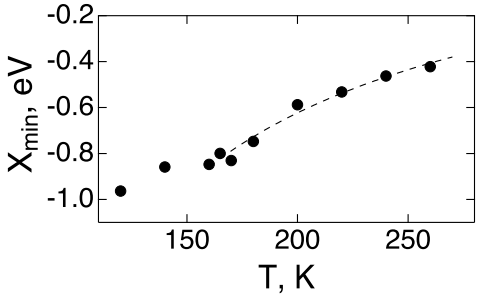

Figure A.20: Dependence of the Minimum of the Free Energy of Electron Transfer in the Oxidized Form of Cyt-C on Temperature. The Dashed Line Shows the Hyperbolic Fit to the Results at $T > T_c$.

invariants[322]

$$p_{21} = \tfrac{1}{2}\langle \sin\theta^2 \cos 2\chi \rangle \tag{A.16}$$

The angle χ is between the plane containing $\hat{\mathbf{n}}$ and $\boldsymbol{\mu}$ and the plane of the water molecule. Figure A.19 shows the distributions of p_{21} at different temperatures. The sharp spike at $p_{21} = 0$ reflects water molecules next to hydrophobic patches of the protein, where water tends to orient in plane of the dividing surface.[365] Changing temperature does not strongly affect the orientational structure in those parts of the interface. The second peak, increasing in amplitude with lowering temperature, is reached at $\theta = 130°$ and $\chi = 0$ and describes the increasing populations of water's hydrogens pointing toward the protein surface, either through hydrogen bonds or through dangling bonds. This is the configuration shown in Figure A.18.

A.2.5 Modeling of Cyclic Voltammograms

The calculations were performed for the reduced current $\psi = i/(\beta e^2 v A \Gamma_t)$ as defined by Laviron.[21] Here, $i = i_c - i_a$ is composed of the cathodic, i_c, and anodic, i_a, currents passing through the area A under the applied voltage with the scan rate v. The equation for the reduced current is given in terms of the surface mole fractions of the oxidized, $x_{\mathrm{O}} = \Gamma_{\mathrm{O}}/\Gamma_t$, and reduced, $x_{\mathrm{R}} = 1 - x_{\mathrm{O}}$, adsorbates; Γ_t is the total

surface concentration. The equation for the current is[20]

$$\psi = (k_{\mathrm{O}}/v^*)x_{\mathrm{O}} - (k_{\mathrm{R}}/v^*)(1 - x_{\mathrm{O}}) \tag{A.17}$$

Here,

$$v^* = \beta e v/k(0) \tag{A.18}$$

is the dimensionless scan rate and $k(0)$ is the rate at zero overpotential, $\eta = 0$, and $\beta = 1/(k_{\mathrm{B}}T)$. Further, the reduced rates for the oxidation and reduction reactions in eq (A.17) are

$$\begin{aligned} k_{\mathrm{O}}(\eta) &= \left[\mathrm{erfc}(\sqrt{\beta\lambda^r}/2)\right]^{-1} \mathrm{erfc}\left(\frac{\lambda^r + e\eta}{2\sqrt{k_{\mathrm{B}}T\lambda^r}}\right), \\ k_{\mathrm{R}}(\eta) &= \left[\mathrm{erfc}(\sqrt{\beta\lambda^r}/2)\right]^{-1} \mathrm{erfc}\left(\frac{\lambda^r - e\eta}{2\sqrt{k_{\mathrm{B}}T\lambda^r}}\right) \end{aligned} \tag{A.19}$$

where ercf(x) is the complimentary error function. The solution for $x_{\mathrm{O}}(\eta)$ is given as[20]

$$\begin{aligned} x_{\mathrm{O}}(\eta) = {} & e^{\frac{1}{v}\int_{\eta_m}^{\eta}(k_{\mathrm{O}}+k_{\mathrm{R}})dz} \\ & - \frac{1}{v}\int_{\eta_m}^{\eta} dz k_{\mathrm{R}}(z) e^{\frac{1}{v}\int_{z}^{\eta}(k_{\mathrm{O}}+k_{\mathrm{R}})dy} \end{aligned} \tag{A.20}$$

where the cathodic sweep runs from η_m to $-\eta_m$ with the scan rate magnitude v. This equation is the solution of the kinetic equation for the surface mole fraction of the oxidized state

$$-\frac{v}{k(0)}\frac{dx_{\mathrm{O}}}{d\eta} = k_{\mathrm{R}} - (k_{\mathrm{O}} + k_{\mathrm{R}})\, x_{\mathrm{O}} \tag{A.21}$$

A.3 Charge Screening

A.3.1 Simulation Protocol

The simulation cell was created by combining PDB coordinate files corresponding to two dummy atoms and a box of SPCE water.[29] The dummy atoms were placed symmetrically a distance R apart from one another along the x-axis and the water

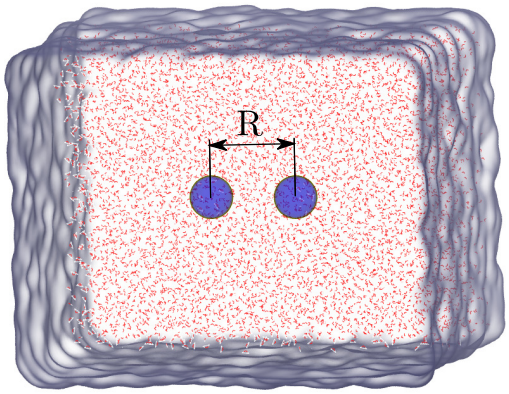

Figure A.21: A Cartoon of the Simulation Cell Including Two Kihara Solutes Separated by the Distance R in the Cubic Simulation Cell Containing SPC/E[29] Water Molecules.

molecules within the distance $R_{0s} = r_{HS} + \sigma_{0s}$ from the dummy atom's center were removed, resulting in 7408 SPC/E water molecules in the box. The solute radius R_{0s} combines the hard-sphere core r_{HS} with van der Waals diameter σ_{0s} appearing in the Kihara potential describing the isotropic solute-solvent interaction

$$u_{0s}(r) = 4\epsilon_{\mathrm{LJ}} \left[\left(\frac{\sigma_{0s}}{r - r_{\mathrm{HS}}} \right)^{12} - \left(\frac{\sigma_{0s}}{r - r_{\mathrm{HS}}} \right)^{6} \right] \tag{A.22}$$

The following parameters were used for the Kihara potential: $r_{\mathrm{HS}} = 2$ Å, $\sigma_{0s} = 3$ Å, and $\epsilon_{\mathrm{LJ}} = 0.65, 3.7,$ and 20.0 kJ/mol. The center of each Kihara solute was shifted from the origin to a distance $\pm R/2$ along the x-axis as illustrated in Fig. A.21. The separation distance between the two Kihara spheres was then varied from 10 Å to 20 Å.

All simulations were performed using the NAMD[172] simulation package with a 2 fs timestep. The system was initialized by first energy minimizing for 1000 steps and then performing a 1 ns NPT simulation allowing the sides of the box to relax around the system. A cubic simulation cell with side length of 60 Å was created by the end of NPT simulations. Following this initial equilibration, a 200 ps NVT equilibration at

Table A.8: Cross Correlation of the Electrostatic Potential $I(R)$ [Eq. (6.13)] in Å^{-1}.

Distance, Å	11	11.5	12	12.5	13.0	14.0	15.0	15.5	16.0	17.0	18.0	20.0
$I(R) \cdot 100$	4.25	3.90	4.34	3.62	3.35	2.62	1.991	1.74	1.95	1.78	1.06	0.72

300 K was performed. The long range electrostatic forces were calculated using the Particle Mesh Ewald (PME) technique with a cutoff distance of 18 Å (also used for the Kihara potential). All forces were calculated at every step along the trajectory and configurations were saved every 10 ps. Simulation trajectory were $\approx$ 90 ns in length, of which 80 ns were used for production.

The Kihara potential was implemented using NAMD's tclBC module and the tclBC configuration file handling both Kihara centers was developed in-house by considering the general relationship between the potential and the force, $\mathbf{F}_{0s} = -\nabla u_{0s}$, with $u_{0s}(r)$ from Eq. (A.22). The dummy atoms added to the system were used to calculate the electrostatic potential at the center of each cavity using NAMD's pair-interaction energy plugin by setting the charge of the dummy atom equal to +1 e. The force calculation for these dummy atoms was turned off throughout the production of trajectory configurations and these two atoms were held fixed by using the `fixedAtom` keyword available within NAMD.

The electrostatic screening between the charges in SPC/E water was calculated from the cross-correlation of the electrostatic potentials at the centers of two Kihara solutes according to the equation (6.13). The results of calculations from the MD trajectories are listed in Table A.8.

A.3.2 Derivation of Equations in (6.14)

Here we provide details of the derivation of Eq. (6.14). It follows from using the Fourier transform in the single particle (first summand) and two-particle (second

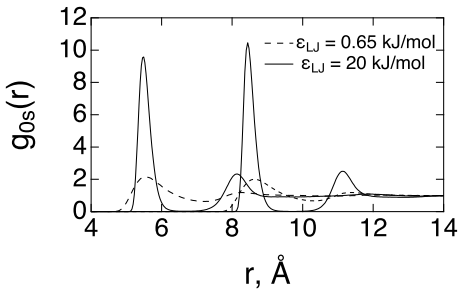

Figure A.22: $g_{0s}(r)$For Kihara Solutes in SPC/E Water with $R_0 = r_{\rm HS}+\sigma_{0s}$ Equal to 5 Å and 8 Å.The Values of the Solute-Solvent Lennard-Jones Energy $\epsilon_{\rm LJ}$Are Indicated in the Plot.

summand) equation for the potential correlation written in direct space in Eq. (6.9). We therefore follow the transformation for each term separately, which we specify as I_1 and I_2. The one-particle term can be written as

$$\begin{aligned} I_1 &= \rho \int d1 \phi_{s1}(1)\phi_{s2}(1) g_{0s}(r_1)^2 \\ &\quad - \rho \int d1 \phi_{s1}(1)\phi_{s2}(1) g_{0s}(r_1) h_{0s}(r_1). \end{aligned} \tag{A.23}$$

the Fourier transforms are performed on the effective electrostatic potentials $\phi_{si}(1)g_{0s}(r_1)$ accounting for the interfacial structure through the solute-solvent pair distribution function $g_{0s}(r)$. The corresponding Fourier transforms become

$$\begin{aligned} \tilde{\phi}_{s1}(\mathbf{k}) &= -4\pi i (\mathbf{m}\cdot\hat{\mathbf{k}})\ f_{0s}(k) \\ \tilde{\phi}_{s2}(\mathbf{k}) &= -4\pi i (\mathbf{m}\cdot\hat{\mathbf{k}})\ e^{i\mathbf{k}\cdot\mathbf{R}} f_{0s}(k), \end{aligned} \tag{A.24}$$

where

$$f_{0s}(k) = k \int_0^\infty dr j_1(kr) g_{0s}(r). \tag{6.15}$$

Examples of $g_{0s}(r)$ for two sizes of the Kihara solute $R_0 = r_{\rm HS} + \sigma_{0s}$ and the Lennard-Jones energies $\epsilon_{\rm LJ}$ equal to 0.65 kJ/mol and 20 kJ/mol are shown in Fig. A.22. For the higher attraction energy, $\epsilon_{\rm LJ} = 20$ kJ/mol, one observes layering between the first and second hydration shells (zero probability to find a water molecule).

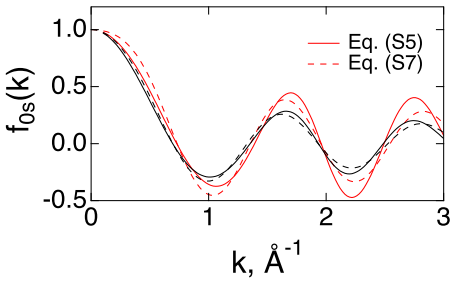

Figure A.23: Numerical Integration in Eq. (6.15)And Fit to Eq. (6.22) for $\epsilon_{\mathrm{LJ}} = 0.65$ (Black) and $\epsilon_{\mathrm{LJ}} = 3.7$ kJ/mol (Red). The Fitting Parameters Are $c = 1.806$, $a = 5.0$ Å and $b = 6.15$ Å (Black) and $c = 2.65$, $a = 5.0$ Å and $b = 6.06$ Å (Red).

The angular integration over the orientations of the solvent dipole **m** and the wavevector **k** then result in the one-dimensional k-integral

$$I_1(R) = \frac{6y}{\pi} \int_0^\infty dk k j_0(kR) f_{0s}(k). \tag{6.14}$$

As is discussed in the chapter 6, the function $f_{0s}(k)$ can be represented by a linear combination of two zeroth-order spherical Bessel functions originating from two blips of the solute-solvent Boltzmann factor

$$f_{0s}(k) = c j_0(ka) + (1-c) j_0(kb). \tag{6.22}$$

Figure A.23 shows the fit of $f_{0s}(k)$ from the direct integration in Eq. (6.15) to Eq. (6.22). Assuming that $f_{0s} \sim \exp[i2bk]$ at $k \to \infty$, one can close the integration contour in the upper half of complex k-plane and assume that $f_{0s}(k)$ is an analytic function of the complex variable k. At $R > 2b$ one then obtains

$$I_1(R) = \frac{3y}{R}. \tag{A.25}$$

We now turn to the two-particle term

$$I_2(R) = \rho^2 \int d1 d2 \phi_{s1}(1) \phi_{s2}(2) g_{0s}(r_1) g_{0s}(r_2) h_{ss}(1,2). \tag{A.26}$$

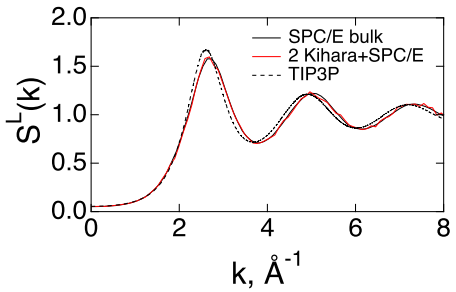

Figure A.24: $S^L(k)$ Calculated for Bulk SPC/E Water and for the Solution with Two Kihara Solutes at the Distance $R = 10$ Å. The Two Lines Are Nearly Indistinguishable on the Scale of the Plot. Also Shown Is the Longitudinal Structure Factor of TIP3P Water.[30] All Results Refer to $T = 300$ K.

By substituting the Fourier transforms of $\phi_{s1}(1)$ and $\phi_{s2}(2)$ and integrating over the orientations of two dipole moments in the liquid and the wavevector **k** we arrive at the result

$$I_2(R) = \frac{6y}{\pi} \int_0^\infty dk f_{0s}(k)^2 j_0(kR) \left[S^L(k) - 1\right] \tag{6.14}$$

Here, $S^L(k)$ is the linear combination of two projections of the solvent-solvent pair correlation function on rotational invariants,[361, 360, 27] h^Δ and h^D. The longitudinal structure factor is a linear combination of the corresponding Fourier transforms specified with tildas

$$S^L(k) = 1 + (\rho/3) \left[\tilde{h}^\Delta(k) + 2\tilde{h}^D(k)\right]. \tag{A.27}$$

The structure factor of bulk SPC/E water was calculated from simulations and used in numerical integration in Eq. (6.14). The perturbation derivation of this equation assigns $S^L(k)$ instead to the solution of SPC/E water with two Kihara solutes. We have calculated $S^L(k)$ both for the solution and for bulk SPC/E water and found the two results nearly indistinguishable (Fig. A.24).

The function $S^L(k)^{-1}$ expands to a linear function of k^2 at low k-values as is shown in Fig. A.25. The expansion is used to construct the Paé form for $S^L(k)$ as

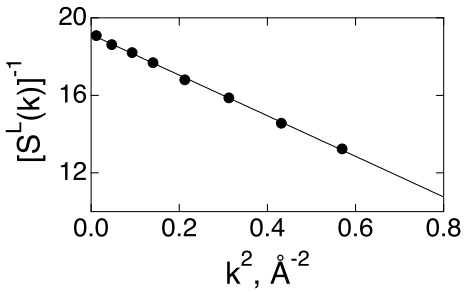

Figure A.25: Linear Fit of $[S^L(k)]^{-1}$ Vs k^2. Points Are Calculated From MD on the Lattice Vectors Consistent with the Simulation Box and the Solid Line Is a Linear Fit $19.14 - 10.47k^2$. The Simulation Results Are for the SPC/E Water at 300 K.

follows

$$S^L(k) = \frac{S^L(0) + \Lambda^2 k^2}{1 + \Lambda^2 k^2}. \tag{6.23}$$

The linear fit in Fig. A.25 is used to calculate $\Lambda = 0.17$ Å for SPC/E water at 300 K. However, as we discuss in the chapter 6, this approximation is not reliable and better estimates of the integrals involving $S^L(k)$ are obtained by using either the Lorentz or the MSA approximations for the longitudinal structure factor.